University of Southampton

Faculty of Engineering and Physical Sciences

School of Engineering

Characterisation of lightning strike induced damage in CFRP laminates and components for wind turbine blades

by

Timothy M Harrell

ORCID: 0000-0002-0783-533X

Thesis for the degree of Doctor of Philosophy

January 2020

Abstract

University of Southampton

Faculty of Engineering and Physical Sciences

School of Engineering

Thesis for the degree of Doctor of Philosophy

Characterisation of lightning strike induced damage in CFRP laminates and components for wind turbine blades

By Timothy M Harrell

To meet worldwide increases in energy demand Wind Turbine (WT) manufacturers are producing longer blades to generate more energy. These blades contain Carbon Fibre Reinforced Polymers (CFRP) in the load carrying structures to lightweight the blade. The introduction of the CFRP composites has presented new challenges in protecting the structure from lightning. The semi-conductive nature of CFRP leads to an additional path to ground for the current in the structure and the anisotropic nature of the material's thermal and electrical properties leads to large amounts of resistive heating especially in the through-thickness direction where the electrical conductivity is the lowest. The aim of this PhD is to devise a new means of assessing the damage and resulting structural behaviour caused by a lightning strike. A modelling framework is developed and validated against high fidelity experimental data that can be used by design engineers to understand the consequences of various lightning damage scenarios and the effectiveness of lightning protection methods. The framework is validated against a representative scale WT sparcap test component in the form of a large panel subjected to compression.

The novel damage model is a thermal-electrical Joule heating model which simulates the resistive heating in a UD laminate with electric field dependent material properties to account for electric breakdown. The damage prediction is then exported into a structural Finite Element Model (FEM) by assuming the damaged elements have different material properties. The structural behaviour under compression loading is the main design driver for long slender WT blades. Therefore, the structural model simulates the behaviour of a damaged laminate in a non-linear post-buckling FEM. To validate and inform the damage model and the FEM two different types of tests were conducted.

The first type of test simulated the lightning strikes and comprised of direct strike and conducted current tests. The effect of conducting current along the fibre direction showed a deleterious effect on the compressive and shear properties of the material. Initial direct strike tests were used to vary the typical lightning parameters to determine the largest influence on damage among peak current, specific energy, or charge. The last direct strike test is conducted on a representative WT sparcap panel. All damaged panels were evaluated using visual inspection, a new thermography technique, and X-ray computed tomography (CT). The newly developed damage model was validated using the experimental observations with the damage area predictions within 15% of the visual observation and the damage depth within 5% of the CT scans. Hence, the electric field dependency was successfully implemented in the model.

The second test type was a structural test that incorporated the development of a new testing methodology named the compression after lightning strike (CALS) test. Large representative

sparcap panel specimens, with and without lightning damage were tested to failure in the CALS rig and Digital Image Correlation (DIC) was used to determine the resulting surface displacements and strains. The structural model closely predicted the compressive behaviour and failure loads identified by the DIC. The resulting structural model calculated the first ply failure stresses from the LaRC failure criteria which were within 8% of experimental values, which provided a successful validation of the modelling framework.

Table of Contents

List of Tables

List of Figures

Research Thesis: Declaration of Authorship

Print name:	Timothy M Harrell
Title of thesis:	Characterisation of lightning strike induced damage in CFRP laminates and components for wind turbine blades

I declare that this thesis and the work presented in it are my own and has been generated by me as the result of my own original research.

I confirm that:

1. This work was done wholly or mainly while in candidature for a research degree at this University;
2. Where any part of this thesis has previously been submitted for a degree or any other qualification at this University or any other institution, this has been clearly stated;
3. Where I have consulted the published work of others, this is always clearly attributed;
4. Where I have quoted from the work of others, the source is always given. With the exception of such quotations, this thesis is entirely my own work;
5. I have acknowledged all main sources of help;
6. Where the thesis is based on work done by myself jointly with others, I have made clear exactly what was done by others and what I have contributed myself;
7. Parts of this work have been published. Please see Appendix F for references.

Signature: Date:

Acknowledgements

I have had so much help from so many people over this project. I am very grateful to everyone and wouldn't be here without it. Firstly, I must thank my supervisory team Ole Thybo Thomsen and Janice Dulieu-Barton. I would also like to thank my SPARCARB colleagues Orestis, Andrea and Evangelos. Also, special thanks to the SPARCARB project partners who helped along the way with specific mentions to Søren and Lisa from Poly-tech; Lars Bo and Boas from LM Wind Power; and Micah from Boeing.

A great deal of thanks for the help of the technical staff at the University of Southampton especially the support from Andy Robinson in the TSRL and Mav, Richard, and Katy in the μ-VIS X-Ray Imaging Centre.

I also would like to give a special thanks to my fellow PhD colleagues who have been there for advice and acted as a sounding board as I tried to piece the fragments of this thesis together. In no particular order, I would like to thank Tobi, Jack, Geir, Saran, Giannis, Dan, and Alex.

I also would like to thank my family for their continued support during the PhD. I apologize that it wasn't "home", but I hope you had fun on our European gallivant.

I have saved the best for last. I want to thank my wife Amanda for all her support. I could not have completed this without you. I hope that I can repay the favour to you.

Definitions and Abbreviations

AI	Action integral, or specific energy
CALS	Compression After Lightning Strike
CAI	Compression After Impact
CC	Continuous Current
CFRP	Carbon Fibre Reinforced Polymers
CT	X-ray Computer Tomography
DC	Direct Current
DIC	Digital Image Correlation
EMF	Expanded Metal Foil
FEM	Finite Element Model
GFRP	Glass Fibre Reinforced Polymer
HAWT	Horizontal Axis Wind Turbine
ICC	Initial Continuous Current
IEC	International Electrotechnical Commission
IRT	Infrared Thermography
L	Longitudinal direction
LaRC	NASA Langley Research Centre but used in context of a failure criteria it is named after
LPL	Lightning Protection Level
LPZ	Lightning Protection Zones
LPS	Lightning Protection System
ROI	Region of Interest
T	Transverse direction
TT	Thru-thickness direction

UD	Unidirectional
USFLD	USer Defined Field subroutine for commercial finite element software Abaqus
WT	Wind Turbines
A	Pre-exponential factor
AI	Action integral or specific energy
AI_{DC}	Specific energy associated with the DC portion of waveform
AI_{Imp}	Specific energy associated with the impulse portion of waveform
AI_T	Specific energy associated with the total waveform
C	Degree of pyrolysis
$\vec{E}$	Electrical field
$\vec{E}_{bdT}$	Electric breakdown strength in the transverse direction
$\vec{E}_{bdTT}$	Electric breakdown strength in the through-thickness direction
E_a	Activation energy
G	Shear modulus
$i(t)$	Electrical current function with time
I_{peak}	Peak current
K	Reaction rate constant
Q	Charge
$\|Q\|$	Absolute value charge
Q_{DC}	Charge associated with DC portion of waveform
Q_{Imp}	Charge associated with impulse portion of waveform
Q_T	Charge associated with the total waveform
R	Gas constant equal to 8.314 J/mol/K
t	Time
t_f	Final time of electrical current waveform

t_1	Time at peak current
t_2	Time at half peak current, known as half time
t_{DC}	Time DC waveform is applied
W_0	Original mass of an object
W_i	Mass of an object at increment i
W_t	Final mass of an object
γ_y	Shear yield strain
ε	Total strain
ε_e	Elastic strain
ε_i	Inelastic strain
σ_L	Electrical conductivities in the longitudinal direction (Chapter 4)
σ_T	Electrical conductivities in the transverse direction (Chapter 4)
σ_{TT}	Electrical conductivities in the through-thickness direction (Chapter 4)
σ	Mechanical stress (Chapter 3,6)
σ_0	Mechanical stress at the horizontal asymptote of the stress-strain curve
σ_c	Critical stress
τ	Mechanical shear stress
ϕ_0	Initial fibre misalignment

Chapter 1

Introduction

1.1 Background and Motivation

Energy demand is rising; according to the International Energy Agency, energy consumption worldwide grew by 2.3% in 2018 which is nearly twice the average rate of growth since 2010 [1]. Wind Turbines (WT) provide a sustainable means of meeting rising worldwide energy demands. WTs are sustainable energy sources as they convert kinetic energy generated from wind into electric energy using a generator that is turned by rotating blades. Furthermore, wind energy is economical. Onshore WTs surpassed both coal and gas as the cheapest energy source in the UK in 2015 [2]. Several studies [3]–[7] have shown that in the G20 countries, the onshore WTs are now on average (or by 2020) the cheapest energy source. Figure 1.1 shows the Lazard study where even high-end estimates of wind energy production cost are lower than coal.

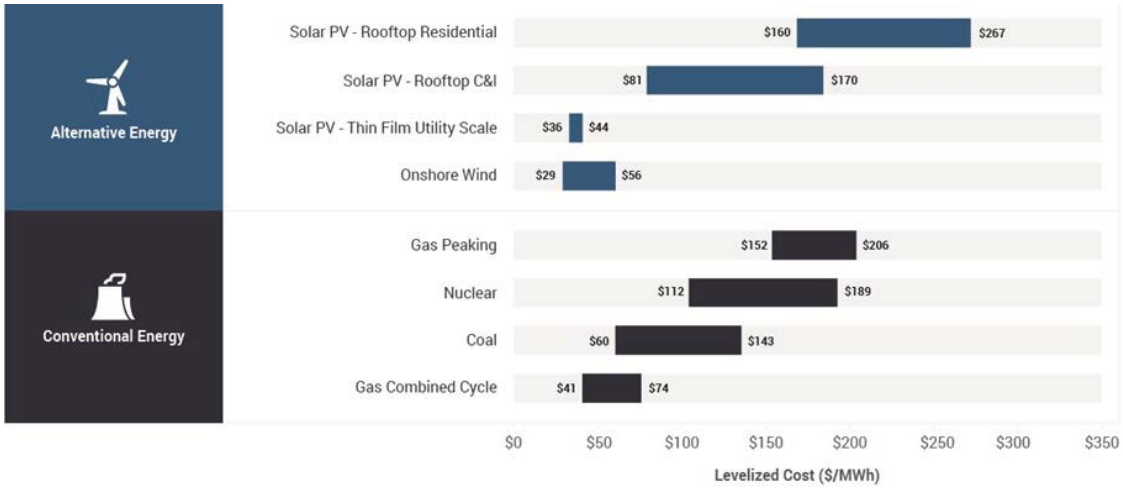

Figure 1.1: Lazard's analysis of LCOE for various energy sources year 2018 [3]

WT emit less carbon into the atmosphere when compared to conventional energy sources and are therefore less polluting. For this reason, many countries have created targets to increase their renewable energy production. The EU is working toward a legally binding target to meet a goal of 20% energy consumption through renewable energy by 2020 [8]. China has set a target of 18% energy production from WTs by 2050 [9]. Denmark is the first and as of this writing the only country to set a target of a 100% share of renewables in final energy (electrical, heating & cooling, transportation) [10]. Hawaii [11] and Puerto Rico [12] have also signed legislation for 100% renewable energy target (electrical). Figure 1.2 shows a map of renewable energy targets around the world [9]–[16]. This demand for renewable energy has increased demand for WTs with large energy production capabilities.

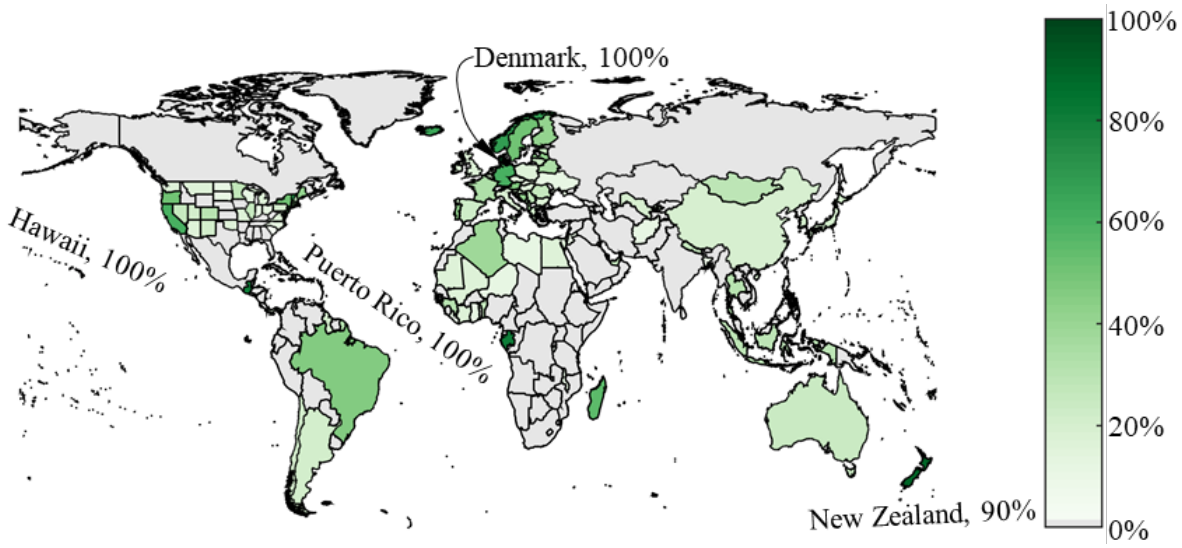

Figure 1.2: Renewable energy targets from around the world with detailed breakdown of the United States in final energy/share of renewable energy in place by May of 2019 (Sources: [9]–[16])

The most commonly used WTs are Horizontal Axis Wind Turbines (HAWTs). The horizontal axis is defined as the rotating axis of the WT being parallel with the ground. All modern large WTs are of the horizontal axis type. They are the most efficient, as they have the highest power coefficient and are the most reliable compared to vertical axis WTs [17]. The current PhD project focuses on the blades of HAWTs. The most efficient way to produce more electric energy from WTs is to increase the blade lengths [18] with a significant gain in power output from increased blade length [20]–[30]; see Figure 1.3.

The rated power of HAWTs is proportional to the swept area of the blades or in other words proportional to the rotor disk diameter raised to the power of 2. As WTs become larger, there is an associated increase in the mass of the blades. Experience shows that the mass of the blade increases proportionally to the blade length raised to the power of approximately 2.2 [30] as shown in Figure 1.4. These increases in blade mass leads to significant increases in gravity and inertia loads, which has knock-on effects to the design of expensive structural components like the drive train, main bearings and generator. In the past, blades were mainly made with Glass Fibre Reinforced Polymer (GFRP) composites. However as the industry is developing and producing larger turbines [18], the introduction of Carbon Fibre Reinforced Polymer (CFRP) materials as part of the blade structure leads to significant reduction of the overall mass of a blade. Figure 1.4 shows the difference in mass between a pure GFRP blade and a blade with both CFRP and GFRP.

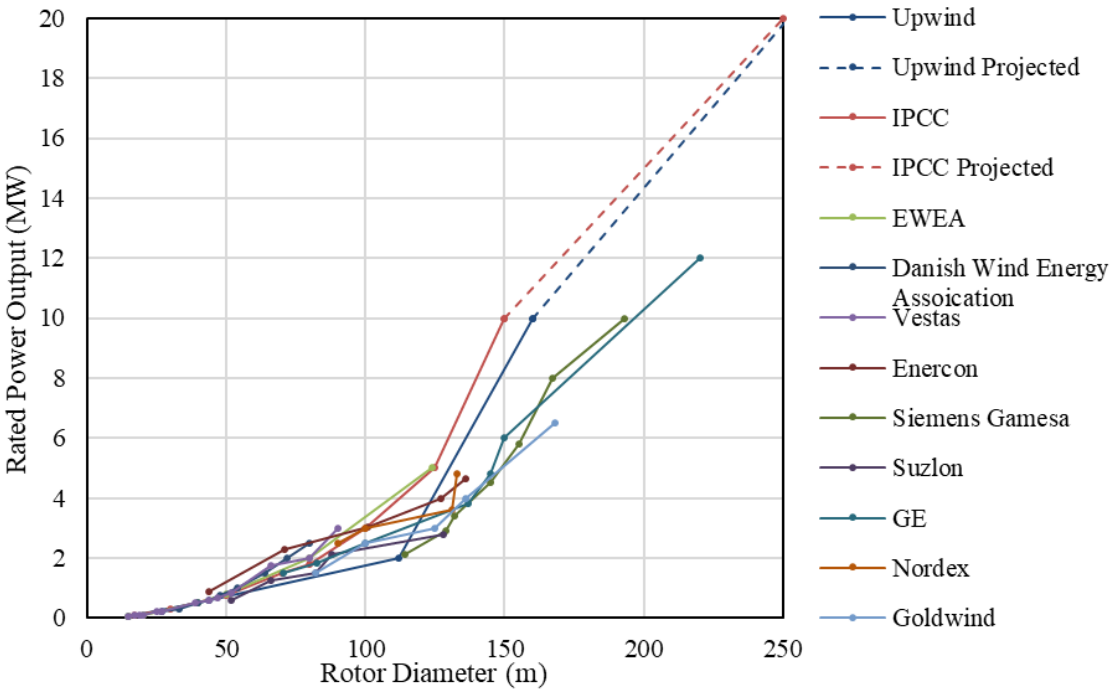

Figure 1.3: Comparison of rotor diameters to power output; data compiled from [19]-[31]

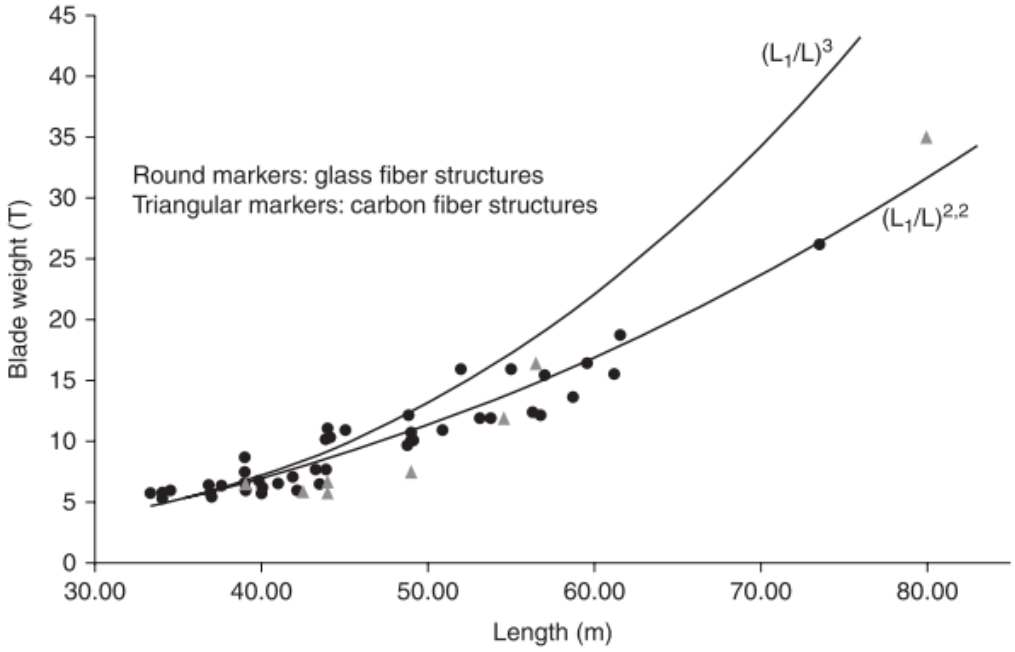

Figure 1.4: Blade mass increase with blade length increase [30]

CFRP material is significantly more costly than GFRP, which in most cases makes it impractical to use for the whole structure. Accordingly, the CFRP materials are used specifically for blade elements that carry significant structural loads. The main application is to carry very large compressive and tensile loads in the sparcaps, when a WT blade is subjected to aerodynamic loading in flapwise bending [32]; see Figure 1.5. The sparcaps are encapsulated in an external shell. The external shell is used to create lift which turns the blade and is designed to transfer the

aerodynamic forces into the sparcap. These shells are typically made of a combination of GFRP sandwich laminates with foam core and monolithic GRFP elements [32].

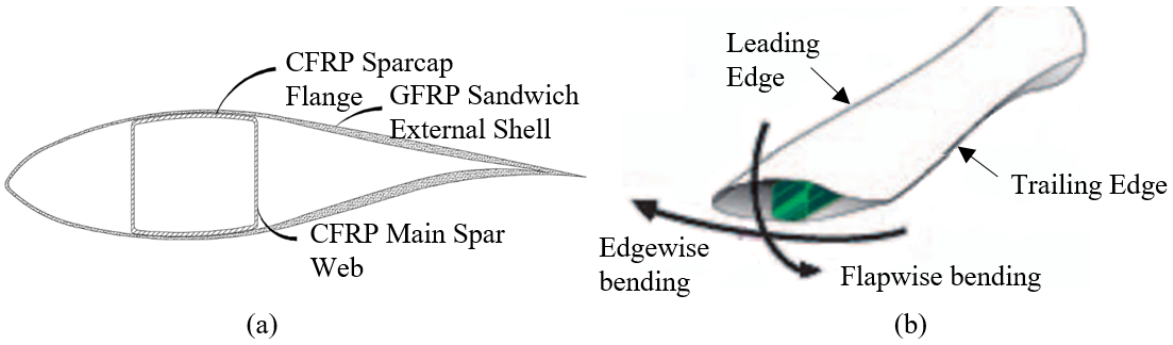

Figure 1.5: (a) Cross sectional view of typical WT blade design and (b) is WT components with loading details for the flapwise and edgewise bending loads [32]

The introduction of CFRP composites has presented new challenges in protecting the structure from lightning. The semi-conductive nature of the CFRP leads to an additional path to ground for the electric current in the structure, and the anisotropic nature of the material thermal and electrical properties leads to large amounts of resistive heating (or Joule heating), especially in the through-thickness direction where the electric conductivity is the lowest. The heating causes elevated temperatures leading to damage in the forms of resin burn off, fibre breakage and delamination [33]–[35]. These damages and their relation to the effects on structural response are not well understood. Therefore, this PhD studies the damage and ultimate structural response of the CFRP materials.

1.2 SPARCARB Project

The current PhD project is part of a larger research project entitled "SPARCARB - Lightning protection of WT blades with carbon fibre composite materials," which is funded by the Marie Skłodowska-Curie ITN EID (European Industrial Doctorate) actions under Horizon 2020. The SPARCARB project combines the industrial knowledge of project partners to address the lack of doctoral-level trained human resources to push forward the research base in the field of lightning protection of CFRP structures, building a proper environment for shifting paradigms in the wind power industry. The project partners include university support from University of Southampton and Technical University of Denmark (DTU), a lightning protection consulting firm Global Lightning Protection Services A/S[1] (GLPS) in Denmark, WT blade manufactures LM Wind Power in Denmark and Nordex in Germany, aircraft manufacturer Boeing in the USA, and carbon fibre materials manufacturer Zoltek in the USA. Industrial placements during the course of this PhD project covered a total of 18 months. This enhanced the PhD project with practical knowledge on

[1] In 2018, GLPS was bought out by Poly-Tech A/S and now operates under the Poly-Tech name

lightning protection of CFRP materials. 15 months was spent with GLPS, along with 6 weeks each at LM Wind Power and Boeing.

Specifically, the scientific and technological challenges related to an effective protection of very large WT blades with CFRP structural elements from lightning-induced damage were studied by 4 early stage researchers (PhD students), one of which being the PhD project presented in this thesis. The SPARCARB project addresses these material-based challenges by developing a comprehensive understanding of the phenomena behind the material and structural damage based on a combined experimental and modelling/computational approach. Based on this, the aim of SPARCARB was to propose, develop and validate design solutions that facilitate a wider and sustainable use of CFRP for blade structures. The results from the SPARCARB project are presented online [36]; project number 642771.

1.3 Aim and Objectives

The main purpose of this PhD is to determine the effect of damage induced by a lightning strike on the performance of CFRP composite structures. Through a unique modelling and experimental framework, a pristine CFRP laminate can be simulated to determine damage from a lightning strike and the results from the model can be used to calculate the residual structural response. The objectives to achieve this PhD are as follows:

1. Experimental investigation of the degradation of mechanical properties of CFRP subjected to electrical current conducted along the fibre direction.
2. Development of coupled thermal-electrical models to predict damage inflicted by lightning strikes in CFRP laminates and components.
3. Validation of the predictive coupled thermal-electrical damage models with results from an experimental investigation on a CFRP sub-structural WT component that was subjected to simulated lightning strikes.
4. Development of structural models that include the coupled thermal-electrical damage model to predict the mechanical failure of CFRP blade materials after a lightning strike.
5. Experimental validation of the predictive structural models using representative CFRP panels that were subjected to simulated lightning strike, and subsequently loaded in compression to simulate the most severe loading condition experience in a wind blade sparcap.

1.4 Novelty

Previous research in the field of lightning induced damage on CFRP materials primarily focuses on the result of experimental studies, in which simulated lightning strikes were produced in laboratory settings and struck on CFRP material coupons [37]–[39], or on models [40]–[43] developed to

determine the associated damage. The simulated lightning strike experiments performed in this PhD exposed previously unnoticed physics, which change the expected shape of the damage zone for unidirectional (UD) CFRP materials. Most of the previously developed damage models aim to predict damage on multidirectional CFRP materials which may mask this damage shape. The damage model developed in this PhD is new, as it includes electric field dependency, which enables accurate simulation of electric breakdown by considering conduction of current transverse to the fibres after the breakdown strength of the material is exceeded. Furthermore, the model was validated using simulated lightning strike tests on UD CFRP material; previously only multidirectional quasi isotropic materials have been studied, which generates a more uniform electrical conduction process compared to UD CFRP material. X-ray Computed Tomography (CT) and infrared thermography (IRT) were used to non-destructively evaluate the extent of the damage in the CFRP panels. These methods were adopted for sub-surface and repeatable measurements of lightning strike induced damage. A new procedure called the 'integration method' was used to analyse the IRT data, which provides a new methodology for the categorizing of damage in CFRP materials, and this was used for the lightning damage specimens. The validated models have direct applicability to understanding the structural capability of CFRPs materials and components post lightning strike and provide improved delineation of the difference in structural capability before and after a lightning strike.

Research on material/structural performance following a lightning strike is scarce, and is limited to simple uniaxial tension or compression loading scenarios on multi-directional materials [35], [44]. In the present PhD, a new testing methodology is developed which is named 'Compression After Lightning Strike' (CALS). The CALS test is carried out on a panel of a size representative of that used in the sparcap structure and replicates the worst-case design loading condition, i.e. the compression load case corresponding to flapwise WT blade bending, which is most often considered to be the critical design driver. The CALS tests were monitored using DIC, which provides the full field strain and deformation to inform on the effect of a lightning strike on the structural performance. The methodologies described above have never before been applied in assessing the effect of lightning strike on CFRP materials and components for WT blade structures.

In summary, the novelty of the research conducted in this PhD is as follows:

1. Identification of unique lightning damage on UD CFRP materials.
2. Development and experimental validation of coupled thermal-electric models for lightning strike induced damage in CFRP materials.
3. The development and experimental validation of a complex structural model to assess the load response, and first ply failure of a CFRP blade component before and after lightning strike.
4. Development of the CALS methodology used to understand the structural response of a sparcap component with lightning damage.

5. Development of an algorithm to categorize lightning damage using thermography data to examine the damage of CFRP materials subjected to a lightning strike event.

1.5 Report Structure

Chapter 2 presents a literature review. The review gives a background of the lightning physics, lightning attachment to a WT blade, previous lightning damage seen on CFRP materials, lightning damage models, and structural response of CFRP materials due to lightning damage. These are presented to give a background for the lightning damage experiments and model and the structural experiments and model. Lastly, in this chapter the current state of lightning protection is presented.

Chapter 3 investigates the degradation of mechanical properties in CFRP subjected to electrical current conducted along the fibre direction. The simulated lightning experiment subjected CFRP strip specimens to lightning current defined by WT blade standards in the fibre direction. The thermal evolution is evaluated, and coupons scale samples are taken from the specimen to test in compression and shear.

Chapter 4 presents five different direct strike tests, where the typical lightning parameters of peak current, specific energy, and charge were varied to determine which had the largest influence on damage. The fifth direct strike test was conducted on a representative WT sparcap sub-structural component; the results are used to validate the damage model in Chapter 5 and the damaged panels were used in the CALS structural tests in Chapter 6.

In Chapter 5, the full modelling approach is outlined and discussed. The development of the lightning damage model is presented. The chapter includes discussion on the electric field dependency, geometry, boundary conditions and plasma channel. The model is validated against the CT scans from the simulated lightning strike experiments and compared to a traditional Joule heating model by comparing the damage area, and depths.

Chapter 6 describes the design of the CALS test rig and the experimental methodology that was developed to understand the change in structural response due to lightning strike. In the chapter, the structural model is developed and validated using the results from the CALS experiments.

The thesis concludes with Chapter 7 where the overarching conclusions are presented along with suggestions for future work.

Chapter 2

Literature Review

2.1 Introduction

In this thesis, lightning strike induced damage on Carbon Fibre Reinforced Polymer (CFRP) materials are studied. CFRP composite materials are generally used as structural components because of their stiffness/strength to weight ratio [45]. An example of a ply and laminate configuration is shown in Figure 2.1. They comprise of carbon fibres and polymer resin, usually an epoxy. The carbon fibres have high strength and high stiffness to density, and they provide stiffness and strength of the resulting composite material. The epoxy resin (or other polymer resin such as polyester, vinyelster, and polyurethane) is the substance that binds the carbon fibres together. Plies are closely packed carbon fibre tows stitched together with all fibres positioned in the same direction as shown Ply 1 of Figure 2.1 [45]. This gives two very distinct principal material orientations: values and properties in the fibre direction are typically denoted by a subscript 1 and called, throughout the thesis, the 'longitudinal direction'. The values and properties in the direction orthogonal to the fibres are typically denoted by a subscript 2 and called, throughout the thesis, the 'transverse direction'. The ply angle, θ, is defined by the angle between the longitudinal (fibre) direction and a reference direction, e.g. a global x direction as shown in Figure 2.1. Multiple plies can be stacked together to create a laminate and are typically labelled by their number from the top outer ply to the bottom outer ply as depicted in Figure 2.1. The laminate stack provides another distinct orientation where values and properties in this direction are typically denoted by a subscript 3 and called, throughout the thesis, the 'through-thickness direction'. Figure 2.1 depicts a unidirectional (UD) stack-up as it is used in many Wind Turbine (WT) blade sparcaps, which allows the fibres to provide the highest stiffness and strength in the loading direction [46].

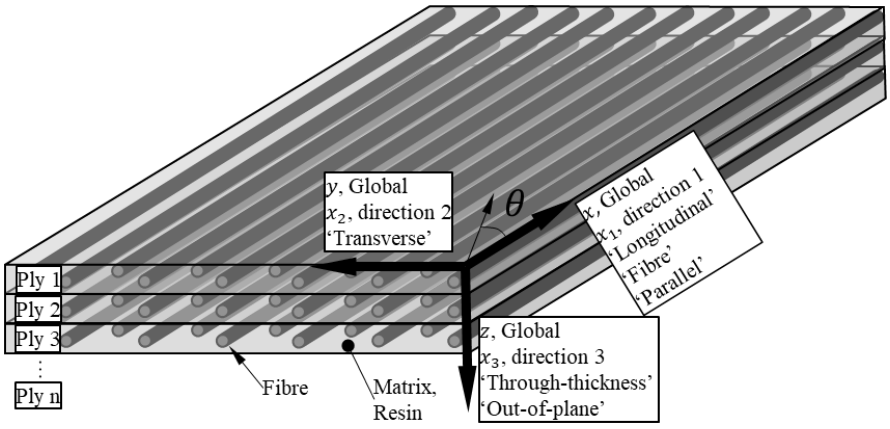

Figure 2.1: Unidirectional ply stack showing three material orientations, and global coordinate system

The literature review aims to provide a background of the current state of the art in research to characterise CFRP materials and components damaged by a lightning strike and their subsequent structural response. The literature review is categorized into sections, which starts with the basics of lightning strike through to the damage it causes in CFRP materials and components specifically in WT blades. The review discusses the standard protection methods provided in the International Electrotechnical Commission (IEC) standard to design Lightning Protection Systems (LPS) and lightning attachment to WT blades. The IEC is an international organizing body, which oversees the development and certification criteria for many industries including the WT industry. IEC 61400 [47] is the standard which details the design requirements for WTs and is divided into 27 parts. Part 24, or 61400-24 [48], is the lightning strike test and protection standard. The next section reviews the two most commonly used methods to protect against direct lightning attachment; metallic mesh and conductive surface application. Next, the current knowledge of damage to CFRP materials from injected current is reviewed. Lastly, the structural response of damaged CFRP materials and components are discussed.

2.2 Lightning physics and its relevance to wind turbine blades

The work by Rakov [20], [80]-[81]; Uman [52], [53]; and Golde [54] provides extensive details on lightning physics and only a brief summary is provided in this section of the thesis as a background for the current work. The lightning phenomenon predates human existence. In fact, lightning may have even been integral in creating the building blocks of life [55]. It is engraved in human civilization and has a place in all religious beliefs, which have stories and mythology centred around lightning and thunder [49]. The first recorded systematic attempts to study lightning began with Benjamin Franklin's proverbial kite experiment [56]. It was this experiment that conclusively showed that clouds were electrically charged. The first quantitative measurements were conducted in the late nineteenth century with the introduction of photographic images of lightning. Researchers Herschel in 1868 [57], Gibbons in 1871 [58], Holden in 1872 [59], and Clark in 1874 [60], were the first to examine the visible spectrum which led Dufay in 1949 [61] and Israel 1956 [62] to tie the visible spectrum to amplitude differences in lightning.

The invention of the streak camera helped to evolve our modern understanding of lightning. A streak camera contains a moving reel of film taking strips of an image at a rapid rate [54], which allowed ultra-fast time-lapse images to be made, and for the first time, was able to show the progression of a lightning strike. An example of a streak camera image is shown in Figure 2.2 [53], which shows conclusively a negative downward leader and an upward connecting leader [53], and provided the basis for the nomenclature associated with descriptions of lightning.

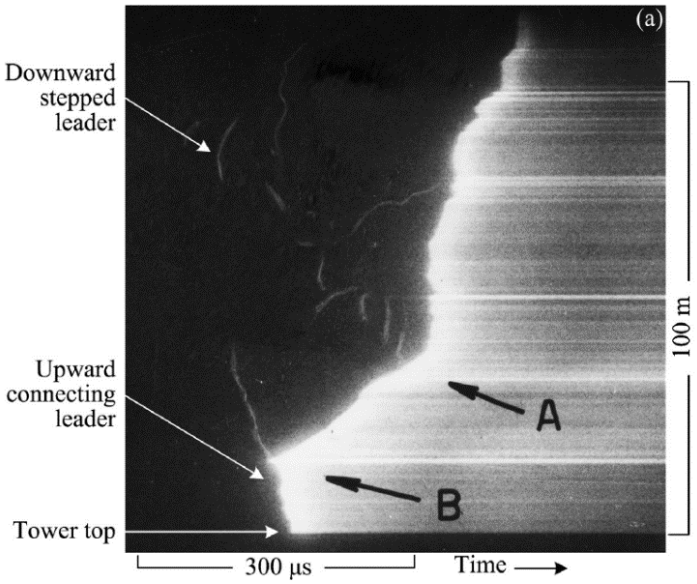

Figure 2.2: Streak camera photograph of a downward lightning flash attaching to a 55m tower on top of Mount San Salvatore in Lugano, Switzerland [53]

The first current waveform readings were taken using oscilloscopes by Stekolnikov and Valeev in 1937 [63], and by Davis and Standring in 1947 [64] using tethered balloons. McEachron, Hagenguth and Anderson [65]–[67] took oscilloscope readings from lightning strikes on the Empire State Building in 1939, 1941 and 1952. These observations and measurements led to researchers studying lightning through devices called lightning recording stations [68]. Similar techniques are still used today and record lightning strikes for regions all over the world through ground-based systems, mobile systems and multiple antennas. These systems along with cloud density maps can estimate how many lightning strikes a structure will receive throughout its lifespan and can be used to determine magnitudes of peak current in a particular lightning strike.

Many researchers use Berger's 1975 research [69] to determine worst case lightning strike scenarios. Over time these cases were implemented into standards to be used to simulate lightning strikes in laboratory settings, e.g. most notably on the protection of aircraft standard SAE ARP5416 [70], and on the protection of WTs IEC61400 [48]. Standardized waveforms represent idealized environments and are applied to structures for purposes of analysis and testing. The waveforms are not intended to replicate a specific lightning event, but rather to be a composite waveform where the effect on materials and structures are those expected from natural lightning [35].

2.2.1 Lightning discharge

Lightning is defined as a transient, high-current electric discharge with a path length that can be measured in kilometres. The primary source of lightning comes from cumulonimbus clouds, or more commonly known as thunderclouds. Thunderclouds are visible aerosol suspended in the earth's atmosphere. The thundercloud is a structure that can be 4 km tall, and because of this height, much of the cloud can be below temperature/pressure levels which causes freezing of the

water vapours [50]. The difference in temperature leads to the formation of charge within a cloud. The exact mechanisms that cause the charge are still being researched. The main theory is that polarized precipitation particles fall through the vertical electric field and collide with small droplets moving upwards due to the updraugths inside the thundercloud [49]. The collision of these droplets removes positive charge from the precipitation particles. The positive charge will concentrate in the highest part of the cloud. This leads to the thundercloud having a bipolar charge structure. The highest part of the cloud will have a large accumulation of positive charge of around 40 Coulombs and the lowest part of the cloud will have a large accumulation of negative charge of around -40 Coulombs [51].

Lightning is categorized based on where the discharge originates and ends. There are four categories of discharge as shown in Figure 2.3: intracloud, cloud-to-ground, air discharges and cloud-to-cloud discharges [51]. Cloud-to-cloud and intracloud are the most common type of discharge accounting for more than 70% of all lightning discharges; however, cloud-to-ground is the most researched area because of its interactions with humans and man-made structures.

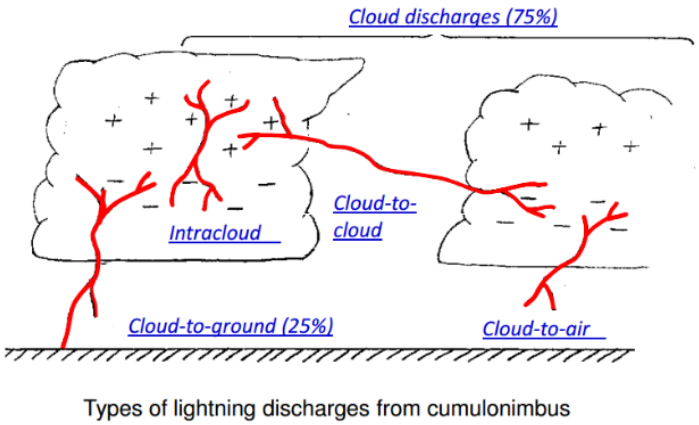

Figure 2.3: Lightning discharge categories for all types of lightning discharge represented by the red lines [51]

It is estimated that 90% or more of global cloud-to-ground lightning is accounted for by negatively charged downward lightning [51]. The other types of cloud-to-ground discharges in order of frequency are negative upward, positive upward, bipolar upward and positive downward [51]. Downward lightning is specified as initiating from the cloud and travelling to the ground, and upward lightning is specified as initiating from the ground and travelling to the cloud. The typical process of a downward leading is depicted in Figure 2.4. The source of the lightning discharge starts in a thunder cloud. In the initial phase there are three regions arranged vertically and indicated by the lettering P, LP, and N for main positive, lower positive charge regions and main negative charge, respectively.

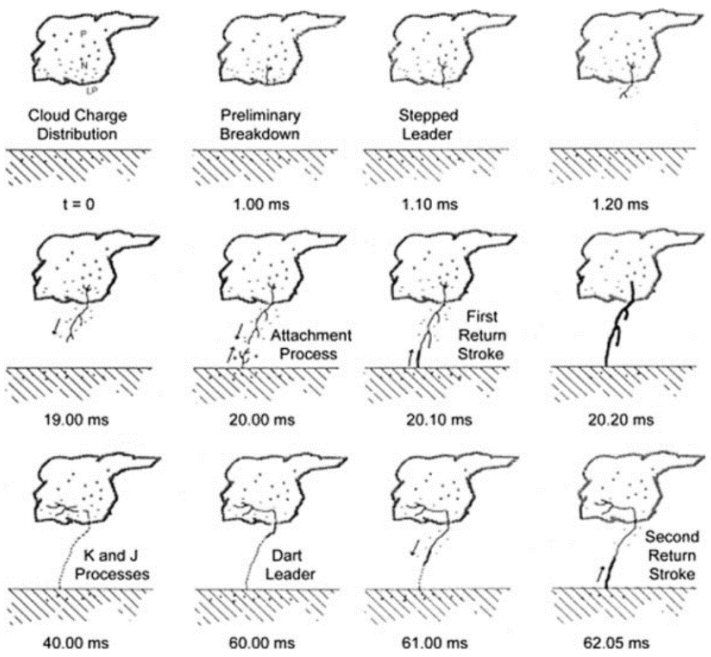

Figure 2.4: Typical downward leading lightning discharge [50]

The phases of a negative downward discharge are called strokes. A typical flash is composed of two stroke types: the initial stroke and the return stroke. The first stroke starts by what is known as preliminary breakdown. The process of the lightning creates a conductive path down to ground through stepped leaders as shown in Figure 2.4 at 1.10ms. Typically, the disturbance in electric field will trigger upward lightning from the ground and the attachment process will happen when the upward lightning and the downward lightning meet creating a channel. The lightning will send current through the channel, which is the first stroke. Typical lightning discharge has 3 to 5 strokes, but the observed ranges have shown that lightning can have 1 to 26 strokes from one flash [51] as shown in Figure 2.5. These 3 to 5 strokes per flash can be common leading, and depending on the lightning density, exposing WT to nearly 30 strikes per year [51].

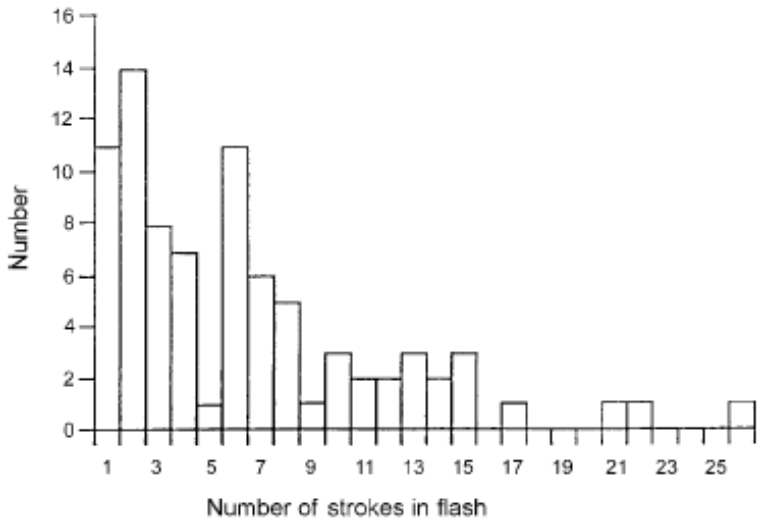

Figure 2.5: Histogram of number of strokes per flash from lightning observations [51]

2.2.2 Lightning attachment to wind turbines

WT structures are highly susceptible to lightning strikes as they are often the tallest structures in the region and pointed at the end. As lightning downward leaders make their path from cloud-to-ground, higher structures are more likely to provide an upward leader to connect a downward leader and create a lightning stroke. Researchers have shown that the propensity for lightning to attach to a structure increases with its height [71], and further that the wind turbine, as the highest structure in the region, is more susceptible to lightning strikes. Additionally, the enhanced electric field at the blade tip, due to the sharp curvature and highest point of the structure, is the most likely place for lightning to attach [72]. Investigations, which consider the location of lightning attachment points along the WT blades [72], [73], have determined that the most susceptible area for a WT to be struck by lightning is at the very tip of the blade. More than 95% of the strikes that attach to a WT occur within the last 10 meters of the blade [74] as shown in Figure 2.6.

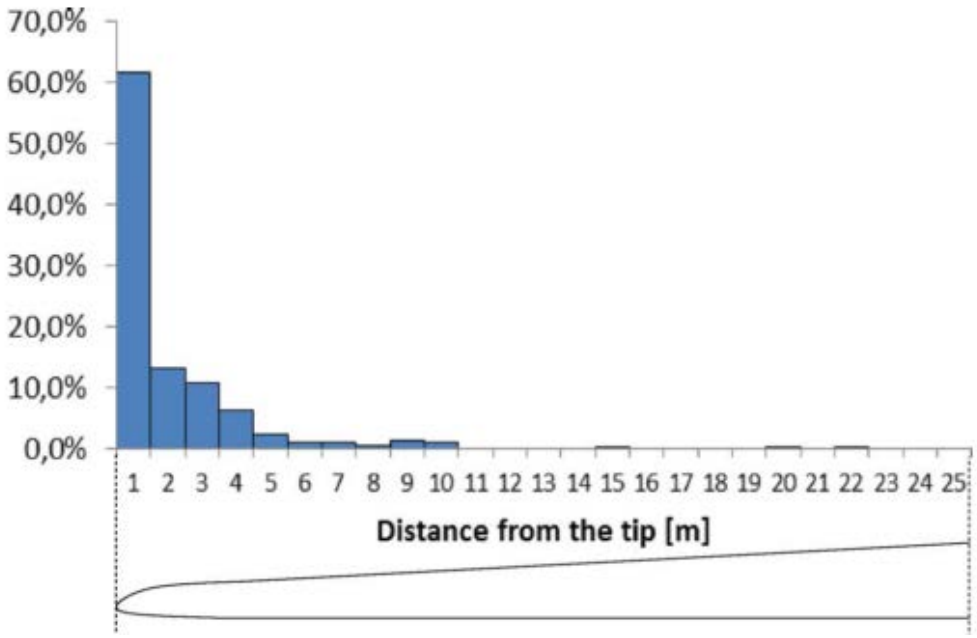

Figure 2.6: Lightning strike attachment points along the length of the blade from various wind turbines located in the US states of Kansas, Texas, and Illinois [74]

As previously mentioned, streak cameras and high-speed images show that most lightning strikes are composed of a downward leader connecting with an upward leader created by the enhanced electric field. The upward leaders are typically created in areas that have sharp radiuses, which on a WT blade is at the blade tip. The most ideal path to ground for a WT is for the lightning to strike a receptor allowing the current to travel down the conductor on a path to ground as shown in Figure 2.7. To aid in this, some WT blades have a metallic tip as a way to conduct the electric current from the lightning strike through a down conductor and into the ground. The down conductor is a thick gauge wire, usually copper or aluminium, which is very conductive and gives the current the least resistive path to ground.

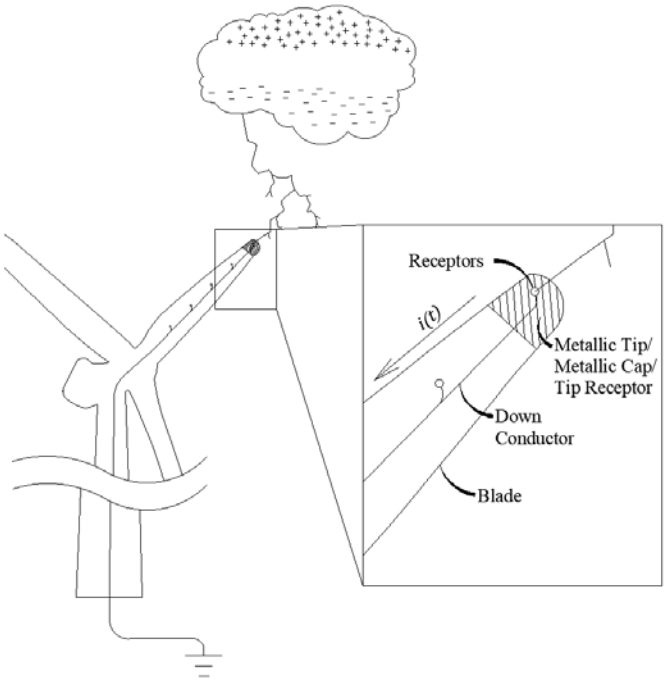

Figure 2.7: Ideal lightning strike path to ground through wind turbine

However, as can be seen in Figure 2.8, lightning attachment does not always take a direct path to the receptors and through the down conductor; in the photograph on the right it is clear the lightning has attached below the tip and is heating the GFRP blade by the electric current travelling on the surface of the blade until it reaches the cap receptor.

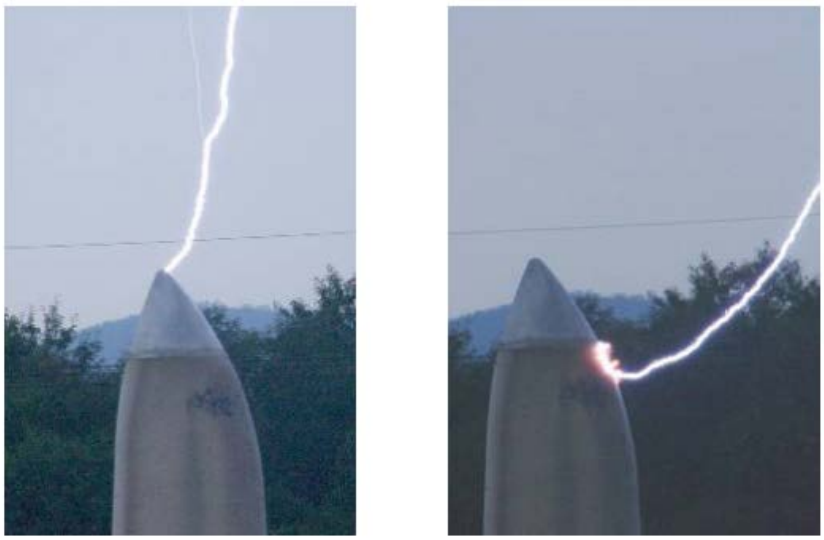

Figure 2.8: Simulated lightning attachment to wind turbine blade with cap type receptor [75]

CFRP sparcaps in WT blades (or CFRP/GFRP hybrid sparcaps) represent a potential conductive path for lightning to travel to ground. There are three potential ways that lightning currents reach the CFRP composites materials/components, as illustrated in Figure 2.9. Scenario 1 is a direct attachment, also known as a direct strike or arc-entry, when a strike directly attaches to the CFRP if the sparcap end too close to the tip of the blade. The likelihood of this occurring is small but results

in the largest current experienced in the CFRP materials, and further generates the most Joule heating as the current is conducting through the most resistive path. Therefore, Scenario 1 typically causes the most damage. If this enters through GFRP material, there is also the potential for delamination between the GFRP external shell and the CFRP sparcaps. Scenario 2 is unintended internal flashover due to large voltage differences between the down conductor and the sparcaps. This happens when down conductors, badly designed side receptors, or additional components such as heating elements are not properly electrically connected or insulated. Flashovers from the current flowing through the down conductor contain only a fraction of the peak current but can still cause damage. There is a larger probability of Scenario 2 occurring with blades that do not have adequate lightning protection. Scenario 3 is the most likely case where the tip receptor intercepts the lightning attachment and the majority of the current is received through the down conductor. A typical design has an LPS with equipotential bonds between conductive elements, which include the structural CFRP materials, to ensure that flashovers cannot occur, but also allows for current in the CFRP sparcaps. Scenario 3 has the highest potential to control the electrical introduction into the CFRP materials, and to distribute the energy through the CFRP material to reduce damage.

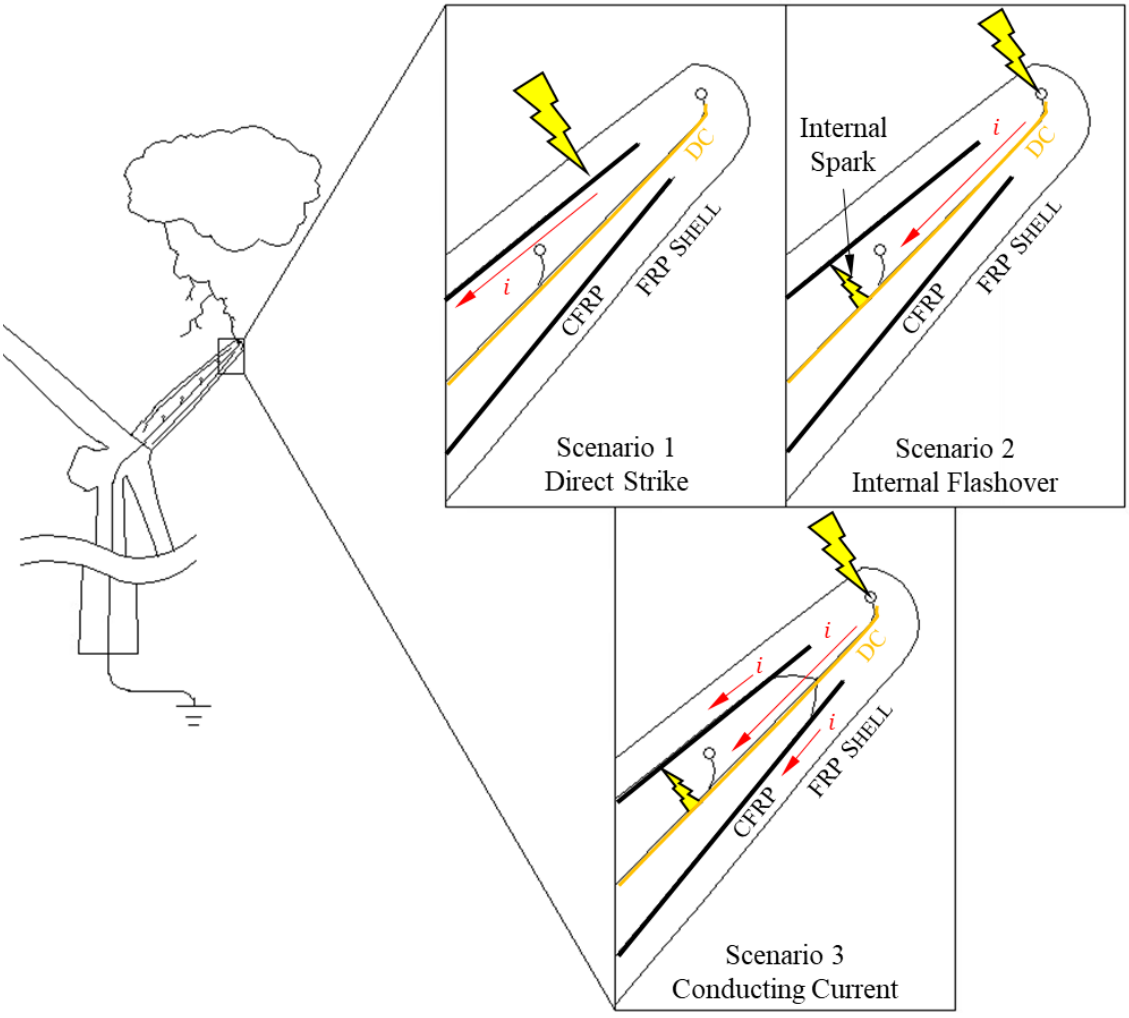

Figure 2.9: Lightning attachment to an example wind turbine showing the typical attachment scenarios 1 to 3: (1) Direct strike, (2) Internal Flashover, and (3) Conducted Current

2.2.3 Lightning current waveforms and the standard 10/350μs waveform

The current from a natural lightning stroke is variable. As discussed previously there are five types of cloud-to-ground: negative downward, negative upward, positive upward, bipolar upward and positive downward. Negative cloud-to-ground represents a typical current profile. Figure 2.10 presents a schematic of the characteristic elements of a downward lightning discharge and an upward lightning discharge. The first injection of current is the first return stroke. The first return stroke is characterised by a rapid rise time of the order of 10 μs with a trailing duration of approximately 100 μs. This is the most distinct characteristic of the downward lightning stroke. Continuous Current (CC) is possible in between strokes with a current range of about 10 A to around 1 kA. In between these portions of a lightning discharge, it is possible to have additional charge transferred by what is known as the M-component. The M-component is defined as a slow charge transfer that grows over a few milliseconds. Similarly, upward lightning strikes have a distinct characteristic current waveform. The initiation process of the upward lightning includes initial continuous current (ICC) in the form of rapid pulses measured in the range of μs to ms. Once the ICC is extinguished a return stroke is seen which holds the same characteristics as downward lightning.

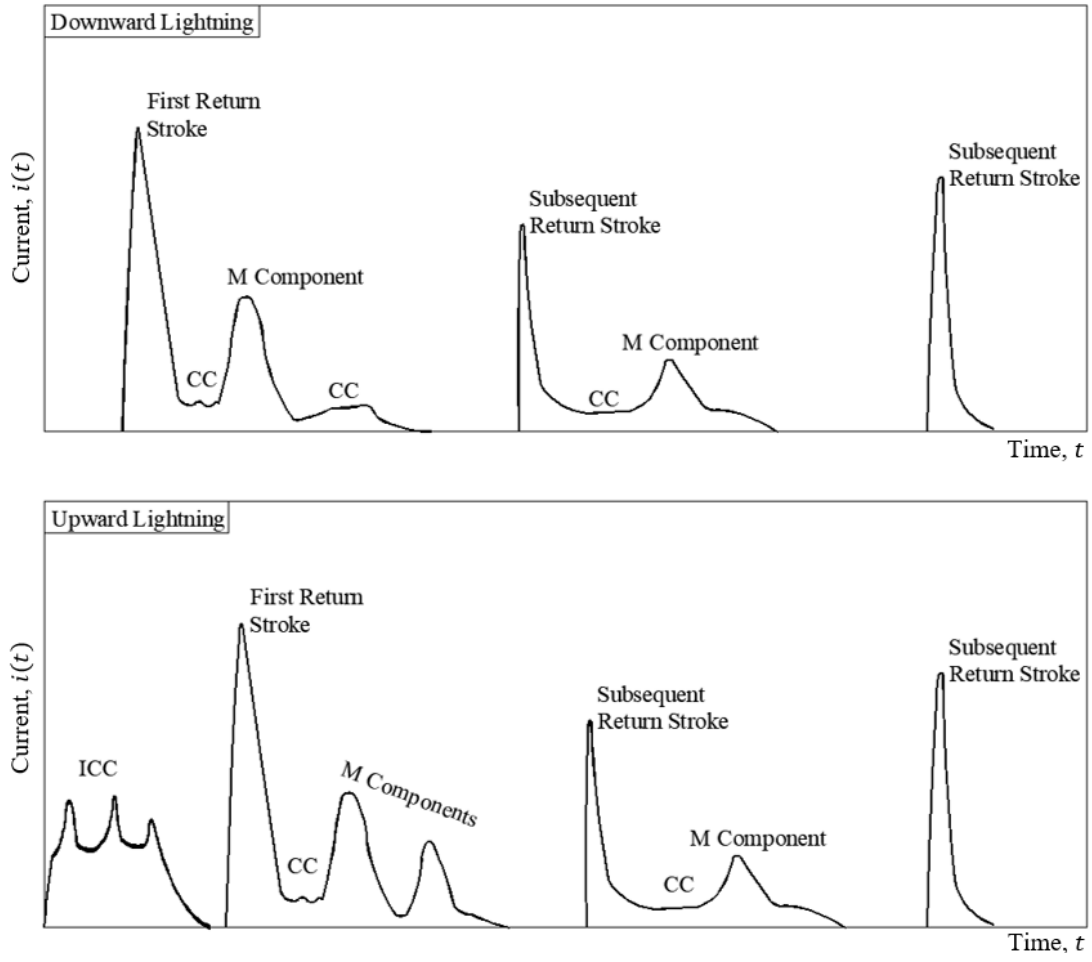

Figure 2.10: Schematic showing the current distribution in a downward (top) and upward (bottom) lightning discharge (adapted from [76])

An example of negative downward lightning discharge on a WT blade is shown in Figure 2.11 where the electric current is shown in red for the time just before and after the lightning strike. The first approximately 8 ms before the first return stroke are small spikes in current that are associated with the formation of an upward leader and at 100 ms the full lightning strike is connected followed by a rapid increase in current. The blue box shows a closer view of the lightning strike on the right. The close-up view shows a single strike with continuous current and one M component until it returns to zero current.

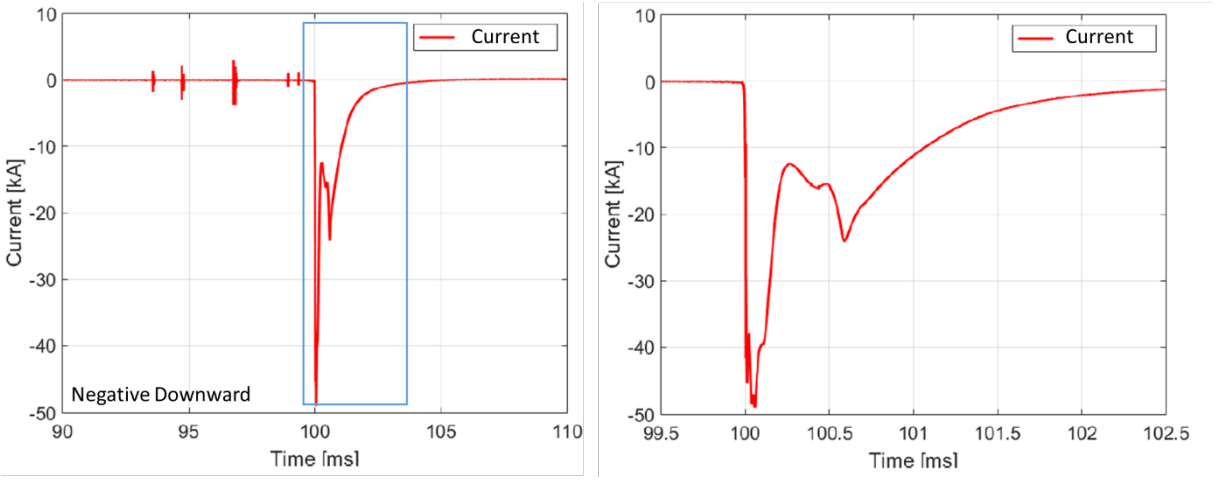

Figure 2.11: Example of a negative downward lightning discharge on an offshore WT blade (left) is the full waveform with time before and after strike and (right) is a close-up view of the stroke [77]

Figure 2.12 shows a negative upward lightning discharge where the blue region highlights the close-up view on the right. The right image shows a rapidly produced ICC with the first return stroke with a peak current just below 25 kA.

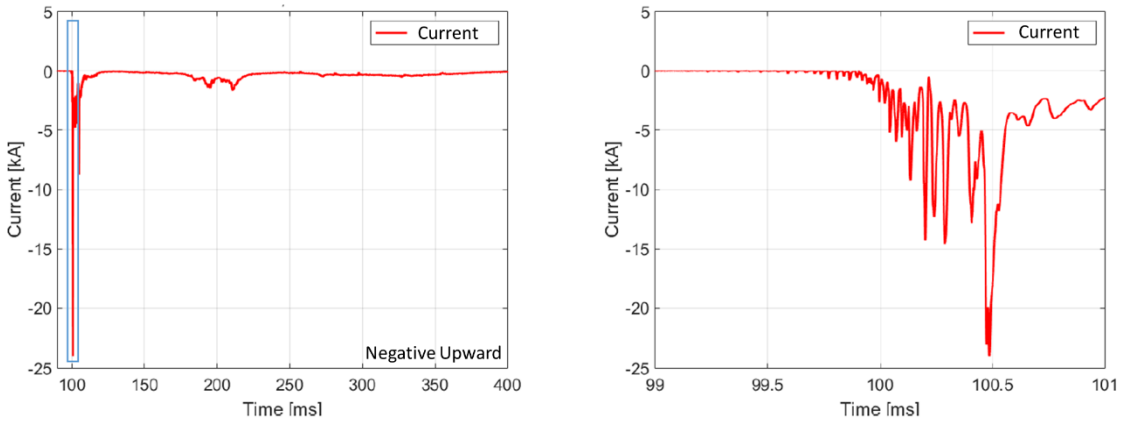

Figure 2.12: Example of a negative upward lightning discharge on an offshore WT blade [77]

Berger's work [69] was used in the WT standards as the basis for the standardized waveform used for testing of materials subjected to a lightning strike, as it provided the statistical basis of a worst case current, duration, and rise time that could be attributed to a lightning discharge. The standard waveform was developed in the IEC 62305 [78] standard to represent a natural lightning strike, and

is implemented in the WT blade lightning protection standard IEC 61400-24 [48]. The waveform mostly used for WT blades is the 10/350µs waveform. Figure 2.13 shows the normalized 10/350µs waveform over 1000 µs. The 10/350µs waveform is defined by 10 µs rise time and a 350 µs half time. The rise time is the time it takes the current to reach the peak current (a value of 1.0 in Figure 2.13) and the half time is the time the waveform is at half of the peak current.

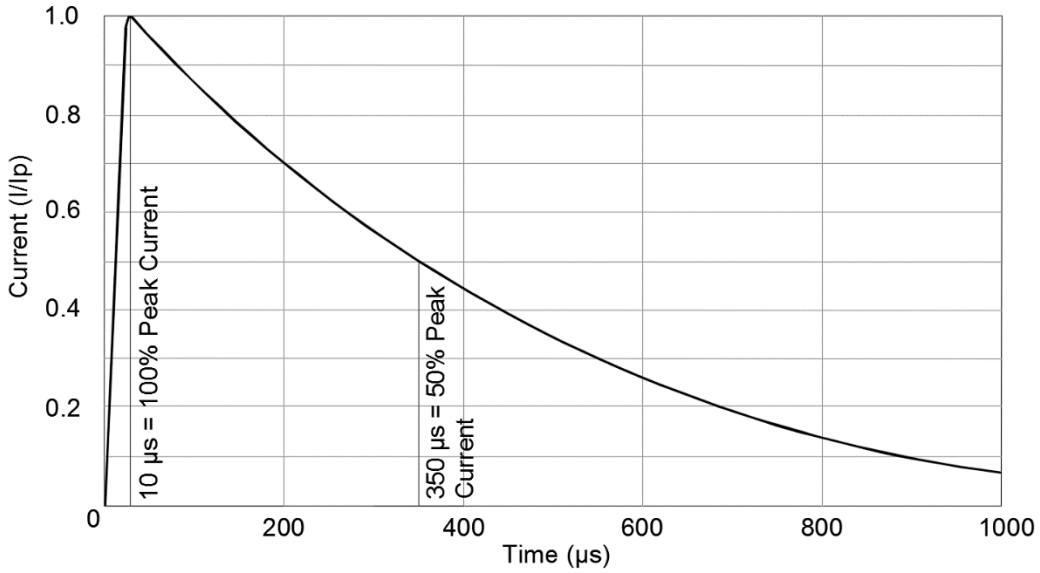

Figure 2.13: Idealized natural lightning strike waveform, 10/350µs waveform, used in the IEC61400-24 wind turbine blade lightning protection standard [48].

SAE-ARP 5412 [70] sub-divides lightning strikes into different components as shown in Figure 2.14. The four different components mimic the natural lightning process. Component A is the first return (or initial) stroke, Component B is the M-component, Component C is the continuing current, and Component D is the return stroke.

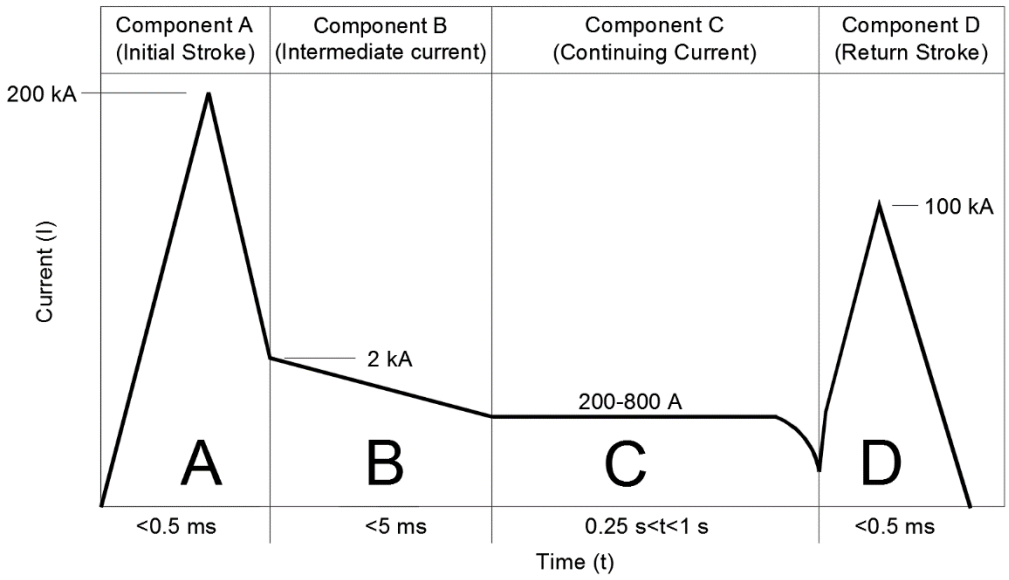

Figure 2.14: Typical lightning stroke waveform defined by SAE-ARP 5412 aircraft standard [70]

The 10/350µs waveform is appropriate for arc-entry situations; see Scenarios 1 and 2 of Figure 2.9. For conducting current cases (Scenario 3 Figure 2.9), the current is typically shared between the down conductor and the CFRP material. For this instance, a different waveform can be used. Based on the work done by Romero [79] a waveform of 10/110µs is identified as a more appropriate waveform for conducting current; see Figure 2.15.

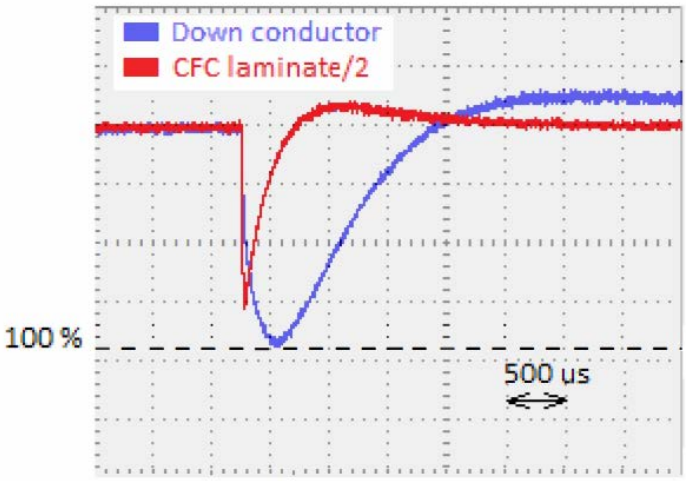

Figure 2.15: Experimental results of the current distribution between the down conductor and the sparcap on a scaled lightning protection system [79]

2.3 Lightning protection for wind turbine blades

Having discussed the types of lightning strike experienced by WT blades, the next step is to describe how WT blades are protected from lightning, which has challenged the WT industry for several years. Many of the concepts developed to protect CFRP materials in WT blades have been inspired from the aviation industry research and solutions. However, there are stark differences in the way WTs are operated when compared to aircraft. One significant difference is that lightning strikes aircraft on average once per year [33]. The number of lightning strikes seen on any WT is based on several factors including the topography of the local landscape, the height of the turbine, and the local lightning density. The WT height is one of the most important parameters affecting the propensity of lightning strike occurrences [80]. One local study in the USA [74] showed that WTs in Texas, Kansas, and Missouri saw an average of 4 lightning strikes per year. Another difference is that aircraft and WTs are experiencing different levels of lightning strike induced electric discharge energies. This is also reflected directly in the way aircraft and WT blade structures are tested. Aircraft structures are tested and subjected to lightning energies of about 2 MJ/Ω [70], whereas WTs are tested and are subjected to lightning energies of about 10 MJ/Ω [48]. Thus, the severity of lightning strike is much more pronounced for WTs than for aircraft structures. Another, major difference is the way aircraft and wind blade structures are inspected. For WTs the standards recommend outer visual inspection once per year [48], whereas the aircraft standard calls for inspection and repair after every strike due to the risk to human safety [70]. These significant

differences change the lightning protection needs for WT blades in comparison with aircraft structures.

The complication with CFRP WT blade parts is that the conductivity of the carbon fibres provides an additional electrically conductive path to ground for the structure. Lightning protection solutions for the aerospace industry, particularly on aircraft and helicopters, often use copper mesh bonded to the outer surface of the composite to reduce the damage and the number of sparks which have the potential to ignite fuel [81]. This method is suitable for direct attachment of lightning, but WTs experience several attachment types. This leads to several complex issues arising for the development of WT solutions, which do not apply to aircraft structures. Several solutions tailored for direct attachments [52], [82]–[84] have been proposed to prevent damage being induced by lightning strikes, but so far no design solution has completely eliminated the problem.

Most blade designs in the past utilized GFRP for the structural blade components. These blades had a common approach to LPS. The GFRP blade's LPS consisted of a number of discrete lightning attachment points, called receptors, and a down conductor inside the blade [80]. The receptors are metallic structures, typically aluminium, which are used to boost the likelihood of lightning strike attachment to a location which will give the least resistive path to ground; see Figure 2.16. Since the GFRP materials are non-conductive, the LPS provides an easy path to ground for the current to flow. If the lightning does not attach to one of the receptors, the current will typically travel on the surface to the receptor causing burning until the current finds the lowest resistive path to ground.

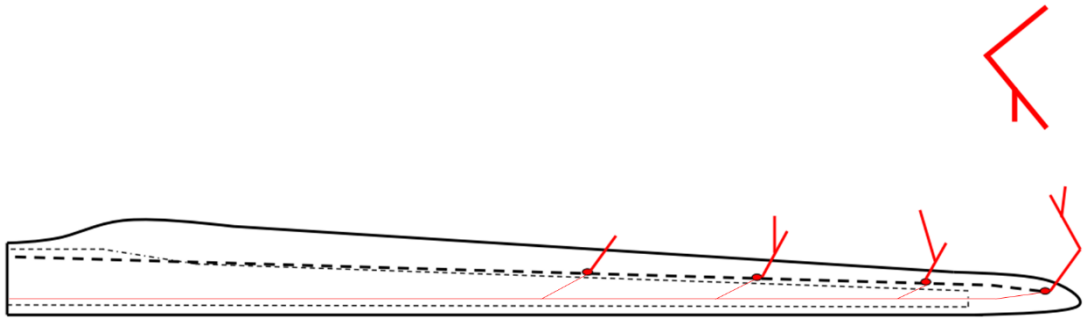

Figure 2.16: Example of LPS with multiple receptors with lightning attachment process [80]

Many different lightning protection solutions have been devised for modern WT blades with CFRP structural components, they commonly consist of one or all of the following: multiple discrete lightning attachment points (receptors) [48], a down conductor inside the blade [47], expanded metal foil [85], and/or equipotential bonds [48]. Various lightning strike mitigation measures currently used in modern WT blades are shown in Figure 2.17. A highly conductive metallic receptor (also called a metallic cap or metallic tip) are typically installed at the tip of the blade, as shown in Figure 2.17 (a) [75]. This part is connected to the down conductor which runs down the middle of the blade. The down conductor is typically a metallic wire (usually copper) which

conducts the current to ground and is typically fashion with or without insulation as shown in Figure 2.17 (e). Metallic mesh or Expanded Metal Foil (EMF), Figure 2.17 (b), are optional protection measures and are installed to protect against direct strikes in the area with the highest risk of lightning attachment. Spaced along the blade lightning receptors, shown in Figure 2.17 (c), are typically installed to give the current a direct path from the insulating fibreglass shell to the down conductor. This lightning receptor is typically a circular metallic dome attached through a hole which connects the lightning receptor to the down conductor. The internal component is usually insulated to prevent internal flashover. Many WT manufacturers use equipotential bonds, as shown Figure 2.17 (d), to prevent internal flashover from the down conductor to the CFRP sparcaps. These bonds are typically made of EMF directly attached to the CFRP laminate and spaced so that the electric potential in the blade, developed from the lightning, will not be greater than the electric breakdown strength.

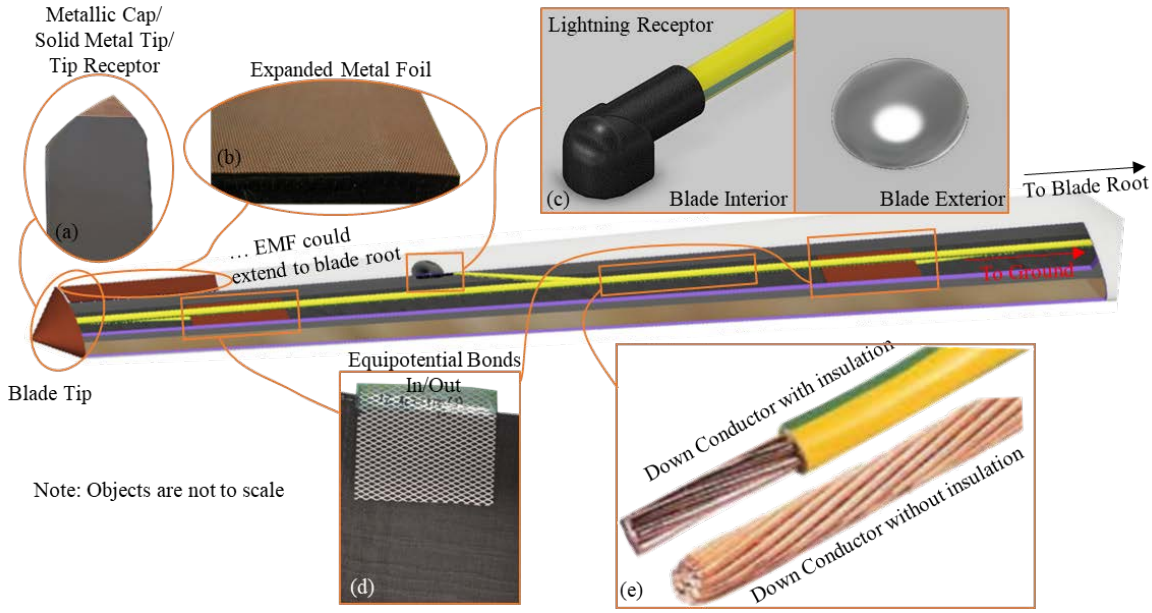

Figure 2.17: Common modern wind turbine blade lightning protection systems with 5 common components: (a) metallic tip receptor [75], (b) expanded metal foil, (c) lightning receptor, (d) equipotential bond, and (e) down conductor with and without insulation

The primary design objectives for a LPS are [81], [83], as follows:

1. To prevent catastrophic structural damage (Direct Effects)
2. Prevent hazardous electrical shocks to occupants (Indirect Effects)
3. Prevent loss of sensitive control equipment (Indirect Effects)

A recent methodology to aid in LPS design for WT blades was developed by Madsen [86] and implemented into the latest IEC standard [48]. A WT blade was partitioned into sections called Lightning Protection Zones (LPZ), as shown in Figure 2.18, according to their risk level based on highest probability of lightning strikes (see Figure 2.6). Their risk level is associated with the likelihood of being hit by a lightning strike as a function of location along the blade length. The

risk level is managed by changing their Lightning Protection Level (LPL) or the maximum peak current experienced in the LPZ. This allows manufacturers to focus on areas which need lightning protection the most and apply the highest mitigation measures.

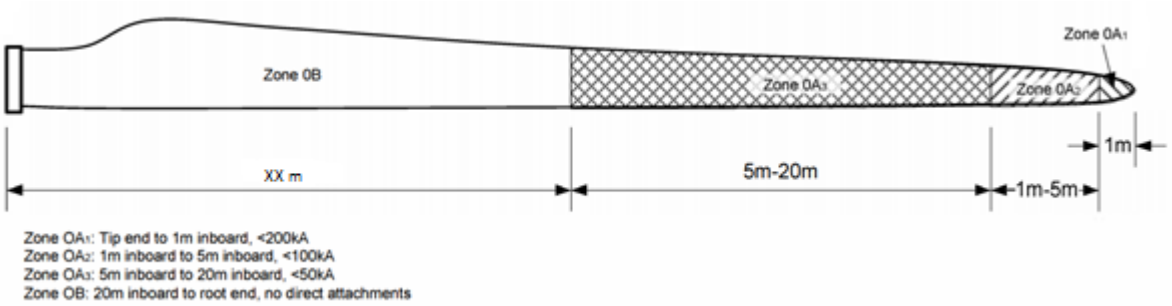

Figure 2.18: Wind turbine blade zoning concept [86]

Direct attachment (Scenario 1 & 2; Figure 2.9) needs lightning protection from direct effects. Almost all of the lightning strike protection solutions for direct attachment include the application of some electrically conductive substance on the surface such as metallic mesh usually copper [33], [87], carbon nanotubes [88], or conductive paints [89], [90].

2.3.1 Metallic mesh

Metallic mesh or EMF is a protective measure applied to CFRP materials to reduce structural damage. Figure 2.19 shows two different metallic mesh structures. The meshes are typically thin flat sheets of metal, usually copper or aluminium, either woven or non-woven, which create an open holed structure [82]. A woven mesh is made from thin wires intertwined together, as shown in Figure 2.19 (a). It is heavier and has higher resistivity at the cross points of the wires. Despite these issues, the Boeing 787 aircraft (all CFRP composite aerostructures design) uses woven mesh to provide protection from lightning strike direct effects [82]. A non-woven mesh, as shown in Figure 2.19 (b), is produced by running metal sheets into a machine that cuts and stretches the metal simultaneously through a pressurized slitting and stretching process. The slits created by a knife allow the metal to be stretched. The process creates a metallic sheet with uniform holes. The finished product has four distinct geometric patterns. The geometric patterns are defined by: the ‘Long Way of the Diamond’ (LWD) - the longest length between links, the ‘Short Way of the Diamond’ (SWD) - the smaller distance between links, the strand width (SW) - the width of the copper strands in the mesh, and the thickness of the mesh. By varying the geometry and thickness of the non-woven mesh, the weight of the mesh can be tailored to the application. Previous research has shown that there is a minimum thickness to ensure the mesh is not vaporized [91].

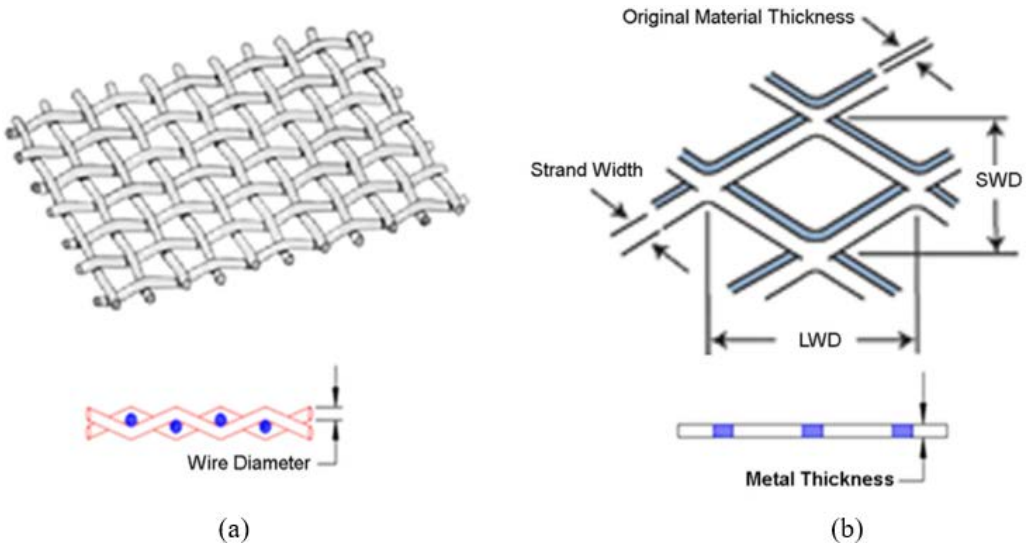

Figure 2.19: Examples of woven (left) and non-woven (right) metallic mesh from [82]

Metal meshes are bonded to CFRP laminates by resin, adhesives, or surface films. The metallic mesh can be bonded to the CFRP laminate in either its pre or post cured condition [85]. This addition adds a conductive path for the lightning to disperse the energy and reduce Joule heating. Figure 2.20 shows the difference in the damage incurred in a lightning strike on a CFRP laminated with and without a metallic mesh. However, adding the metallic mesh to the entire blade is cost and weight prohibitive [82].

Figure 2.20: Lightning damage on unprotected CFRP laminate (left) and CFRP laminate with copper mesh (right) [85]

2.3.2 Conductive surface application (paints & molten metal)

Similar to adding metallic mesh, CFRP materials can be protected from lightning by spraying molten metal or conductive paints onto their surface [83]. The molten metal applied to the surface creates a conductive path that enables attachment and conduction of the lightning current. The drawbacks to this method are the additional paint has a minimum thickness of 0.1 mm to ensure that the paint has coated every part of the component which can add more mass than needed and it is also cost prohibitive [92].

Conductive paints are another option, which are manufactured by adding metal particles to the paint. The paint surface is far less conductive than the molten metal surface and is only achieved by random contacts between neighbouring metal particles [92]. Figure 2.21 shows an example of the significant reduction in damage by applying conductive paint to the surface of a CFRP panel that is struck by lightning [34]. The drawbacks to this method are the lower conductivity compared to e.g. conductive meshes, and the difficulty in obtaining a uniform paint layer thickness, which tampers with the effectiveness of the paint [89].

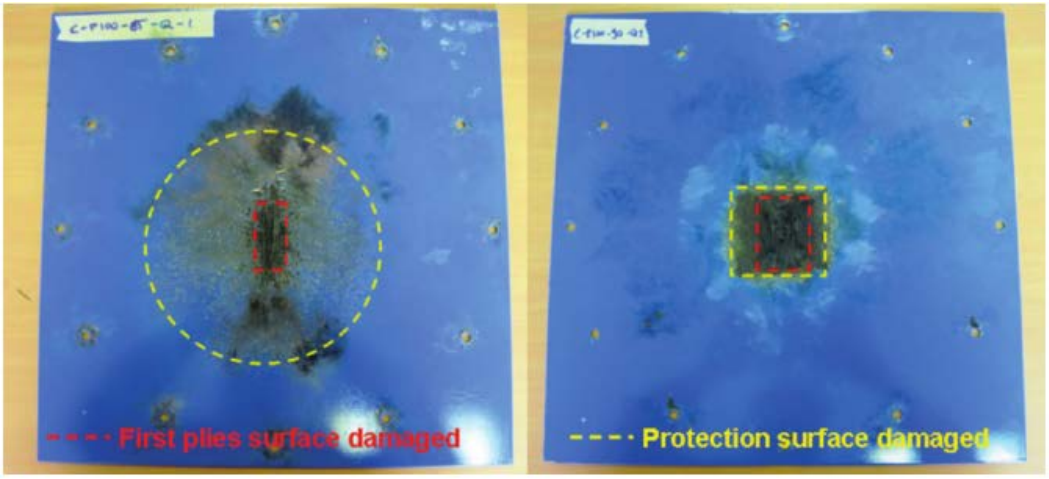

Figure 2.21: Panel subjected to simulated lightning strikes with (left) having no protection and (right) having conductive paint [34]

2.4 Damage and effects of lightning strike on CFRP materials

Buildings and structures that are prone to lightning have developed protection systems, which divert the current to ground through a down conductor [49], [52]. WTs, similarly, have LPS, but damage is still induced when lightning hits areas that are not intended to transfer current. Therefore, it is necessary to protect vulnerable areas at risk to lightning strikes. The effects of lightning strikes on structures have been divided into two different categories: direct effects and indirect effects [83]. Direct effects are the effects of lightning at the location of attachment with the structure and indirect effects deal with damage to electrical system due to oversupply of current to the system from a lightning strike [83]. As discussed previously, CFRP materials have been implemented into WT blades and have the potential to be subjected to 10 MJ/Ω of energy from a lightning strike [48]. This can result in serious structural damage up to and including a loss of a blade [75] as shown in Figure 2.22.

Figure 2.22: The remainder of a blade detached from a wind turbine due to lightning damage [75]

A classification chart, depicted in Figure 2.23, proposes the possible causes of damage to WT blades [93]. This chart categorises serious damage from catastrophic events that shut down WTs to minor events that require no work to fix. Carefully examining this chart shows that damage is mostly related to inadequate lightning protection. The first column is broken down into severity of damage. Following the connected links shows that the most catastrophic damage is associated with lack of lightning protection countermeasures. When there are adequate countermeasures the damage from a lightning strike can be repaired without replacement of an entire blade.

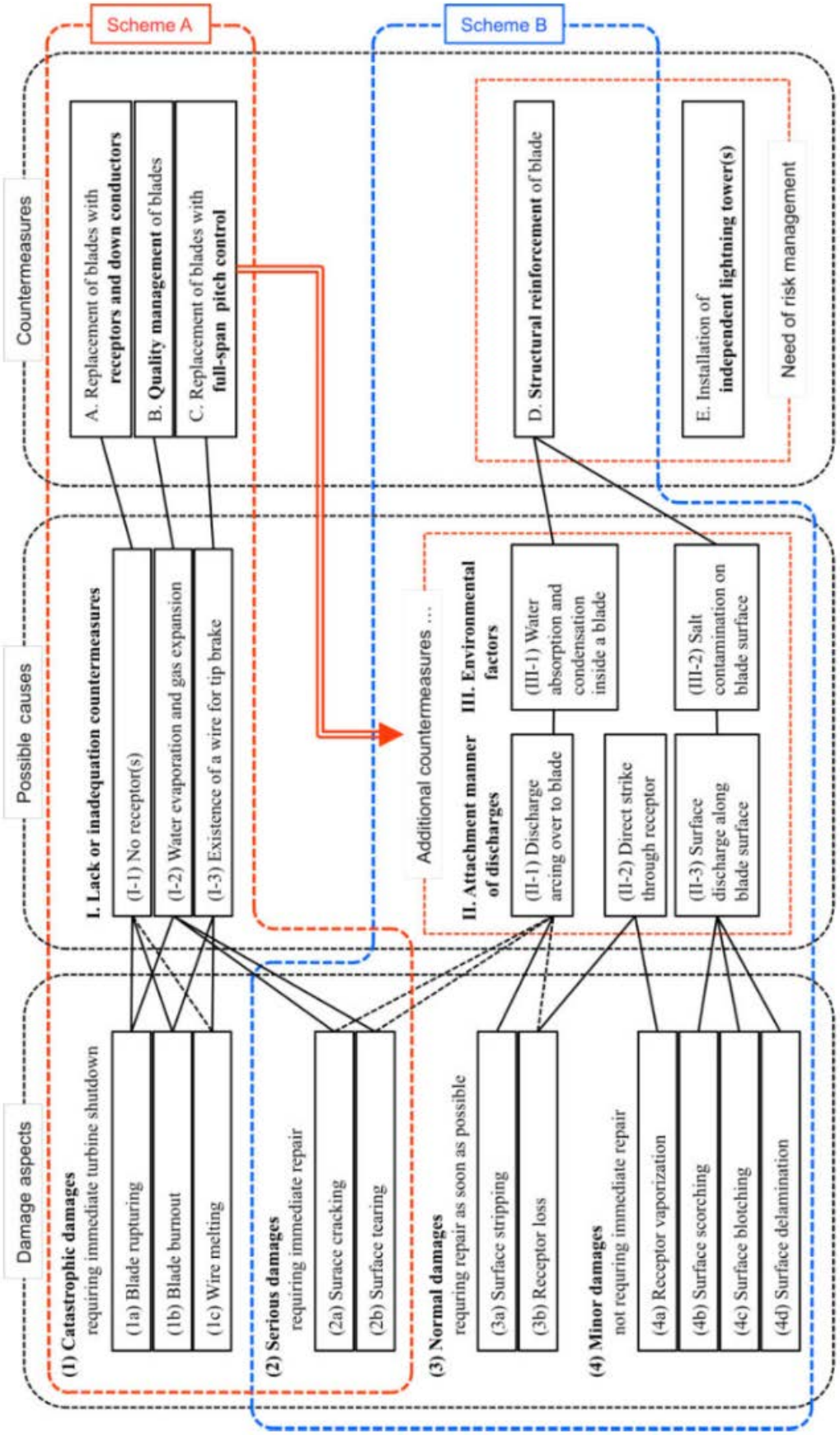

Figure 2.23: Schematic of relationship between damage and countermeasures [93]

2.4.1 Direct effects from lightning attachment

The effects from direct attachment of lightning on all material systems can be categorized into the following five features [81], [83]:

1. Melting or burning at lightning attachment points
2. Resistive temperature rise (Joule Heating)
3. Magnetic forces
4. Impact damage from acoustic shock
5. Arcing and sparking at bonds, hinges and joints.

The above direct effects associated with the interaction of lightning on CFRP materials are shown in Figure 2.24. The application of current through the channel is initially small and gradually grows [34], [94] as indicated by the different colour channels in Figure 2.24, which increase with the time increments (t1, t2, and t3) and changes the application of current density on the surface. The channel is restricted by the paint, which results in dielectric breakdown [34], [89]. The interaction between the vaporization of the protection and the paint layer must be considered to correctly simulate the expansion of the arc root [34]. The Joule heating effect is associated with heating of the CFRP material by the current and is typically considered to be the cause of melting and resistive temperature rise near and around the attachment point [34], [35], [39], [40], [46], [83], [95], [96]. Radiative flux transfer plays an important role in high temperature arcs and can also be used to determine the temperature rise under the channel [34]. Thermal flux is associated with the conduction of current from the plasma to the structure [34]. The acoustic forces are from overpressure events due to the fast deposit of energy during the ignition stage of the arc [34] that do not always make a significant impact. However if the arc is concentrated by an insulating feature such as paint or insulated surface, then the acoustic forces can increase and become a major contributor to damage [38], [89]. The magnetic force induced by the current circulation also makes a significant contribution to the mechanical constraint in the arc column and in the material [34]. The sparking and arcing at the bonds are typically associated with dielectric breakdown near or around holes. The current travels down the fibres and if the fibres end due to a hole, sparking can occur [83]. This is a large concern for aircrafts as they contain fuel which can combust in the presents of arcing or sparking.

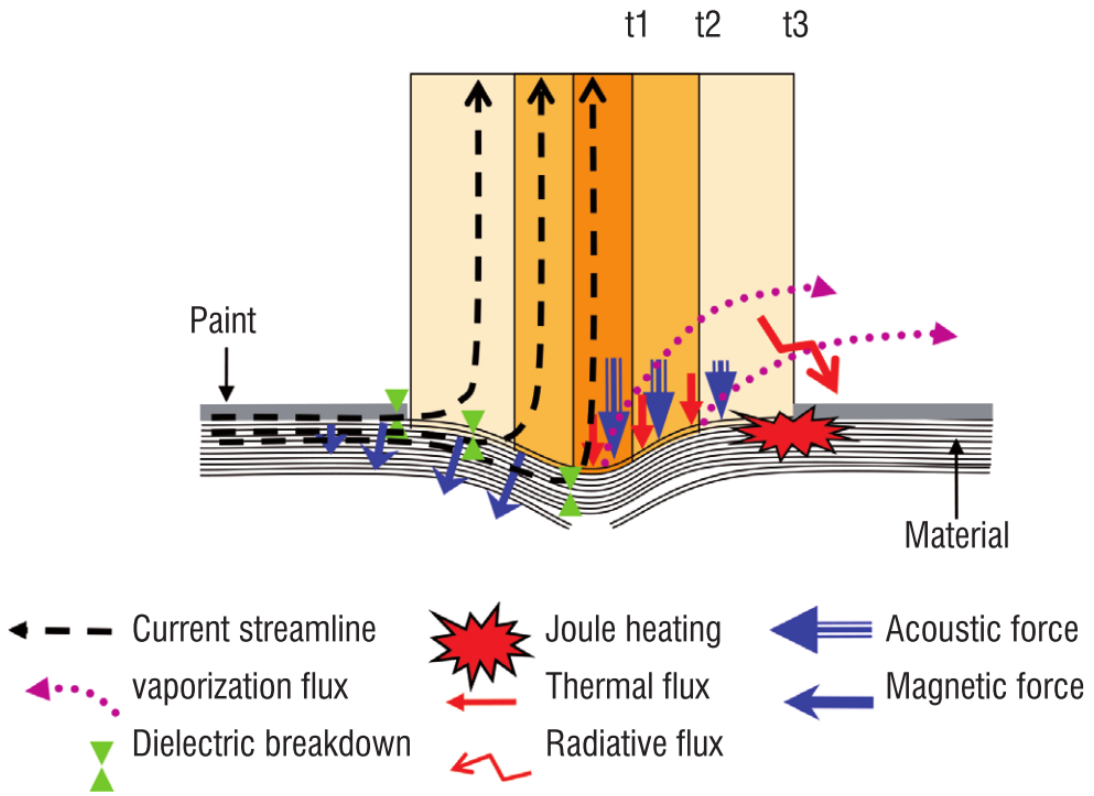

Figure 2.24: Schematic of various loading conditions from a lightning stroke on a CFRP panel at the attachment point [34]

The mechanisms described above result in different degrees of damage severity for different materials. The main variables that effect the severity are the electrical and thermal conductivity of the material. Conductive metallic skins will melt with long duration currents being applied, but the area of damage is primarily concentrated to the attachment point [83]. Materials like CFRP typically have 1000 times lower electrical conductivity in the fibre direction than metals and an additional 1000 times lower electrical conductivity in the transverse direction [83]. Usually damage occurs either at or in the near vicinity of the attachment point, as the arc searches for a conductive path. For materials that are practically non-conductive like GFRP, the lower conductivity will result in the increasing of all five direct effects, listed above, until the current ultimately punctures the GFRP. This can result in catastrophic damage, especially in a pressurized system where GFRP materials struck with lightning can be completely destroyed. Examples of damage are shown in Figure 2.25. The metal material (left Figure 2.25) shows a damage shape nearly circular with melting and charring near the attachment point. The CFRP material (middle Figure 2.25) shows damage fibres being exposed and loss of resin near the attachment point. The GFRP material (right Figure 2.25) shows a completely destroyed radome from an aircraft.

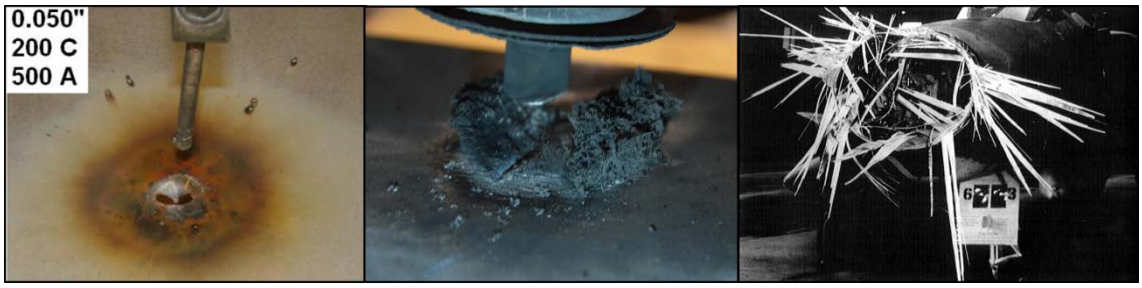

Figure 2.25: Lightning direct effects on aluminium [97] (left), pultruded CFRP (middle), and GFRP [83] (right)

First return strokes are responsible for rapid thermal heating, magnetic and acoustic shock forces, and arcing. For CFRP structures, rapid thermal heating due to high impulse currents induce temperatures in the range of hundreds to thousands of degrees Celsius [98]. Figure 2.26 illustrates the typical temperatures predicted during a lightning strike ply-by-ply alongside the exposure and decay times. This leads to loss of resin due to pyrolysis and fibre loss due to ablation. As mentioned previously the conductivity of the laminate is largest in the longitudinal direction, which leads to heat damage spread disproportionally along the conductive fibre direction as they conduct the electrical current as shown in Figure 2.27. The figures show two ultrasonic inspections with quasi-isotropic laminates damaged by a lightning strike. The damage spreads with the direction of the fibres as shown by the text indicated the ply angles.

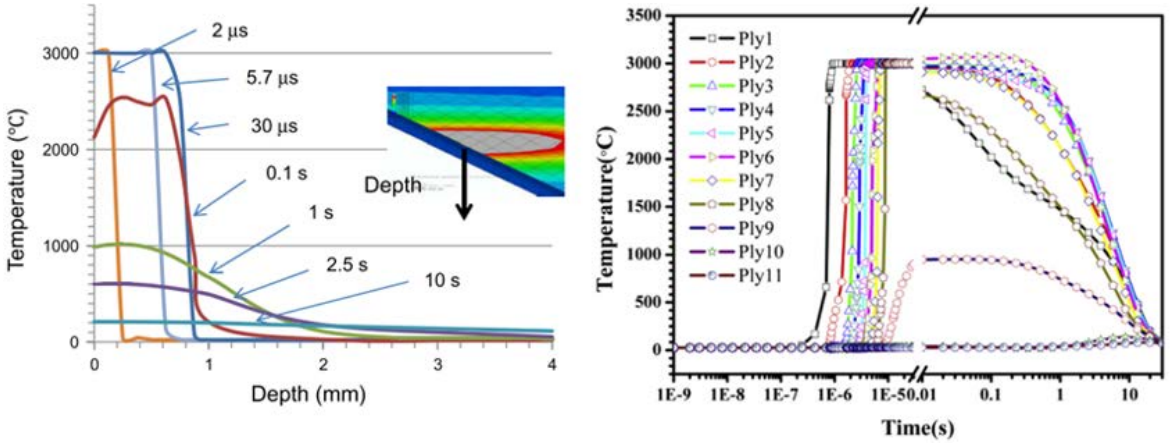

Figure 2.26: Example of a temperature profile through the depth of a quasi-isotropic CFRP from (left) Ogasawara [39] and (right) temperature response through time and ply from Dong [98]

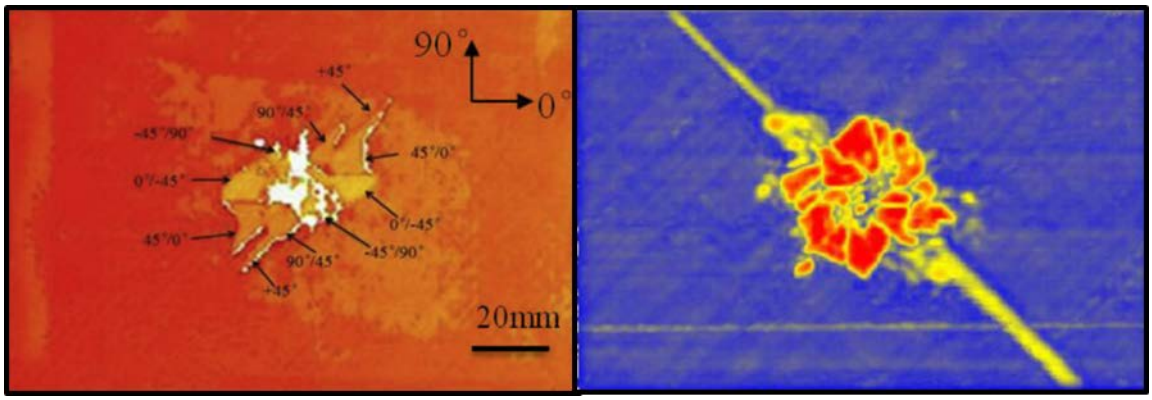

Figure 2.27: Two examples of damage area after lightning strike by ultrasonic C-scan result on quasi-isotropic CFRP samples: (left) 40kA peak current 4/20μs waveform damaged laminate [98] and (right) 40kA peak current 2.6/10.5μs waveform damaged laminate [99]

The continuing current is responsible for hole burning or arc root erosion [84], which is mainly associated with the duration of the elevated temperatures and resulting in additional pyrolysis (or melting) until the material is removed all the way through the thickness. In WTs, this typically effects the air termination system by removing metal from the receptor. However, it can also affect the residual strength of CFRP materials if they are supplied with enough current to heat the material.

2.4.2 Indirect effects from lightning attachment

Indirect effects are typically associated with electrical transients in conductive components which can lead to electrical current being sent to sensitive devices. This issue is mainly associated with aircraft, where sensory and other sensitive devices can be affected due to extraneous current. In WT blades, the indirect effects that damage the CFRP structures are associated with induced voltages. An example transient simulation, which shows the voltage difference, can be seen in Figure 2.28. These induced voltages between the down conductor and the CFRP can cause flashovers if not properly managed; this can be seen in Scenario 2 as described in Figure 2.9. The voltages rapidly increase with the length of the blade to reach the breakdown voltage of air/insulating material between the down conductor and CFRP material [100].

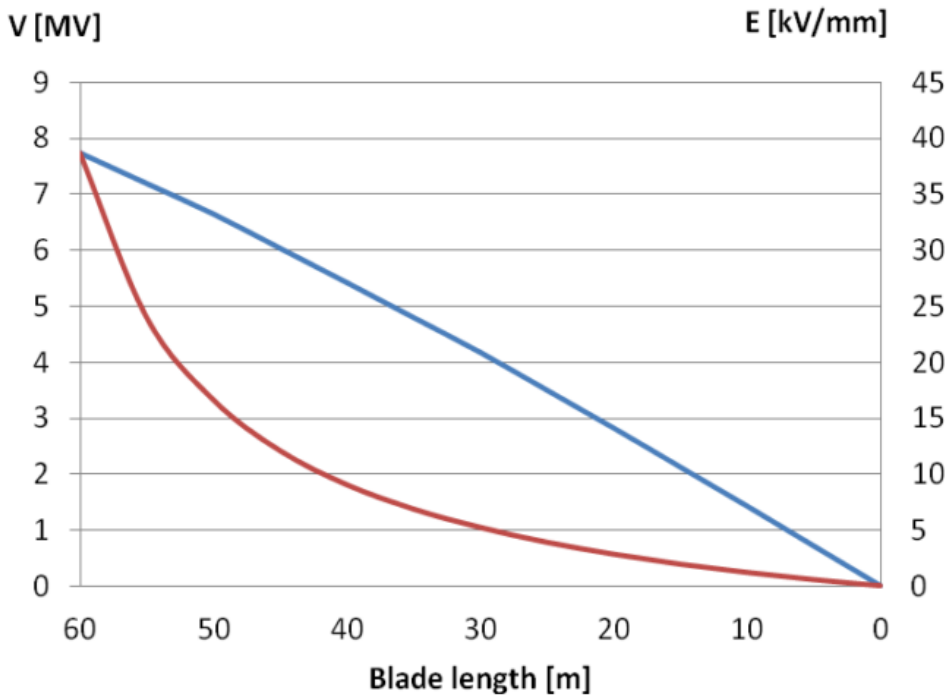

Figure 2.28: Maximum voltage difference from simulation of negative first return stroke between a lightning conductor (blue) and average electric field (red) [80]

2.4.3 Simulated lightning strike testing of direct attachment

Researchers have used simulated lightning strikes in a laboratory setting to understand the damage observed on CFRP materials. These experimental methodologies were initially used to inspect metal damages on aircraft [101]. Figure 2.29 shows one of the first published reports on CFRP materials by Feraboli [35]. The direct effects on CFRP materials from a 10/25μs lightning waveform was examined through microscopy and UV dye penetrant [35]. The results indicate that there is a potential for cracking and burning near and around the attachment point. However, the lightning waveform currents applied to the samples were less than the design lightning waveform from the IEC standard or SAE standard. The specimens were also quasi-isotropic leading to a more isotropic electrical conductivity and thermal conductivity in terms of the laminate.

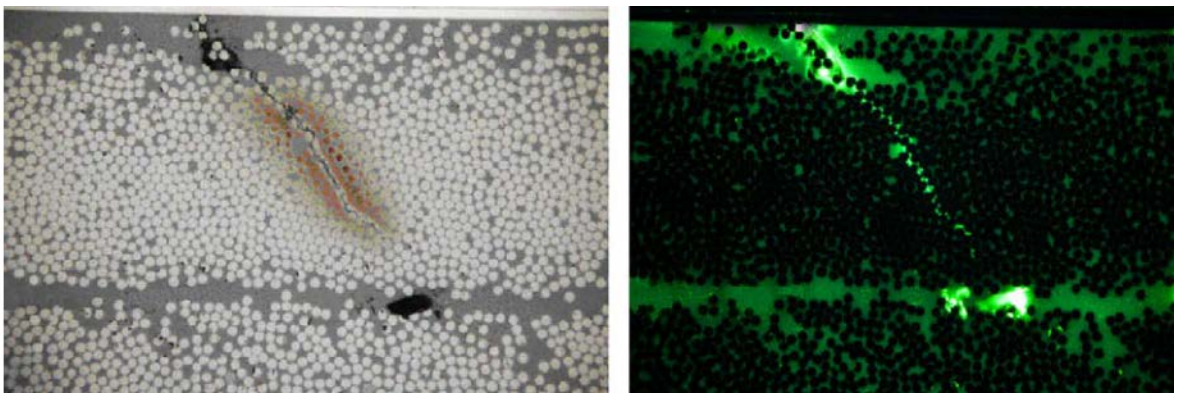

Figure 2.29: Micrograph of CFRP damage from a lightning strike near the attachment point where (left) is an inspection of cross-section under a brightfield illuminate under a microscope and (right) is an inspection of the cross-section under UV illumination and dye penetrant [35]

The method to simulate the lightning strike is through a spark gap with some form of a high current generator. The setup typically includes a high voltage capacitor and resistor stack to adjust the waveform, and a mechanical switch to initiate the strike. This method of using a spark gap test, which simulates an impulse waveform to detect and categorize damage, has been used in several studies [38], [39], [87], [99], [102], [103]. Although none of these studies have reached the Level 1 lightning strike that WTs can be subjected to (i.e. up to 10 MJ/Ω), the tests adequately show the effects of lightning on CFRP materials. However, they only simulate the impulse component, which leaves the question of damage associated with the full lightning stroke.

2.5 Damage modelling of lightning strikes in CFRP materials

Many researchers have developed models aiming to predict evolving damage to CFRP materials due to lightning strike. The first approach was to employ plasma flow-oriented simulations. Brocke [104] simulated the difference between CFRP and metals for arc entry and continuing current. Lago's [90], [105] model used free-burning arc simulations to determine the temperature profile around the arc; however, these models did not deal with CFRP damage resulting from the raised temperatures.

Haigh Taylor [106] explored damage by applying mechanical impulse forces orthogonal to the surface of a plate to study whether mechanical impact can accurately predict damage induced by a lightning strike on CFRP materials. Lepetit et al [107] further explored the impact by combining the thermal and mechanical equations to simulate the stresses and strains on CFRP materials and validate with experimental data. These models ignored the electrical and thermal properties and their dependency on the lightning strike parameters, and consequently have limited ability to predict damage because they did not account for Joule heating effects. As during a lightning strike rapid heating occurs due to Joule heating and this is widely considered to be the main source of lightning induced damage [34], [38], [108]–[113].

Typically, heating effects are modelled by adopting a Joule heating modelling framework, which essentially constitutes a coupled thermal-electrical model formulation used to predict the rise in temperature due to an applied electric current. Ogasawara [39] used a coupled thermo-electric finite element model to simulate the heat response of a CFRP material during a lightning strike and used the heat response to calculate damage through a pyrolysis equation. The damaged area, as shown in Figure 2.30, was estimated using temperature profiles from the results of the coupled thermo-electric mode. The predicted damage obtained from the FEM is observed to be under the attachment point. The laminate is quasi-isotropic which shows the spreading of the heat in the direction of the fibres and a predominate damage area are seen from elements which were exposed to heat above the degradation temperature 500°C.

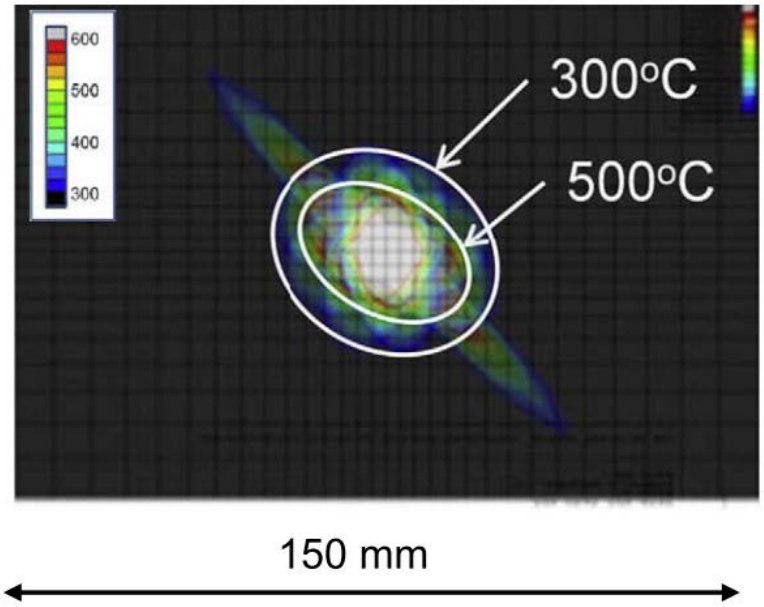

Figure 2.30: Estimation of damaged area from superposed contour curves obtained by finite element analysis [39]

Abdelal [40] expanded the work by Ogasawara by including temperature dependency of the electrical and thermal material properties. The method was used to show the difference in response to lightning strike of a composite material with and without a copper mesh protective layer. Dong [98] further improved on this method by defining the electrical properties based on a pyrolysis equation which uses the Arrhenius equation to predict the mass loss due to elevated temperatures. However, this approach exaggerates the temperature evolution because the model does not distribute the electrical current in the regions containing high electric fields, which can lead to overestimations of the damage in the through thickness direction of the composite laminate [114].

2.6 Structural response of CFRP materials after lightning strike

The damage modelling approaches described in the previous section are useful in understanding the potential extent of the lightning damage in a composite structure, but they do not provide any insight into the effect of the lightning strike on the structural performance. The most important aspect from an engineering point of view is to understand the impact of such damage on the structural response of the CFRP component/structure. To provide insight into how the loading condition, material, component thicknesses, and the risk of lightning damage, impact on the structural response recourse is made in two studies [74], [115]. A reference 88 meter WT blade with a rated power output of 10 MW designed by the Technical University of Denmark (DTU) is selected to examine the typical loading and material thicknesses used in a blade [115]. The probability of a direct lightning strike (Scenario 1; Figure 2.9) is used to determine the risk of a lightning strike along the blade length [74]. Figure 2.31 shows the material thicknesses and probability of a lightning strike on one plot along the blade length. Figure 2.31 (a) shows that the

blade is mostly made of UD plies (shown as UNIAX) along the blade lengths. The probability of lightning strike is shown as a histogram of the total number of lightning strikes along the length of a typical WT blade. Since most of the lightning strike happen at or near the blade tip, Figure 2.31 (b) shows a condensed version of the plot 30 m from the blade tip. Using this figure, a region of interest can be defined by where the cumulative lightning strike probability will be less than 5%, which is 10-20 meters from the blade tip as shown in Figure 2.31.

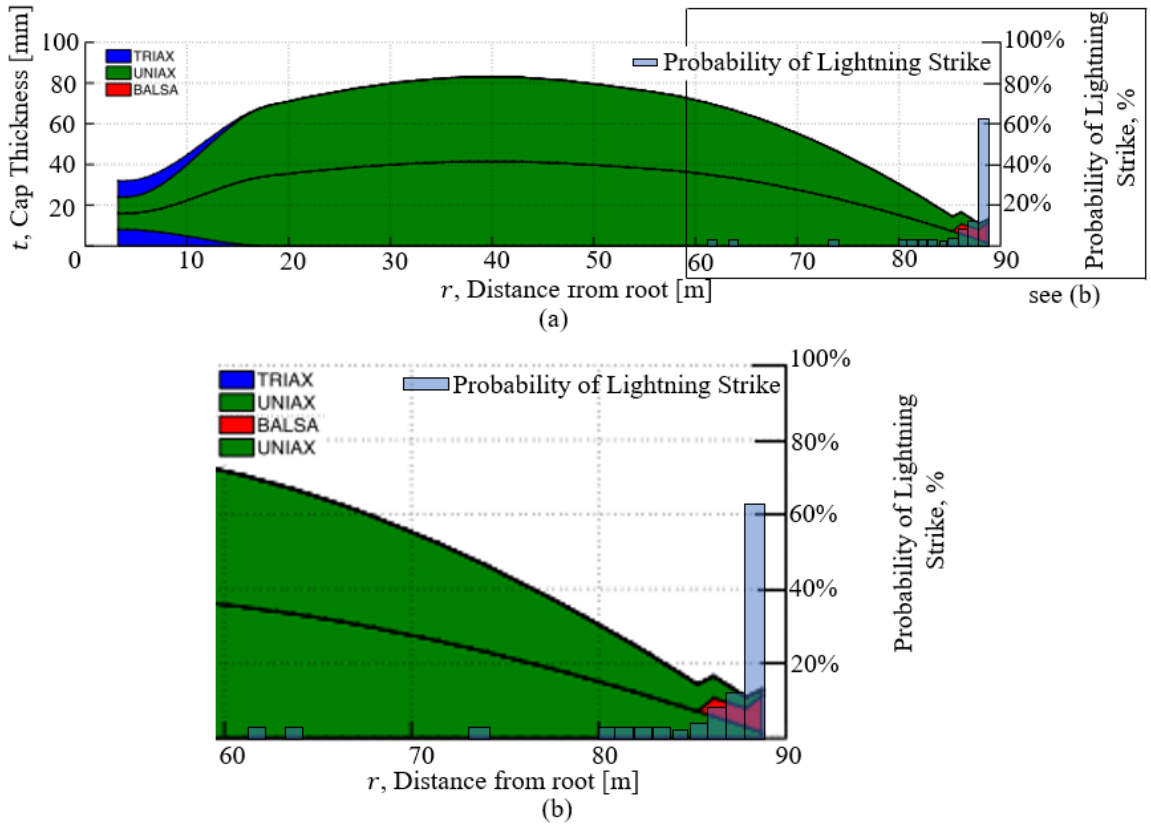

Figure 2.31: (a) Radial variation of sparcap thickness of the DTU wind turbine blade [115] plotted with lightning strike probability [74] along the whole length of the blade and (b) being the same as (a) but for the region of interest near the blade tip.

The region of interest defined using Figure 2.31 identifies a section of the blade that is typically made with fully UD laminates with relatively small thicknesses (>5 mm). The primary reason for the use of UD plies at this location is to carry tension and compression loads generated in the sparcaps due to the bending moments induced by the aerodynamic loading in flapwise bending (see Figure 1.5 (b)). Tension failure for a UD laminate being loaded in the fibre direction is defined by fibre fracture. This is not a likely scenario in a WT blade, but a direct attachment of a lightning strike may change the mechanical properties including the strength in tension. The key parameters to define failure for tension is the longitudinal direction (direction-1) strength, X_T, and the transverse direction (direction-2) strength, Y_T. These strengths may change due to lightning strike damage, but usually not by a significant amount because they are fibre dominated properties. The fibres are resistant to damage caused by Joule heating process because they have a much higher melting point (3000°C) when compared to the resin (300-500°C) [116]. Feraboli [35] performed

both tensile and compressive tests on coupons damaged with simulated arc entry lightning testing, as shown in Figure 2.32. The results confirmed that the tensile strength is less severely affected than compressive strength. For a 50 kA lightning strike, the damage CFRP sample had reduced tensile strength properties by 22% and compression strength by 31% when compared to an undamaged sample. In the same work, the tensile and compressive stiffnesses showed little change on average from the undamaged samples but did show large variability at the higher current levels especially for compression; see Figure 2.32 (right). Heidlebaugh [117] similarly presented test results for uniaxial tension and compression tests conducted on coupon specimens. These results showed a similar trend with compression being more sensitive to decreases in strength when damage was induced. Feraboli [35] and Heidlebaugh [117] did not address the full lightning waveform, and applied the current on small width coupons that concentrated the arc.

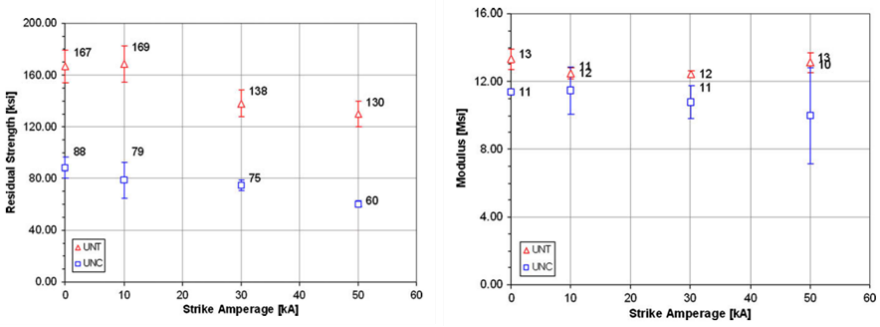

Figure 2.32: Residual tension/compression strength (left) and modulus (right) as a function of peak current [35]

As previously discussed, the effects from lightning strike induced damage are more pronounced for compression failure. Compression failure is more complex than tensile failure because it is primarily a matrix dominated failure mode [118]–[120]. Fibre kinking is the primary cause of compression failure which is typically initiated by microbuckling [118]. The instability causes the matrix to deform by shear as shown in Figure 2.33 (a). The model typically defines the deformation angle of the shear failure, called the 'kink band' by the angle β. The kink band is related to the misalignment frame as shown in Figure 2.33 (b). The initial fibre misalignment, ϕ_0, is the angle which the fibres are misaligned relative to the reference frame (typically ~1-5 degrees for UD laminates). These misaligned fibres cause eccentric loads in the laminate and reduce the compressive capability. The Budiansky and Fleck model [121] is typically used to predict the critical stress where fibre kinking will start. The model predicts the critical stress (σ_c) to be:

$$\sigma_c = \frac{G}{1 + \frac{\phi_0}{\gamma_y}} \tag{2.1}$$

where G is the shear modulus, γ_y is the shear yield strain calculated by the shear yield stress divided by shear modulus ($\gamma_y = \tau_y/G$). As can be seen the critical stress is highly dependent on the shear modulus G.

For the elastic perfectly plastic case, the model predicts the critical stress to be [118]:

$$\sigma_c = \frac{G}{\phi_0 + \gamma_y} \tag{2.2}$$

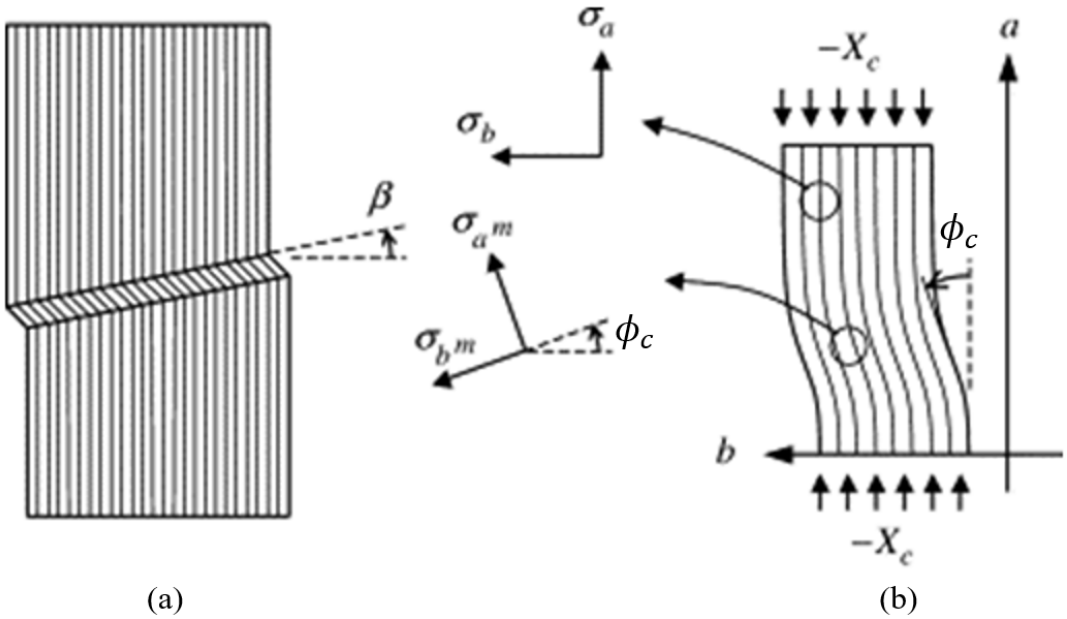

Figure 2.33: CFRP compression (a) fibre kink band failure mode with the compressive (b) misalignment frame [119]

The effects of changing the shear modulus and the fibre misalignment has a large effect on the critical stress [118]. Examples of the critical stress due to microbuckling with different parameters are shown in Figure 2.34 [118]. This chart indicates the reduction in shear modulus results in a lower critical stress causing fibre kinking. As mentioned in section 2.5, resin melting (or evaporating) from elevated temperature due to Joule heating is the primary cause of damage in CFRP materials. Losing resin has a large effect on the compressive capability [116].

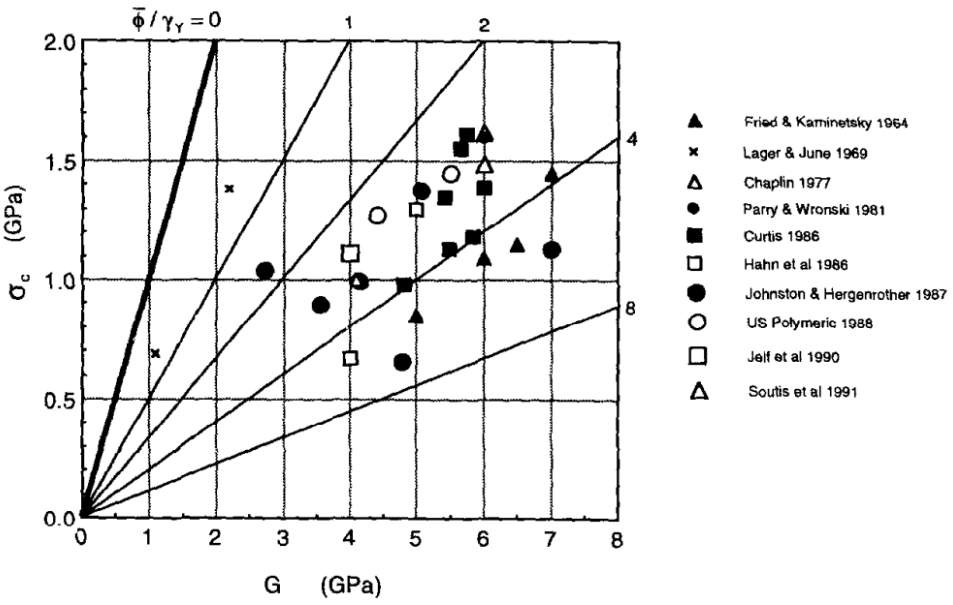

Figure 2.34: Elastic-ideally plastic predictions, compressive strength σ_c vs shear modulus G [118]

There is very little research published on the post lightning strike damage strength of CFRP materials and components. Kawakami [122] used compression after impact (CAI), as defined by ASTM D7136/D7137 [123], tests to compare different types of lightning damage because CAI tests are widely used for testing of aircraft structural composite materials. They are considered to be one of the most critical tests for certifying composite materials for aircraft structures [124]. Figure 2.35 shows the results from the test. They were conducted by subjecting small (140 mm by 140 mm) CFRP test specimens (effectively coupon level tests) to impact loading inflicted by a standardized blunt object to create impact damage labelled as 'Impact' in Figure 2.35 and compared to lightning damage impact labelled 'Lightning' in Figure 2.35. The panels were then fitted into a CAI panel compression rig that restricted the buckling modes, which ensured that only compressive load was applied. The load was taken to material failure and the results were compared. The tests showed that for the residual strength to decrease the lightning events typically had an order of magnitude higher energy level [122]. This result shows that impact and lightning damage have completely different responses to the induced damage. Although the energy levels were an order of magnitude different, the energy levels tested for the lightning cases were for typical lightning strike events and the residual strength was reduced by more than 40% [122].

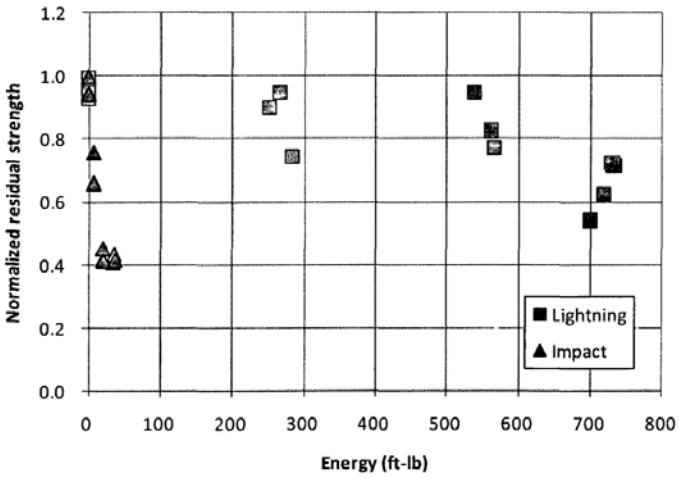

Figure 2.35: Comparison of normalized residual strength of CAI tests subjected to impact damage and lightning damage [122]

The work of Kawakami [122] appears to represent a move forward in regard to the assessment of the effect of lightning strike on CFRP materials. However, the research focused on the conventional CAI test, which uses small scale/size coupon specimens that do not include structural scale features and more importantly capture the interactions between material failure, delamination and structural scale stiffness driven failure/collapse mechanisms such as buckling and post-buckling responses. Thus, the compressive loading condition in the thin laminate configuration in the region of interest of a WT blade (see Figure 2.31) increases the likelihood of buckling and inducing failure by a complex post-buckling response, which would be promoted by lightning strike induced damage. There is a clear need for more detailed investigations than those of CAI scaled test on larger more realistic structural plates representative of the sparcap.

Wang [125] modelled lightning damage through a Joule heating model and subsequently modelled residual strength through a structural model. The lightning model used an ablation mechanism in areas of high heat flux to model the removal of carbon fibre to determine fibre damage. The ablative damaged regions were characterized as fully damaged (100%) with the regions damaged by pyrolysis range from 0% to 100% damage. Based on the estimated damaged areas, residual strength predictions were obtained using a FEM with fully damaged elements deleted and partially damaged elements assigned a percentage of their stiffness or strength properties based on the pyrolysis predictions. The residual strength structural FE model used the Hashin criteria to modify the element until the laminate's ultimate failure load was reached. The results of Wang's were for tensile case (not as critical). The predictive models showed that all strengths were above 80% of the undamaged (pristine) strength of the composite. This model is a first step into the structural response, however, the more critical case is to understand the response in compression.

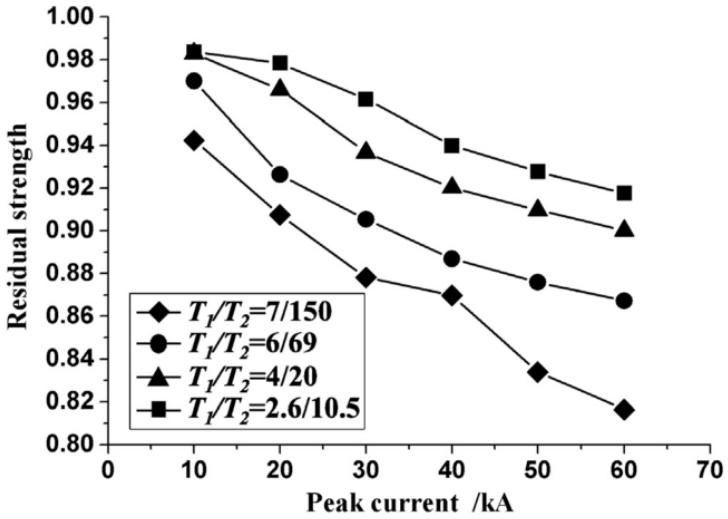

Figure 2.36: Prediction of residual strength on CFRP laminate subjected to different waveforms [125]

2.7 Summary

The literature review reveals a need for the development of a deeper understanding of lightning damage on WTs with CFRP structural blade elements. Previous tests such as [35] and [122] have shown (on coupon level) direct strikes cause large amounts of damage and this damage severely effects the residual properties, but there has been little research on the conducted current situation (Scenario 3; Figure 2.9) which is the most common lightning exposure event to a CFRP material. This justifies an investigation into the effects on UD CFRP materials subjected to these types of lightning scenarios and is investigated in Chapter 3.

Similarly, previous tests of direct strikes have been primarily on multi-directional (typically quasi-isotropic) coupon sized samples [33], [38], [39], [109]. The conductivities of the quasi-isotropic laminates limit the anisotropic nature of the CFRP and mask the physics from a more anisotropic material such as a UD laminate. Previous damage models have attempted to determine the factor that plays the largest role in damage to CFRPs [112], [113]. This justifies an investigation of direct lightning strikes on UD laminates to determine the differences in damage on UD materials and an investigation of the dominate cause of damage (peak current, charge, or specific energy). Chapter 4 presents the outcome of a number of simulated lightning strike tests conducted in a specially adapted test facility.

Previous damage models have shown an ability to predict damage states in CFRP material exposed to lightning [40], [90], [105], [114], [125]. The work described in Chapter 4 reveals different damage shapes induced from lightning events on UD laminates, which were not predicted by conventional models. Therefore, an investigation was conducted to devise a new modelling approach to predict damage in UD materials. Chapter 5 presents the outcome of the new damage model approach and the results compared against experimental results from Chapter 4 and a conventional model.

Previous work [35], [37] showed a large effect on the ability of composite materials to carry compression after CFRP materials have been exposed to lightning strikes. However, these were on coupon level tests. Hence it is necessary to provide an understanding of the structural response in compression of CFRP materials damaged from lightning on a structural scale. To the best knowledge of the author, this has never been investigated before. Therefore, a buckling/post-buckling structural loading condition is explored in the thesis. Chapter 6 explores these structural scale effects experimentally by subjecting lightning damage specimens (from Chapter 4) to compressive loading and a model which uses damage from the lightning damage model to manipulate the material properties and determine a first failure load from a structural post-buckling model.

The literature review has clearly demonstrated the gaps in research, which confirm that the research done for the PhD is novel. The research objectives listed in Chapter 1 (section 1.3) were defined by the knowledge gaps found from the literature review and define the research described in the remainder of the thesis.

Chapter 3

Experimental Investigation of Degradation of Material Properties in CFRP Laminates Subjected to Electric Current Conducted Along the Fibre Direction

3.1 Introduction

Conducted current lightning strikes in WT blades are typically defined by a rapid (<1000μs) impulse current which attaches directly to the carbon reinforcement in the sparcap. Although, such events are non-synonymous to the explosive nature of the direct strike, it is the most common event experienced by CFRP components in WT blades equipped with lightning protection systems. Typically conducted current strikes are introduced into the CFRP laminates through equipotential bonds, see Scenario 3 in Figure 2.9. The research presented in this chapter investigates the reduction or degradation of the mechanical properties of CFRP laminates caused by a simulated lightning strike, where the CFRP laminates investigated are representative of materials used in current WT blade structures. The work focuses on the effects of simulated lightning strike induced damage on the load response and failure behaviour of CFRP laminates subjected to shear and compression loading. The work in this chapter fulfils Research Objective 1 "Experimental investigation of degradation of mechanical properties of CFRP subjected to electrical current conducted along the fibre direction" and has been published in the following journal paper:

[96] "T. M. Harrell, O. T. Thomsen, J. M. Dulieu-Barton, and S. F. Madsen, "Damage in CFRP composites subjected to simulated lightning strikes - Assessment of thermal and mechanical responses," *Compos. Part B Eng.*, vol. 176, no. November, p. 107298, Nov. 2019."

3.2 Methodology

3.2.1 Specimen Manufacturing

Eight CFRP unidirectional (UD) five ply laminate specimens were manufactured using the carbon/epoxy material system PX-35 from Zoltek. The eight laminates were manufactured using vacuum liquid resin infusion producing CFRP laminate strips with dimensions of 500 mm long x

50 mm wide x 4.5 mm thick. The specimens were chamfered at the ends with an approximate 1:4 taper to expose the carbon fibres and provide a connection point. Silver conductive paint and copper plate were added to the tapered sections to aid in conducting the electric current to the exposed fibres. Figure 3.1 shows an example of the manufactured CFRP strips.

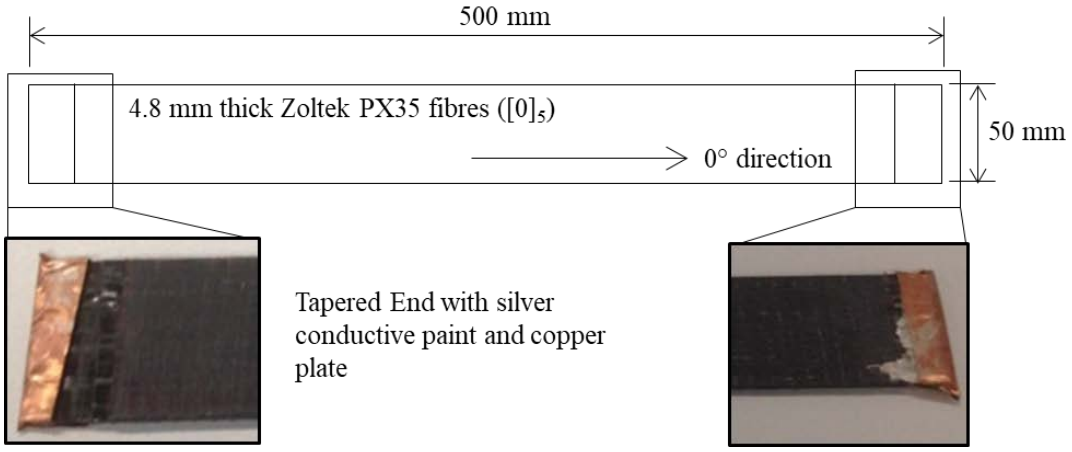

Figure 3.1: CFRP strip specimen with dimensions and plating used in simulated lightning strike experiment

3.2.2 Simulated Lightning Strike Experiments

The CFRP strip specimens were subjected to electrical current with three different waveforms. The first waveform examined was a unipolar 10/350µs waveform simulating the first return stroke during a direct strike according to IEC 61400-24 Ed1.0 [47]. The second was a unipolar long stroke component (or DC) also defined by the IEC standards. The third waveform was a combination of the 10/350µs and DC waveforms. All of the current components were tested using the conducted current test method provided in Annex D3.4 of IEC 61400-24 Ed1.0 [47]. An example of the test setup and the current path during the testing is shown in Figure 3.2.

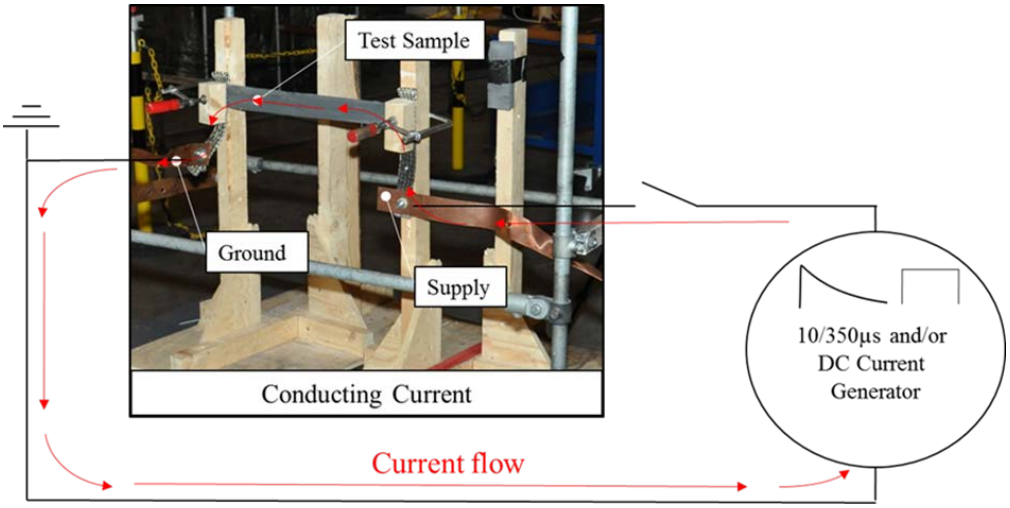

Figure 3.2: Electrical circuit describing the current introduction into the CFRP sample through conducted current superimposed on an image of the experimental setup

The initial stroke waveform was an impulse which is defined by three characteristic parameters; the peak current value (I_{peak}), the rise time to reach the peak current (t_1), and the time at which the current decays to half of the peak current (t_2), also known as the half time. The DC current is defined by the peak current value (I_{peak}), and the duration (t_{DC}), and these parameters are shown in Figure 3.3. The charge, Q, and the specific energy or action integral, AI, are used to compare different waveforms and are calculated from the beginning of the waveform or 0 to the final time at the end of the waveform or t_f as follows:

$$Q = \int_0^{t_f} i(t)\, dt \tag{3.1}$$

and

$$AI = \int_0^{t_f} i^2(t)\, dt \tag{3.2}$$

Typically, the charge is associated with severity of heating or burn through of the material and the action integral is associated with melting of the poorly conductive material.

Table 3.1 provides an overview of the characteristic parameters used in the lightning strike tests. These comprise of three different waveforms that are considered representative of the exposure experienced by WT blades in operation: DC, Impulse, and Impulse+DC. The Impulse+DC waveforms have split the lightning parameters into impulse and DC by providing the first number as the impulse portion and the second number in the round brackets as Impulse(DC).

During the simulated lightning strike experiments, an infrared camera was used to capture the thermal evolutions. The infrared camera was a PYROVIEW 640L, which is an uncooled micro-bolometer array with 640 × 480 pixels. The maximum image capture rate of 50Hz was used. The camera captured one full surface of the specimen. The post-processing of the thermal data was based on data captured from the middle of the CFRP specimens (about 40% of the specimen width). This was done to ensure that influence from the connections and any flame ignition had only a small or little influence on the results. All thermal data from the middle of the specimen was averaged at each captured frame to gather a temperature evolution over time. This was done to remove outliers and determine the temperatures seen by the material testing coupons.

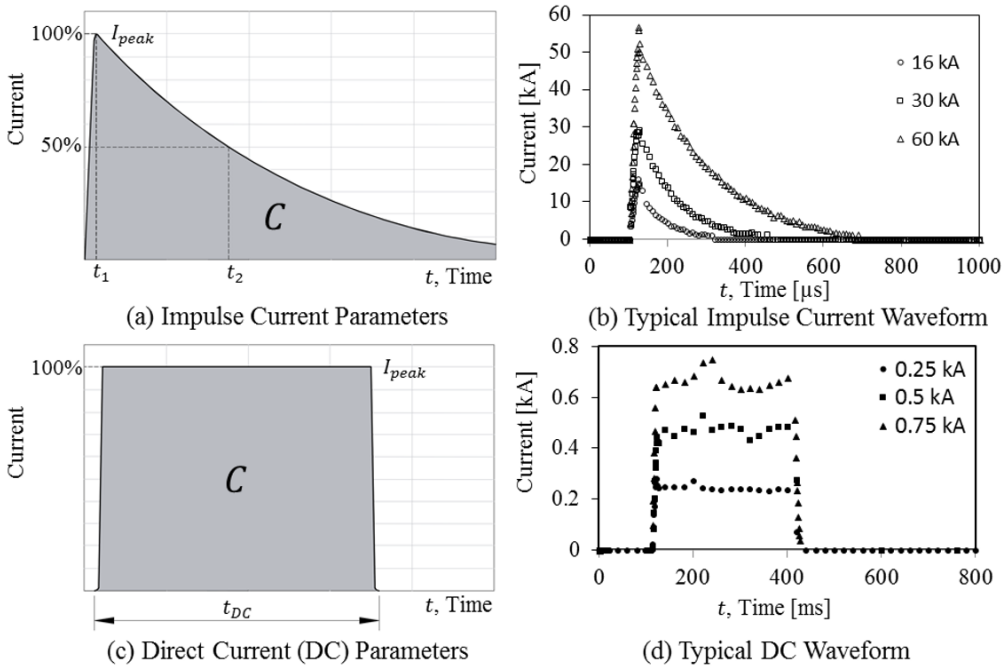

Figure 3.3: Lightning strike waveform with parameters for (a-b) impulse waveform characterization, and (c-d) DC waveform characterization

Table 3.1: Test parameters defined for the simulated lightning strike tests: Peak current, waveform, charge, and specific energy applied to the specimens

Specimen	Peak Current [kA]	Waveform Characterization (Impulse t_1/t_2) (DC t_{DC})	Charge [C]	AI [kJ/Ω]
DC1	0.293	314.4	73.2	17.59
DC2	0.531	317.6	141.1	66.94
DC3	0.753	319.6	201.3	134.5
Impulse1	16.2	15.8/50.8	2.13	10.61
Impulse2	34.4	14.6/88.0	4.46	73.9
Impulse3	56.8	15.4/128.8	9.29	263
Impulse+DC	51.5(1)	15.8/110 (622)	8.1 (540.1)	227(498)

3.2.3 Compression and Shear Coupon Test Specimens

Compression and shear tests were conducted according to ASTM D6641 [126] (compression) and ASTM standard D5379 [127] (Iosipescu V-notch test), respectively. The coupon specimens were manufactured by waterjet cutting from the vacuum infused CFRP strips. The layout of the test specimen waterjet cutting scheme is shown in Figure 3.4.

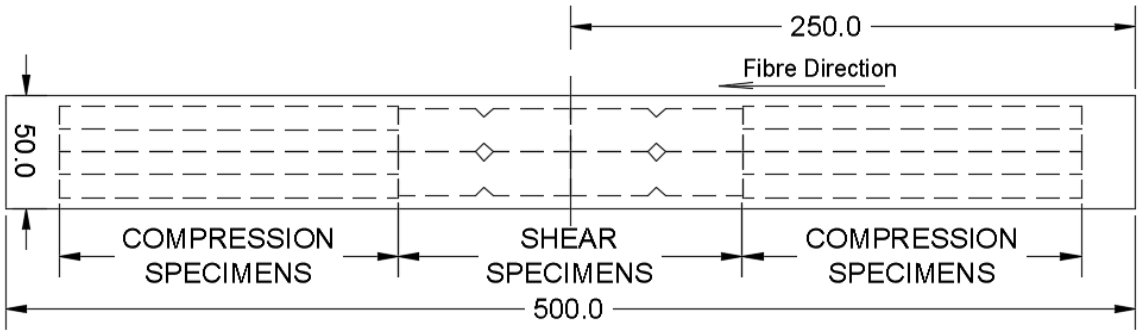

Figure 3.4: Waterjet cutting scheme for CFRP compression and shear test specimens

The compression test specimens were 10 mm wide x 150 mm long and were mounted with end tabs made of S-glass with a 1:4 tapered section. The end tabs were bonded to the specimens using Araldite 4858. An example of the compression sample is shown in Figure 3.5 (a). The compression tests were conducted using an Instron 100 kN servo-hydraulic test machine with a loading rate of 0.2 mm/min in accordance with ASTM D6641 [126].

An example of the Iosipescu V-notch shear test specimens is shown in Figure 3.5 (b). The shear tests were conducted using an Instron 50 kN electro-mechanical test machine with a loading rate of 0.5 mm/min in accordance with ASTM standard D5379 [127].

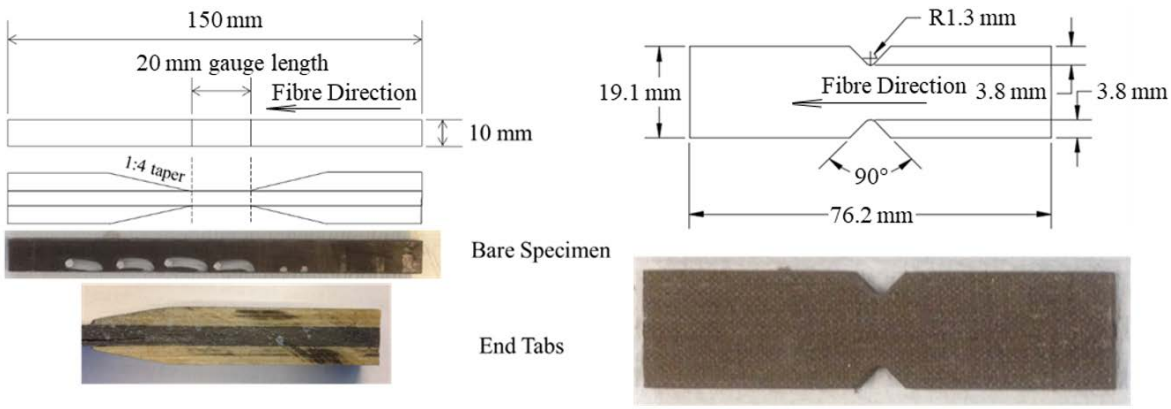

Figure 3.5: Compression specimen dimensions and image of a typical sample (b) shear specimen dimensions and image of a typical sample

Four control specimens that had not been subjected to simulated lightning strikes were also tested in compression and shear. Three damaged specimens from each test configuration (see Table 3.1) were tested in both compression and shear. A total of 50 tests were conducted; 25 in compression and 25 in shear. The obtained results for the lightning strike damaged specimens were compared to the results obtained for the pristine (undamaged) CFRP specimens. Table 3.2 summarizes the adopted test matrix.

Table 3.2: Test matrix for compression and shear coupon tests

Residual Strength Specimen	Type	Nominal Thickness [mm]	Gauge Width [mm]	Repetitions
Control-C	Compression	4.8	10	4
DC1-C	Compression	4.8	10	3
DC2-C	Compression	4.8	10	3
DC3-C	Compression	4.8	10	3
Impulse1-C	Compression	4.8	10	3
Impulse2-C	Compression	4.8	10	3
Impulse3-C	Compression	4.8	10	3
Impulse+DC-C	Compression	4.8	10	3
Control-S	Shear	4.8	11.5	4
DC1-S	Shear	4.8	11.5	3
DC2-S	Shear	4.8	11.5	3
DC3-S	Shear	4.8	11.5	3
Impulse1-S	Shear	4.8	11.5	3
Impulse2-S	Shear	4.8	11.5	3
Impulse3-S	Shear	4.8	11.5	3
Impulse+DC-S	Shear	4.8	11.5	3

3.2.4 Digital Image Correlation

Digital Image Correlation (DIC) was used to obtain full field measurement of the strains on the specimen surface during testing. As the specimens were already black, they were coated with only a thin layer of black paint to make a uniform surface and then speckled with white paint as opposed to the more conventional white background with black speckles. Images were captured with an 'E-Lite LaVision' camera equipped with a Sigma 105 mm lens. The load levels were recorded from the test machine as the images were captured simultaneously using the software package DaVis 8.3 [128]. The experimental setup is shown in Figure 3.6. The DIC was processed through the DaVis correlation software to determine the strains. The post-processing used a substep size of 55 x 55 pixels and a step size of 21.

To determine the adequacy of the DIC measurements, strain gauges were mounted on the back side of the control samples. A 350Ω linear pattern strain gauge (CEA-06-250UW-350) was used for the compression test specimens, and a 350Ω shear pattern strain gauge (EA-06-062TV-350) was used for the shear specimens. The stress-strain data collected using strain gauges showed a good correlation with the DIC measurements; see Figure 3.7. The maximum difference between the two measurement techniques was determined by calculating the Young's or shear moduli. It was found to be less than 4%. Due to the good correlation, DIC was used for the remainder of the tests to ensure any resin lost during the lightning test was not added back with the application of the strain gauges.

For the DIC measurements, a Region of Interest (ROI) was defined in the gauge sections of the specimens as shown in Figure 3.8. The DIC data was post-processed by taking the mean of the

strains measured over the ROI. For the compression tests, the strains were averaged over 50% of the gauge section length. This was done for the ROI to avoid stress concentration due to load introduction from the end tabs. For the shear specimens, the strains were averaged over the whole gauge section was used for the ROI as proposed by [129], [130]. The averaged strains measured over the ROI zones were referenced against the average (or nominal) stresses in the gauge zone defined by the force measured by the load cell divided by the gauge zone cross section areas.

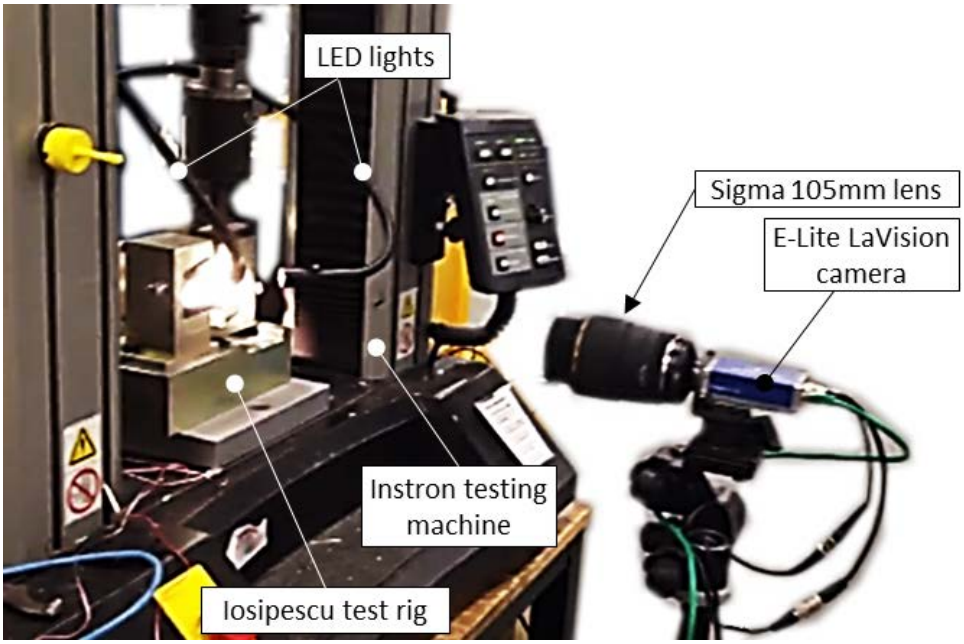

Figure 3.6: Experimental setup for Iosipescu tests

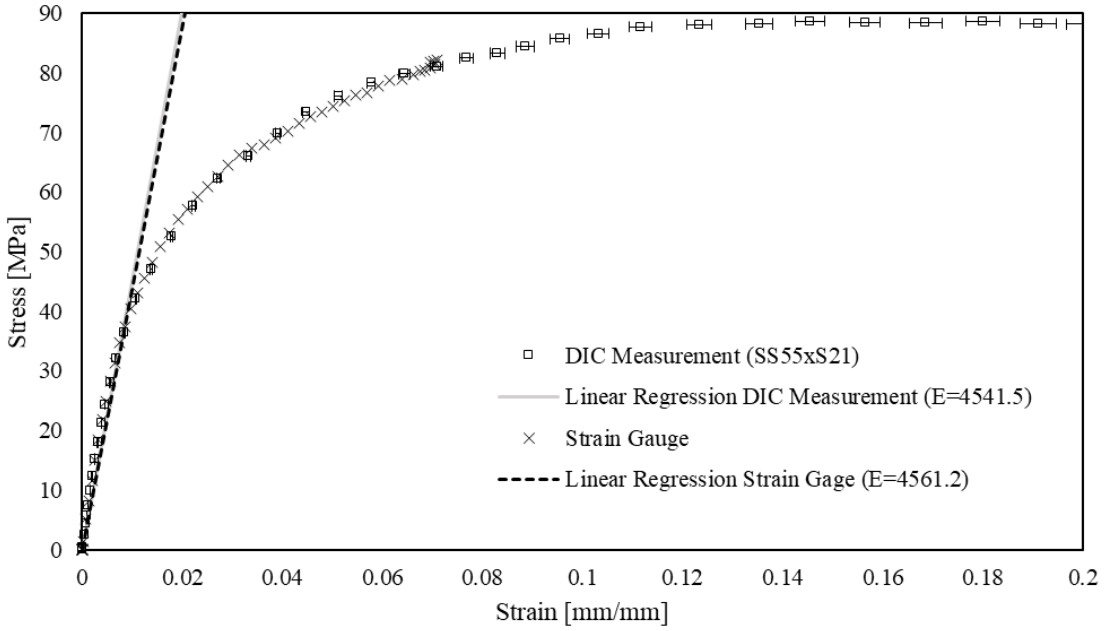

Figure 3.7: Sample stress-strain curve obtained for Iosipescu test - Strain gauge and DIC measurement data

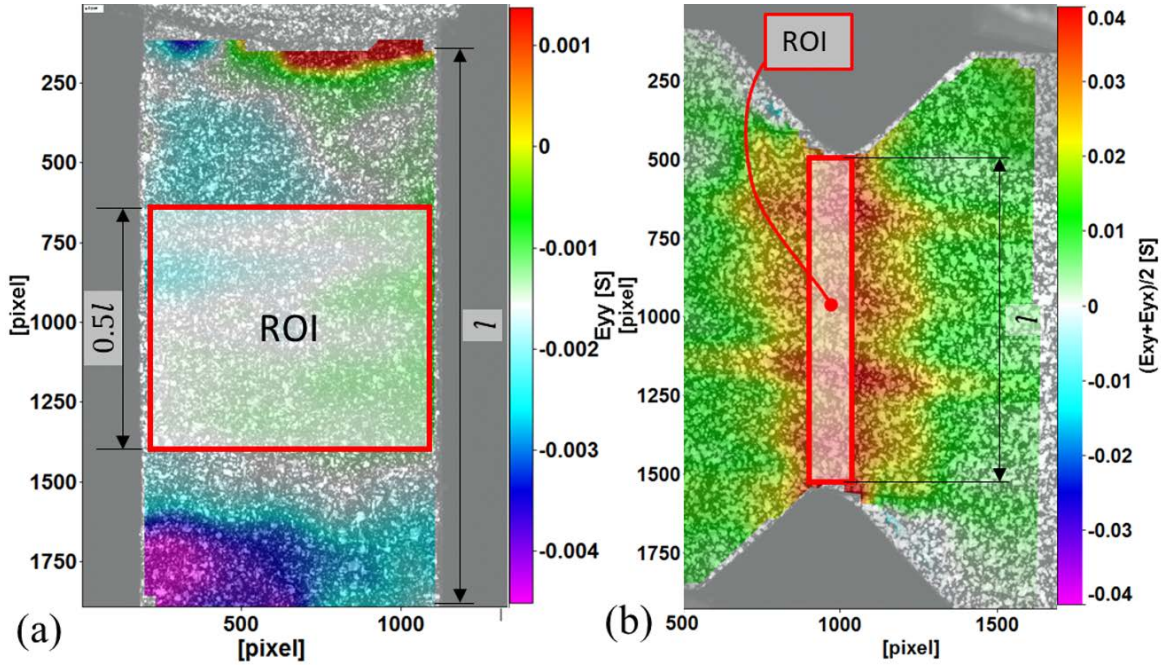

Figure 3.8: Example of DIC ROIs: (a) compression specimen, and (b) shear V-notch specimen with an overlay of the ROI area used to calculate the average compression and shear strains

3.2.5 Determination of Failure Initiation Stress

When conducting the tests, it was important to determine at what stress/strain levels damage initiated in the specimens. To assess this, the methodology devised by [131], [132] was employed. The method assumes that the total strain measure can be split into an elastic part and an inelastic part as follows:

$$\varepsilon = \varepsilon_e + \varepsilon_i \tag{3.3}$$

where the elastic part is $\varepsilon_e = \sigma/E$, and the 'inelastic' part is assumed to follow the nonlinear relation:

$$\varepsilon_i = a \ln\left(1 - \left(\frac{\sigma}{\sigma_0}\right)^m\right) \tag{3.4}$$

which is often adopted for the modelling of metal alloy plasticity [131].

In Eqs. (3.3) and (3.4), E is the Young's modulus, σ_0 is the horizontal asymptote of the stress-strain curve, the parameter m relates to a strain hardening rule of the material, and a scales the magnitude of the inelastic strains. It should be noticed that, in this work, the inelastic strain ε_i accounts for the cumulative effects of (resin/matrix) plasticity, micro-cracks and geometrically nonlinear effects [133] due to fibre rotations etc. Therefore, the fitting parameter m does not represent strain hardening in any physical sense, and the expression for ε_i is merely to be seen as a nonlinear fitting law. Following this, an appropriate definition of onset point of damage/nonlinearity can be adopted

as occurring when the gradient of the tangential stiffness changes sign. Following this the 'failure initiation stress' can be defined as suggested in [132]:

$$\frac{d^3\sigma}{d\varepsilon^3} = 0. \tag{3.5}$$

The stress-strain response of the V-notch shear specimens is significantly influenced by the matrix material and therefore can be expected to exhibit substantial nonlinearity, whereas the compression tests are expected to display a more linear stress-strain response. Accordingly, the methodology outlined for estimating the onset of nonlinearity, defined as the failure initiation strength, was only used for the shear tests. The data fitting was carried out by a least squares method and implemented in the commercial software Maple 2017 [134].

3.3 Results

Seven of the manufactured CFRP strips were subjected to simulated lightning strike events. Three specimens were subjected to long stroke direct current and labelled 'DC' in Table 3.1, and three specimens were subjected to a unipolar current and labelled 'Impulse' in Table 3.1. Finally, one specimen was subjected to a combined impulse and long stroke and was labelled 'Impulse+DC' in Table 3.1. The resistance of the CFRP strips was large (200 mΩ over 50 cm) and the Impulse waveform achieved was a 15/110μs waveform.

3.3.1 Damage Introduction

The temperature evolution during the DC, Impulse, and Impulse+DC tests were similar, as shown by images captured by the infrared camera in Figure 3.9, where the temperature increase distributed evenly throughout the samples. The largest increase in temperature corresponded to the largest specific energy used in the lightning tests. The DC tests yielded very little audible acoustic response and led to little or no visual indication of damage of the specimens. In contrast, the Impulse and Impulse+DC tests were much louder and rapid events with bright flames emitting from the current injection points that dissipated within a few seconds.

The images shown in Figure 3.9 were captured using a Nikon digital SLR camera and a PYROVIEW 640L infrared camera. Figure 3.9 splices white light images (Nikon) on the left with the thermal images (PYROVIEW) on the right. The white light images had an exposure time of 5 seconds that allowed the accumulation of light intensity to be captured throughout the tests. The thermal images were taken from the image frame immediately after the lightning strike test or where the maximum heating of the specimens occurred.

During the DC tests there were no visual indications of suspected damage in the white light images captured and as shown on the right in Figure 3.9 (a) the infrared image displays a uniform increase in temperature. The Impulse tests also showed no visual indication of damage despite the appearance of sparks and flames as described above. In Figure 3.9 (b), the white light image on the left does show flames and sparks, but these are products of air ignition between the metallic contact point and the CFRP testing material, as the combustion temperature of the CFRP was not reached. This is confirmed in the thermal images captured after the dissipation of the flames. These show a uniform temperature increase in the sample both where the flames appeared at the contact points, as well as in the middle where no flames appeared. The Impulse+DC tests displayed more extensive visual indication of damage, with flames engulfing the sample and lasting several seconds longer than end of the current supplied to the sample; see Figure 3.9 (c). In these tests, the combustion point of the specimens was reached, igniting the epoxy matrix. Although all samples showed increases in temperature only one sample, Impulse+DC, showed visible signs of damage.

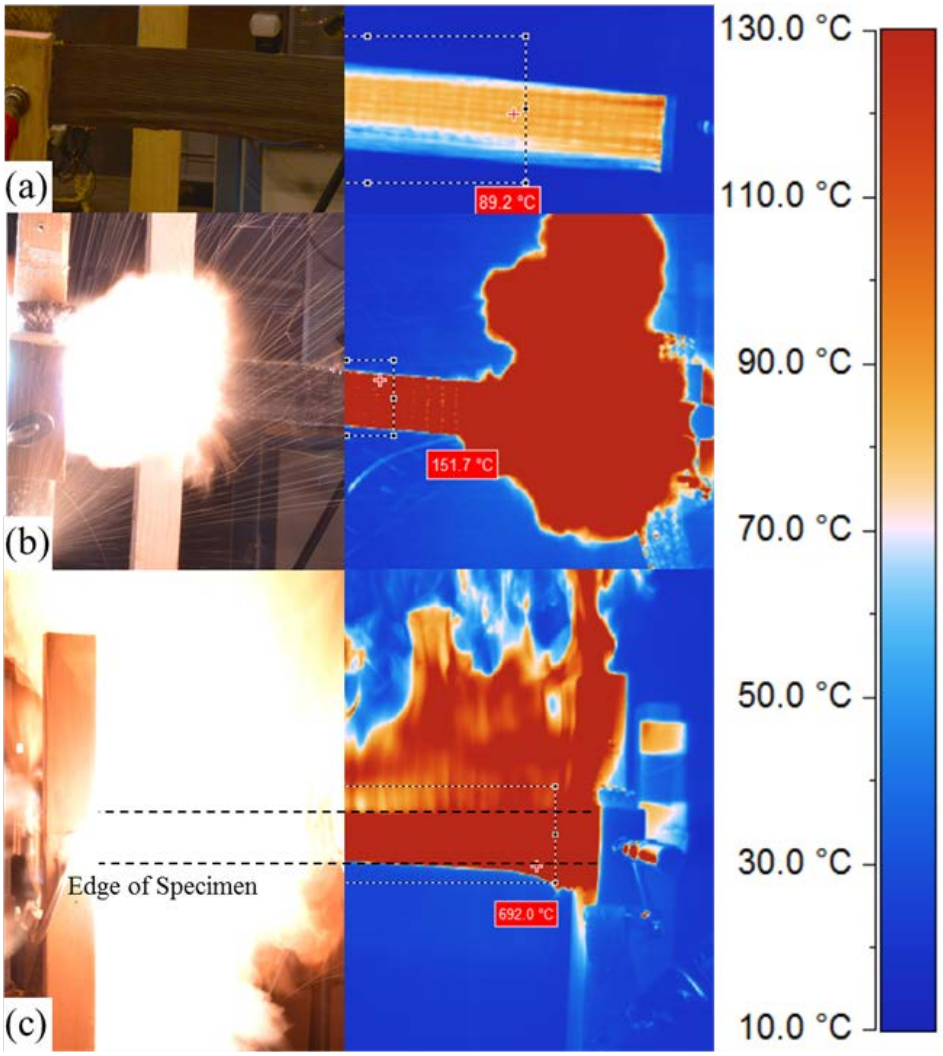

Figure 3.9: Selected photos and thermal images from: (a) DC tests, (b) Impulse test, and (c) Impulse+DC test

The thermal data was recorded to find the maximum temperature during the lightning strike tests. The temperature data recorded at the centre of the specimens is shown in Figure 3.10. The thermal data results show that the maximum temperature always occurred after all the current was injected. This data can determine which CFRP specimens went above the glass transition temperature of 79°C for the resin system tested, and how long the specimens were above the glass transition temperature. The DC2-3, Impulse2-3 and Impulse+DC specimens all reached temperatures above the glass transition temperature for extended periods of time. Impulse+DC reached a temperature, which caused ignition of the sample and caused the sample to burn during the test. The second apparent peak of the Impulse+DC at 11s is due to flames that extinguished in the frame of the measurement.

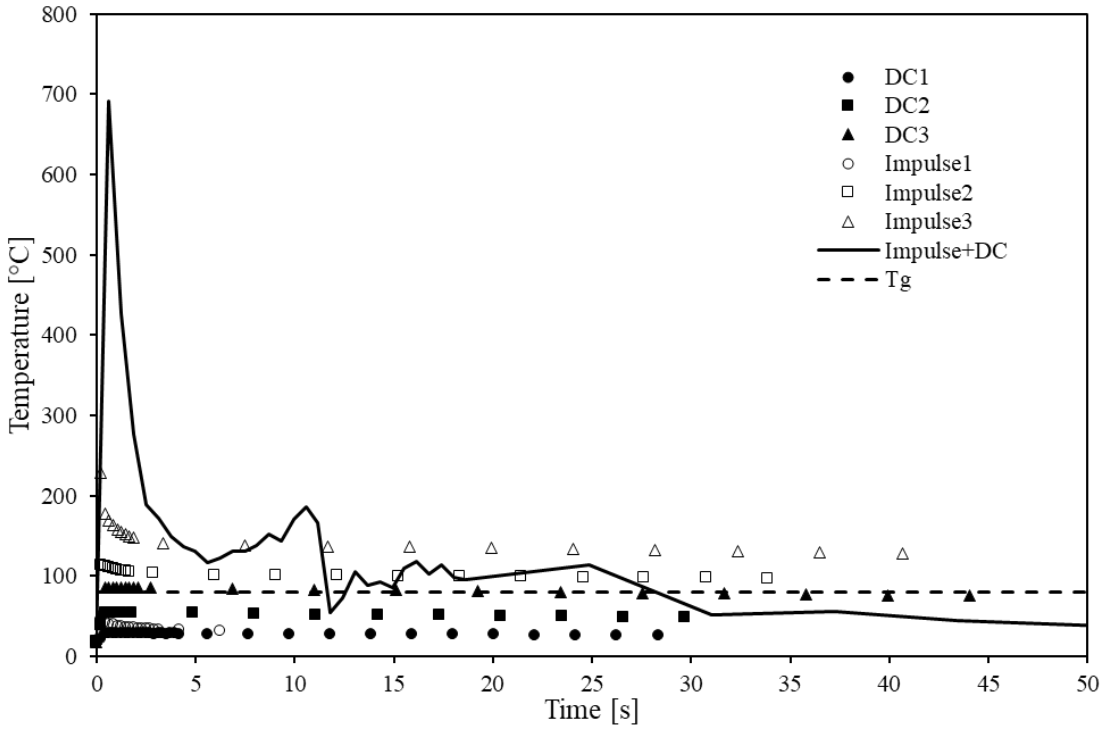

Figure 3.10: Average temperature measured at the centre of the specimens during lightning strike tests

3.3.2 Visual Inspection

The damaged specimens were inspected visually to assess the damage inflicted to the CFRP materials. The focus of the inspection was to identify fibre, resin, and delamination damage apparent on the surface. The visual inspection was conducted by eye both with and without a 10x magnification optical loupe to allow for a more detailed assessment of the surface. On the DC and Impulse specimens damage was concentrated near the connection points. For the DC and Impulse specimens, the only visible damage found was underneath the connection points, with the likely cause being the transfer from metallic connection to the CFRP, and on specimen Impulse3 within a distance of 2 cm from the connection point. Selected images from the DC3 and Impulse3

specimens are shown in Figure 3.11. In the areas where the coupons were cut out, see Figure 3.11 (a) and (b), the material showed no visual signs of damage. Further, Figure 3.11 (c) shows what a typical cross section looks like for all the Impulse and DC samples. This typical cross section has no signs of damage, and there are no visible bulges on the top surface to suggest internal delamination damage. Figure 3.11 (d) the image shows damaged fibres, loss of resin, and glass fibre stitching from the dry fabric pulled away from the specimen. However, the damaged area near the connection point is not used in the coupon tests.

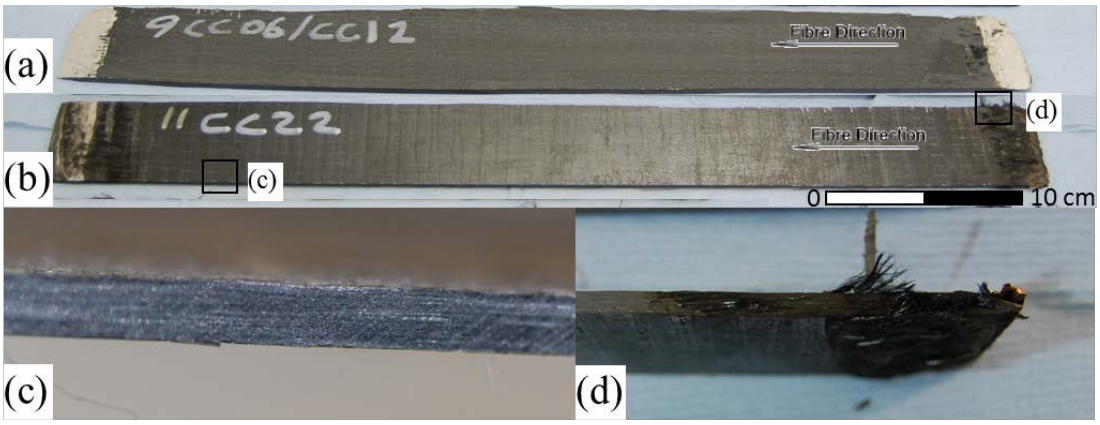

Figure 3.11: DC (a) and Impulse (b) post lightning strike damaged specimens with selected cross section images showing (c) typical non-damaged cross section observed for all DC and Impulse specimens (the image shows specimen Impulse3) and (d) damage cross-section c

The Impulse+DC specimen shown in Figure 3.12 displays extensive damage. Both the top and bottom surfaces show resin damage from the flames burning the laminate, as indicated in Figure 3.12 (a). Almost all the cross section has exposed fibres and stitching as shown in Figure 3.12 (b). The resin in between the layers has burnt away which can be seen from the outer surface of the cross section, see Figure 3.12 (c). Figure 3.12 (d) and clearly shows delaminated plies.

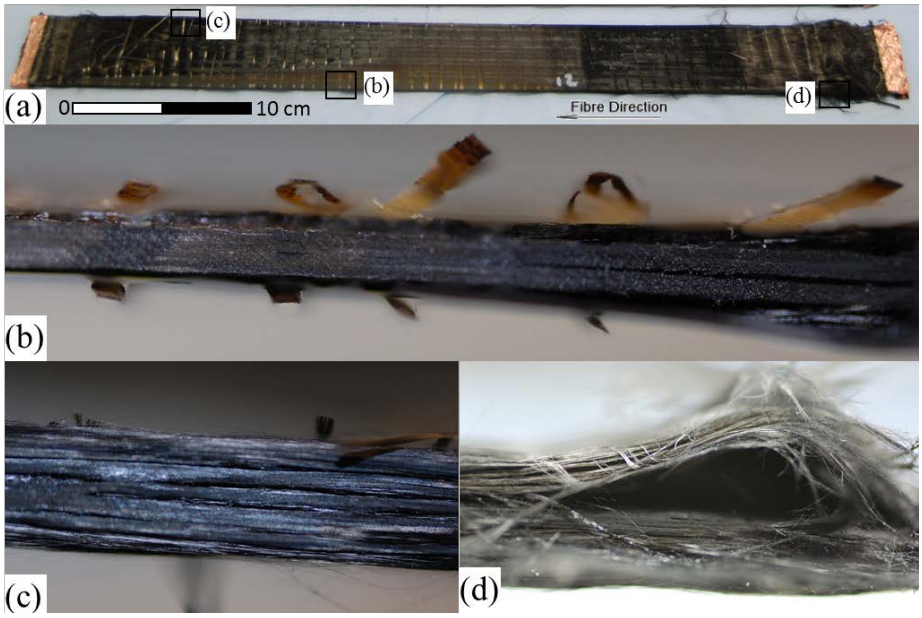

Figure 3.12: Impulse+DC: (a) post lightning strike damage specimens with selected cross section images showing typical damage cross section with (b) glass fibre stitching pulled away from the laminate, (c) typical damaged cross-section, and (d) most severely damage

3.3.3 Residual Strength

After the simulated lightning strike tests, the coupon specimens were cut out, and the compression and shear tests described above were carried out. The tests were conducted to failure of the specimen to capture the residual (or remaining) strength after specimens were exposed to the lightning strike damage. The stress was calculated on the gross cross-sectional area before damage. All specimens failed in the gauge section and displayed acceptable compression or shear failure modes as prescribed in the ASTM standards.

The mean strengths of the compression and shear test specimens that were subjected to lightning strikes were compared to the strengths obtained for pristine/undamaged specimens labelled 'control'. The strength reduction of the damaged specimens relative to the pristine/undamaged specimens are calculated by equation (3.6):

$$\%\, Reduction\ = \left(\frac{(\sigma,\tau)_{control} - (\sigma,\tau)_{sample}}{(\sigma,\tau)_{control}} - 1 \right) 100\% \qquad (3.6)$$

where $(\sigma,\tau)_{control}$ is the compression/shear failure stress of the undamaged specimen and $(\sigma,\tau)_{\text{sample}}$ is the compression/shear failure stress of the damaged specimen.

Table 3.3 shows the results obtained for the CFRP specimens loaded in compression. The negative % Reduction means that the average compressive strength was slightly larger than the control samples but is within the overall noise of the test setup. The CoV shows there is a large variability in the results of the tests. The variability increases as the lightning strike severity increases. The

level of damage induced lightning strike displays a high degree of variability and since the compression test specimens of a larger damaged strip specimen the actual volume in the gauge zone of the tested samples will display a large degree of variability. Thus, the observed high CoV for the tested samples that were exposed to the most severe lightning strike conditions display a large variability in the measured compressive strength. Table 3.4 presents the results obtained for the CFRP specimens loaded in shear. The coefficient of variation for the shear tests were less variable.

Table 3.3: Compression test results of control specimen and damaged specimens showing

Specimen	Mean Compression Strength [MPa]	Standard Deviation [MPa]	Coefficient of Variation [%]	% Reduction
Control	754.7	20.9	2.8	-
DC1	768.9	55.5	7.2	-1.9%
DC2	727.0	45.7	6.3	3.7%
DC3	702.6	33.4	4.8	6.9%
Impulse1	625.8	19.9	3.2	17.1%
Impulse2	679.0	67.3	9.9	10.0%
Impulse3	613.4	27.4	4.5	18.7%
Impulse+DC	215.6	41.5	19.2	71.4%

Table 3.4 shows the results obtained for the CFRP specimens loaded in shear.

Table 3.4: V-notch shear test results of control specimen and damaged specimens

Specimen	Mean Shear Strength [MPa]	Standard Deviation [MPa]	Coefficient of Variation [%]	% Reduction
Control	87.6	0.70	0.8	-
DC1	83.6	1.02	1.2	4.5%
DC2	79.0	0.67	0.8	9.8%
DC3	81.1	3.13	3.9	7.4%
Impulse1	85.5	2.61	3.1	2.4%
Impulse2	80.5	4.18	5.2	8.1%
Impulse3	81.0	0.19	0.2	7.5%
Impulse+DC	49.9	0.67	1.3	43.0%

From Table 3.3 and Table 3.4 it is observed that the measured residual strengths are reduced only moderately for the DC and Impulse specimens. However, the Impulse+DC case represents the most severe simulated lightning strike action on a small cross section, and much more severe strength reductions are seen, with 71.4% reduction for the compression specimens, and 43% for the shear specimens.

3.3.4 Residual Modulus

The Young's (E) and shear moduli (G) for both damaged and pristine specimens were also evaluated from the test data following the procedures outlined in ASTMD6641 [126] and ASTMD5379 [127]. The results are shown in Figure 3.13, and it is observed that only moderate changes to E and G were experienced for the DC and Impulse specimens. However, the Impulse+DC specimens showed significant reductions in both Young's (E) and shear moduli (G). The residual compressive modulus is reduced to almost a third of its pristine/undamaged value.

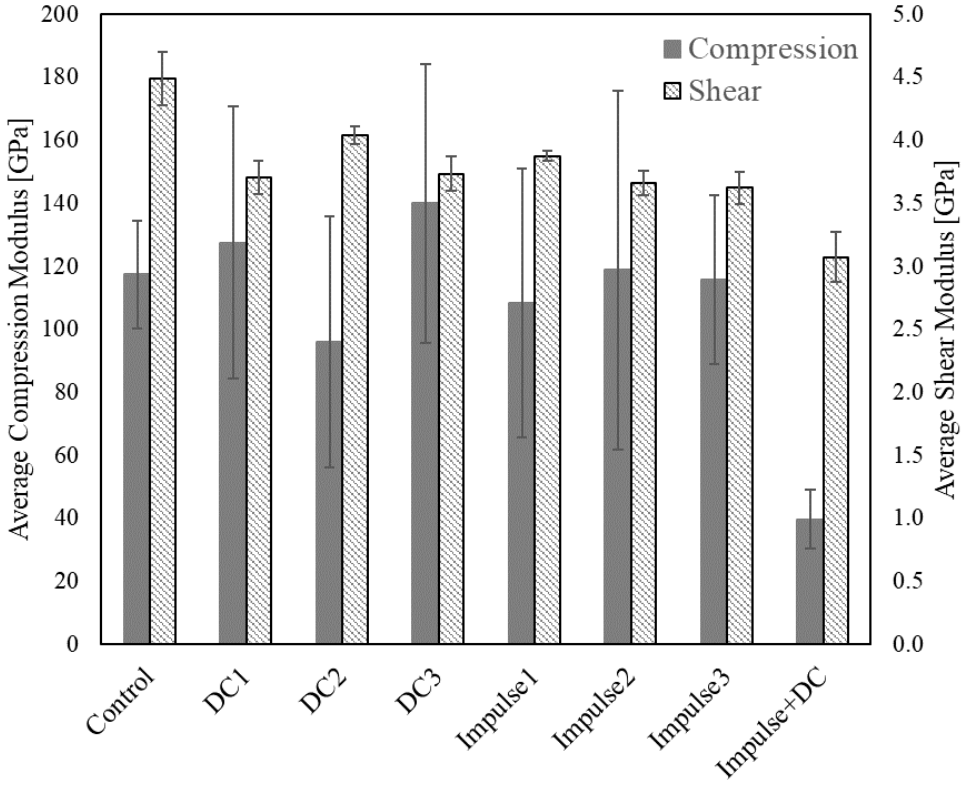

Figure 3.13: Residual compression and shear modulus based on specimen waveform

3.3.5 Stress Strain Relationship

The stress vs strain relations were also recorded for all the test specimens, and typical stress-strain curves are shown in Figure 3.14 for the compression tests, and in Figure 3.15 for the shear tests. A significant change of the stress-strain response is observed for all cases (i.e. DC, Impulse and Impulse+DC), even for the DC and Impulse specimens where the residual strengths and moduli only changed modestly as shown in Table 3.3 and Table 3.4 and Figure 3.13. In particular, it is observed that as the lightning strike energy level increases, the nonlinearity of the stress-strain response as well as the strain to failure increases. The specimens subjected to the lightning strikes with the largest specific energy and charge display the highest level of non-linear behaviour. It is especially obvious for the Impulse+DC specimen, which displays the largest reduction of the

stiffness and the earliest departure from linear behaviour. The former suggests that the failure initiation shear strength of the CFRP specimens, as defined in Eqs. (3.3) - (3.5), reduces with increasing lightning strike energy levels.

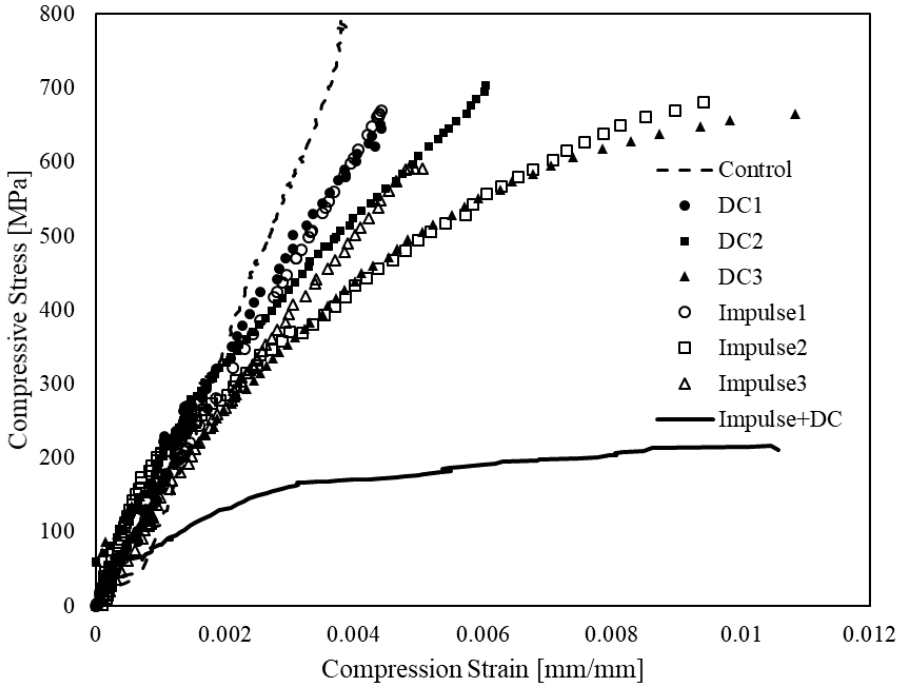

Figure 3.14: Typical stress-strain curves recorded for compression specimens

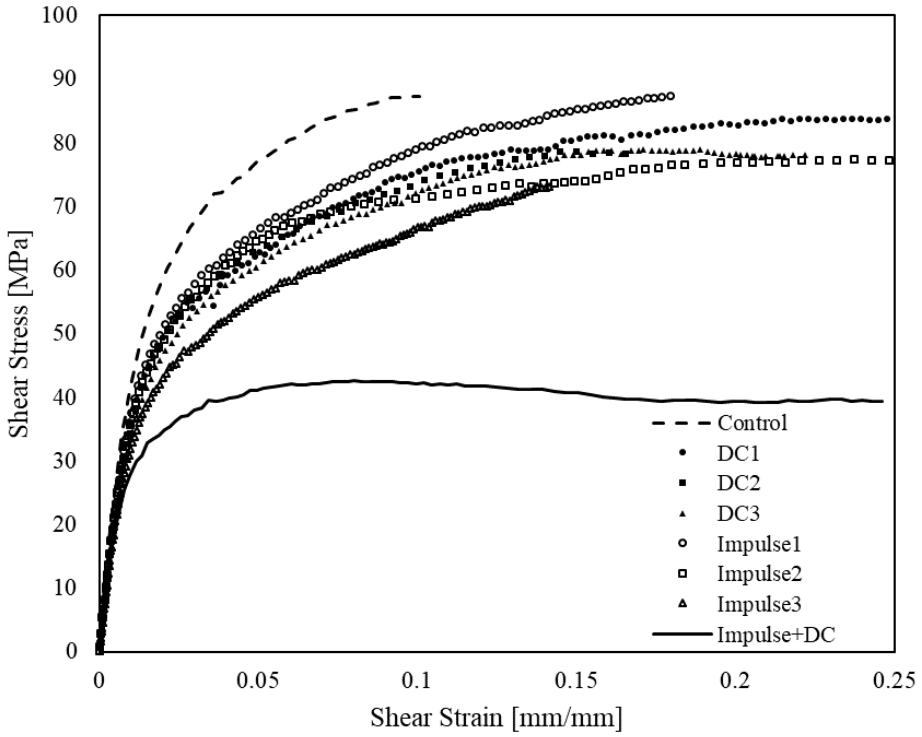

Figure 3.15: Typical stress-strain curves recorded for shear specimens

3.3.6 Failure Initiation Stress

The failure initiation stress values, as defined in section 3.2.5 and Eq. (3.3) - (3.5), for the shear test specimens are shown in Table 3.5.

Table 3.5: Failure initiation stress for damaged shear samples

Specimen	Failure Initiation Stress [MPa] (mean)	Standard Deviation [MPa]	% Reduction
Control	16.2	0.82	-
DC1	12.3	0.20	24.2%
DC2	13.8	1.03	14.6%
DC3	12.7	1.13	21.5%
Impulse1	13.7	0.40	15.4%
Impulse2	13.0	0.27	19.7%
Impulse3	10.3	0.59	36.3%
Impulse+DC	6.4	1.77	60.8%

The failure initiation strength provides a quantitative measure of the stress where nonlinear stress-strain behaviour initiates. It is observed from Table 3.5 that this reduces significantly even for DC and Impulse simulated lightning strike events that led to modest changes of (initial) stiffness (E and G) and compressive/shear strengths, and where only limited visual damage could be identified. For the worst-case scenario of the Impulse+DC simulated lightning strike event, is it also clear from Table 3.5 that significant damage has been introduced. The initiation point of nonlinear behaviour/response has been reduced by 60%, for that specimen. This reduction can be seen in Figure 3.14 and Figure 3.15, as well as in Table 3.4 which shows a significant reduction in shear strength.

3.4 Discussion

The research presented proposes a procedure with results to evaluate the damage inflicted to CFRP materials from exposure to a severe simulated lightning strike event. The series of simulated lightning strike tests conducted represent common exposure (Impulse 1-3 and DC 1-3) to overly exposed (Impulse+DC) lightning situations experienced by WT blades manufactured using CFRP composite materials. The samples tested were scaled down versions of a typical sparcap. The tests conducted aimed at exposing the CFRP samples with lightning current, providing a certain degree of damage (reduction of residual strength). The current magnitudes and hence current densities chosen may be exceeding the actual exposure for profiles being part of a real sparcap in a wind blade. To compare the results of the present tests with the exposure of actual blades in service, the current densities for the actual sparcap geometry must be carefully assessed by analysis or current distribution testing according to IEC 61400-24 Ed2. This means that the Impulse1-3 specimens

were struck with a maximum current of 60 kA; this scales to an average cross-section (500 mm x 5 mm) to have a similar current density level on the specimen as a typical WT blade sparcap exposed to a “Lightning Protection Level 1” or LPL1 from the IEC61400-24 WT lightning standard [47]. The DC1-3 specimens were made to match the Impulse1-3 action integrals (AI) to a maximum of 200 C. The combined Impulse+DC case is an extreme case which is not a realistic lightning strike scenario but shows the full damage which can be caused in a CFRP material when exposed to a large amount of electrical current.

During a lightning strike event, the CFRP material typically can experience significant heating exceeding glass transition or combustion temperatures. For CFRP materials that have been exposed to lightning strikes that cause combustion/burning, significant damage will be inflicted including loss of loss of resin, fibre breakage, and delamination. This in turn can lead to significant changes (reductions) of the mechanical response of the material, demonstrated by the findings described in the previous section of this paper. Similar results show that CFRP materials exposed to fire (i.e. exposure to elevated temperatures) can experience a significant loss of strength and stiffness with a clear correlation to their mass loss [116]. This indicates that thermal effects and degradation play a large role in determining the influence of lightning induced damage on the strength, stiffness and overall load response of CFRP materials. Although the amount of mass loss was measured for all specimens, only the Impulse+DC had a significant loss of mass to account for the significant loss in mechanical properties.

The strong correlation between sample temperature and the severity of a lightning strike event is indicated in Figure 3.16, which shows the surface temperature rise measured on the CFRP specimens using an infrared camera, and the charge and specific energy associated with the specific simulated lightning strike tests conducted. It is clear that the larger the amount of energy the higher the temperature. The Impulse+DC showed a recorded a maximum temperature at or above the maximum recordable temperature for the camera, which clearly indicates that it had received the largest amount of lightning specific energy and charge.

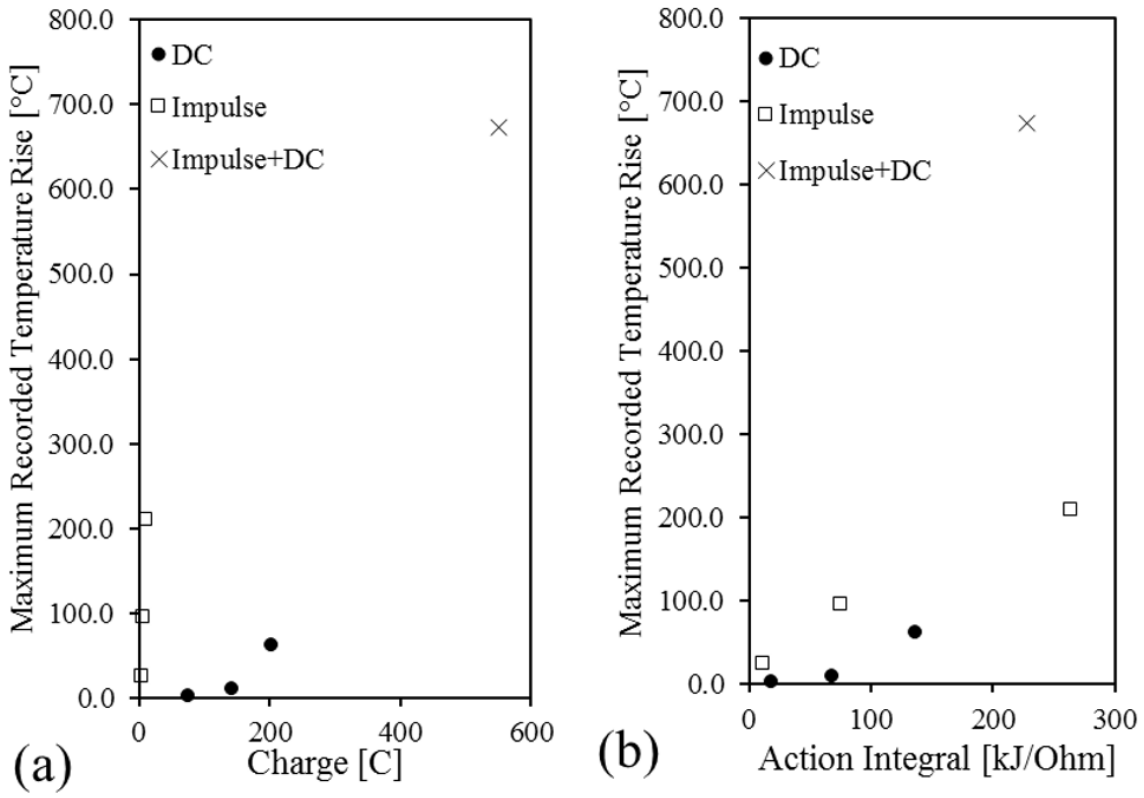

Figure 3.16: Maximum temperature rise measured on the CFRP specimen surfaces using vs (a) charge and (b) action integral (specific energy) associated with specific simulated lightning strike tests

It is observed from Figure 3.16 that the Impulse+DC tests conducted led to far higher specimen temperatures than the DC and Impulse tests, indicating much more damage being inflicted during the former. This corresponds very well with the results presented in section 3.3 where it was shown that the Impulse+DC tests inflicted very significant damage leading to large reductions of strength, stiffness, and failure initiation strength.

Although the visual inspections conducted on the DC and Impulse coupon tests did not reveal any significant damage, the mechanical tests revealed that both types of simulated lightning strikes reduced the strength for both the compression and shear load cases. This trend can be identified by evaluating the (residual) compression and shear strength measured for the CFRP specimens that did not combust (i.e. DC1-3 and Impusle1-3) against charge, see Figure 3.17, and specific energy, see Figure 3.18, of the simulated lightning strike. From Figure 3.17 and Figure 3.18 it is observed that the specific energy appears to have a stronger effect in reducing the residual strengths than the charge of the lightning strike event. It should also be noted that even though the simulated lightning strike waveforms displayed large variations with respect to the amount current and charge injected into the specimens, it is clear that the both the DC and Impulse test specimens display a clear strength reduction correlation with respect to the specific energy.

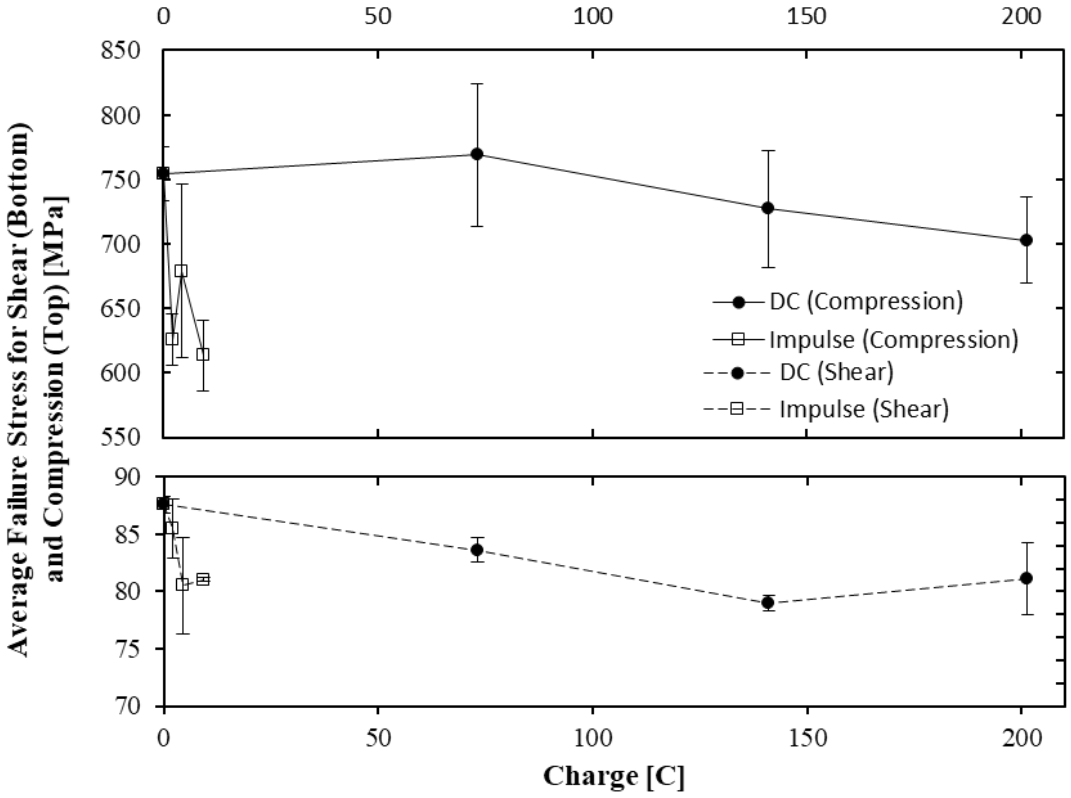

Figure 3.17: Residual Strength of damaged and undamaged CFRP specimens vs charge

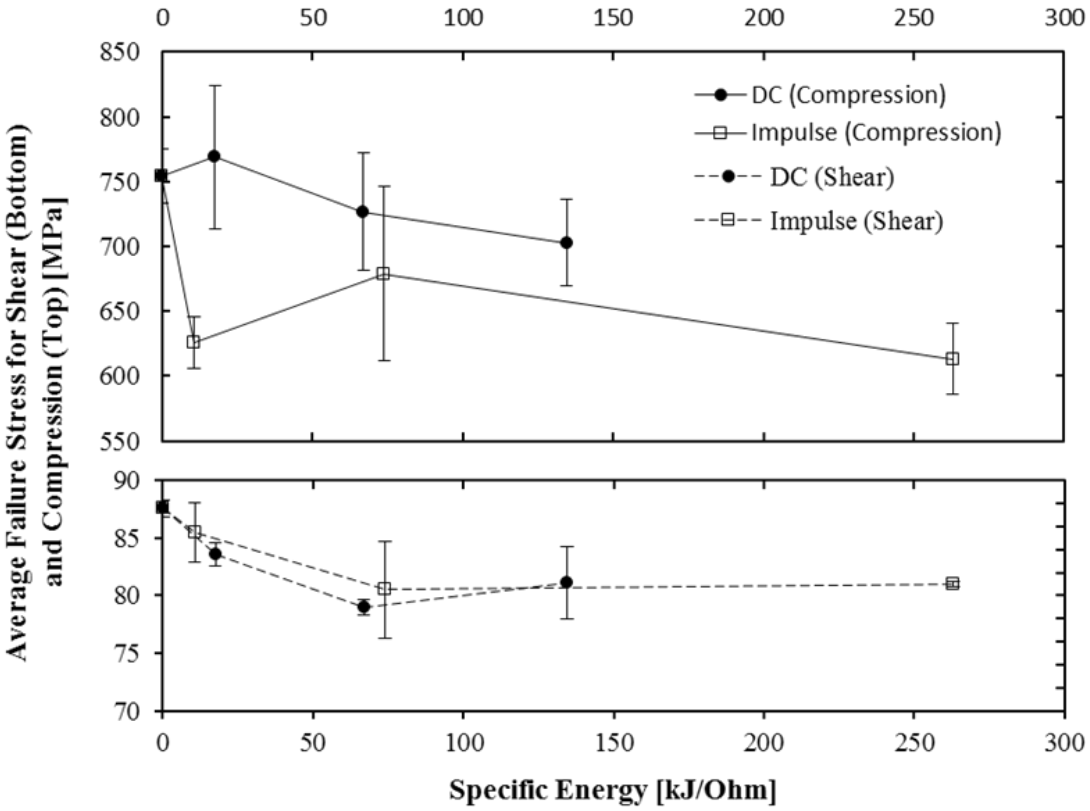

Figure 3.18: Residual Strength of damaged and undamaged CFRP specimens vs specific energy

3.5 Conclusions

The results of a comparative investigation of the damage induced by a lightning strike through conducted current in CFRP materials has been presented. The focus of this investigation has been to measure the residual mechanical properties of CFRP specimens post lightning strike, as well as the recording of the temperature evolution during simulated lightning strike events. In addition to visual inspection, the mechanical testing encompassed assessment of the residual compression strength, the shear strength and the material stiffnesses (Young's and shear moduli), measured using ASTM standard test methods, as well as estimation of the overall change of stress-strain response due to lightning strike.

Seven CFRP strips were subjected to simulated lightning strike events characterised by three different waveforms considered representative for the exposure experienced by WT blades in operation: DC, Impulse, and Impulse+DC. The recorded temperatures and the mechanical tests have shown that the most significant damage was induced to the CFRP specimens, which experienced the highest temperature and combustion/burning.

The compression tests showed that impulse current has a more severe impact on the compression strength than DC current, with a strength reduction of approximately 19% caused by a 60 kA 10/110μs waveform (10 Coulomb). In comparison, a 7% reduction of the compression strength was observed for the case of a 0.75 kA long duration (200 Coulomb) DC current. There was little difference between the effects caused by impulse and DC currents on the shear strength with 7-8% reduction for both the impulse and long duration currents.

The most severe damage was inflicted by combined impulse and DC currents (Impulse+DC), which resulted in reductions of the compression strength of more than 70% and more than 40% for the shear strength.

Chapter 4

Characterisation of Lightning Strike Induced Damage in Unidirectional CFRP Laminates

4.1 Introduction

As mentioned previously, CFRP materials are increasingly being used in Wind turbine (WT) blades as load carrying components such as sparcaps (see Figure 1.5). The semi-conductive nature of the CFRP laminates lead to an additional path to ground for the current in the structure and the anisotropic nature of the material's thermal and electrical properties leads to large amounts of resistive heating especially in the through-thickness direction where the electrical conductivity is the lowest. This causes lightning protection of the blades to be more challenging than traditional WT blades without CFRP materials. Yasuda et al [93] proposed a classification of lightning damage in WT blades with CFRP materials. This classification chart shows that the largest cause of damages seen on the blades are from lightning and this is typically due to inadequate lightning protection systems. Previous studies [33], [35], [38], [42] have presented lightning strike damage on quasi-isotropic (multi-directional) CFRP materials typically used in aircraft structures. As WT sparcaps are typically constructed with unidirectional (UD) laminates, the previous work on quasi-isotropic laminates is not as applicable. Moreover, the lightning protection standard for WT blades are defined in the International Electrotechnical Commission (IEC) 61400-24 [48], which stipulates that WT blades must be able to withstand a lightning strike of 10 MJ/Ω, i.e. 5 times larger than the aircraft lightning protection standard.

To develop an understanding of the effects of damage in CFRP laminates exposed to different lightning parameters five direct strike experiments were conducted on UD CFRP laminates which are representative of WT laminates. The tests were conducted at Global Lightning Protection Services A/S (GLPS) in Herning, Denmark (2018 Poly-Tech A/S). Their laboratory setup is capable of producing the 10MJ/Ω energy level required by the IEC 61400-24 [48] lightning protection standard. The following sections describe the lightning testing facility used for the experiments along with the types of simulated lightning strikes that can be achieved. The chapter presents the lightning strike tests conducted and the induced damage from the experiments determined through three damage techniques: visual inspection, X-ray Computed Tomography (CT) and Infrared Thermography (IRT). Temperature profiles and evolutions are produced from a

thermal camera during the testing. The damage results from the test are used to characterise the typical damage types resulting from the experiments as well as identifying the different damage modes from the thermal evolutions. The damage sizes as a result from the simulated lightning tests are compared to the lightning parameters used to determine the most representative parameter to the damage size. The results of these tests are in partial fulfilment of Research Objectives 3 and 5 as the samples are used as validation for the model in future chapters (Chapter 5 and Chapter 6).

4.2 GLPS Lightning Strike Testing Facility

The setup at GLPS includes two generators, which in tandem can produce the 10/350µs waveform (or Component A from SAE ARP5416 [70]), and the continuing current (Component C from SAE ARP5416 [70]). A schematic overlay of the system is shown in Figure 4.1 (a). The impulse generator has several large capacitors which are capable of producing impulse currents like the 10/350µs lightning waveform. When the capacitors are charged, a mechanical trigger sends the current through the electrode and into the spark gap. A spark is generated which allows current to conduct from the electrode to the sample. The DC generator contains many batteries connected in series which produce DC waveforms to mimic the continuing current waveform. An 'arc-entry' or direct strike is associated with the current being supplied orthogonal to the surface of the sample. This event corresponds to Scenarios 1 & 2 in Figure 2.9 (page 16). For CFRP materials, this is the worst-case condition for the electric current to conduct into the CFRP, because the electrical conductivity in the through thickness direction is the lowest; typically, 3 orders of magnitude lower than in the fibre direction [46]. An image of the current flow through an arc entry experiment is shown in Figure 4.1 (b). During an arc entry test, the current flows from the generator through the electrode. The red directional lines show the current flow through the system. It shows the current flows from the generator through the electrode to the sample. The sample then conducts the current to the grounded connections.

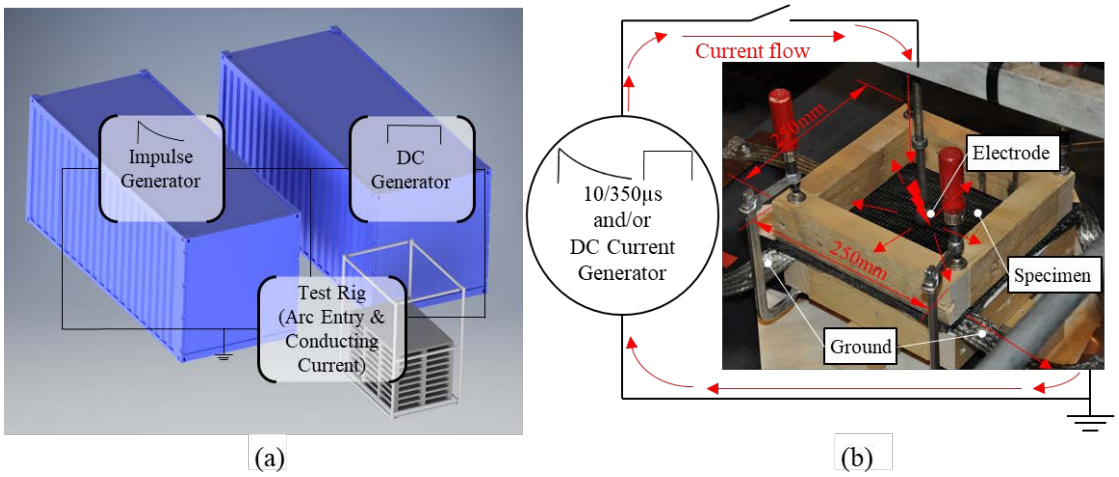

Figure 4.1: (a) GLPS testing equipment and (b) a simplified pictorial schematic of current flow through an arc entry

4.3 Simulated Lightning Strike Experiments

The lightning tests were carried out to determine the influence of different electric current parameters, using three different waveforms: impulse, DC, and oscillating. An impulse waveform is typically defined by three characteristic parameters; the peak current value (I_{peak}), the rise time to reach the peak current (t_1), and the time at which the current decays to half of the peak current (t_2), also known as the half time. When an impulse waveform is hard to achieve in the laboratory, an oscillating waveform is used, which is defined with similar parameters to the impulse but differs by repeated transitions from positive to negative currents similar to a decaying sine wave. The DC current is defined by the peak current (I_{peak}), and the duration the current is applied for (t_{DC}). These parameters are shown in Figure 3.3 (page 46) for the impulse and DC waveforms, and in Figure 4.2 for the oscillating waveforms. The charge, Q, and the specific energy or action integral, AI, are used to compare different waveforms and are calculated as follows:

$$Q = \int_0^{t_f} i(t)\, dt \tag{4.1}$$

and

$$AI = \int_0^{t_f} i^2(t)\, dt \tag{4.2}$$

where t_f is the final current time, and $i(t)$ is the current level at any time t.

The absolute value of charge, $|Q|$, is proposed in the current work to make comparative assessments between oscillating and impulse waveforms defined as:

$$|Q| = \int_0^{t_f} |i(t)|\, dt \tag{4.3}$$

For the DC and impulse waveforms, Q and $|Q|$ are the same but for the oscillating waveform the Q is zero and $|Q|$ is not. Therefore, the DC and impulse waveforms are evaluated by charge, Q, and oscillating waveforms are evaluated by absolute value of charge, $|Q|$.

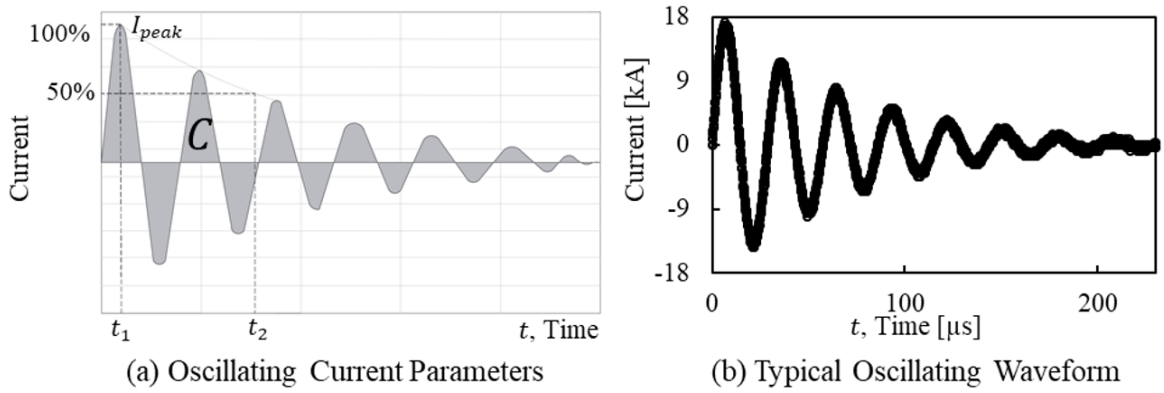

Figure 4.2: Lightning strike waveform characteristics with parameters for (a-b) an oscillating waveform

4.3.1 AE1: Influence of repeated lightning strikes

The AE1 test was conducted to determine the influence of repeated lightning strikes. The fabric was woven which was different from the remaining tests, and therefore the experiment details and results are presented in Appendix A. Although, not compared against the other results, this set of test provided important data about delamination.

4.3.2 AE2: Variation of inductance

Four CFRP laminate specimens were manufactured using a carbon/vinyl ester material system with PX-35 fibres from Zoltek Technologies, referred to as 'Zoltek' throughout the remainder of the thesis. A 1.6 m pultruded plate was manufactures and cut into specimens with dimensions 400 mm long x 200 mm wide x 5 mm thick. The specimens were chamfered at one end with an approximate 1:4 taper to expose the carbon fibres and provide a connection point.

Figure 4.3 (a) shows the setup for the AE2 simulated lightning strike experiments, the specimen is clamped to the ground at the chamfered end with the electrode spaced vertically approximately 20 mm in a location roughly above the centre of the CFRP specimen. The AE2 test was conducted to determine the effects of similar specific energies into the CFRP laminate samples but with slightly reduced peak currents. This was done by adding inductance to the system through the use of a coil; shown in Figure 4.3 (b). The coil had holes at multiple locations which allowed for changing the number of windings used during the test. Increasing the number of windings increased the inductance which changes the waveform. All the waveforms applied to the specimens for test AE2 are shown in Figure 4.4. The changes from the coil can be seen in the waveforms. AE2-1 had no inductance included in the system and has the highest peak current and shortest half time. The inductance was increased for the remaining samples and the resulting waveforms (AE2-2 to AE2-4) show a reducing of the peak current and a spreading of the half time which increases the phase of the oscillations.

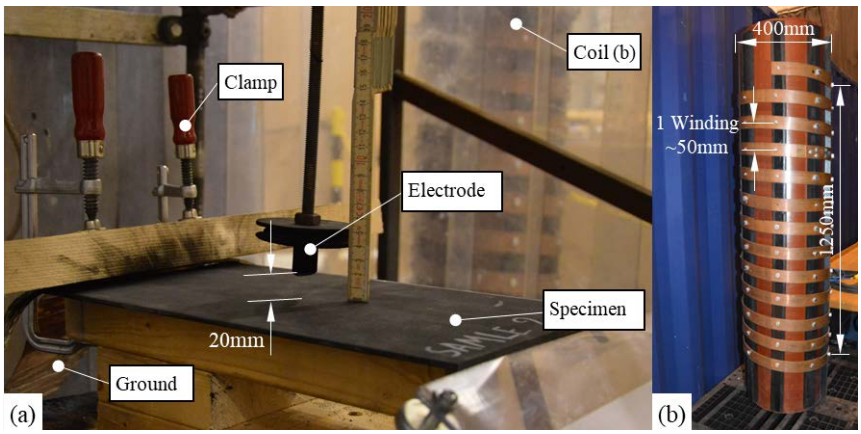

Figure 4.3: Simulated lightning strike test setup for both (a) the AE2 test and the AE3 test and (b) showing the coil used in AE2 with dimensions

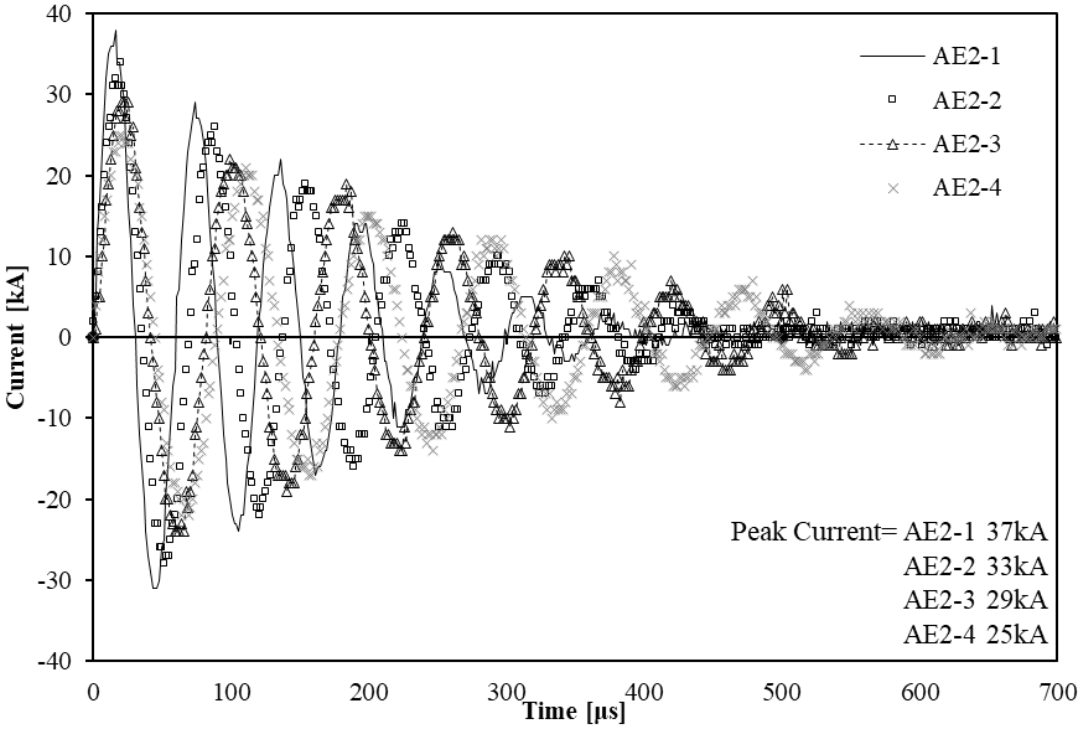

Figure 4.4: AE2 current waveforms

Table 4.1 provides an overview of the characteristic parameters used in the AE2 lightning strike tests. The resulting absolute value of charge, peak current, specific energy, and inductances are provided to define the waveforms.

Table 4.1: Test parameters defined for the simulated lightning strike test AE2: peak current, the waveform characteristics, charge, and specific energy applied to the specimens and the amount of inductance used for the different test setups

Specimen ID	Peak Current [kA]	Waveform Characteristics (Impulse $t_1/t_2/t_f$) [µs]	$\|Q\|$ [C]	AI [kJ/Ω]	Inductance [µH]
AE2-1	37	14/197.6/408	3.92	73	0
AE2-2	33	20/188.4/480	4.07	67	3.32
AE2-3	29	20/265.2/619	4.43	63	13.27
AE2-4	25	23/301.2/700	4.50	56	29.87

4.3.3 AE3: Variation of charge

Four specimens were manufactured using a pultruded carbon/vinyl ester material system with PX-35 fibres from Zoltek. The test specimens were cut from the pultruded plates with final dimensions of 400 mm long x 200 mm wide x 5 mm thick. The specimens were chamfered at one end with an approximate 1:4 taper to expose the carbon fibres and provide a connection point.

The AE3 specimens were setup in the same configuration as the AE2 specimens, see Figure 4.3 (a). The AE3 test was conducted to investigate if lightning strikes of different charge inflict different levels of damage. The DC currents applied to the specimens were in accordance with the IEC standards and the only variation was the amount of time the DC waveform was applied, t_{DC}. All

the waveforms applied to the specimens for test AE3 are shown in Figure 4.5. The change in the t_{DC} is seen by the amount of time the waveform is at/near the peak current. Since the amount of charge applied to the sample is an integration of the current with respect to time, the smallest charge for the AE3 specimens is AE3-1 and the largest is AE3-4.

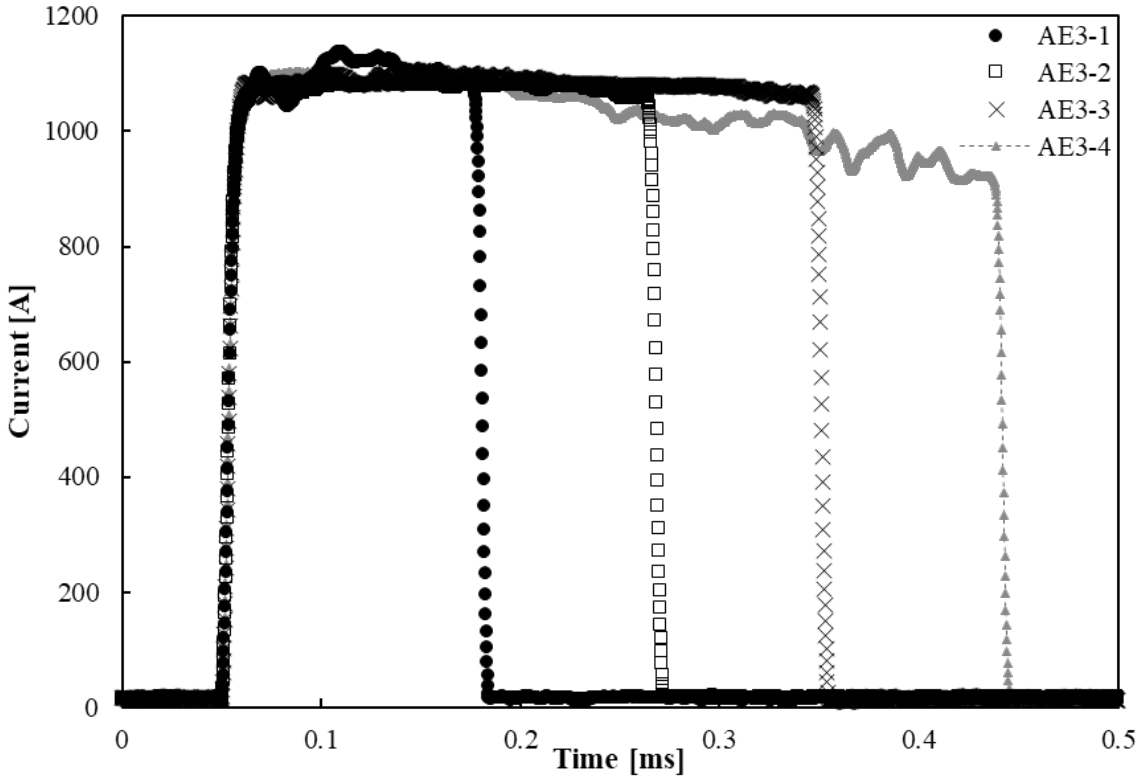

Figure 4.5: AE3 current waveforms

Table 4.2 provides an overview of the characteristic parameters used in the AE3 lightning strike tests. The resulting total charge, peak current, specific energy, and waveform characteristics are provided to define the waveform.

Table 4.2: Test parameters defined for the simulated lightning strike test AE3: peak current, the waveform characteristics, charge, and specific energy applied to the specimens

Specimen ID	Peak Current [A]	Waveform Characteristics t_{DC} [ms]	Q [C]	AI [kJ/Ω]
AE3-1	1138	127	145	150
AE3-2	1091	215	235	246
AE3-3	1108	293	325	346
AE3-4	1103	364	402	412

4.3.4 AE4: Full 10/350µs + DC waveform

The panels for the AE4 test specimens were manufactured using vacuum resin infusion with a similar material system used in WT sparcaps by industry. The selected system contained Zoltek PX-35 dry fabric plies and Baxxodur 5300 epoxy system. A total of 13 specimens were

manufactured with dimensions of 250 mm long and 250 mm wide. Seven UD laminates were made with 5 plies resulting in a total laminate thickness of 4.35 mm, and six UD laminates were made with 10 plies resulting in a total laminate thickness of 8.70 mm. All the plates were post cured at 70°C for 6 hours. The individual specimens were chamfered along the four edges of the plate with an approximate 1:4 taper to expose the carbon fibres and provide a connection point.

Figure 4.6 shows the setup for the AE4 simulated lightning strike experiments, which comprises the specimen clamped to the ground at their chamfered ends. The electrode was equipped with a jet diverter and was spaced vertically approximately 20 mm in a location roughly above the centre of the CFRP specimen. The waveform used was a combination of both an impulse and a DC waveform. The impulse was applied first, followed immediately by the DC current, thus making it a combined impulse and DC waveform. The desired impulse waveform was the 10/350μs to simulate the first return stroke during a direct strike according to IEC 61400-24 Ed1.0 [48], and the desired charge was met with the remaining DC portion.

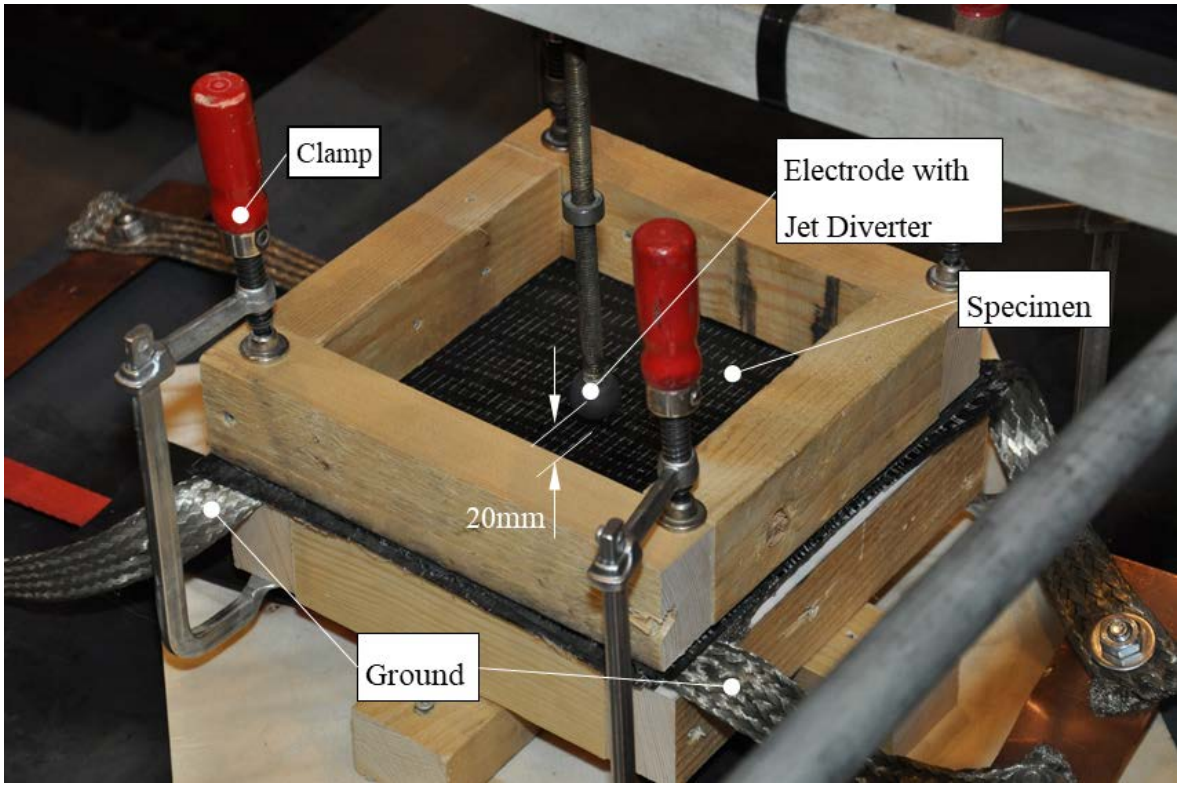

Figure 4.6: Simulated lightning strike test setup for the AE4 test

Table 4.3 provides the results from the lightning strike test where the charge (Q) and specific energy (AI) are split into their component forms and are shown as XX(YY) where XX is the impulse portion and YY is the DC portion.

Table 4.3: Test parameters defined for the simulated lightning strike test AE4: peak current, the waveform characteristics, charge, and specific energy applied to the specimens

Specimen ID	Num. of Plies	Peak Current [kA]	Waveform Characteristics (Impulse $t_1/t_2/t_f$) [μs] (DC t_{DC}) [ms]	Q [C] Impulse(DC)	AI [kJ/Ω] Impulse(DC)
AE4-01	5-ply	29.6(1.0)	21/277/726 (48)	8.93(46.4)	154.8(28.2)
AE4-02	5-ply	29.2(1.0)	20/268/689 (47)	8.36(46.7)	142.6(29.2)
AE4-03	5-ply	27.0(0.6)	22/206/593 (172)	5.64(103)	88.49(47.7)
AE4-04	5-ply	64.4(0.6)	25/202/1023 (110)	18.8(69.9)	525.1(32.0)
AE4-05	5-ply	65.2(0.9)	23/338/1205 (109)	26.4(70.1)	880.9(33.5)
AE4-06	5-ply	97.0(0.9)	17/145/1122 (116)	26.5(98.9)	1075(69.2)
AE4-07	5-ply	96.0(0.5)	25/132/840 (192)	20.6(105)	870.3(37.2)
AE4-08	10-ply	28.5(0.8)	18/208/604 (55)	7.50(44.8)	123.5(23.7)
AE4-09	10-ply	33.6(0)	18/229/650 (-)	7.91(0.00)	136.6(0.00)
AE4-10	10-ply	60.8(0.9)	24/318/977 (79)	21.8(69.5)	730.8(43.5)
AE4-11	10-ply	62.4(0.9)	26/354/1089 (79)	24.8(70.6)	872.3(47.9)
AE4-12	10-ply	99.0(0.4)	19/144/907 (48)	22.0(19.9)	912.1(1.90)
AE4-13	10-ply	98.0(0.4)	21/194/951 (213)	25.9(95.7)	1135(27.0)

From Table 4.3, it is observed that the charge primarily comes from the DC portion and the specific energy primarily comes from the impulse portion. For comparison sake, Table 4.4 shows the sum of charge from the DC and impulse in a new quantity called Q_T, and the sum of the specific energy from the DC and impulse in a new quantity called AI_T, where the subscript "T" stands for total. Since DC and impulse currents were applied together, each portion can be shown as a percentage of the total. Two additional parameters are introduced in Table 4.4: Q_{DC}/Q_T, the charge from the DC portion (Q_{DC}) divided by the total charge, and AI_{Imp}/AI_T, the specific energy from the impulse portion (AI_{Imp}) divided by the total specific energy. These parameters show that the majority of the charge is from the DC portion of the waveform (on average >80%) except for AE4-09 where the DC generator did not trigger, and the specific energy is primarily from the impulse portion of the waveform (on average >90%).

Table 4.4: Sum of charge and specific energy for the AE4 tests

Specimen ID	Q_{DC}/Q_T [%]	Q_T [C]	AI_{Imp}/AI_T [%]	AI_T [MJ/Ω]
AE4-01	84%	55.28	85%	0.18
AE4-02	85%	55.01	83%	0.17
AE4-03	95%	108.32	65%	0.14
AE4-04	79%	88.69	94%	0.56
AE4-05	73%	96.45	96%	0.91
AE4-06	79%	125.43	94%	1.15
AE4-07	84%	125.6	96%	0.91
AE4-08	86%	52.3	84%	0.14
AE4-09	0%	7.91	100%	0.14
AE4-10	76%	91.27	94%	0.77
AE4-11	74%	95.4	95%	0.92
AE4-12	47%	41.94	99.8%	0.91
AE4-13	79%	121.56	98%	1.17

4.3.5 AE5: Sparcap sub-structure simulated lightning strike with 10/350μs waveform

The AE5 tests use a scaled representative sparcap component. The 10/350μs waveform is used because it is the design idealized lightning scenario that a WT blade needs to withstand and be tested/certified against in the IEC 61400-24 [48]. The panel was 8-ply UD laminate of 800 gsm carbon fibre fabric (Panex-35 by Zoltek) and manufactured using vacuum liquid resin infusion with an epoxy system of Epilox ER5300 resin/EC5310 hardener. The thickness was such as to represent a section of the sparcap 15m from the blade tip and they were 500 mm wide, which is a typical width in the same region. All the plates were post cured at 70°C for 6 hours.

A total of 20 specimens were made for the AE5 tests with the same basic 8-ply UD panel. To investigate the effect of surface layers on the specimens, three different surfaces were used: ten specimens had no surface layer and were labelled as “Bare”; five specimens had two plies of Gurit 250 gsm E-glass as the top layers in the ply stack and were labelled “Fibreglass”; and a further five specimens had copper mesh on the top of the ply stack and were labelled “Copper Mesh”.

The final test plates had dimensions of 550 mm long and 500 mm wide with thicknesses of 7 mm for the bare specimens, 8.5 mm for the fibreglass surface specimens and 8 mm for the copper mesh surface specimens. One edge was chamfered to an approximate 4:1 taper to expose the fibres for electrical grounding as shown in Figure 4.7. Six of the specimens were set aside to be used as control (undamaged) specimens in the mechanical testing described in Chapter 6: 2 x bare surface, 2 x fibreglass surface, and 2 x copper mesh surface, with the 14 remaining specimens that were subjected to direct lightning strike tests.

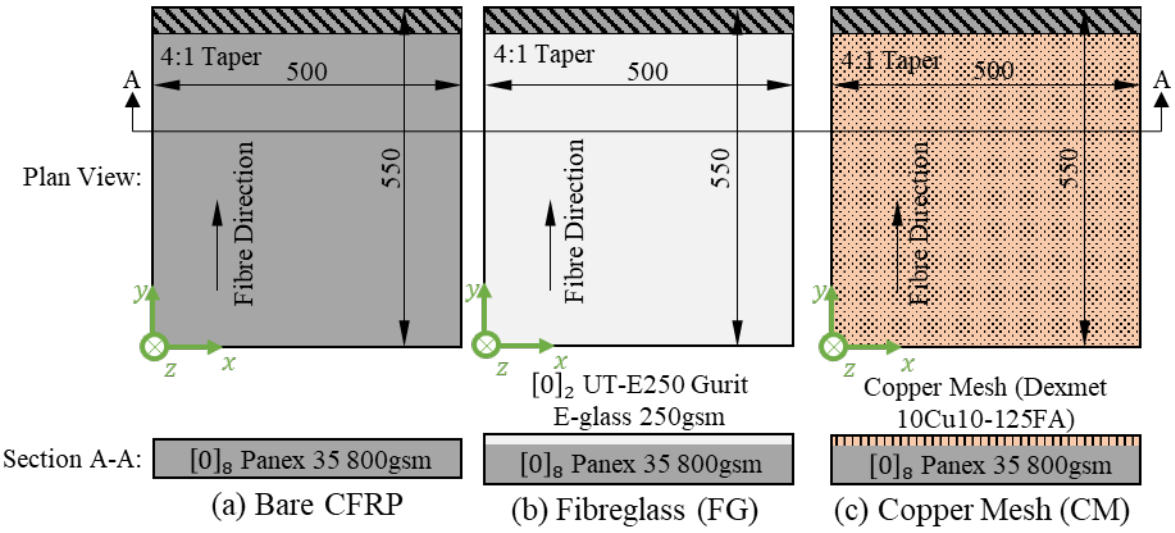

Figure 4.7: Specimens for AE5: (a) bare CFRP, (b) fibreglass, and (c) copper mesh

Figure 4.8 shows the setup for the AE5 simulated lightning strike experiments, which comprises of the specimen clamped to the ground at their chamfered end. The electrode was equipped with a jet diverter and was spaced vertically approximately 20 mm in a location roughly above the centre of the CFRP specimen. The CFRP panel specimens were subjected to electrical current with a unipolar 10/350µs waveform simulating the first return stroke during a direct strike according to IEC 61400-24 Ed1.0 [48]. The peak currents applied to the samples were 50, 75, 100, and 125 kA.

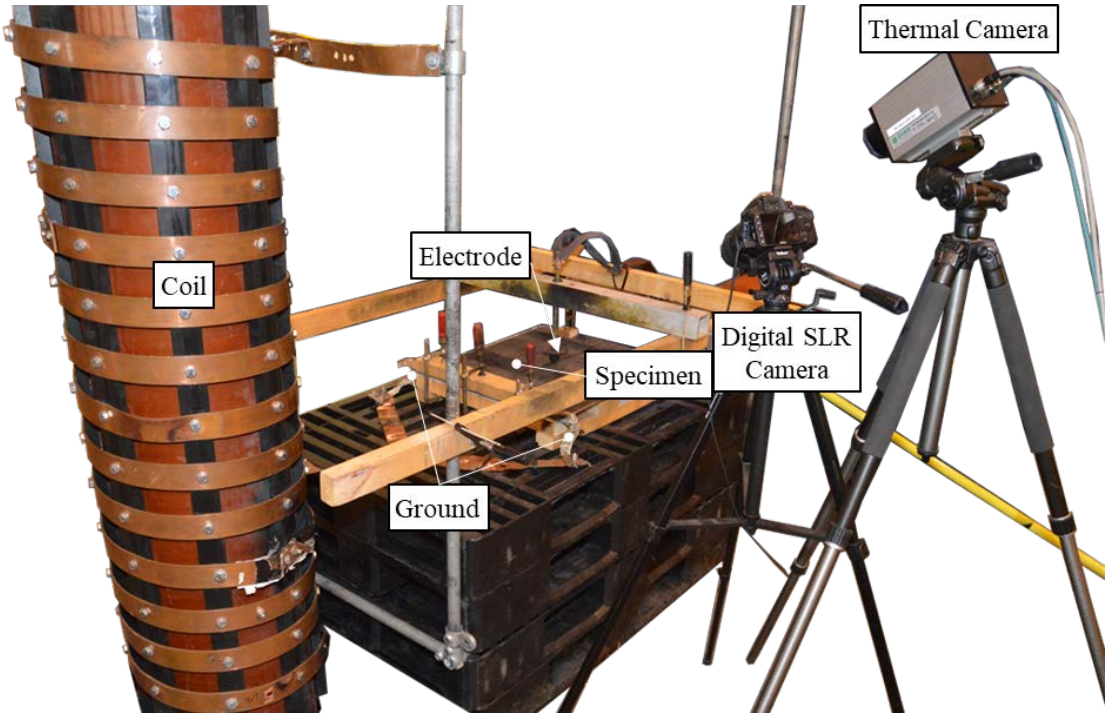

Figure 4.8: Experimental setup for AE5 simulated lightning strike tests

Table 4.5 provides an overview of the characteristic parameters used in the AE5 lightning strike tests. The samples are labelled as AE5-XX-YZZ where “XX” indicates the approximate peak current, “Y” indicated the specimen number, and “ZZ” indicates the surface type. The resulting

total charge, the waveform characteristics, peak current, and specific energy are shown in Table 4.5.

Table 4.5: Test parameters defined for the simulated lightning strike test AE5: peak current, the waveform characteristics, charge, and specific energy applied to the specimens

Specimen ID	Surface Type	Peak Current [kA]	Waveform Characteristics (Impulse $t_1/t_2/t_f$) [μs]	Q [C]	AI [MJ/Ω]
AE5-50-1	Bare	56.4	10/109/441	23.6	0.60
AE5-50-2	Bare	54.7	10/88/338	16.8	0.47
AE5-75-1	Bare	79.7	11/124/526	33.3	1.40
AE5-75-2	Bare	79.4	13/132/530	34.3	1.47
AE5-100-1	Bare	102.6	12/144/593	55.0	3.06
AE5-100-2	Bare	102.9	11/130/571	50.1	2.73
AE5-125-1	Bare	125.1	13/57.6/502	39.9	2.01
AE5-125-2	Bare	124	12/20.4/502	32.0	1.36
AE5-50-1FG	Fibreglass	53.9	12/77.2/384	16.2	0.40
AE5-75-1FG	Fibreglass	76.4	15/134/603	35.7	1.46
AE5-100-1FG	Fibreglass	100.3	12/123/602	45.4	2.20
AE5-50-1CM	Copper Mesh	50	10/80.8/387	21.1	0.55
AE5-75-1CM	Copper Mesh	80	10/136/502	35.3	1.49
AE5-100-1CM	Copper Mesh	102	10/66/487	34.4	1.43

4.4 Thermal evolution during lightning strike simulation

During the simulated lightning strike experiments, an infrared camera was used to capture the temperature evolution during and after the tests. A PYROVIEW 640L infrared camera comprising of an uncooled micro-bolometer array with 640 × 480 pixels was used to capture the temperature evolutions on the surface of the CFRP specimens/panels during the lightning strike tests AE1-AE5. A frame rate of 50Hz was used to capture the images, which is not sufficient to capture the temperatures during the lightning strike waveform but is sufficient to provide an indication of the specimen heating and cooling after the lightning strike.

An example of an image of the panel captured by the thermal camera is shown in Figure 4.9. The outer perimeter of the top surface of the panel is shown by the dashed line. It is clear that a large temperature evolution occurs at the attachment point. Three data sets were recorded from the thermal video: the maximum temperature recorded, a temperature profile along the fibre direction through the centre of the simulated lightning attachment point, T_L, and a temperature profile along the transverse direction through the centre of the simulated lightning attachment point, T_T. Although the temperature shown in Figure 4.8 is at a maximum of 100°C, lightning strikes can cause much higher temperatures. The maximum temperature recording limit for this camera is 692°C which is also referred to as the saturation temperature.

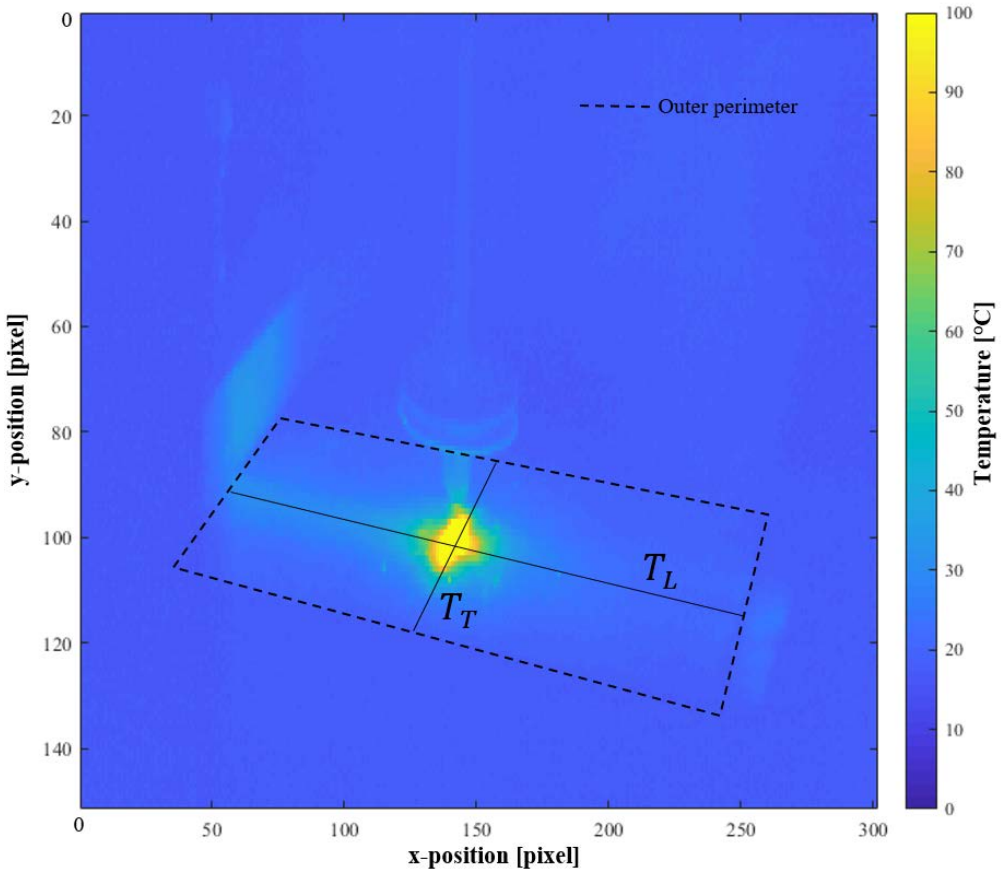

Figure 4.9: Example thermal image from lightning strike test 0.5 seconds after a simulated direct lightning strike

Figure 4.10 presents a typical maximum temperature evolution in test specimen AE2-1. The plot is a maximum temperature recorded on the full array of data from each image. The temperature rapidly increases from the ambient when the simulated lightning strike attaches. After the lightning strike is extinguished, the thermal decay is evident with temperatures returning to near ambient to around 100°C within a second. However, sometimes a small fire is ignited due to the lightning strike, which lasts about 2 seconds, when this happens, the maximum temperature remained at the saturation temperature until the flame is extinguished. The saturation temperature for this camera is shown as a dotted line in Figure 4.10 to show why the recording did not surpass this limit.

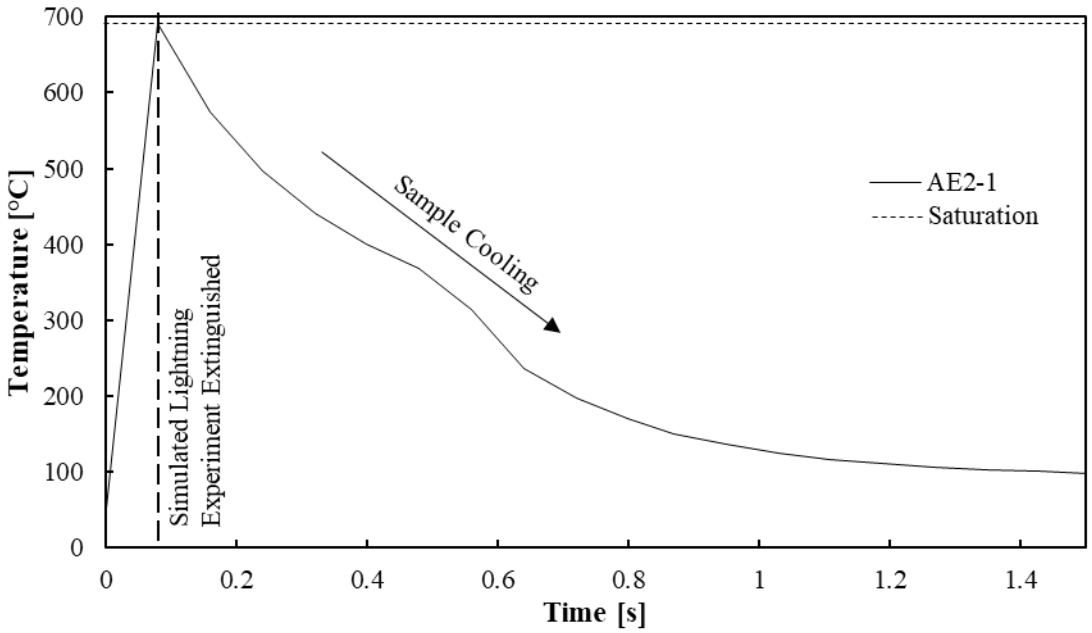

Figure 4.10: Example of the maximum temperature recorded from test specimen AE2-1's lightning strike test

Figure 4.11 shows a typical temperature profile along T_L and Figure 4.12 shows a typical temperature profile along T_T taken at three different times following a lightning strike: 0.16 s, 0.4 s, and 1.11 s. The data is centred at the lightning strike attachment point and the distances are measured from the centre. Comparing these two plots allows for the determination of whether the fibre or transverse directions are receiving more heat. Further discussion of this comes in the general discussion section of this chapter.

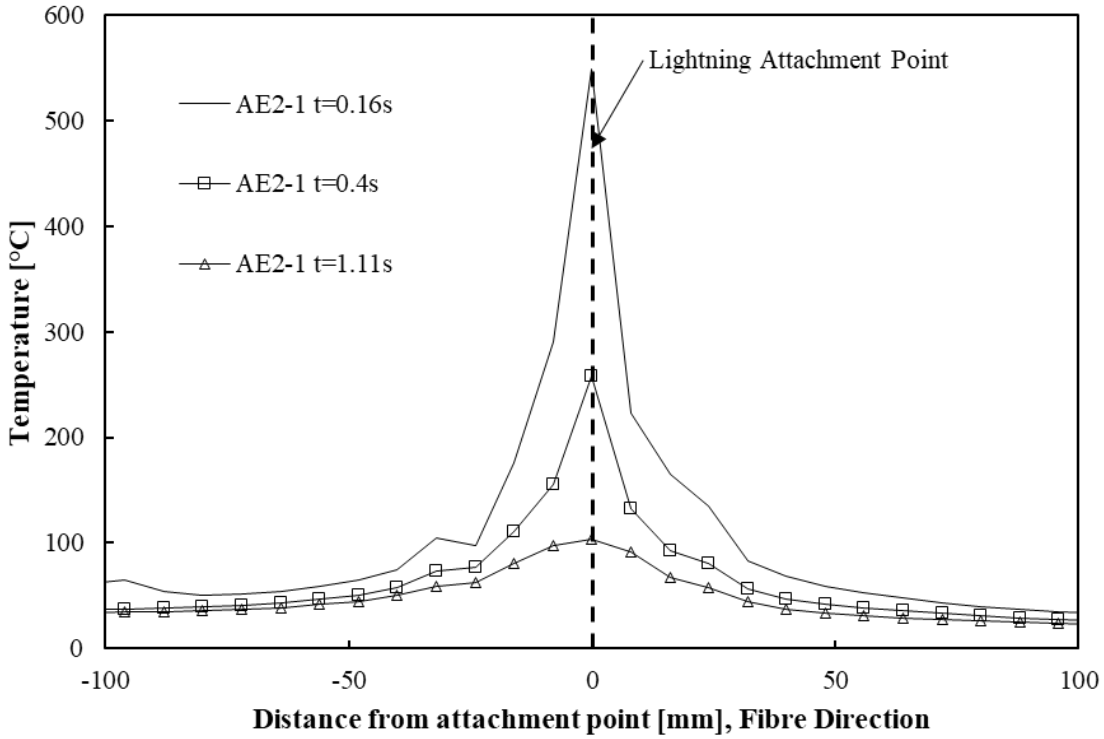

Figure 4.11: Example longitudinal direction temperature profile for specimen AE2-1 at 0.16 s, 0.4 s, and 1.11 s

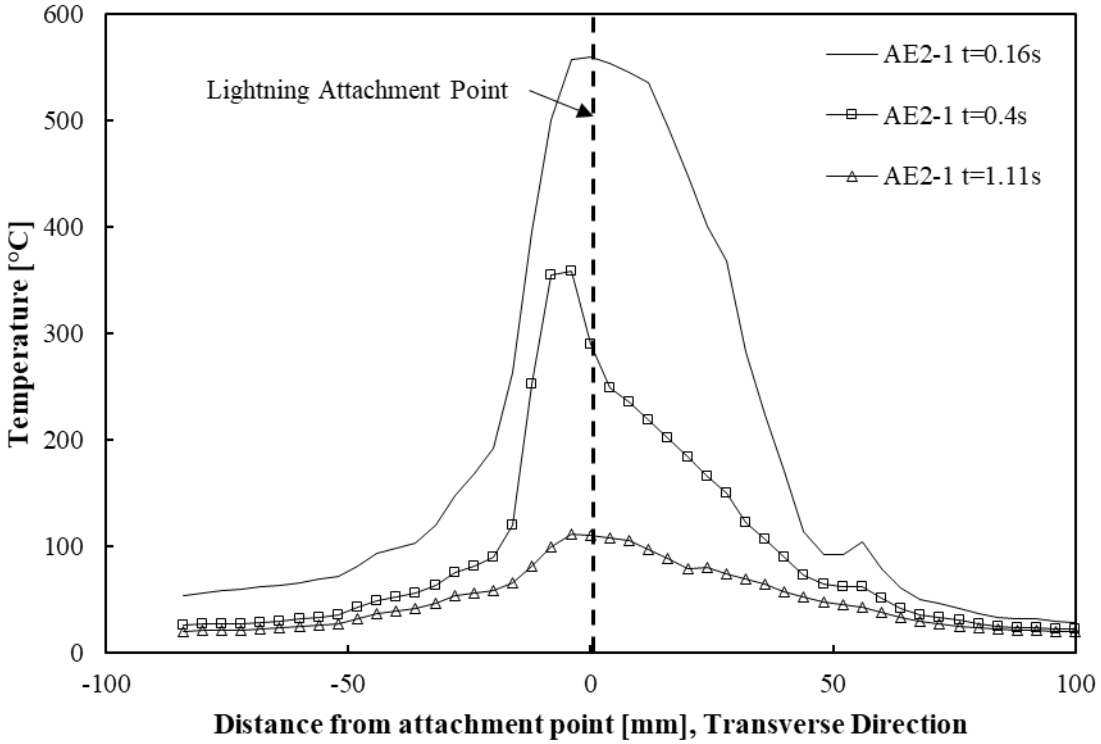

Figure 4.12: Example transverse direction temperature profile for specimen AE2-1 at 0.16 s, 0.4 s, and 1.11 s

4.5 Damage inspection methods after lightning strike

Three different inspection methods were used to investigate the extent of the damaged zones in the CFRP panels: visual inspection, Infrared Thermography (IRT), and X-ray Computed Tomography (CT). The results for the visual inspection matched closely with the thermography. However, the results from thermography provided more detailed and repeatable data, and therefore the visual inspection method and results are presented in Appendix A.

4.5.1 Infrared Thermography (IRT)

Infrared Thermography is a non-contact method in which a thermal camera is used to detect damage in a specimen by measuring the change in surface temperature. To detect damage, it is usual to use a heat source such as a camera flash or heat lamp to provide a heat input; this is called active thermography. The thermal camera captures images prior to the heat input, and readings are captured throughout the heating and cooling process of the specimen. Defects will arrest the heat conduction as they generally have a different thermal conductivity to the undamaged material, as shown in Figure 4.13 (a), and the heat on the surface of the sample does not diffuse as quickly as that of the surroundings. This difference allows for sub-surface defects to be identified. For more detailed information about thermography see Maldague [135] and Ibarra-Castanedo [136].

The arrangement used for thermography inspection in the present work is shown in Figure 4.13 (b). The arrangement has 4 components: (1) IR camera, (2) flash/heat source, (3) test specimen/sample, and (4) computer. The heat source was a Bowen studio flash and the thermal camera used was a Cedip silver 480m. The specification of the equipment used are presented in Table 4.6 along with the recording frame rates and durations. The position of the flash for this procedure is at the front of the sample adopting a technique known as 'reflection thermography'.

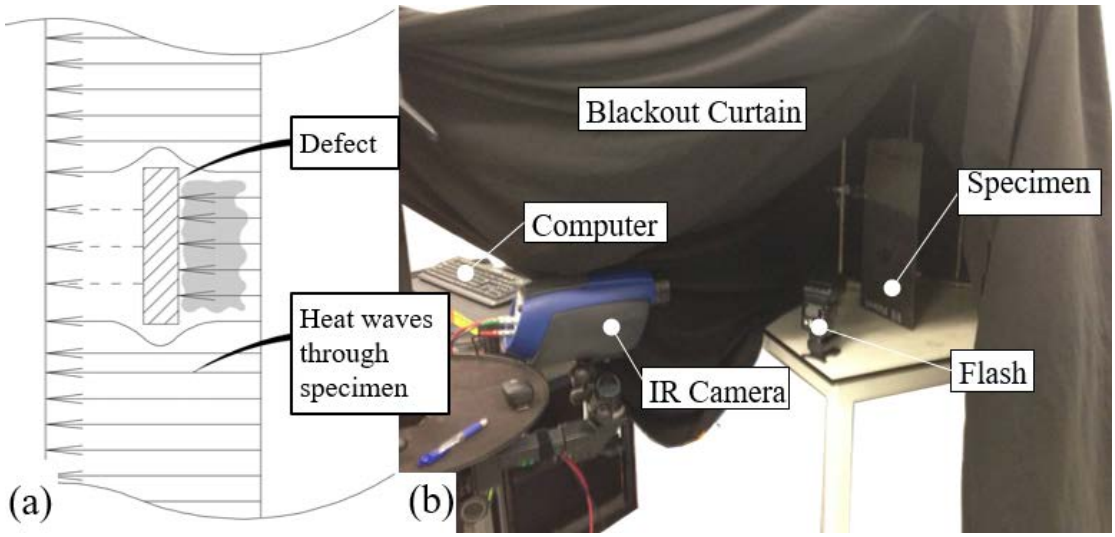

Figure 4.13: (a) Thermography setup and (b) Temperature profile through sample with defect

Table 4.6: Thermography equipment specification

Equipment	Description	Specification
Photo Detector	Model	Cedip silver 480m
	Thermal sensitivity	20 mK
	Sensor	InSb 320x256 px cooled FPA
	Spectral range	3.6-5.6μm
	Recording frame rate	383 Hz
	Recording duration	3000 frames (7.8 s)
Photographic Flash	Model	Bowens 1000 Pro
	Power	1000Ws
	Flash Duration at Full Power	1/2100s

To better analyse the thermographic images, a new post processing method is devised to provide a quantitative value (or metric) to identify the severity level of damage induced by the lightning strike. As mentioned above, in thermography, damage can be identified by monitoring the heat diffusion through the specimen. The method proposed exploits this feature by taking the integral of the temperature recorded by each pixel in the thermal image series with respect to time. The integral is then subtracted from an integral obtained from the temperature image series associated with a reference pixel located in a region where there is no damage (or rather where it is assumed

that there is no damage). The “integration method” is carried out in three steps as shown in Figure 4.14:

1. An image series is captured by the IR camera which is long enough to fully capture the thermal decay. The temperature data from each pixel in the image series is assembled into a 3D matrix as shown in Figure 4.14 (a),
2. Remove any bias such as the reflection of the cooled IR detector by subtracting the first image from the rest of the data set as shown in Figure 4.14 (b), and
3. Numerically integrate the temperature data with respect to time using the trapezoidal rule, implemented in Matlab [137], as shown in Figure 4.14 (c).

The integration is executed from the time of the heat input until the specimen returns to ambient temperature. As shown in Figure 4.14 (c), the integral for the reference pixel is subtracted from all the other pixel integrals. The result also shown in Figure 4.14 (c), is a spatial array that includes the temporal information from the image series that provides a clear indication of the extent of the damage. The Matlab script for this procedure is included in Appendix B.

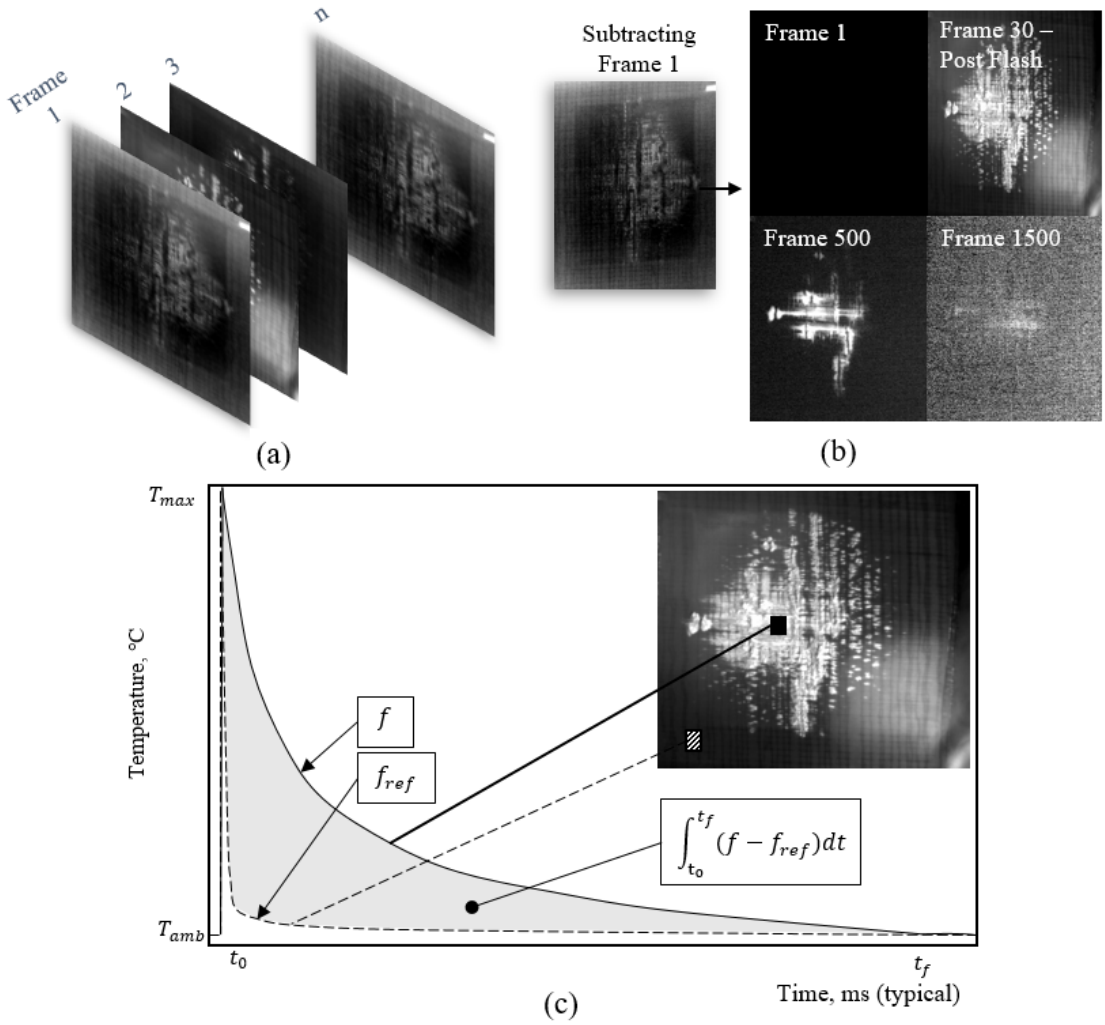

Figure 4.14: (a) Organization of thermal images stacked as 3D matrix for analysis in Matlab, (b) thermal images of lightning strike damaged specimen at different time steps after flash with subtraction of the first image, and (c) typical readout from thermography experiment where the dashed black line is the reference non-damaged inspected area and the solid black line is the damaged region. The grey area in the temperature profile shows the integration taken for the thermography analysis

The plot of the damage severity obtained for specimen AE3-4 from the integration method is shown in Figure 4.15 (a), which displays typical characteristic features as obtained for the other specimens. The extent of the lightning damage area is clearly visible, and the severity of the damage is indicated by the large numerical values of the damage metric. The regions that are charred have a lower damage severity than the damage at the lightning attachment point. The integration method was used to quantify similar damage types as shown for specimen AE3-4 (Figure 4.15 (a)), similar to [138].

To identify similar damage types, characteristic threshold pixel values were selected. These threshold values were set based on visual inspection and evaluated as the values which were at least 3 standard deviations away from the reference non-damaged regions integrated values. The values at each pixel were compared to the selected threshold values and binarized by assigning a value of 1 if the value was above the threshold and 0 if the value was below the threshold. Each different

test setup requires slightly different threshold values depending on the amount of heat input supplied. The heat input is affected by factors such as the flash lamp being located at different distances from the inspected test sample, power supplied by heating source, and exposure time of heating source. For AE3, a threshold for 'charred damage' was set to 1.0 and the results are shown in Figure 4.15 (b). A 'surface damage' threshold of 5.0 was adopted and an example of the results are shown in Figure 4.15 (c). With the image binarized, a count of the number of pixels above the threshold values can be used as the total pixel area of the damage. The count is then multiplied by the spatial resolution squared to determine the physical damaged area. These resulting areas are then further used to evaluate damaged areas vs lightning parameters from the simulated lightning strike experiments. The results of these comparisons are provided in the results section. The threshold values and spatial resolutions for test AE2-AE5 are presented in Table 4.7.

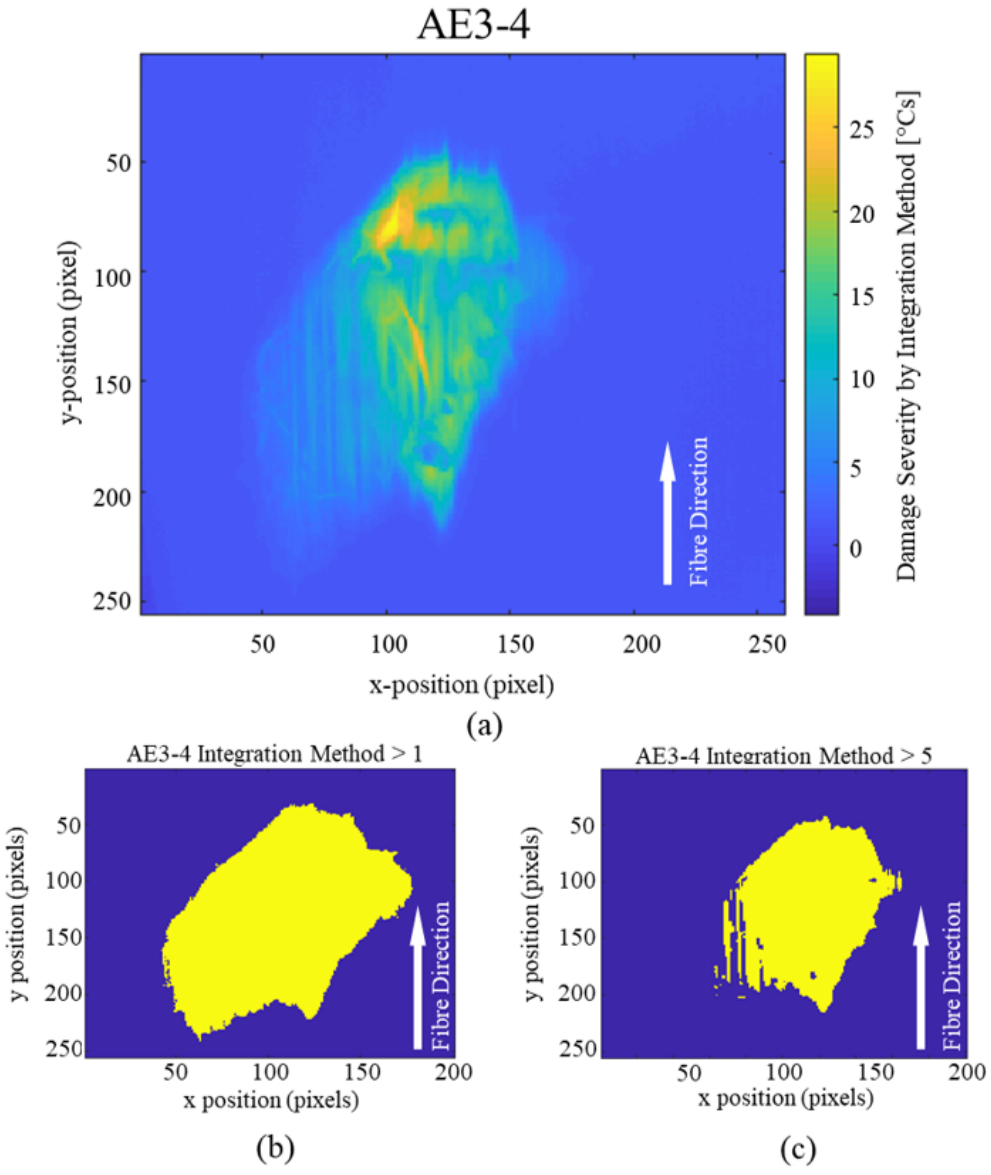

Figure 4.15: Thermography results for specimen AE3-4 where (a) is the nominal integration method measurement, (b) is the charred damage thresholded image, and (c) is the surface damage thresholded image

Table 4.7: Thermography damage severity thresholds and spatial resolution

Test Specimens	Charring Damage Threshold [$°Cs$]	Surface Damage Threshold [$°Cs$]	Spatial Resolution [px/mm]
AE2	1.0	5.0	0.73
AE3	1.0	5.0	0.73
AE4	1.0	5.0	1.02
AE5	2.0	8.0	1.56

4.5.2 X-ray Computed Tomography (CT)

X-ray Computed Tomography is a 'non-destructive' method in which several X-ray images are taken of a sample and the corresponding images are reconstructed into a three-dimensional object [139]. For this research, the X-ray CT measurements were conducted using the University of Southampton's 225kV/450kV Nikon/Metris custom X-ray scanning machine. A 225kV X-ray source was used with a 2000x2000 sensor to capture the X-ray images. The resolution of the scans for specimens AE2-AE4 was 0.1088 mm/voxel and due to its larger scale for specimens AE5 the resolution was 0.222 mm/voxel.

Two different methods were used to analyse the data. The first method was a thresholding procedure where the remaining undamaged thickness was through a projection. This process is called the "threshold-based method". The CT images were run through a data processing procedure in the image processing software ImageJ [140]. The X-ray images are a set of voxels which have a certain bit-depth. The initial CT images were 32-bit and were scaled to 8-bit making it quicker to process. Figure 4.16 shows an example of the X-ray binarization process. A typical example of a slice in the through thickness direction is shown in Figure 4.16 (a) for specimen AE3-2 with regions of very high bit values caused by tungsten deposits from the electrode. Tungsten is much more dense than the carbon fibre and it results in very high voxel bit values (shown as white particles in Figure 4.16 (a)). These tungsten deposits were found in samples AE1-AE3 at the attachment point, and clearly have an undesirable effect on the X-ray images, so the electrode was equipped with a jet diverter which prevented the electrode from depositing tungsten particles in AE4 and AE5 samples.

To determine the thickness, the X-ray volume data is binarized by picking a certain bit level as a threshold which includes the full sample volume. The threshold level needs to be low enough to include the full sample volume and exclude the non-sample volume like air and any X-ray setup equipment. The result leaves an image stack in a binary format with the sample volume voxels values at 255 and the other voxels at 0 as shown in Figure 4.16 (b). To remove the effect of the tungsten particles, a procedure called "Analyse Particles" in ImageJ was run. This process finds enclosed areas in an image. A minimum size can be set in the analyse particles function which will return only objects that are above this volume. Setting this minimum size to a significantly high

value returns the sample volume without the including the effects of the tungsten deposits. The regions with the tungsten particles were shaded in red to indicate their location and is shown in Figure 4.16 (c). After this procedure, only the remaining CFRP sample volume was left, and this volume is shown in Figure 4.16 (d).

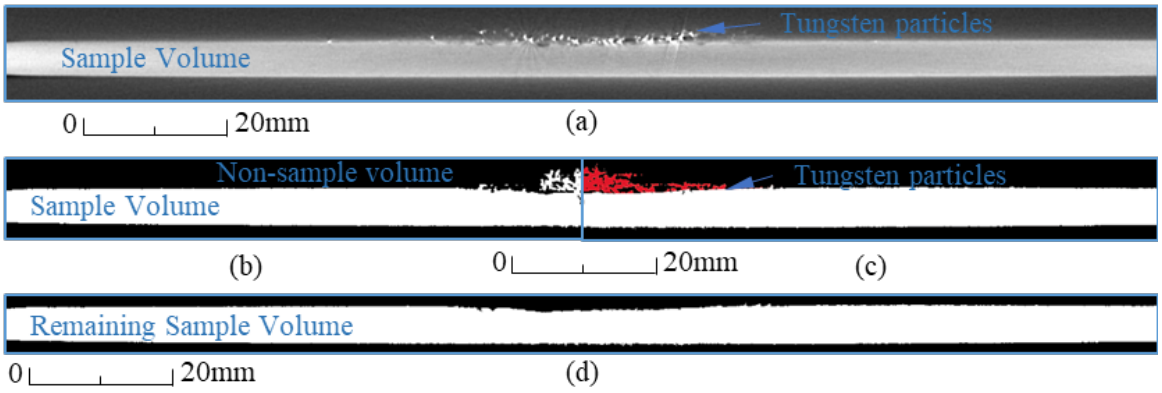

Figure 4.16: (a) X-ray CT of specimen AE3-2 showing a sliced image through the thickness, (b) processed threshold showing binary image where white is associated with the full volume, (c) is a processed image with the erroneous particles shown in red, and (d) is a sliced image of the fully processed remaining CFRP volume

Each image slice was combined into a single image by summing the slices in a process called "Z-project". A graphical description of the voxel values and their directions are shown in Figure 4.17 (a) where the 255 values are the remaining sample volume and the 0 values are the remaining voxel values. The number of slices is shown in the z-direction with an index i. The voxels were summed together in the z-direction through all the slices and divided by binary value 255. This results in a count of the number of voxels which are assigned 255 in the z-direction or simply put the number of remaining sample voxels in the z-direction. The count is then multiplied by the spatial resolution to translate the image stack into millimetres as follows:

$$h(x,y) = \sum_{i=1}^{n} \frac{v(x,y,z_i)}{255}(\varphi) \tag{4.4}$$

where h is the thickness, v is the voxel binary value at the x, y, and z location, i is the index of volume values in the z direction, n is the total number of voxel values in the z direction, and φ is the spatial resolution.

The resulting images obtained from the process are presented as 32-bit real data with x and y position datum at the centre point of the damage and the 32-bit greyscale values providing the remaining thickness of the sample, as shown in Figure 4.17 (b). The raw (32-bit real data) image data was interrogated in a Matlab [137] routine with the minimum thickness of each column (y direction) across the width of the sample was collected and arranged in a damage depth plot as shown in Figure 4.17 (c).

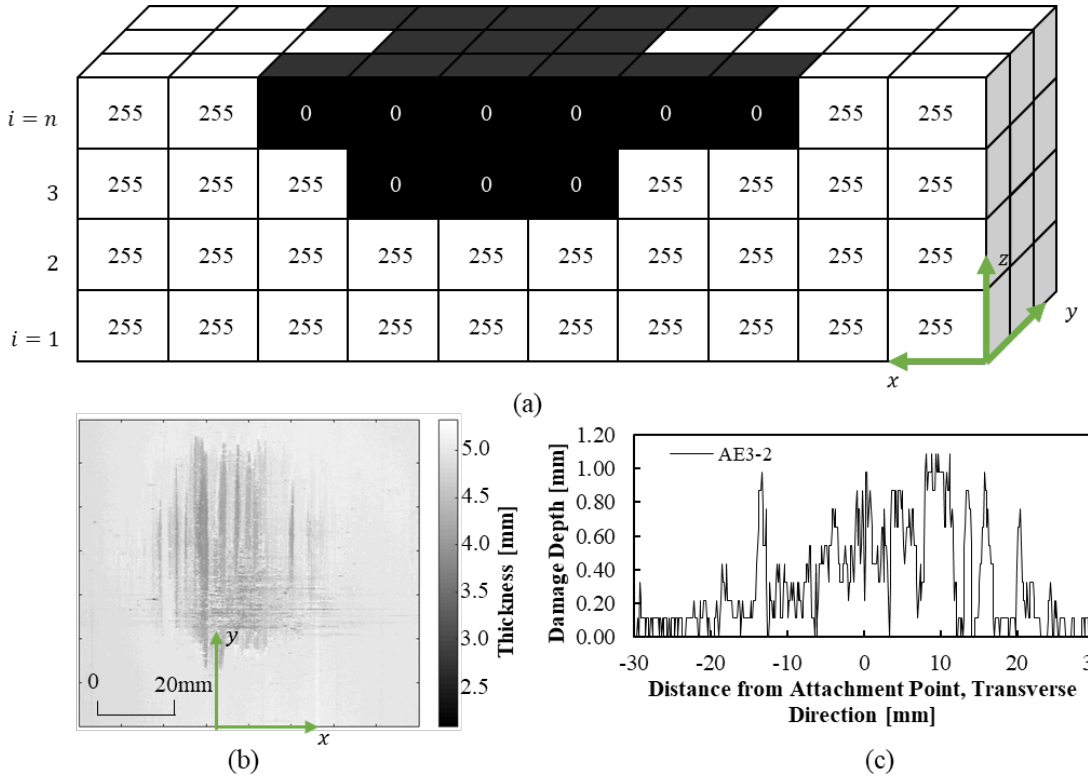

Figure 4.17: (a) An example result of the binarization process to a X-ray CT image showing the directions, thickness values and voxel values, (b) shows the 32-bit Real image of thickness values from the Z-project process associated with the AE3-2 damaged specimen and (c) shows the maximum damage depth plot processed from the Matlab script

The threshold-based method was efficient for the carbon/vinyl ester pultruded specimens (AE2-AE3). However, for panels AE4 and AE5 the results were inconclusive as the carbon/epoxy heavyweight fabrics were difficult to automatically distinguish between damage and non-damage as there was not enough contrast between the damaged region and the non-damaged region. Although the issue was not able to be parsed automatically, the damage was easily spotted by eye as can be seen in Figure 4.18. Figure 4.18 (a) shows the cross-section where damage is identified in the top plies and Figure 4.18 (b) shows a plan in the depth of the sample which clearly shows the damage by eye. The darker regions are associated with less dense material from processes such as material removal during the lightning strike event. To determine a damage depth, a second method was devised, herein referred to as the "manual threshold-based method". In this method, the CT images were captured, reconstructed and imported into ImageJ. The volumes were converted to an 8-bit image format, so all the voxel values were at max 255. Following this, the image stack was converted back to a 16-bit image format without scaling the voxel greyscale values. This ensured that everything within the volume had a maximum greyscale value of 255, and after this each slice was examined manually for damage. The damaged area in each of the image slices was selected manually with a polygon selection tool. An example of a typical damage identification and selection polygon is shown in Figure 4.18 (c). The voxels in this slice had a value of 1000 added to their original greyscale values. This was done to ensure that all damaged voxel bit values were

above 255 and could easily be thresholded. Once the values were thresholded the same threshold-based method was used to find the thickness.

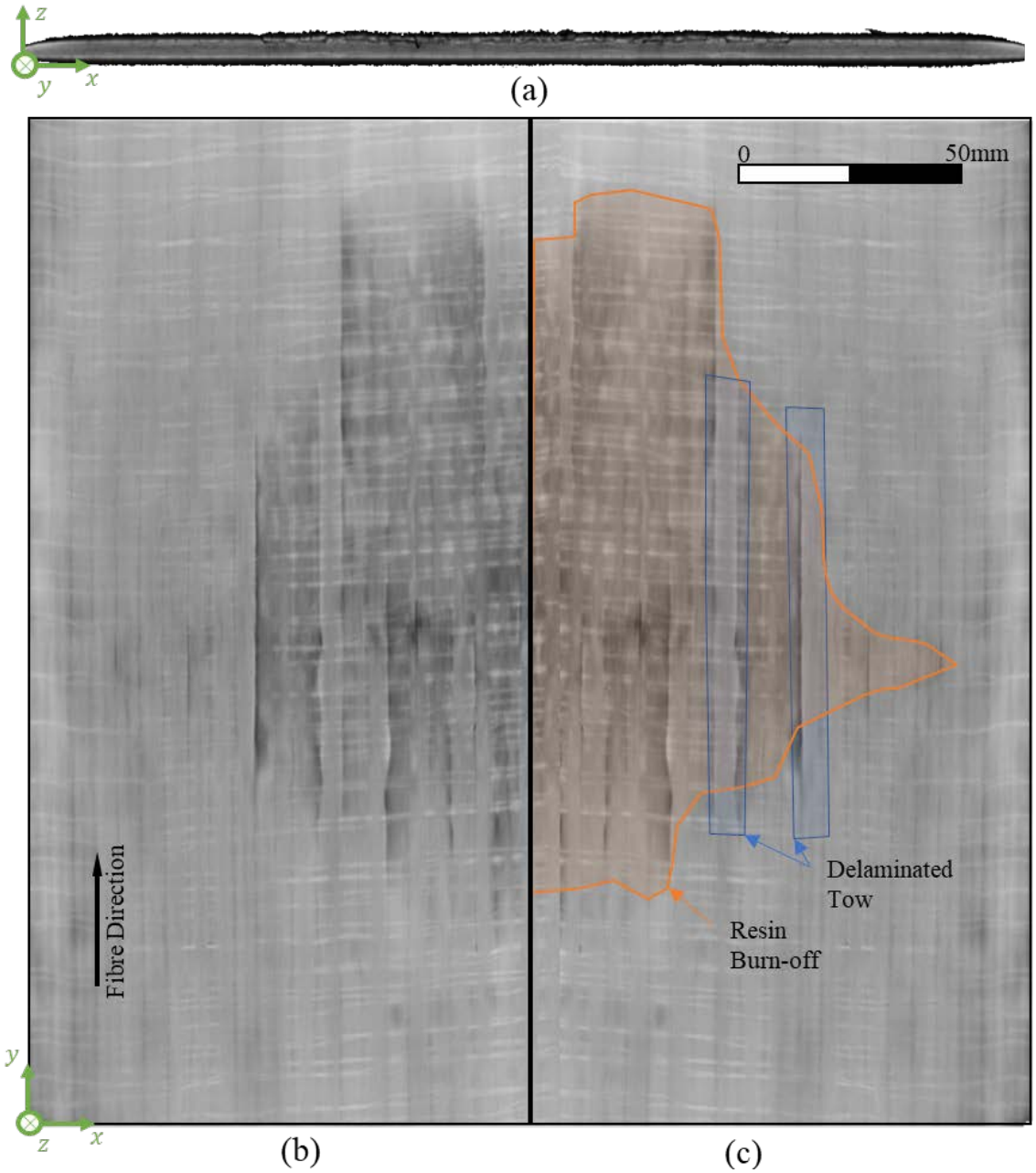

Figure 4.18: CT Results AE4 (a) cross-sectional view, (b) plan view original, and (c) plan view with damage polygon selection and description

4.6 Results and Discussion

4.6.1 AE2: Variation of Inductance

All AE2 specimens displayed surface damage and charred damage around the lightning attachment point, with the damaged areas appearing in an elliptical shape with the major axis in the direction

transverse to the fibres. The surface damage consisted of exposed fibres, resin damage and charring damage consisted of blackened soot and small redeposits of material on the surface.

Figure 4.19 shows the damaged area identified by the IRT integration method. The surface damage was constant for all the parameters showing no significant increase in surface damage due to an increase in lightning parameters peak current, absolute value of charge, and specific energy. There is an increase of charring damage areas that was observed due to increasing peak current and specific energy (Figure 4.19 (a) and (c)) but reversed for increasing absolute value of charge (Figure 4.19 (b)).

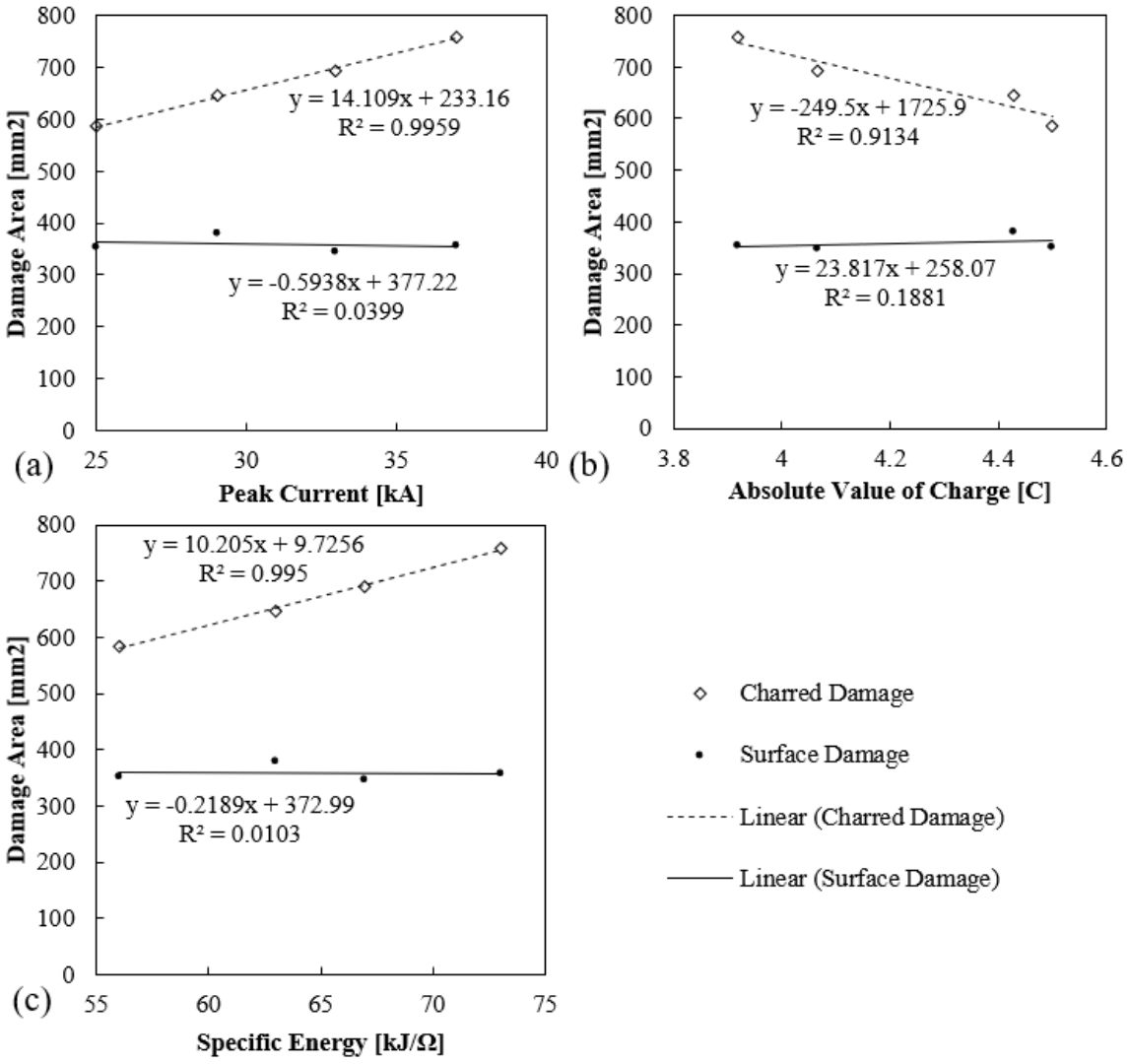

Figure 4.19: Thermography damage area results for test specimens AE2 against (a) peak current, (b) absolute value of charge and (c) specific energy

Figure 4.20 presents the damage depths determined from the X-ray CT data. The results show that the damage depths were a maximum of 8.8% of the total laminate thickness. There are sharp edges enclosing the damage depth. This type of damage profile indicates that the removal of material was likely due to an ablation process rather than a pyrolysis process, as the pyrolysis process removes

material due to sustained heat and therefore has more gradual transitions of thickness. The ablation process typically evaporates the material quickly and results in fast removal of the heat, like a laser ablation process. The ideal shape for an ablation process would be similar to a square wave, however due to the heterogeneous material properties a perfect square wave will not be achieved as seen in Figure 4.20. The resin is burnt off and the fibres are left intact, which accounts for the profiles of the damaged depth plots seen in Figure 4.20.

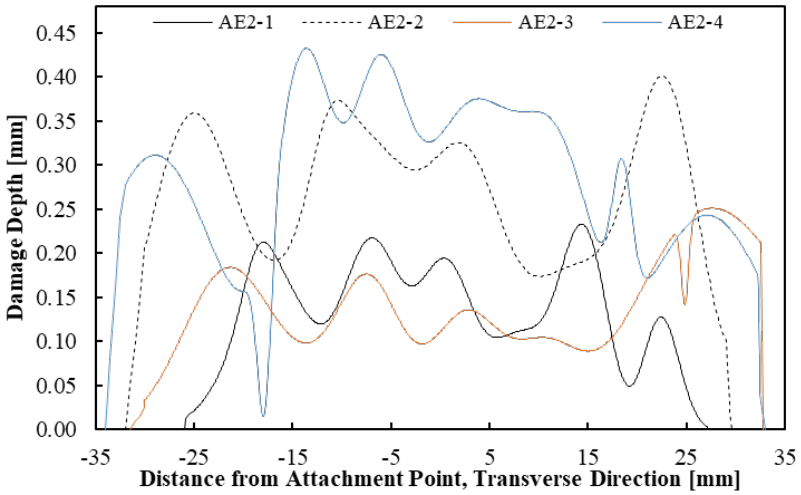

Figure 4.20: Maximum damage depth measurements from CT depth analysis AE2 specimen

4.6.2 AE3: Variation of Charge

Four AE3 CFRP specimens were subjected to simulated lightning strike events. All AE3 specimens displayed surface damage, primarily in an elliptical shape with the major axis in the longitudinal direction parallel with the fibres. The surface damage consisted of exposed fibres, resin damage and charring damage consisted of blackened soot and small redeposits of material on the surface.

The thermography results are shown in Figure 4.21. The resulting damage shows a nearly linear correlation between surface/charred damage vs charge and specific energy with relatively high R^2 values; see Figure 4.21 (b)-(c). The opposite trend was shown for surface/charred damage vs the peak current and the resulting trend R^2 values; see Figure 4.21 (a). The apparent negative slope is artificial as the magnitude of the peak currents varied by less than 0.2 kA and are associated with differing levels of charge and specific energy, indicating that the aforementioned lightning parameters have more influence on the extent of the damage area.

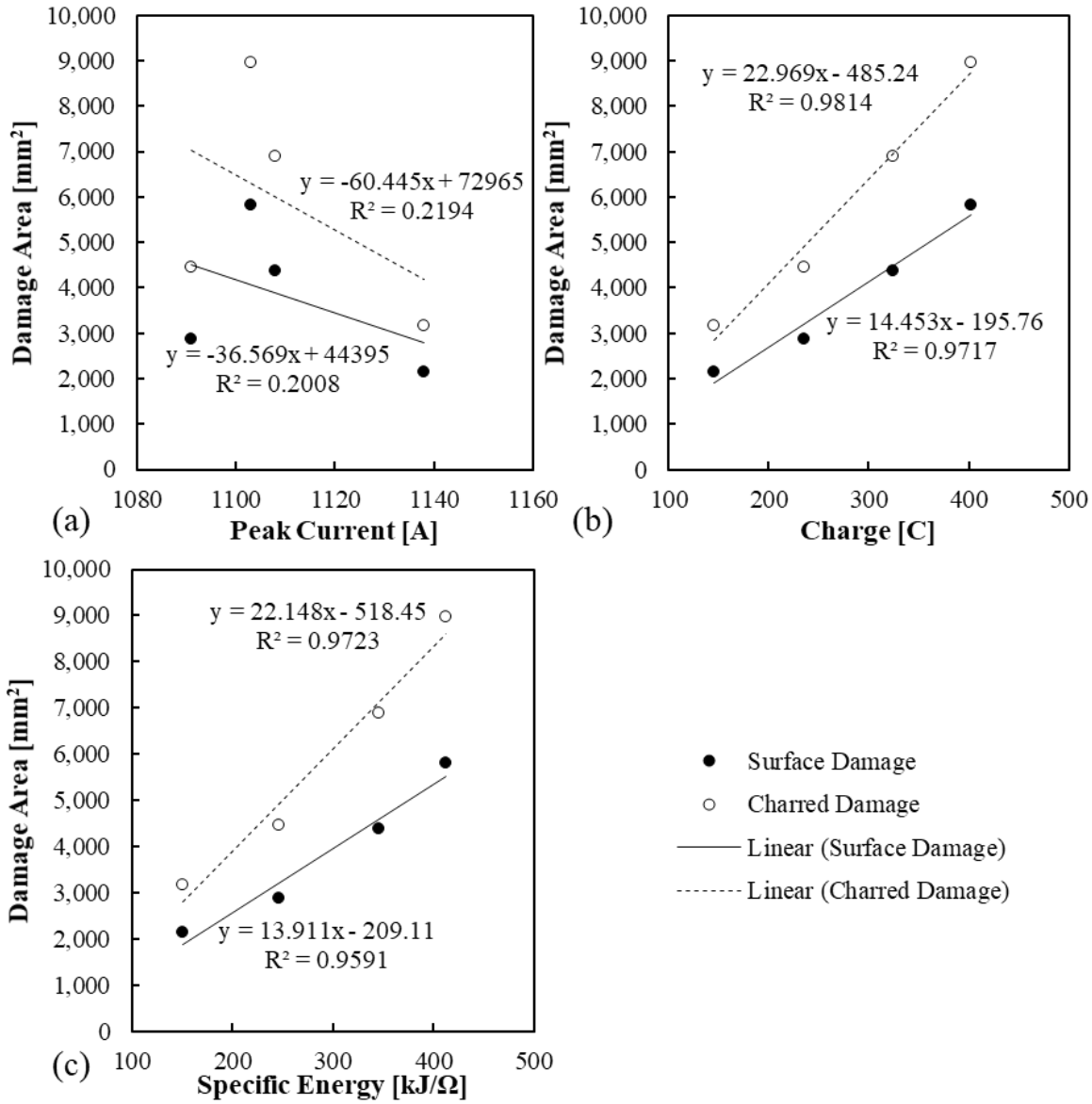

Figure 4.21: Thermography damage area results AE3 against (a) peak current, (b) charge and (c) specific energy

The visually identified damage, and the X-ray CT scans showed similarly shaped surface damage with resin burnt away. Further inspection into the depth of the specimen did not reveal discernible delamination or other damage below the surface damage. An example of the cross section in the thickness direction and a plan view sub-surface of the top surface from the X-ray CT scan of specimen AE3-4 is shown in Figure 4.22.

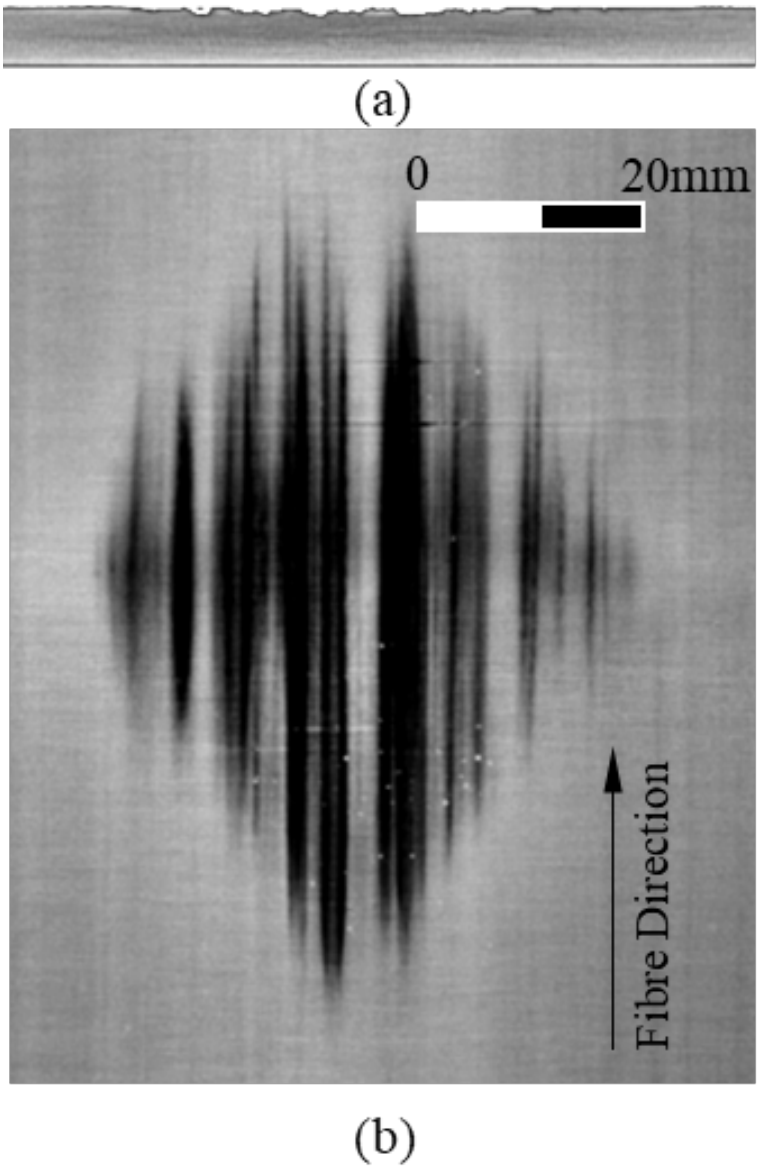

Figure 4.22: X-ray CT images of damage in specimen AE3-4 where (a) is the cross-section through the thickness and (b) is the top plan view

Figure 4.23 presents the damage depths determined from the X-ray CT data. The results show that the maximum damage depth was around 30-32% of the total laminate thickness. Contrary to the previous impulse damage (AE2) from Figure 4.20, the damage was more smoothly transitioned from the edges of the damage to the maximum. This indicates that the damage is more similar to a pyrolysis process.

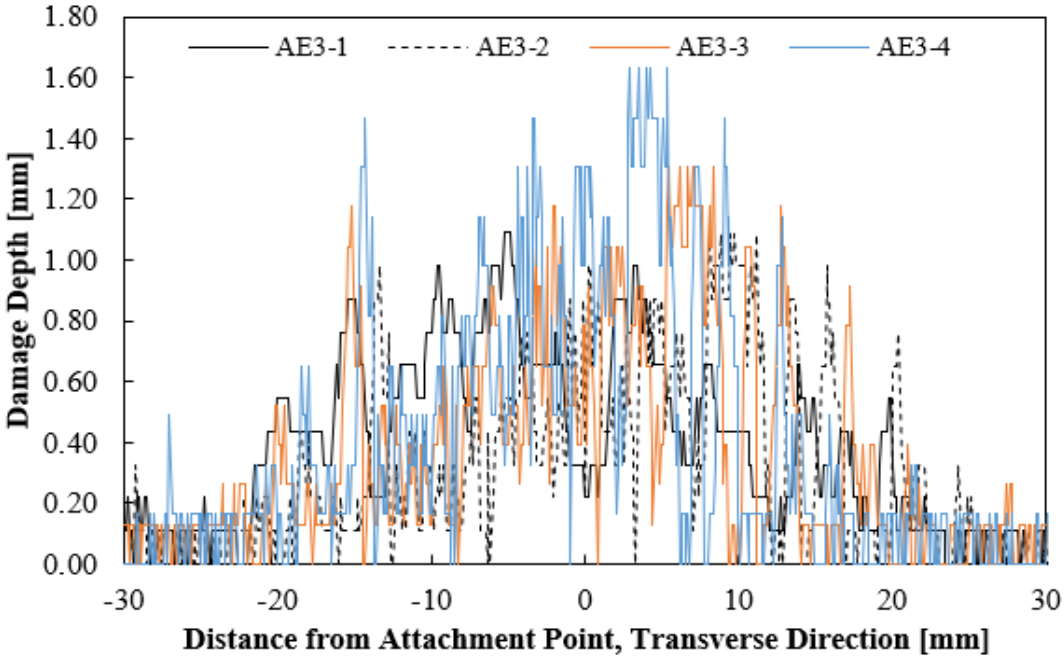

Figure 4.23: Maximum damage depth measurements from X-ray CT damage depth analysis of AE3 specimens

4.6.3 AE4: 10/350µs waveform

All AE4 specimens displayed surface damage and charred damage around the lightning attachment point, with the damaged areas appearing in an elliptical shape with the major axis in the direction transverse to the fibres. The surface damage consisted of exposed fibres, resin damage and charring damage consisted of blackened soot and small redeposits of material on the surface.

The damaged area thermography results vs the peak current, charge and specific energy are shown in Figure 4.24. Figure 4.24 (a) – (c) all show a similar result with the increasing peak current, charge, and specific energy all increasing the damaged area. The R^2 values can indicate which trends have a closer fit to the data. The specific energy had the highest R^2 values for all the damage trends.

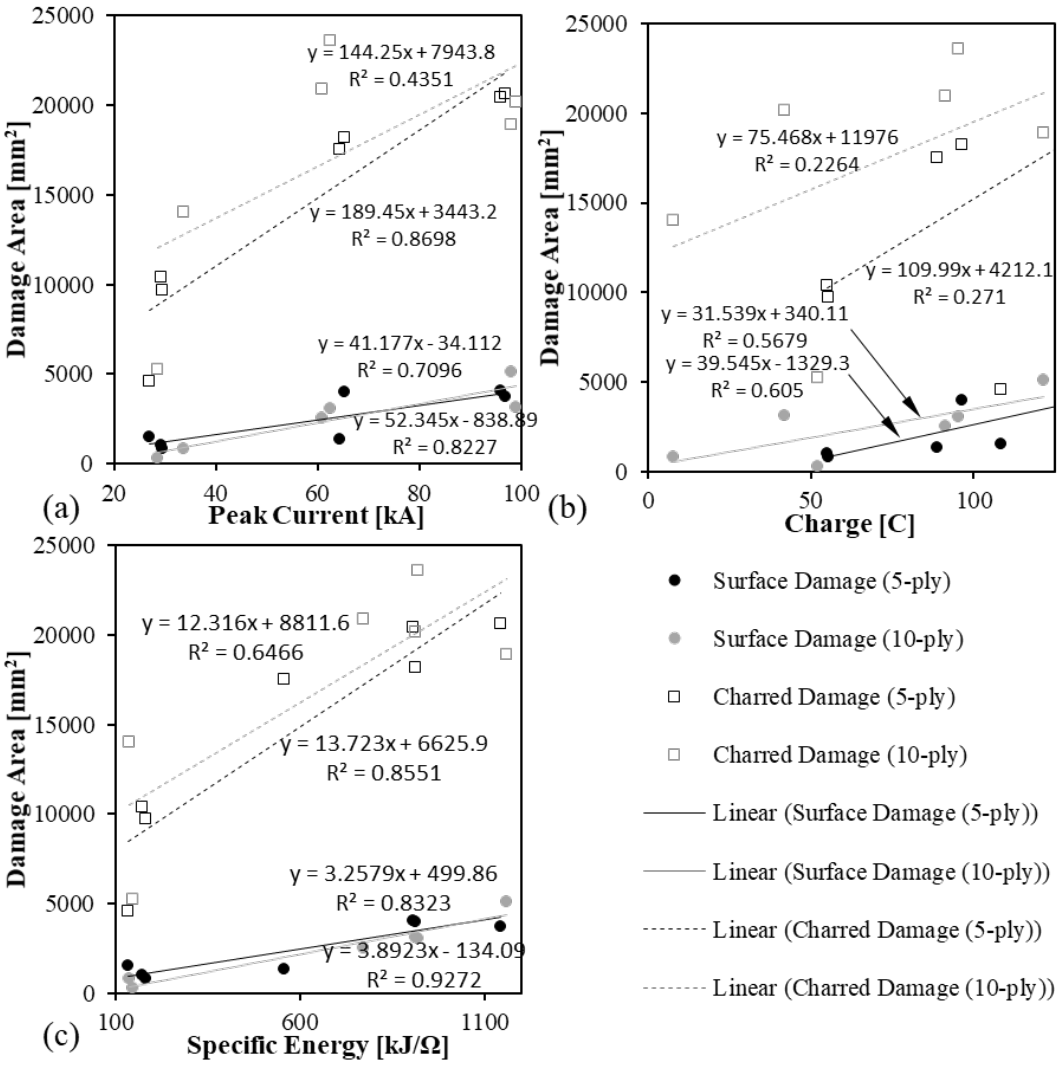

Figure 4.24: Damaged areas identified by thermography against the (a) peak current, (b) charge and (c) specific energy for specimens AE4

In Figure 4.25, the total charge and total specific energies have been separated into the contributions stemming from the impulse and DC waveforms. From Table 4.4 (page 73), it is seen that more than 80% of the charge comes from the DC portion of the waveform and more than 90% of the specific energy comes from the impulse portion of the waveform. This enables separation of cause and effect. Assessing the R^2 values (least square fitting correlation) indicated in Figure 4.25, it is observed that the surface and charred damage fits closest to specific energy. The thermography results indicate the same correlation as the visual inspection. Figure 4.25 shows the thermography results with impulse vs DC and specific energy vs charge. Checking the R^2 values, the surface and charred damage fits closest to the specific energy. Separating the impulse and DC allows for a cause vs effect analysis. Figure 4.25 (b) and (c) show the R^2 values have the tightest fit between impulse and DC components which indicates that most of the damage is contributed by impulse. The R^2 values from Figure 4.25 (a) and (b) show that the best predictor of damage is specific energy. The R^2 values from Figure 4.25 (c) and (f) show that the lowest R^2 values were associated with the DC portion of the waveform.

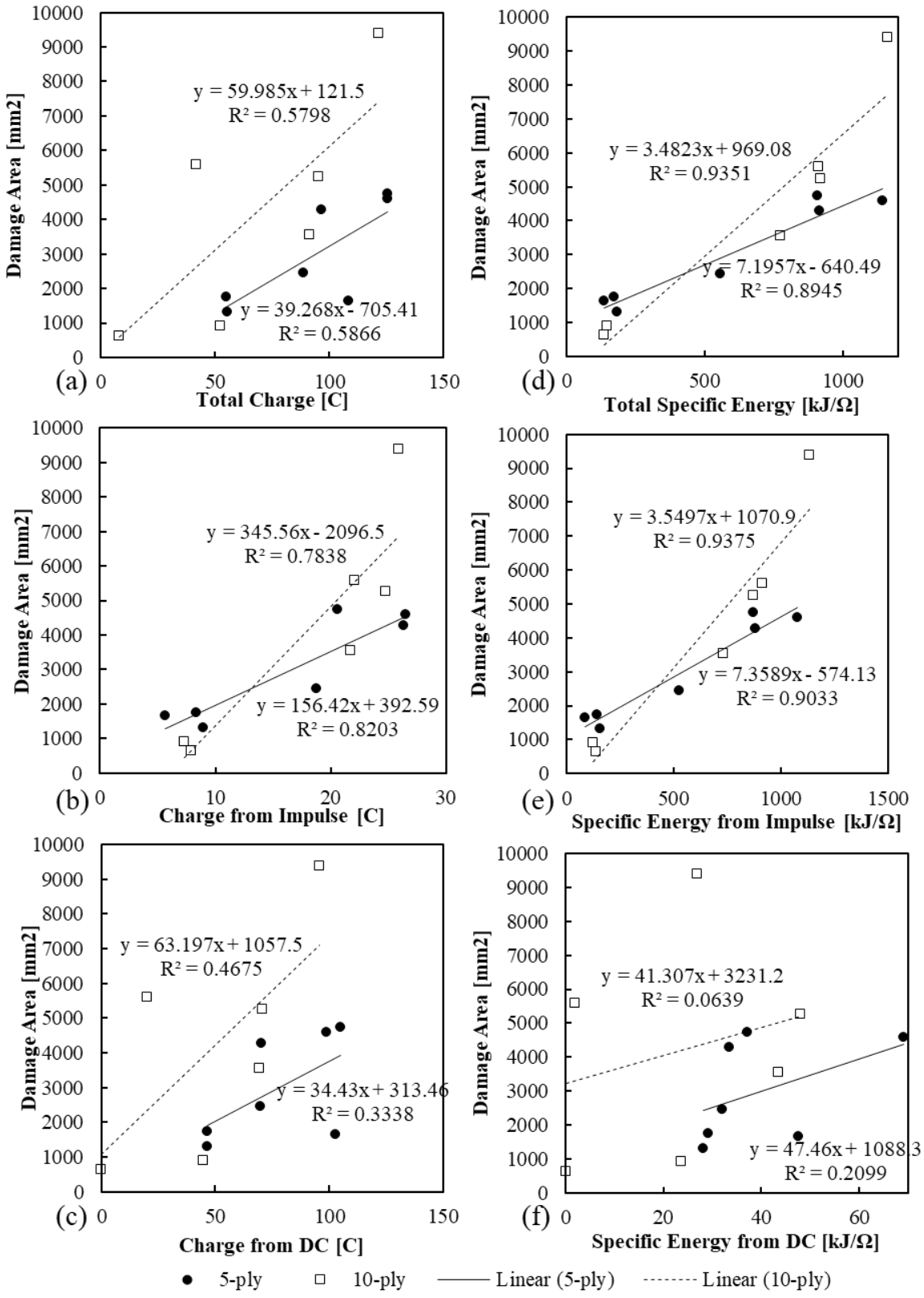

Figure 4.25: Charge and specific energy vs damaged areas identified using thermography from the 5-ply and 10-ply AE4 specimens comparing the charge and specific energy against the total, impulse and DC portion of the waveform. (a) is the charge from the total waveform, (b) is the charge from the impulse portion, (c) is the charge from the DC portion, (d) is the specific energy from the total waveform, (e) is the specific energy from the impulse portion, and (f) is the specific energy from the DC portion

Figure 4.26 presents the damage depths determined from the X-ray CT data. The results show that the damage depths were maximum for the highest lightning strike intensities. At the highest intensities, the maximum damage depth was 41% of the total laminate thickness. The damage was more smoothly transitioned from the edges of the damage to the maximum. This indicates that this is more similar to a pyrolysis process.

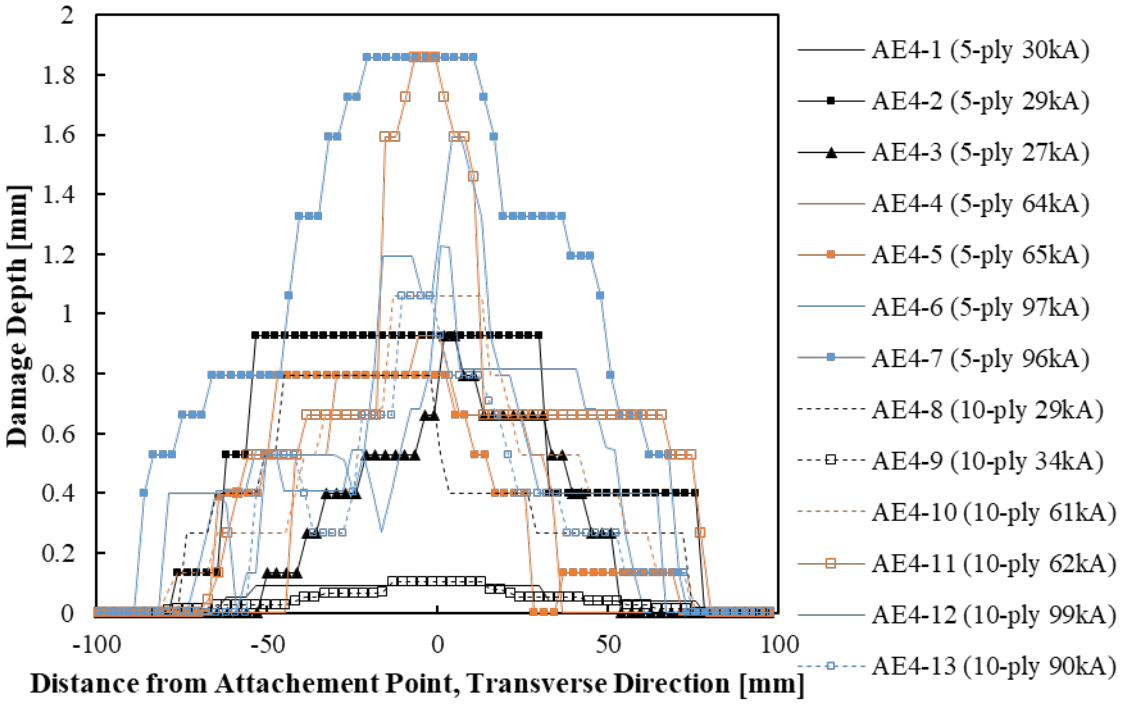

Figure 4.26: Maximum damage depth measurements obtained from X-ray CT depth analysis for the AE4 specimens

4.6.4 AE5: Sparcap sub-structure simulated lightning strike with 10/350µs waveform

Thirteen specimens were subjected to simulated lightning strike events for the AE5 (see section 4.3.5 for details of the specimen configurations and Table 4.5 for applied lightning waveforms). The results for the bare surface specimens were similar to the results obtained for the AE4 specimens. The shape of the damage area was elliptical with the major axis being in the transverse direction and the minor axis being parallel to the fibre direction. The bare surface specimens displayed increased damage area with increasing peak current, which subsequently increased the charge and energy. An example of the observed bare surface specimen damage is shown in Figure 4.27 (a). The damage observed for the fibreglass surface specimens was dissimilar to that observed for the bare specimens. Thus, the shape of the damaged area for the fibreglass specimens was elliptical as well, but with the major axis directed along the fibre direction and the minor axis directed along the transverse direction. Similarly, to the AE4 specimens, as the peak current increased, the amount of damage also increased. The surface damage areas were significantly larger than observed for all other specimen configurations (AE1-AE4), but with no significant

charred damage. Moreover, a portion of the fibreglass surface was completely delaminated from the base CFRP laminate. Figure 4.27 (b) shows an example of a damaged observed for the fibreglass surface specimen. The copper mesh surface samples remained intact as shown in Figure 4.27 (c) and there was no damage that included visibly exposed fibres. The surface damage observed for the copper mesh surface samples only showed small areas with loss of copper mesh and burnt off resin. Charred areas were measured as areas which had small spots of damaged copper mesh.

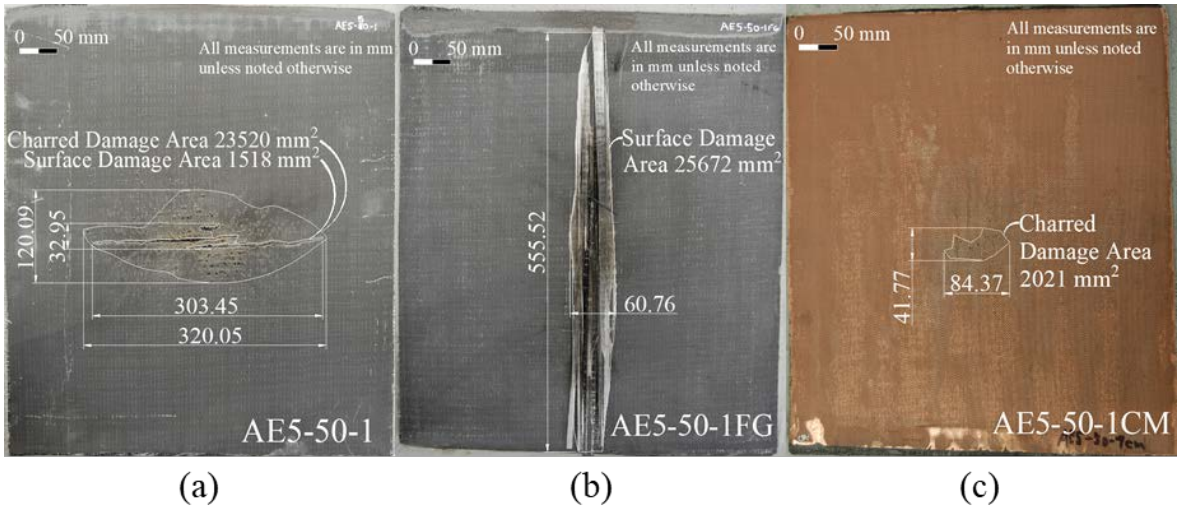

Figure 4.27: Visual inspection of the AE5 specimens subjected to 100 kA: (a) bare surface specimen, (b) fibreglass surface specimen, and (c) copper mesh surface specimen

The damaged area thermography results vs the peak current, charge and specific energy are shown in Figure 4.28. Figure 4.28 (a) – (c) all show a similar result with the increasing peak current, charge, and specific energy all increasing the damaged area. The R^2 values can indicate which trends have a closer fit to the data. The specific energy had the highest R^2 values for all the damage trends. The significant results show that the difference in surface types has a drastic difference in the amount of damage. The surface damage was practically zero for all copper mesh specimens. The bare specimens were similar to the AE4 tests. The fibreglass specimens were dramatically different, showing 8 times more damage area than in the bare specimens.

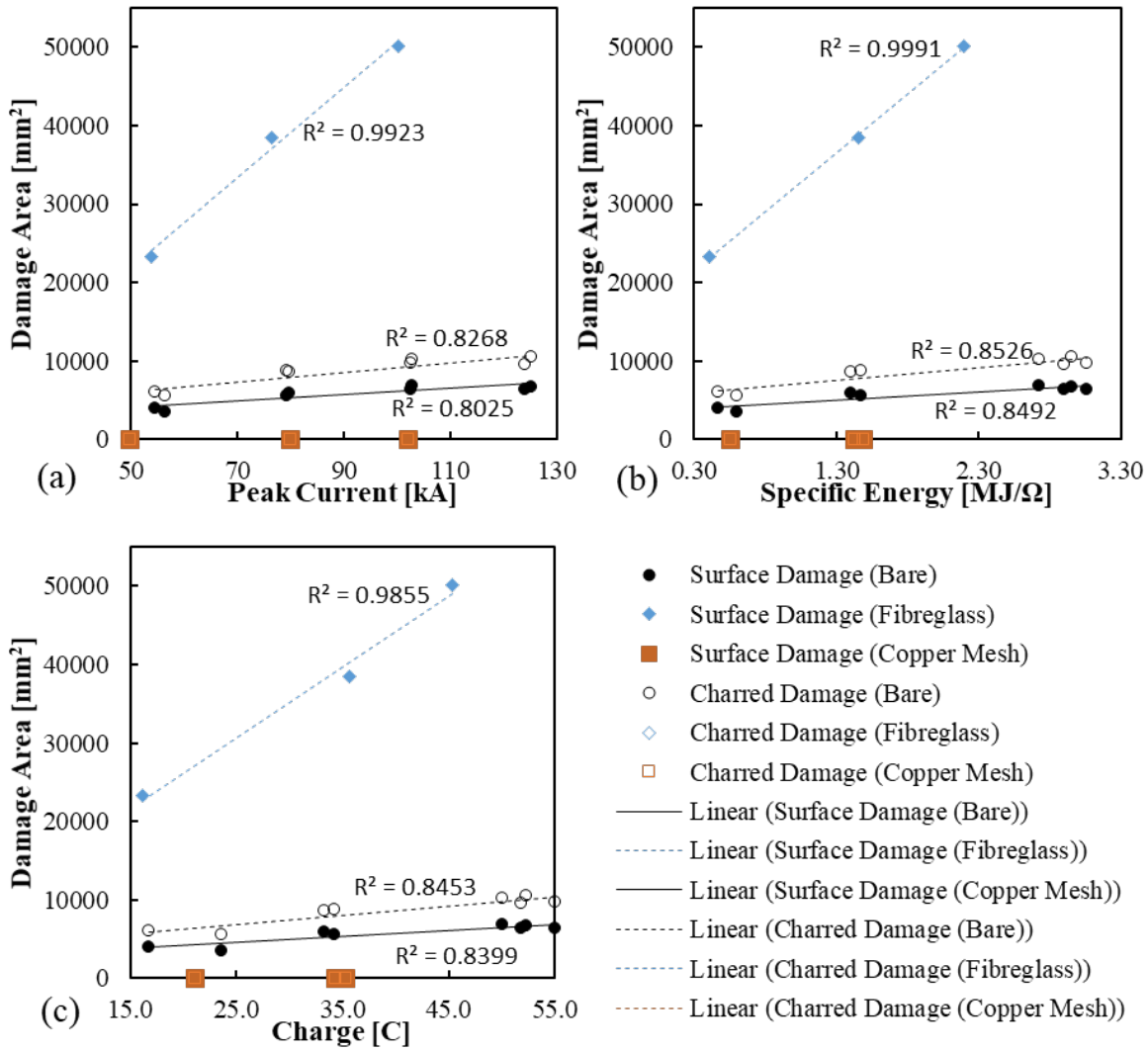

Figure 4.28: Damaged areas recorded using thermography for the AE5 specimens vs (a) peak current, (b) charge and (c) specific energy

X-ray CT images were also captured and reconstructed for the AE5 specimens. Figure 4.29 (a) shows a cross-sectional view of bare surface specimen and Figure 4.29 (b) shows a plan view of the same specimen. The results are very similar to the observations for the AE4 specimens.

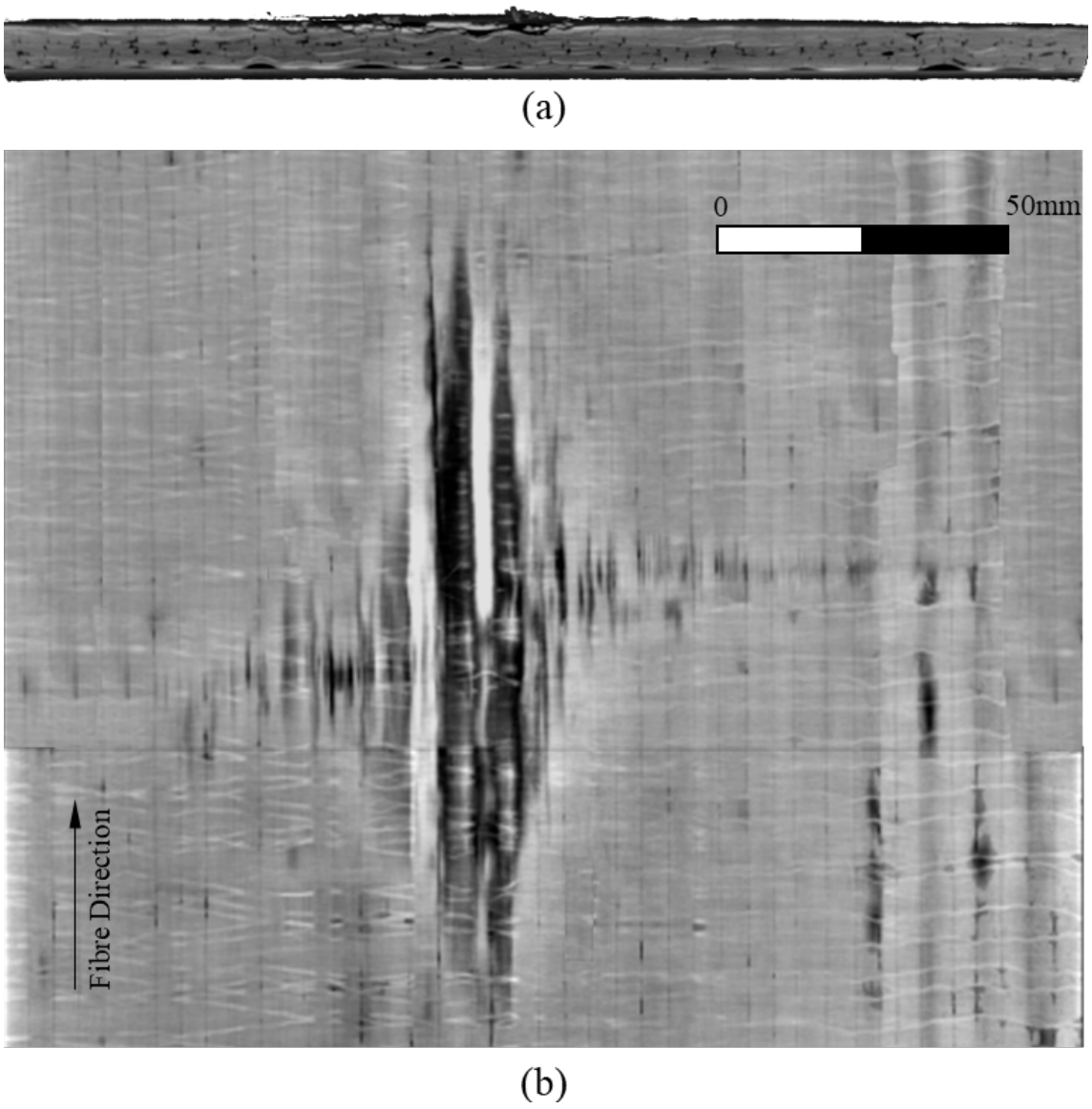

Figure 4.29: X-ray CT images of damaged bare surface specimen AE5-100-1 which was subjected to 100 kA peak current 10/350μs lightning waveform: (a) cross-sectional view and (b) plan view

Figure 4.30 shows the X-ray CT images obtained for the fibreglass surface specimens AE5-100-1FG subjected to 100 kA peak current 10/350μs lightning waveform. Figure 4.30 (a) shows a cross-sectional view of the damage specimen, from which it is seen that the damage penetrated through the full laminate thickness. The back side, or opposite side from the lightning attachment, of the laminate has broken in the transverse direction. Furthermore, a delaminated region is observed one ply thickness above the back side. Figure 4.30 (b) shows the sub-surface plan view, which indicates a very low-density region indicated by the dark colour in the image. The damaged region starts in the middle of the specimen and extends along in the fibre direction.

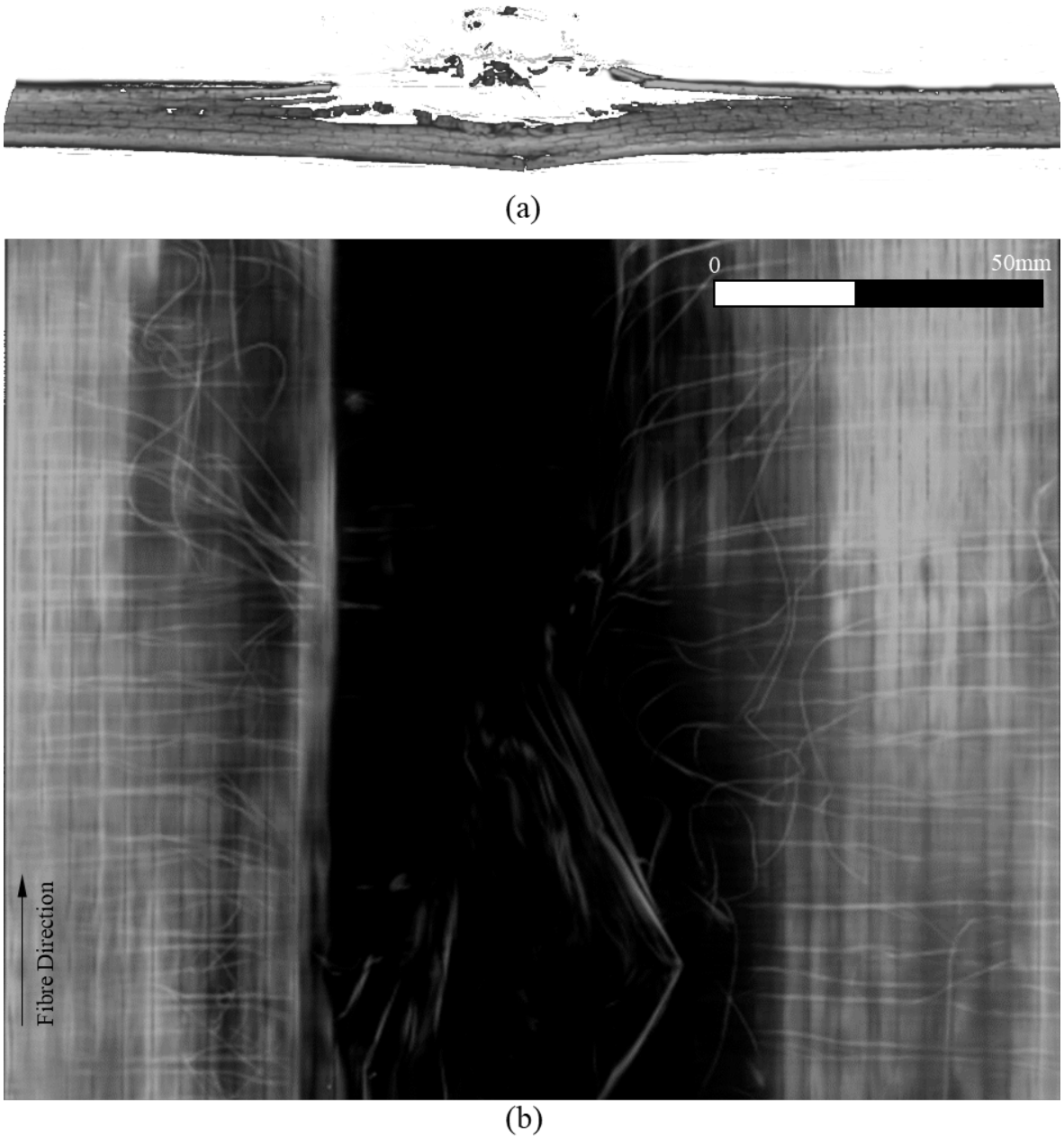

Figure 4.30: X-ray CT images of damaged fibreglass surface specimen AE5-100-1FG which was subjected to 100 kA peak current 10/350μs lightning waveform: (a) cross-sectional view and (b) plan view

Figure 4.31 shows X-ray CT images obtained for the copper mesh surface specimens AE5-100-1CM subjected to 100 kA peak current 10/350μs lightning waveform. Figure 4.31 (a) shows a cross-sectional view, from which no damage can be observed, i.e. no noticeable damage in the CFRP laminate, no delaminations, and no separation between the copper mesh and the CFRP laminate. Figure 4.31 (b) shows a plan view of the copper mesh surface, and from this image it is observed that some of the copper mesh is burnt off. Figure 4.31 (c) shows the first CT slice with the CFRP laminate, and from this it is clear that only the copper mesh and not the CFRP laminates were damaged from the lightning strike.

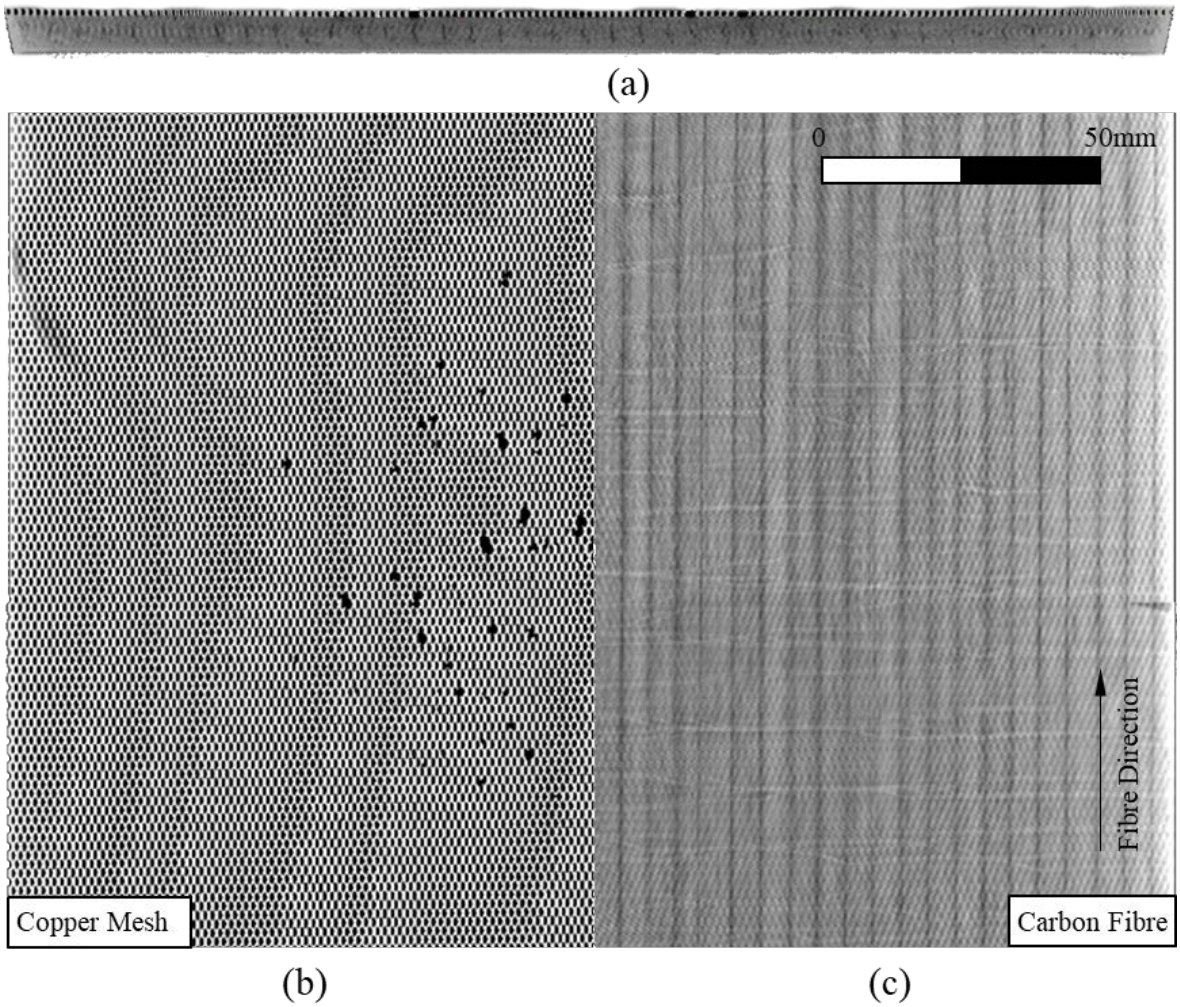

Figure 4.31: X-ray CT images of damaged copper mesh surface specimen AE5-100-1CM subjected to 100 kA peak current 10/350μs lightning waveform: (a) cross-sectional view, (b) plan view of the copper mesh surface and (c) plan view of the top surface of the CFRP underneath the copper mesh surface

The depth of damage was calculated by using the CT slices from the CFRP laminate only. Figure 4.32 shows the damage depth obtained for all the AE5 samples. The maximum damage depth measured for the bare surface specimens was 35% relative to the undamaged CFRP laminate thicknesses, 100% for the fibreglass surface specimens, and 0% for the copper mesh surface specimens.

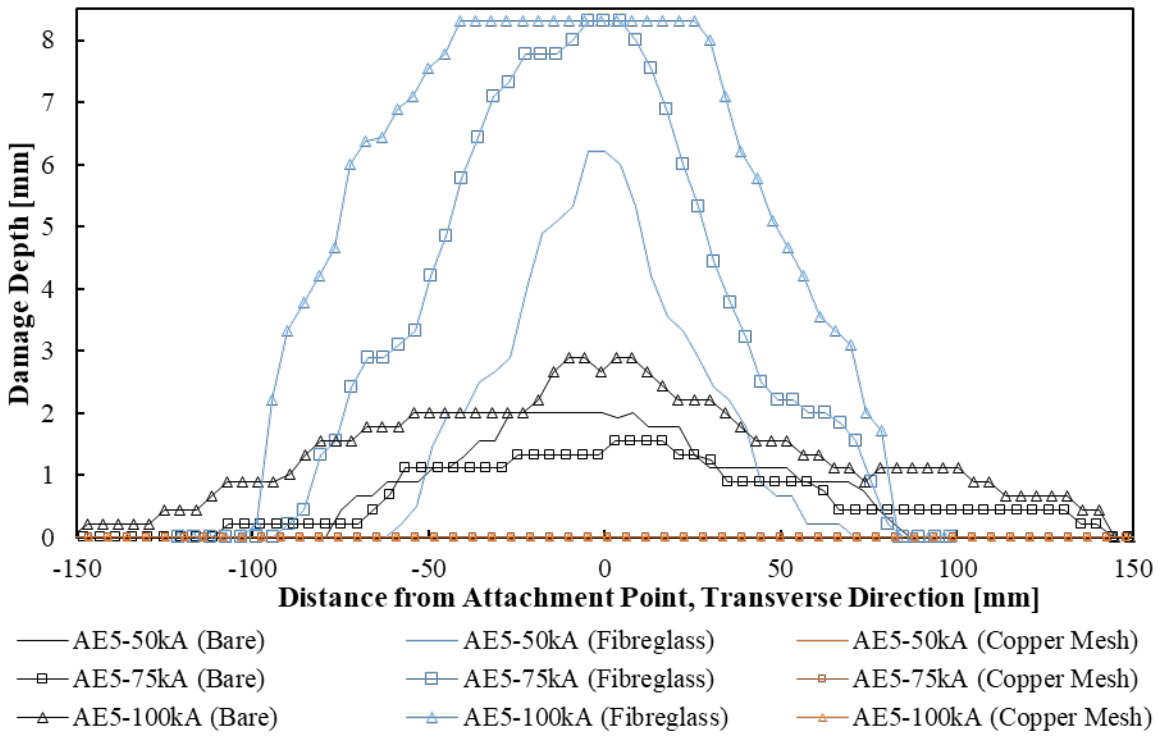

Figure 4.32: Maximum damage depth measurements obtained from X-ray CT depth analysis for the AE5 specimens

A thermal image video was captured with the thermal camera to study the temperature distribution on the surface of the composite specimens during and after the lightning strikes. The saturation temperature for this camera is 692°C. The temperature data recorded for the AE5 specimens is shown in Figure 4.33. The temperature responses were vastly different for the different specimen surface types. The bare surface specimen started with a large increase in temperature with the maximum temperature reducing to under 100°C around 10s. The fibreglass surface samples held the heat much longer than the other specimens with specimens holding heat over 300°C for more than 50s. This is due to the concentration of the arc, which caused more heat to be induced. The copper mesh surface specimens rapidly cooled back to near ambient temperature in less than 1s. This is due to the higher electrical conductivity in the copper mesh which spreads the arc across the surface more rapidly and reduces the Joule heating effect.

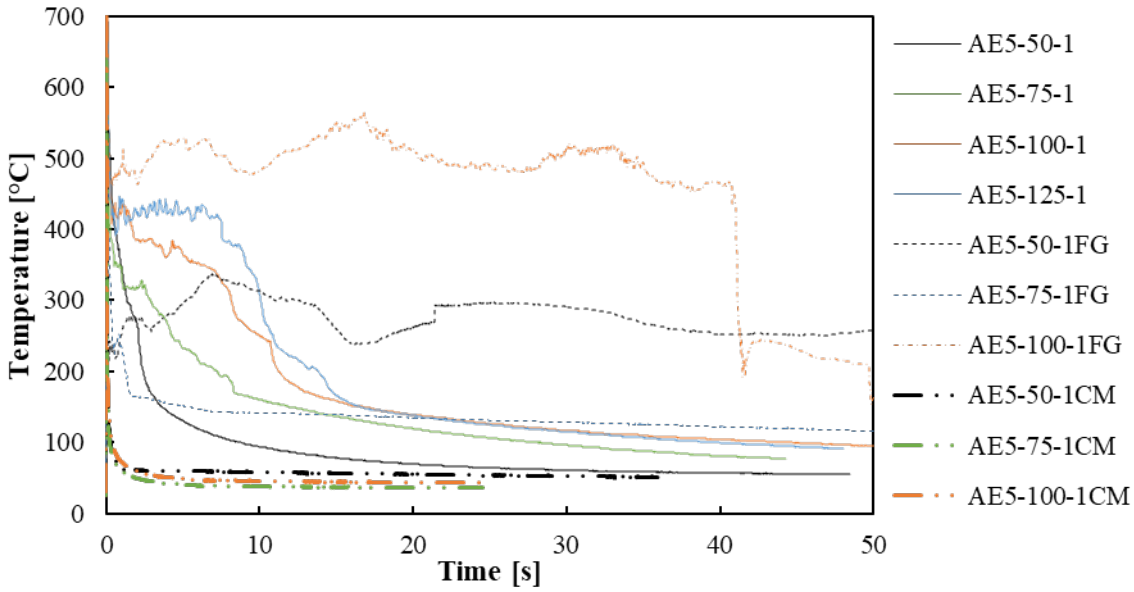

Figure 4.33: Maximum temperature evolution for AE5 specimens

The temperature profile recorded in the longitudinal and transverse directions of the AE5 specimens are shown in Figure 4.34, Figure 4.35 and Figure 4.36 at three specific image frames (times of 0.047s, 0.109s, and 5.0s after the lightning strike). The temperature distribution observed for the bare surface shows a rapid decrease in temperature in the longitudinal direction Figure 4.34 (a). The temperature distribution for the bare surface shows much wider Joule heating spread in the transverse direction Figure 4.34 (b). This is an expected result after seeing the damage being more in the transverse direction.

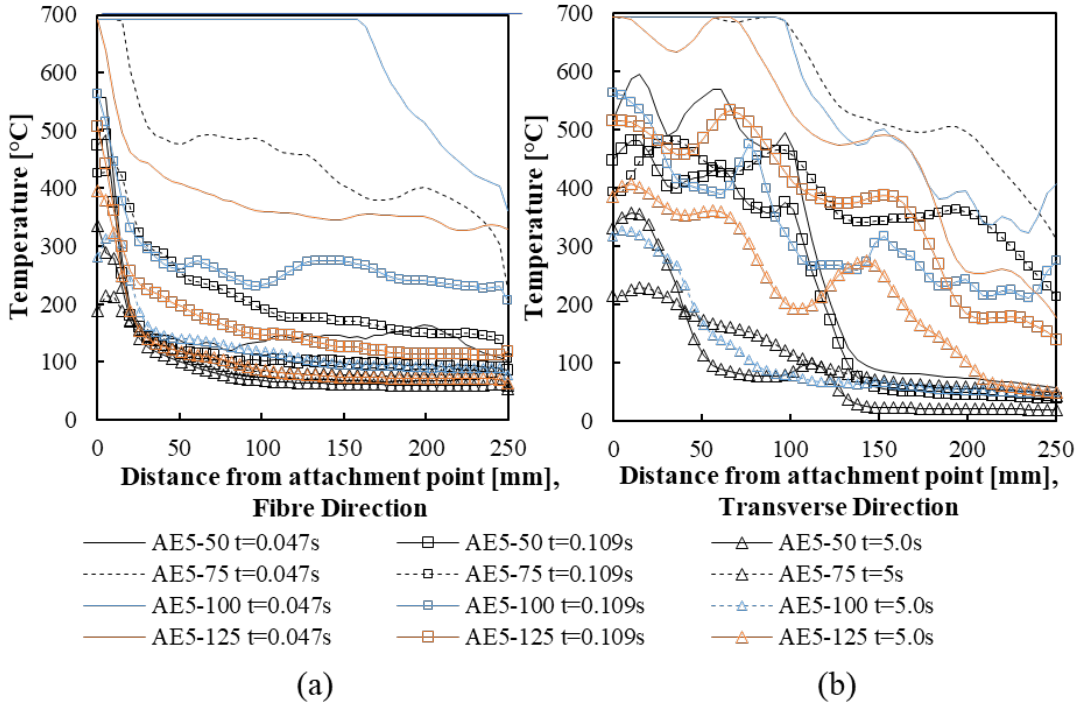

Figure 4.34: Temperature distributions observed for the bare surface AE5 specimens: (a) fibre direction and (b) transverse direction

For the fibreglass surface AE5 specimens, the recorded temperature profiles align with the observed damage pattern as the measured temperatures are higher in the longitudinal (fibre) direction rather than in the transverse direction.

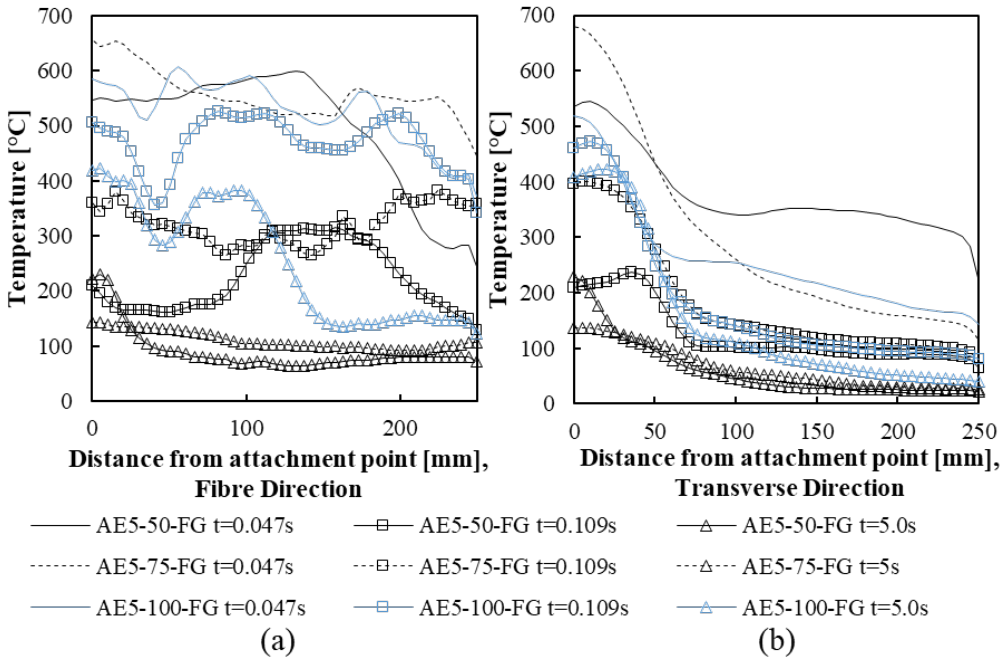

Figure 4.35: Temperature distributions observed for the fibreglass surface AE5 specimens in the (a) fibre direction and (b) transverse direction

The copper mesh surfaced specimens showed a much smaller temperature rise than the other surface types, see Figure 4.36. The longitudinal direction and transverse directions were similar in size and profile, indicating that the current flows in a circular or nearly circular pattern.

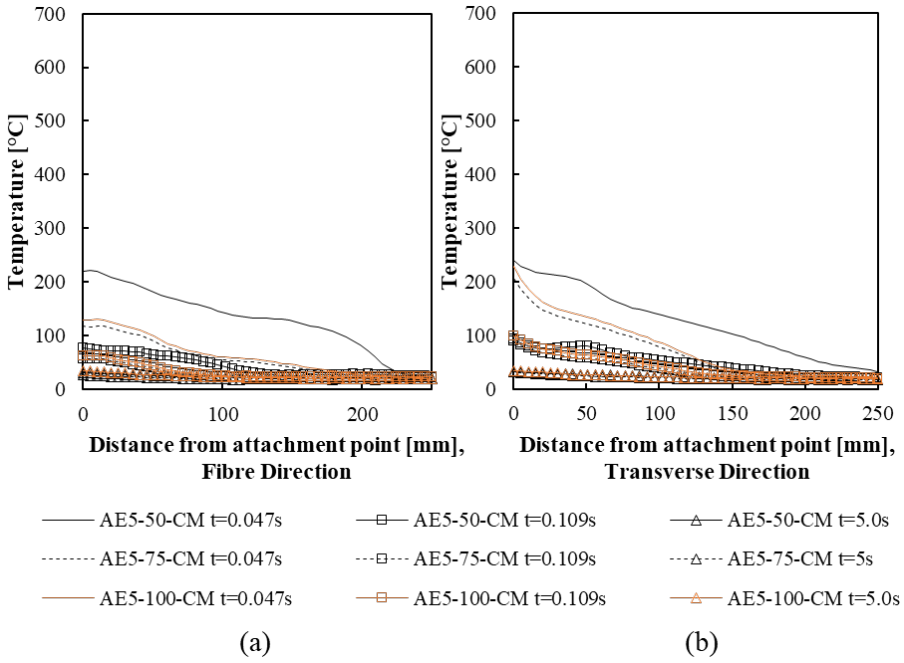

Figure 4.36: Temperature distributions observed for copper mesh surface AE5 specimens: (a) fibre direction and (b) transverse direction

4.7 Overall observations and key outcomes

4.7.1 Damage Categorization

The lightning strike experiments have provided a comprehensive set of data regarding direct attachment lightning strike induced damage in UD CFRP materials. In section 4.6, damage was generally assigned to be surface and charred damage. From the lightning strike experiments reported in this chapter, the induced damage can be further attributed to four different damage types: fibre breakage, delaminations, resin burnoff, and charring. From the experiments conducted, surface damage was associated with fibre breakage, delamination, and resin burnoff. Charred damage was found to encompass all the described damage types, with fibre breakage present at the centre of the surface damaged region. Figure 4.37 shows an image of fibre breakage observed on specimen AE3-2 using an optical microscope. This damage is severe because the loss of fibres has a major effect on the local area strength and stiffness, especially for thin laminates.

(a)

(b)

Figure 4.37: Typical fibre breakage damage from AE3-2 experiment where (a) is a close-up image of fibre breakage taken on Nikon DSLR with an 80 mm lens and (b) is a micrograph of fibre breakage at 100x magnification

Delaminations are sub-surface damage in which plies separate from each other causing reduction of the laminate stiffness strength, particularly compressive strength due to enhanced propensity for local buckling failure [141]. Moreover, delamination cracks can cause additional damage by

propagating throughout the structure. This type of defect was found through X-ray CT scans and also cutting the specimens followed by cross section evaluation and microscopy. Examples of lightning strike induced delaminations are shown in Figure 4.38 for specimens AE4-12 and AE4-1.

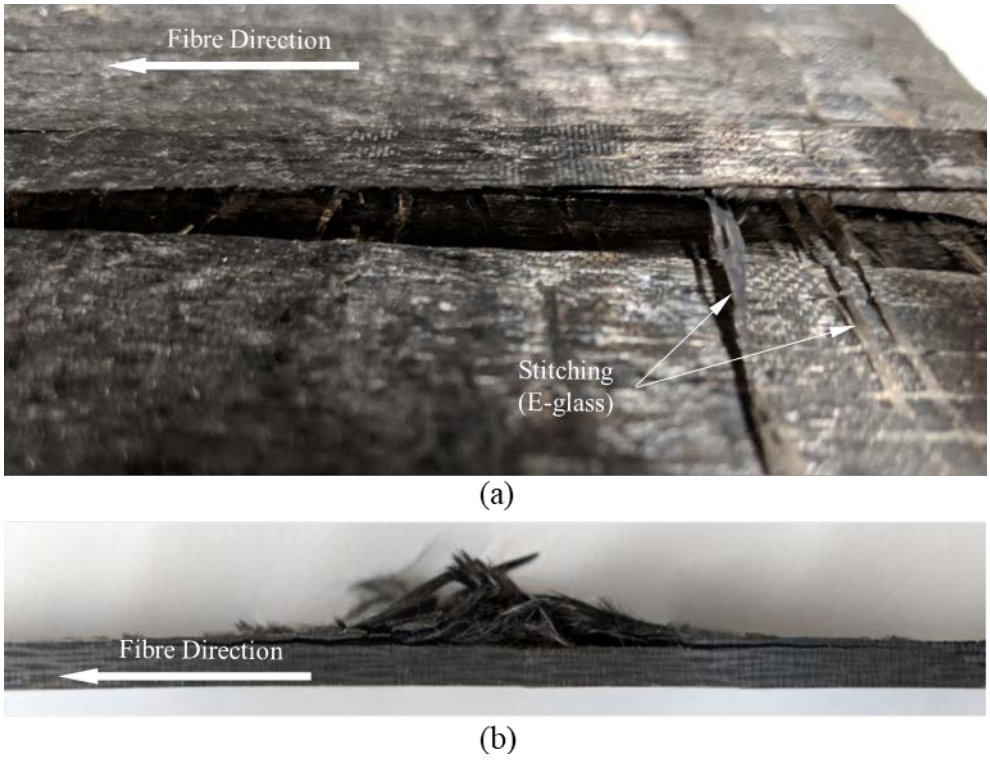

Figure 4.38: Typical lightning strike induced delamination: (a) close-up image of delamination damage in AE4-12 using Nikon DSLR with a 50 mm lens and (b) macro image of delamination in AE1-4 taken using Nikon DSLR with a 50 mm lens and 10x macro lens attachment

The third damage category is resin burnoff as shown in Figure 4.39. The polymer resin type used in most WT blade structures is epoxy which decomposes when subjected to temperatures between 300°C and 500°C [142]. Above 500°C, the material will char, and ablation will begin above 3000°C [142]. The local compressive strengths and stiffnesses are affected when there is no matrix to support the fibres and hold them in place.

Figure 4.39: Close-up image of the area with resin burn off in specimen AE3-4 taken using Nikon DSLR with 50 mm lens. Undamaged area is shaded.

Charring is characterised by the burning of material, usually on the surface as shown in Figure 4.40. It is hypothesized that this does not exert a significant effect on the strength, as it is mainly a surface imperfection, and as it is typically not associated with loss of fibres or resin burnoff as has been observed in microscope investigations.

Figure 4.40: Close-up image of charring damage from specimen AE2-4 taken using Nikon DSLR with 50 mm lens

Figure 4.41 displays temperature profiles recorded for specimens AE3-2 and compares the temperature evolution for the surface damage region and the charred damage regions. The observed trend is that the charred damage areas cooled more rapidly than the surface damaged areas.

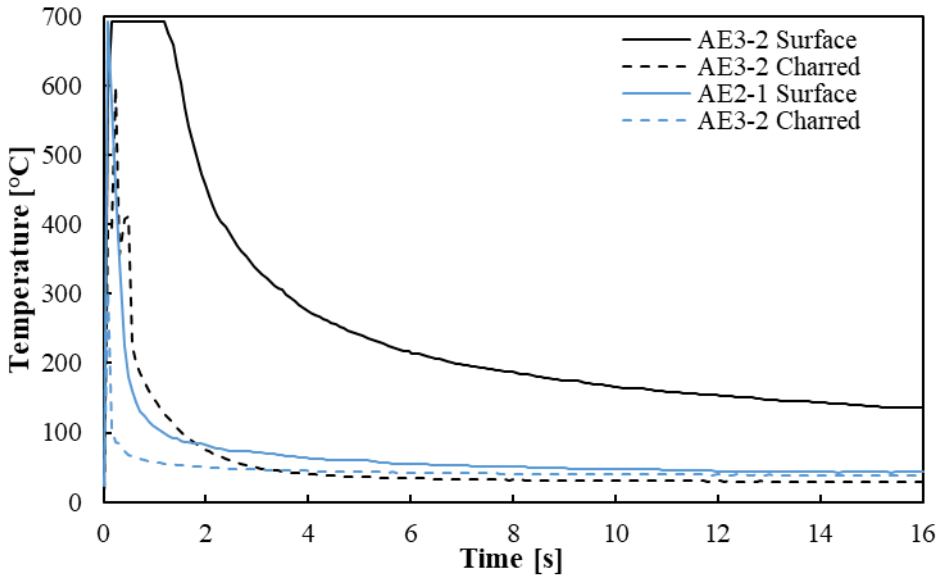

Figure 4.41: Temperature evolution of the charred damaged areas and surface damaged areas for the AE3 specimens

4.7.2 Damage in Transverse Direction (Transvers to Fibres)

For all the impulse bare surface specimen configurations AE2, AE4 and AE5 (bare), it was found that upon lightning attachment the arc "spread" most significantly in the direction transverse to the fibre orientation. This was observed for both the oscillating and impulse currents. Figure 4.42 presents the results of the damage lengths for all the specimens UD CFRP test specimens subjected to impulse/oscillating current waveforms (AE2, AE4, and AE5 bare surface). Figure 4.42 (a)-(c) all show a similar trend with the damage lengths increasing with increasing peak current, charge and specific energy. It shows that as the damage increases through, the ratio goes down. However, when assessing the ratio of the damage lengths in the transverse direction to the damage length in the longitudinal direction, the average l_L/l_T ratio was approximately 5.11. This observation has not previously been reported in literature to the best knowledge of the author. Moreover, in previous research on lightning strike simulation, the ratio of longitudinal to transvers direction damage due to lightning strike has been reported to be in the range 0.28-0.63 [40], [108], [110] which is the opposite effect where it extends much further in the longitudinal direction than the transverse direction. The phenomena observed experimentally in this research may be attributed to a special condition presented when lightning strikes a UD laminate as used extensively in the load carrying elements of WT blades (especially in the blade regions with the highest risk of lightning strike attachment), whereas the majority of previous research has been conducted for quasi-isotropic laminate configurations that are relevant for composite aero-structures. This shows that there is a

clear need for the development of a new modelling methodology to accurately simulate lightning strike phenomena associated damage in WT blade structures. A new approach and methodology have been developed to model such phenomena in this PhD project, and this is discussed in Chapter 5.

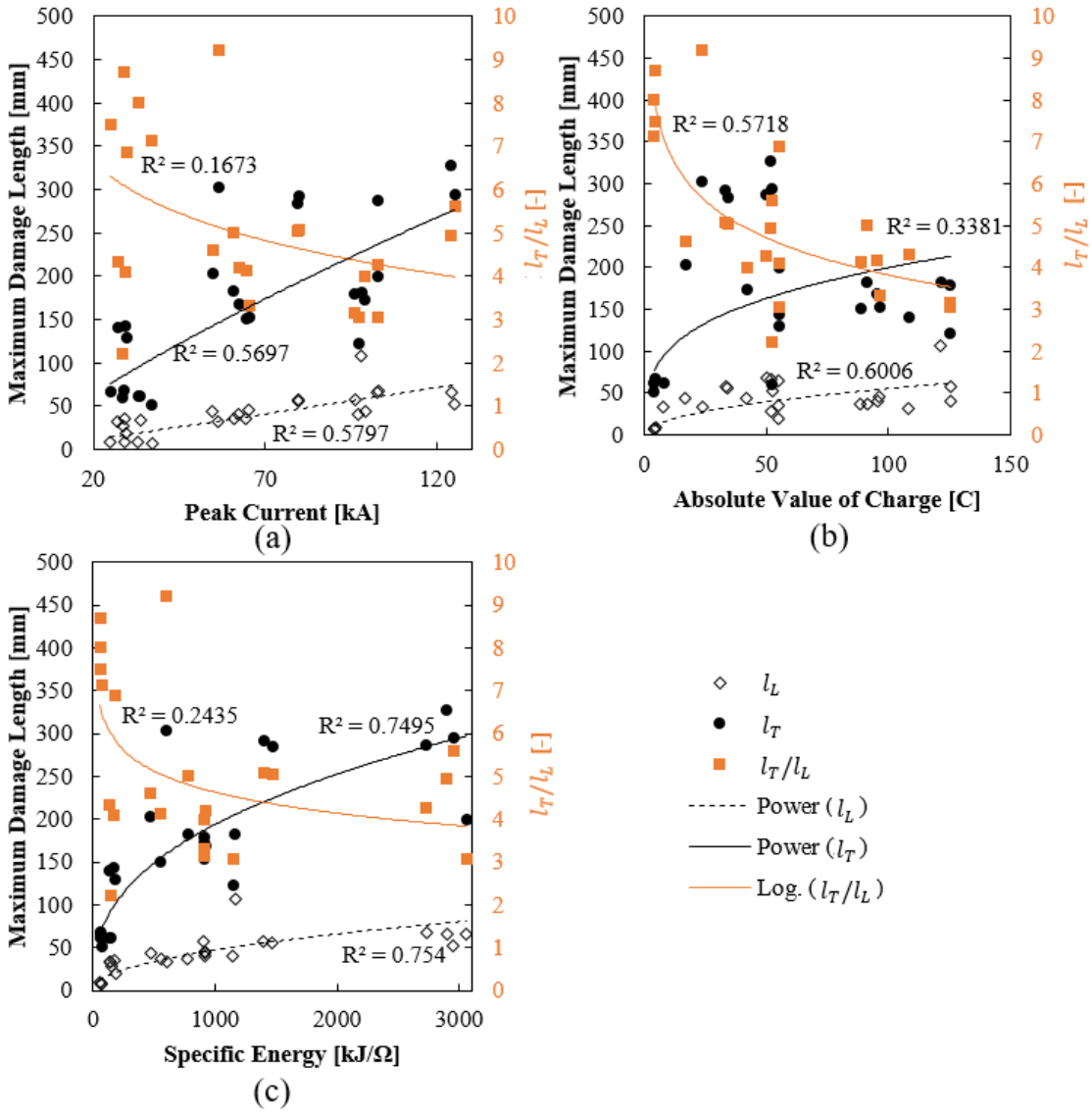

Figure 4.42: Damage lengths results in the longitudinal (fibre) direction l_L and transverse direction l_T with the ratio of transverse length to longitudinal length (l_T/l_L) for all UD CFRP test specimens subjected to impulse/oscillating current waveforms (AE2, AE4, and AE5 bare surface) against (a) peak current, (b) absolute value of charge and (c) specific energy

4.7.3 Comparison of Damage Characteristics

In the results and discussion sections of this chapter, linear regressions were used to assess the correlation between lightning strike induced damage and key lightning strike quantitative metrics including peak current, specific energy, and absolute value of charge. In all cases, specific energy has been found to display a relatively higher R^2 value when assessed against damage area, thus indicating that this metric displays the best correlation with induced damage. For a more complete

analysis, all the observed data were compiled and compared to each other. Figure 4.43 and Figure 4.44 show the damage area vs absolute value of charge and specific energy, respectively. It is clearly observed that a simple linear regression does not fit closely with the experimental data. Subsequently, various polynomial and power law fitting functions were assessed with their ability to fit the experimental data, and it was shown that the best fits were obtained by power laws.

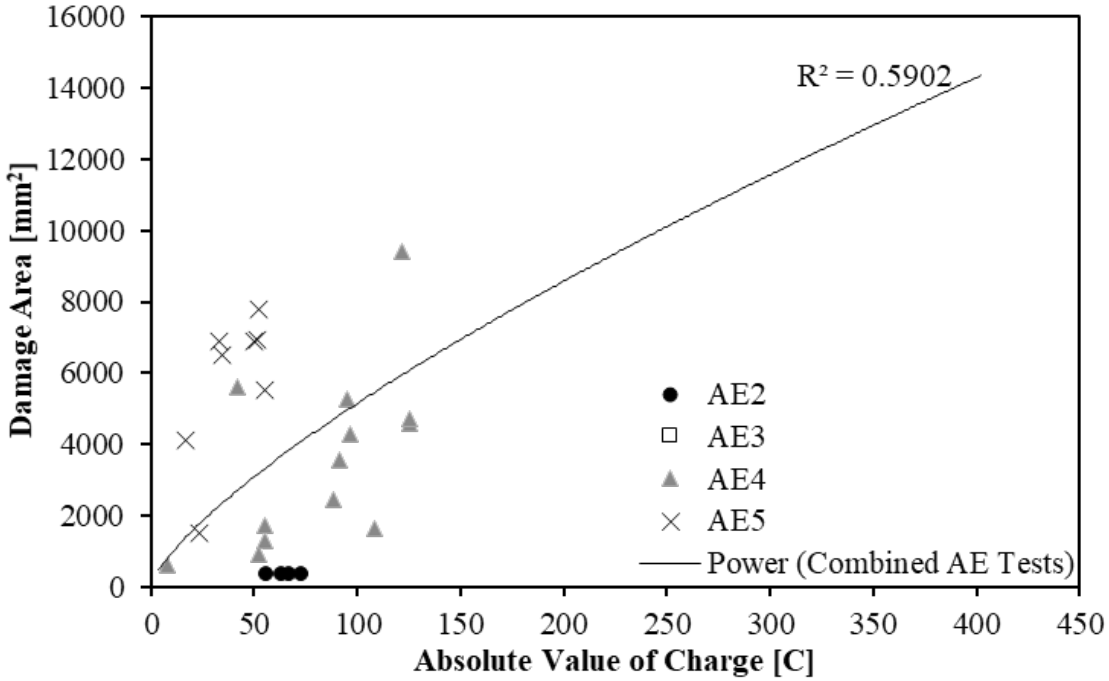

Figure 4.43: Regression analysis of damage area vs absolute value of charge with power law curve fit to all AE2-AE5 test specimens

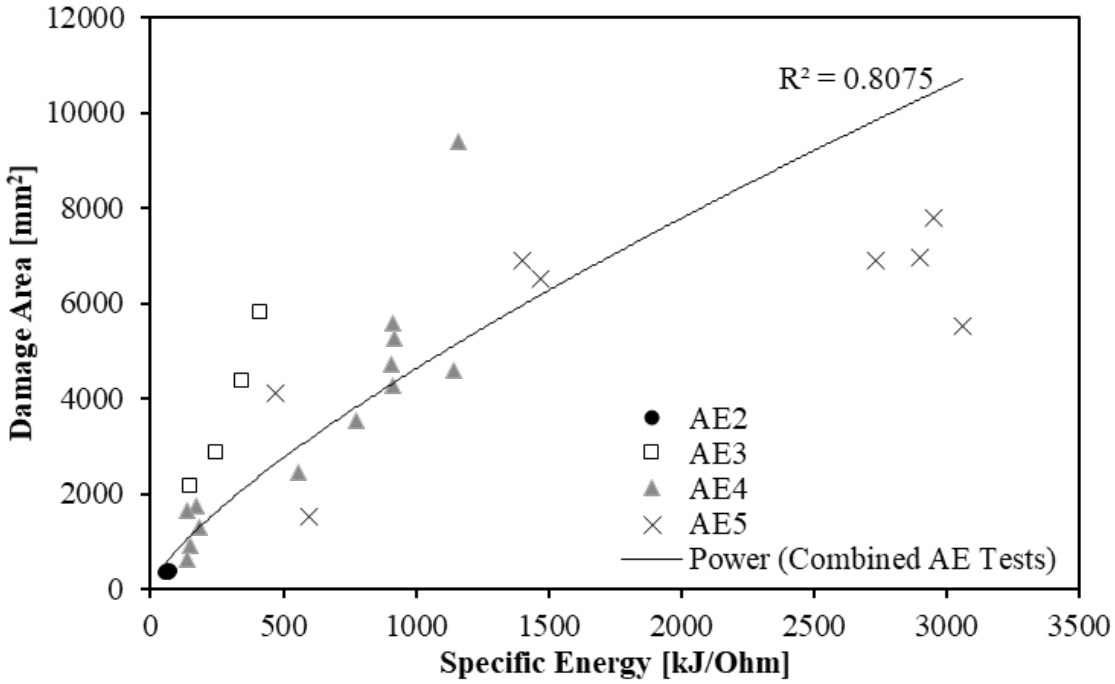

Figure 4.44: Regression analysis of damage area vs Specific Energy with power law curve fit to all AE2-AE5 test specimens

From Figure 4.43 and Figure 4.44 it is clearly seen that the best fit correlation coefficient (is obtained for Damage area vs Specific Energy with $R^2 = 0.8075$ against $R^2 = 0.5085$. This is important as the results indicate that the specific energy is more predictive of the damage area. Hence oscillating waveforms may be used where an impulse waveform is not achievable as the oscillating waveform is relatively easier to obtain ultimately offering a more straightforward means of lightning strike damage testing.

4.8 Summary

The results of lightning strike induced damage on UD CFRP laminates from four direct strike tests have been presented. The focus of this investigation was to determine the typical damage on UD CFRP materials. The lightning strike damage was evaluated by visual inspection, X-ray CT, and IR thermography to determine the induced damage from a simulated lightning strike. The results were categorized into 4 different types of damage seen: fibre breakage, resin burn off, delamination, and charring damage which were similar to previous tests on quasi-isotropic laminates [33], [35], [38], [42]. However, the damage shapes and sizes were very different to the quasi-isotropic results, as discussed in section 4.7.3, which showed that the damage propagated in the transverse direction. The reason for this was not confirmed but assumed to be due to the large electric field and the insulating nature of the UD CFRP. The electric field would increase until a critical event would trigger electric flow in other direction. This event is called electric breakdown and is discussed in section 2.4. This hypothesis is later evaluated in Chapter 5 through a finite element model. In addition to the damage inspections, surface temperatures on the laminate were recorded during the lightning strike tests. The temperature recordings also confirmed that the heat conducted in the transverse direction and held in that direction which led to the damage. The temperature recordings were also used to check the difference between the charring damage and the surface damage (i.e. fibre breakage and resin burnoff).

In the AE5 test, different surface treatments were assessed and was shown to have a large effect on the results similar to results previous studies on copper mesh [85] and surfaces which insulate the laminate such as paint [89].

A comparative study of the damage to absolute value of charge and specific energy was presented. The results indicated that the specific energy lightning parameter has a closer trend to the magnitude of the surface damage.

Chapter 5

Damage Modelling in CFRP Materials Subjected to Lightning Strikes with Electric Field Dependent Material Properties to Account for Dielectric Breakdown

5.1 Introduction

The modelling of a lightning strike on CFRP materials involves many complexities. Through an extensive literature review, it has been revealed that there are two main contributors to damage in CFRP materials due to lightning strikes: thermal damage and mechanical damage [34]. It has been found that the thermal effects due to Joule heating are the major contributor to damage in CFRP panels [34], [35], [39], [40], [46], [95], [96]. To accurately capture the physics of the induced damage, a fully coupled multi-physics modelling approach is required that includes the thermal, and electrical responses.

Chapter 4 has presented several experimental results which has been used to characterize the damage into four types: fibre damage, resin burnoff, delamination, and charred damage. Previous attempts during this PhD [143], [144], have predicted these events but whilst the predicted damaged areas matched the experimental observations in approximate size, it did not display the correct (as experimentally observed) features in terms of directionality relative to the fibre direction and shape. This suggested that the initial model proposed did not capture the key physics of the problem sufficiently accurately. As a consequence, the modelling approach was revisited and a more comprehensive multi-physics model was proposed, in which the electric field dependency was incorporated in the interaction between the fibres/layers and the laminate surface to simulate electric breakdown phenomenon. With this added complexity, only resin burnoff (or resin damage) was studied to determine the adequacy of the model with clear observation made from the X-ray CR scans in section 4.6.4. This revised model although more simplistic in its damage outputs, adds complexity by the addition of electric field dependent material properties. This approach is similar

to including temperature dependent material properties in the formulation. The model created here, and subsequent validation fulfil Research Objectives 2 and 3.

5.2 Modelling Framework

The key deliverable or outcome of this PhD project is a validated modelling framework that can predict lightning strike induced damage to a CFRP laminates and in turn use the results from the damage model to predict the loading response and residual strength. This approach can be achieved in various ways, but for this research, the developed modelling framework consists of a three-step modelling process. A diagram of the developed modelling framework is shown schematically in Figure 5.1. The three stages of the developed modelling approach are:

1. A coupled electrical-thermal meso-scale model (called the ‘Damage Model’), which for given material properties and lightning strike parameters can predict resin damage due to Joule heating.
2. Translate and transfer the meso-scale laminate damage predictions into a structural scale CFRP laminate panel or plate model representation. This is achieved by conducting what can be referred to as a point cloud transformation.
3. A structural model for the damage CFRP laminate. For this research, the damaged CFRP plate is modelled on the structural scale using geometrically nonlinear finite element (FE) analysis with an aim to simulate the load response, first ply failure and buckling behaviour of the damaged laminate when subjected to compression loading (considered as the critical design driver as explained previously in Chapter 2).

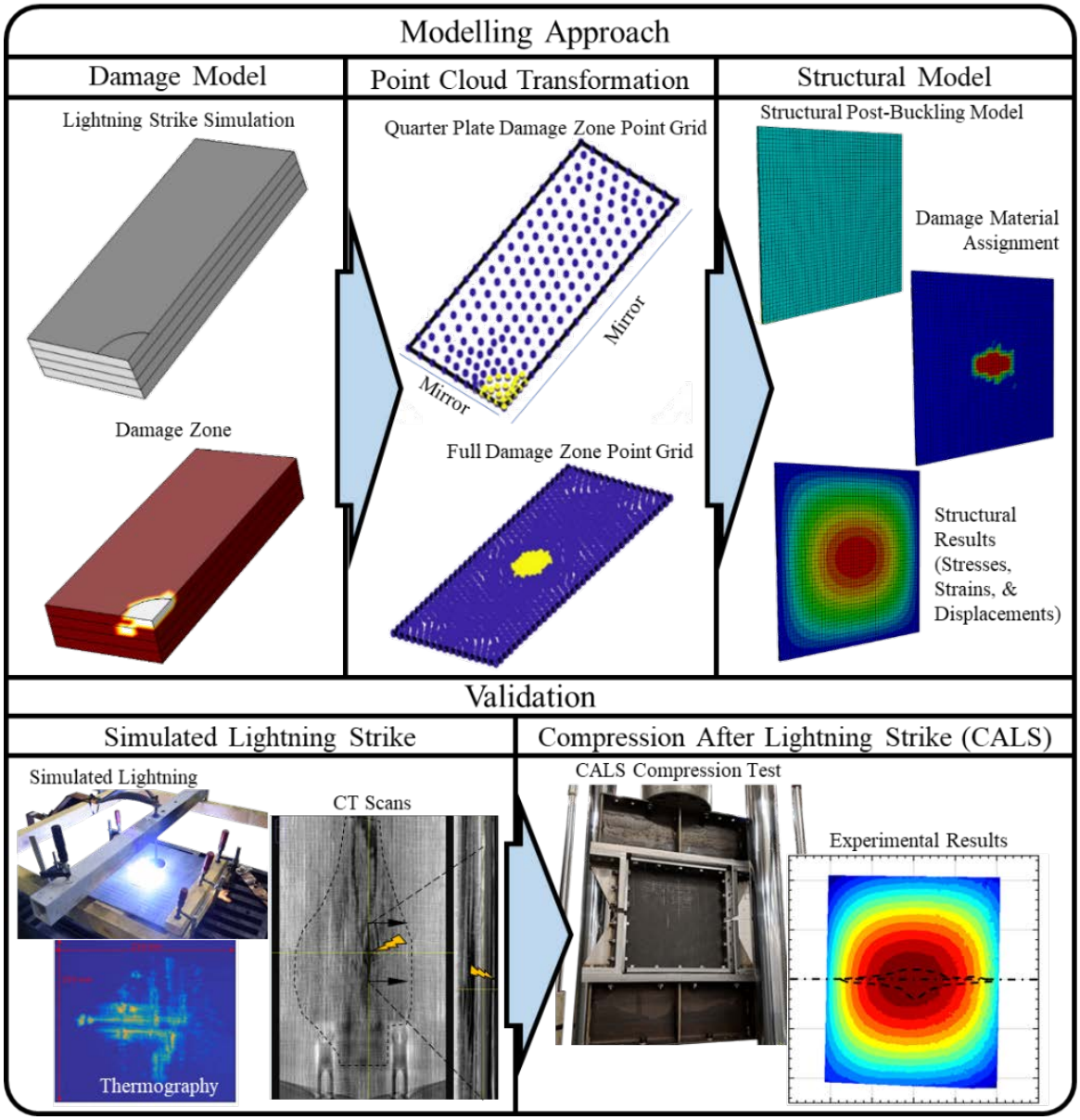

Figure 5.1: Modelling framework developed

The first stage of the modelling, i.e. the meso-scale damage model, involves a time dependent Joule heating finite element model, as it is assumed that the cause of damage can be linked to heating, whereas other sources of damage such as acoustic and electromagnetic shock (see section 2.4 and Figure 2.24 on page 29) are assumed to not contribute. The Joule heating response is simulated using a coupled time dependent multi-physics model which couples the electrical (Maxwell) and thermal (heat transfer) equations and solves these simultaneously to predict the heat response of the considered CFRP panels through time. The model has added complexity with electric and thermal dependency as well as resin damage predictions. The electric field dependency uses the electric field output to modify the electrical conductivity of the constituents. The modification is applied

when the electric field is greater than the breakdown strength[2] (physical unit of kV/mm). If the breakdown strength is exceeded, the conductivity is increased significantly to allow the conduction of electrons [145]. The temperature dependency uses the temperature outputs to change the thermal properties of the constituents, similar to previous studies [40]. Further to this, the predicted temperature evolution is used to determine damage through pyrolysis calculation/evaluation by adopting a pyrolysis model. The output of the model is the resin damage from the thermal effects.

Stage 2 of the developed modelling approach exports the predicted damage pattern/zones into a structural FEM of a representative CFRP panel/plate on a structure/component scale. The Damage Model (stage 1 of modelling approach) has been developed and executed through the maths and FE solver package COMSOL 5.4 [146] and the subsequent structural scale modelling of the lightning strike damaged CFRP laminated panel/plate was developed and executed using the FE package Abaqus 6.14 [147], with the damage predicted using the Damage Model imported into the structural scale FEM, see Figure 5.1. To link the Damage Model and structural scale FEM, or rather to translate the details of the predicted damage zone from the Damage Model to the structural scale FEM, the predicted damage zone is described in (or outputted as) a point cloud. The point cloud is mirrored in the x and y directions, Figure 5.1, to transfer the predicted damaged zone from the quarter laminate (meso-scale model) to a structural panel/plate FEM. The transfer is conducted using a specially written MATLAB [137] code, which imports the point cloud damage field data as a field variable into Abaqus.

The third step in the proposed methodology is the prediction of the structural response of a lightning strike damaged representative CFRP laminate panel/plate. In this context, representative means that the CFRP panel is scaled with respect to thickness, width, characteristic length, and mechanical load to closely resemble a CFRP wind blade sparcap laminate close to the blade tip, where the propensity for direct lightning strike is the highest (as discussed in Chapter 2, section 2.6). In the structural scale FEM, the material properties in the zones predicted to be damaged are changed from the undamaged state to assumed damaged properties. For simplicity, the zones that are predicted to be damage are simply attributed with zero stiffness in the structural scale FE model. Following this, geometrically nonlinear load response and postbuckling analyses were conducted using the structural scale FEM considering both undamaged and lightning strike damaged CFRP panels (representing a WT blade sparcap) subjected to compression. The results of structural modelling show degradation of stiffness and ultimately loss of strength due to lightning strike induced damage.

[2] Dielectric (breakdown) strength is measured as the maximum voltage required to produce a dielectric breakdown through a material. [145]

The predictions of the proposed meso-scale Damage Model have been validated through simulated lightning strike experiments, where the damage induced has been characterised using NDE techniques discussed in Chapter 3 and Chapter 4, i.e. visual inspection, X-ray CT imaging and IR thermography. To benchmark and validate the predictions of the structural scale FEM for representative CFRP laminate plates, plates that have been subjected to simulated lightning strikes have been subjected to compression loading testing in a new and specially developed (in this project) test called 'Compression After Lightning Strike' (CALS). In this test rig, the damaged CFRP panel specimens have been subjected to compression loading which ultimately led to buckling and post-buckling structural responses.

5.3 Lightning Damage Model

5.3.1 Joule Heating Formulation

A thermal-electric damage model has been implemented to determine the damage from heating imposed on a WT blade laminate due to a lightning strike. Thermo-electric models are able to show the effect of heating due to electrical current differences, also referred to as Joule heating or resistive heating. A Joule heating model is constructed by coupling of the Seebeck, Peltier, and the Thomson effects [148]. The time varying heat transfer equations are [148]:

$$\rho C_p \frac{\partial T}{\partial t} + \nabla \cdot q = Q$$
$$q = -\kappa \nabla T + PJ \qquad (5.1)$$

where ρ is the density of the material, C_p is the heat capacity, T is the temperature, t is time, q is the energy density heat flux, Q is the Joule heating equation ($Q = J \cdot \mathrm{E}$), κ is the thermal conductivity, P is the Peltier coefficient, and J is the current density.

The electric balance equations (or Maxwell equations) are [148]:

$$\nabla \cdot J = 0$$
$$\mathrm{E} = -\nabla \mathrm{V} \qquad (5.2)$$

where J is the current density, E is the electric field, and V is the electric potential. The related constitutive equations which are set for orthotropic materials are:

$$q = [P] \cdot J - [\kappa] \cdot \nabla T$$
$$J = [\sigma] \cdot (E - [S] \cdot \nabla T) \qquad (5.3)$$
$$Q = J \cdot E$$

where $[P]$ is the Peltier coefficient, $[\kappa]$ is the thermal conductivity, $[\sigma]$ is the electric conductivity, $[S]$ is the Seebeck coefficient.

5.3.2 Dielectric Breakdown

Typically, the input data for Joule heating models for CFRP composites are the continuum electrical and thermal properties corresponding to individual plies, which are most often UD. The data are then used for analysis of the response of multi-layer and multidirectional laminates. Most of the previous investigations that are available in open literature [39], [40], [108] address lightning strike damage effects in CFRP materials used for aerostructures which typically have laminates stacked in a quasi-isotropic layup making the electric and thermal responses closer to that of an isotropic material. Results obtained for quasi-isotropic laminate configurations would not be representative for laminates that are much more orthotropic, as e.g. a typical WT blade sparcap laminate. The quasi-isotropic laminate could mask important physical phenomena and damage that would be seen with UD laminates. Previous damage models found in literature [39], [40], [108] have not included the effect of the electric fields. Due to the absence of this, it is difficult to assess if the electric fields assumed or imposed in previous are large enough to produce electric breakdown.

Electric breakdown is a physical phenomenon that can occur when electric current flows through an insulator, and it only occurs when the electric field exceeds the breakdown strength [145]. Note that the breakdown strength is expressed in the unit kV/mm. In other words, any electric field applied that is less than the breakdown strength will not allow current through the insulator. For insulators (including air), this value is typically determined experimentally [145]. For fibre reinforced polymer materials, i.e. composite materials, the polymer resin is an insulator. The breakdown strength is included in the model developed in this project, such that an electric current can flow in directions other than the conductive fibre direction if a given threshold is met. This threshold is the electric breakdown strength. The breakdown strength for the composite laminate assembly is different in the transverse and through-thickness directions, as distribution and amount of polymer resin (epoxy in this case) are different in the 2 directions due to the manner in which the layered laminate stack is compacted, infused and consolidated. Therefore, there are two different conditions set based on whether the electric field can breakdown in the transverse direction, $\vec{E}_{bdT}$ and the through-thickness direction, $\vec{E}_{bdTT}$. Once the breakdown strength for that direction is exceeded, the electrical conductivity for that direction is changed to something suitably high. This can be seen in Figure 5.2. The red area indicates a region which the electric field has exceeded the through-thickness direction breakdown strength, the blue region has exceeded the transverse direction breakdown strength, and the grey region has an electric field that exceeds neither. The red

regions are associated with having larger conductivities in both the transverse and through-thickness directions. Therefore, a yellow line representing current flow can be seen flowing in both directions. In the blue regions only, the transverse direction is exceeded and accordingly only the current flow is in the transverse direction.

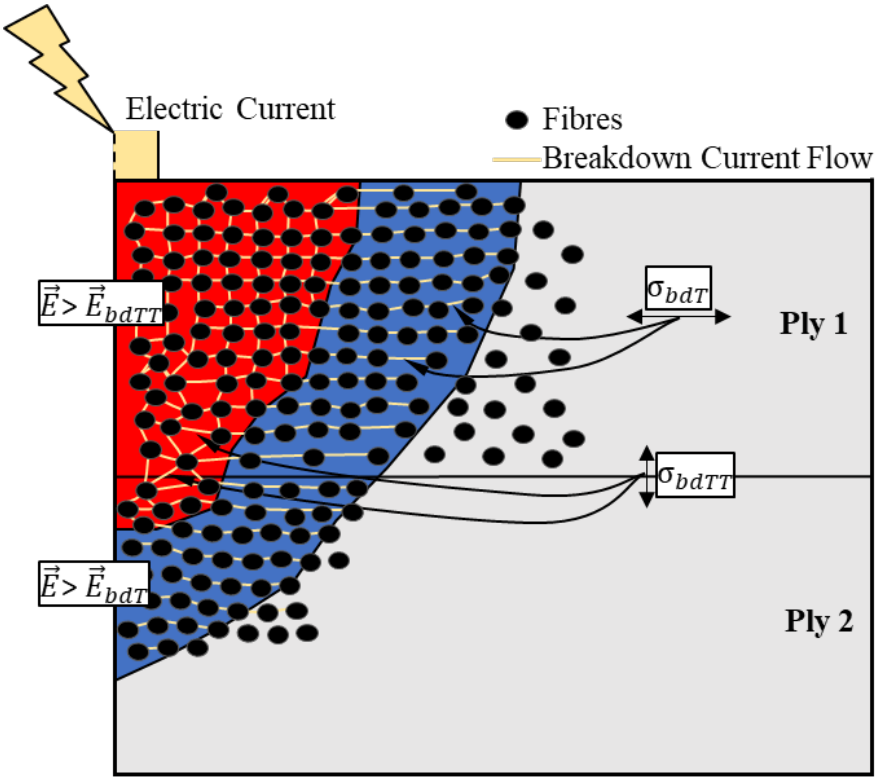

Figure 5.2: Surface discharge and electrical current paths considering the two different breakdown conditions: (Red) electric field greater than the breakdown strength in the through-thickness and transverse directions, and (Blue) electric field greater than the breakdown strength in the transverse direction

5.3.3 Plasma Channel

In traditional coupled thermal-electrical models, the plasma channel is most often considered to be a static channel, which applies current to the surface of a circular area with a certain radius, typically defined to be 10 mm [40]. However, experimental evidence [149] suggests that the radius changes during lightning attachment. Wang [149] has proposed an empirical equation to predict the diameter of the plasma channel, expressed in terms of the peak current and time, based on the Braginskii model:

$$r_p(t) = 0.97 \cdot I_{peak}^{1/3} t^{1/2} \tag{5.4}.$$

Equation (5.4) describes the expanding plasma channel where the peak current, I_{peak}, is in unit kA, the time, t, is in unit of μs, and the predicted plasma channel radius, r_p, is in millimetres [149]. Figure 5.3 shows the radius of the current at different times during the model.

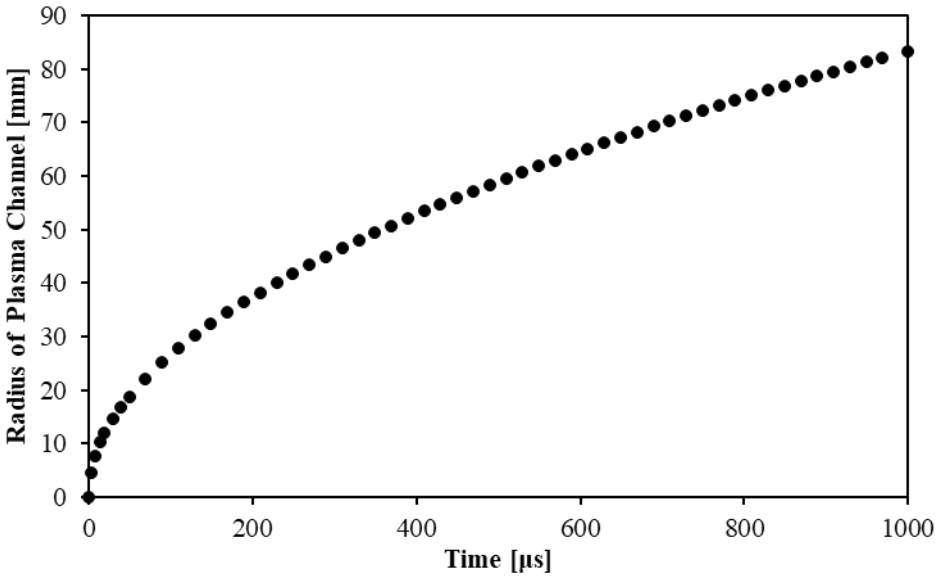

Figure 5.3: Radius change of plasma channel through time assuming Braginskii model [149] used in Damage Model

5.3.4 Pyrolysis Modelling

For the modelling framework developed for this research, a kinetic pyrolysis equation has been adopted to determine resin damage [150], expressed in terms of the degree of pyrolysis referred to as C. The degree of pyrolysis is typically defined as:

$$C = \frac{W_0 - W_i}{W_0 - W_t} \tag{5.5}$$

With the degree of pyrolysis attaining values between 0 and 1, where 1 indicates the material is completely burnt away and 0 indicates that no pyrolysis has occurred. In equation (5.5), W_i is the mass, W_0 is the initial mass, and W_t is the final mass. Taking the derivatives of C with respect to time t gives the rate of pyrolysis, which can be expressed as a nth-order chemical reaction kinetic equation, Bai [150]:

$$\frac{dC}{dt} = K(T)(1 - C)^n \tag{5.6}$$

where n is the reaction, and $K(T)$ is the reaction rate constant, which is described by the Arrhenius equation [40]:

$$K(T) = Aexp\left(-\frac{E_a}{RT}\right) \tag{5.7}.$$

In equation (5.7), A is the pre-exponential factor, E_a is the activation energy, and R is the gas constant equal to 8.314 J/mol/K. The activation energy for the Baxxodur epoxy resin used in the CFRP laminates was found to be 40 kJ/mol/K [39].

The pyrolysis behaviour for investigated CFRP material was evaluated using a thermogravimetric (TGA) analyser. The results of the TGA analysis are shown in Figure 5.4.

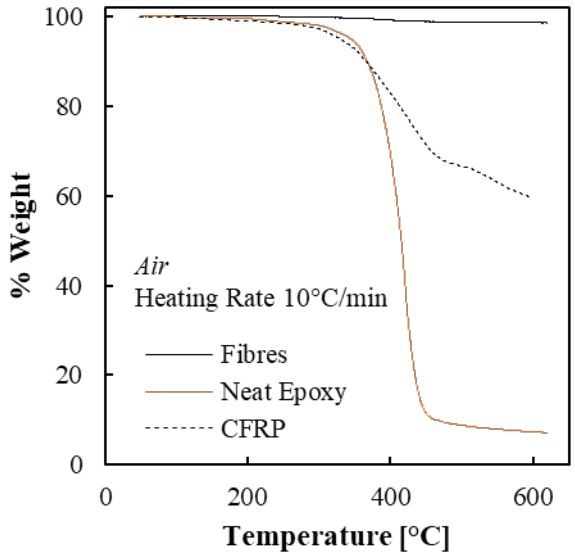

Figure 5.4: Thermogravimetric analysis results in air with heating rate of 10°C/min for the composite components used in this study. The results include all the carbon fibre/epoxy composite laminate with the "CFRP" being the infused laminate, the "Neat Epoxy" being the Baxxodur epoxy resin, and the "Fibres" being the Panex-35 fibres [142].

The integrated form of the pyrolysis equation is generally expressed as [150]:

$$C_{TOT} = 1 - \left((n-1)Aexp\left(-\frac{Q}{RT}\right)t + 1\right)^{\frac{1}{1-n}} \tag{5.8}$$

The so-called Scheil superposition principle [98] is commonly used to calculate pyrolysis during lightning strike events, and according to this pyrolysis equation can be expressed in the form [98]:

$$C_i = 1 - \left((n-1)Aexp\left(-\frac{Q}{R(T_{i-1}+T_i)/2}\right)t_i + 1\right)^{\frac{1}{1-n}} \text{ where } i = 1,2,\dots j \tag{5.9}$$

where T_i is the temperature at time t_i, C_i is the pyrolysis at time t_i. The time variable starts at t_0 with T_0 being the initial temperature.

5.3.5 Lightning Current Waveform

Figure 5.5 shows the currents used for the model as well as the experimental waveforms observed during the simulated lightning strike tests. As reported in Chapter 4 section 4.3.5, several tests were conducted for the AE5 test configuration (see Table 4.5 page 75). Bare surface specimens were used for comparison. The AE5 specimens were subjected to four different loading conditions. Here,

the experimental data obtained for the AE5-50, AE5-75, AE5-100, and AE5-125 tests were used for the current waveforms. A simplified current waveform was used for the model, which matched closely to the experimental waveform.

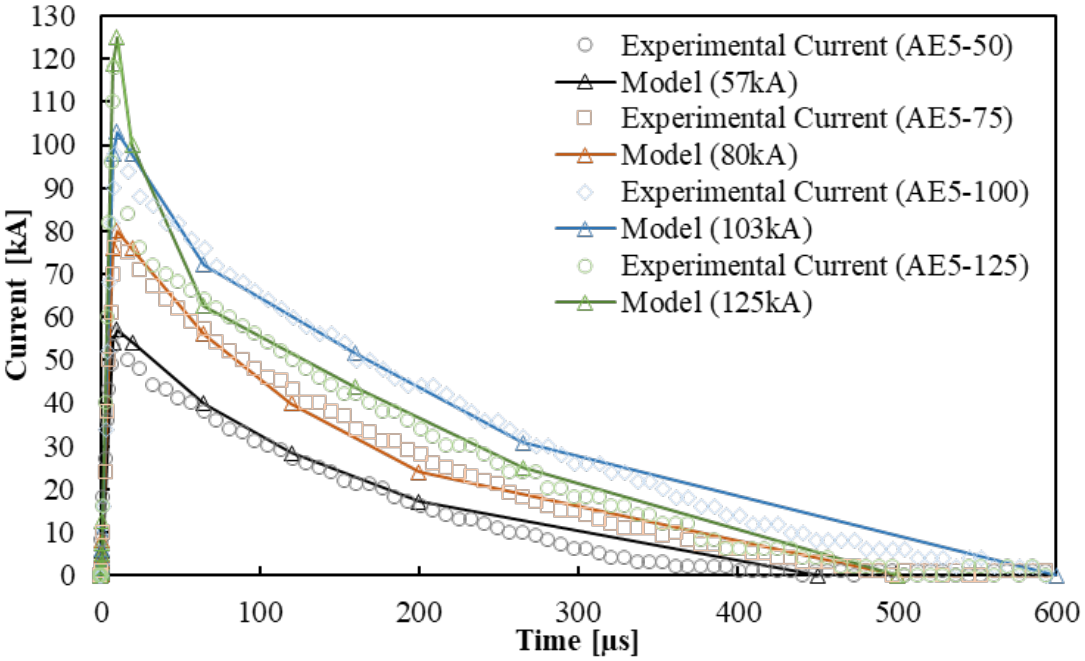

Figure 5.5: Simplified 10/350µs waveform used for modelling and experimental waveforms observed during simulated lightning strike tests AE5-50, AE5-75, AE5-100, and AE5-125.

5.3.6 Finite Element Model (FEM)

Figure 5.6 shows the geometry, boundary conditions, and mesh of the model. The CFRP composite panel specimens were made of carbon fibre/epoxy with an 8-ply unidirectional layup. The FE simulation reduced computation time by assuming the panel, the loading and the boundary conditions have 2 symmetry planes. Accordingly, symmetry conditions are imposed on the symmetry planes (xz and yz planes) as seen in Figure 5.6. This means that only a quarter plate FEM is considered. The dimensions of the quarter plate are 250 mm x 250 mm x 6.8 mm. The electric current is applied to the top surface of the model by imposing a normal current density, meaning that the current is orthogonal to the top surface of the plate. The imposed current density is calculated by finding the current at each time step (see Figure 5.5), and then dividing this by an assumed circular area (plasma tunnel radius) at each time step by adopting the radius, r_p, from equation (5.4).

In the FEM one side surface was grounded, where the copper grounds were used in the experimental study (section 4.3.5, Figure 4.8). The FE mesh has 33,815 continuum solid elements, see Figure 5.6. A fine mesh was implemented near the attachment point with element lengths of 1 mm, and a coarser mesh was implemented away from the attachment point with element lengths of

25 mm. Eleven elements were used through the thickness; 2 elements for ply 1,2 and 3 and 1 element through the thickness for the remaining plies.

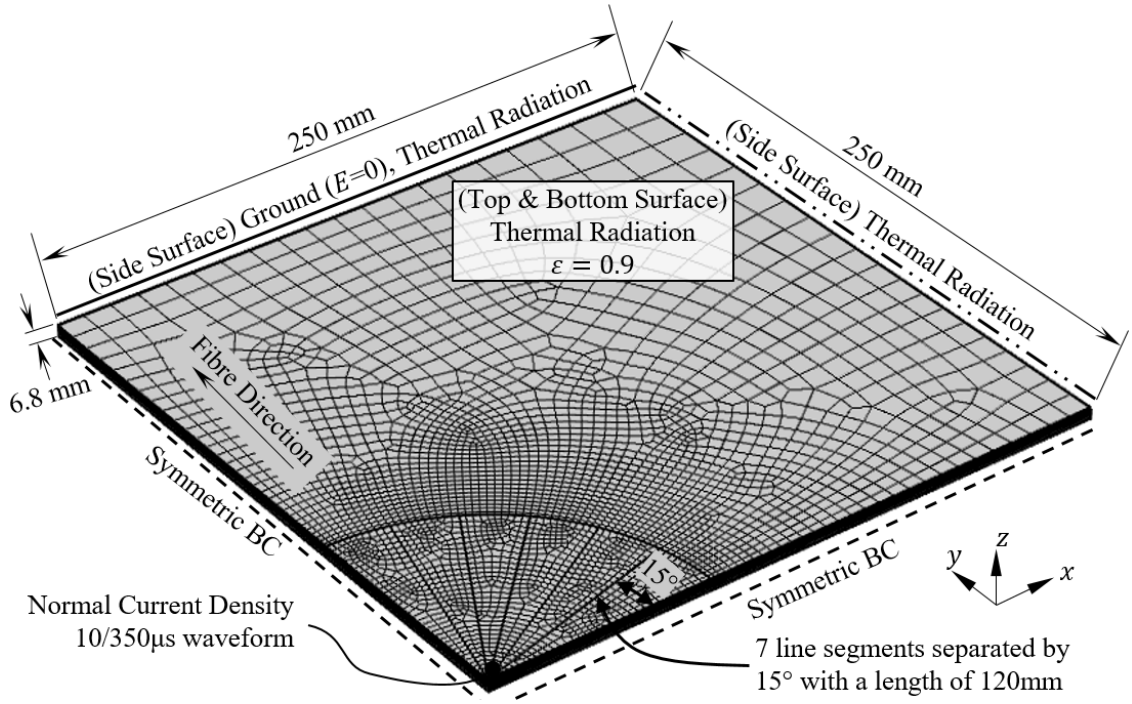

Figure 5.6: Quarter plate FE model with imposed boundary conditions

5.3.7 Material Properties

The properties of the CFRP material was assumed to be dependent on both the thermal and electric fields. The temperature dependent properties assumed for the mass density, specific heat, and thermal conductivities are quoted in Table 5.1 [142].

Table 5.1: Temperature dependent material properties used for the FE model [142]

Temp. $[°C]$	Specific Heat $C_p \left[\frac{J}{kg \cdot K}\right]$	Density $\rho \left[\frac{g}{cm^3}\right]$	Longitudinal Thermal Conductivity $\kappa_L \left[\frac{W}{m \cdot K}\right]$	Transverse Thermal Conductivity $\kappa_T \left[\frac{W}{m \cdot K}\right]$	Thru-Thickness Thermal Conductivity $\kappa_{TT} \left[\frac{W}{m \cdot K}\right]$
20	1350	1.5	10	0.77	0.87
80	1350	1.5	10	0.87	0.87
300	2100	1.1	10.5	1.5	1.5
3300	1900	1.1	12	2	2
>3300	6000	1.1	12	2	22

Based on the assumption of electric breakdown (section 5.3.2), the electric field dependency was added to the model. The electrical conductivities of CFRP materials can be described in terms of a symmetric second order tensor, with the material displaying 3 mutually perpendicular symmetry

planes thus making the material orthotropic. Accordingly, the principal electrical conductivities can be described in the form [142]:

$$\sigma = \begin{bmatrix} \sigma_L(\vec{E}) & 0 & 0 \\ 0 & \sigma_T(\vec{E}) & 0 \\ 0 & 0 & \sigma_{TT}(\vec{E}) \end{bmatrix} \tag{5.10}$$

where σ_L, σ_T and σ_{TT} are the electrical conductivities in the fibre (longitudinal – L), transvers (T) and through-thickness direction (TT), respectively, and $\vec{E}$ is the electrical field.

The electric breakdown is based on the discharge of air which is typically assumed to be 30 kV/mm [145], and this value is assumed as the electric breakdown in the transverse direction, i.e. $\vec{E}_{bdT}$ = 65 kV/mm. The through thickness electric breakdown is considered to $\vec{E}_{bdTT}$ = 200 kV/mm based on [151].

Table 5.2: Electric field dependent material properties [142], [145], [151]

State	Longitudinal Electrical Conductivity $\sigma_L \left[\frac{S}{m}\right]$	Transverse Electrical Conductivity $\sigma_T \left[\frac{S}{m}\right]$	Thru-Thickness Electrical Conductivity $\sigma_{TT} \left[\frac{S}{m}\right]$
$\vec{E} < \vec{E}_{bdT}$	22000	56	5.43
$\vec{E} > \vec{E}_{bdT}$	22000	110000	5.43
$\vec{E} > \vec{E}_{bdTT}$	22000	110000	110000

5.3.8 Damage Zones

The coupled thermal-electric model is used to predict the temperature evolution associated with a direct lightning strike event, and the predicted temperature field is used to predict the extent of resin pyrolysis that this causes. The extent of the pyrolysis determines the amount of damage inflicted. The simple flow chart shown in Figure 5.7 shows how damage is predicted.

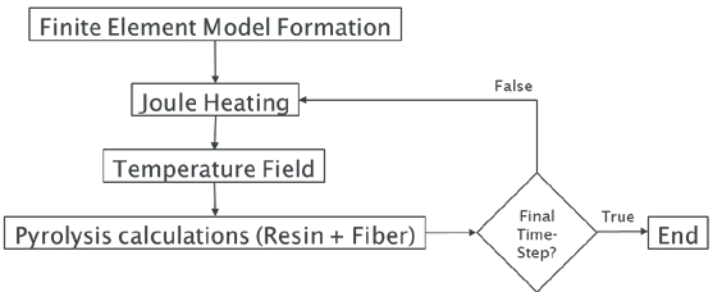

Figure 5.7: Damage Model flow chart

5.4 Damage Characterisation of Experimental Results

The validation compares the damage depth, shape, and size of the Damage Model, a conventional damage model and the experimental results from the AE5 bare surface test specimens (section 4.6.4). The results for the ply area are re-evaluated in this chapter for a better comparison between the FEM and the X-ray CT data. The areas when compared to the FEM are evaluated via a ply-by-ply basis because the proposed Damage Model uses continuum elements which are evaluated at the Gaussian points. Therefore, a method was devised to determine the results on a ply-by-ply basis rather than a slice by slice basis to provide a more accurate comparison of the results. The X-ray CT scans were separated into different volumes which represented a single ply. This was done by taking the total number of slices of the complete material volume and dividing by the total number of plies in the laminate. Then, the slices were evenly distributed over the total volume, thus leaving the resulting volumes as a representative volume of each ply. A representative image of this process is shown in Figure 5.8 on an example damaged specimen AE5-50-1. The 3D view of the CT image shows the full volume of the specimen with the coordinate system. The number of slices is typically measured in the z-direction as it represents the thickness dimensions of the specimen. The orange blocks represent an extracted volume of each ply which are used for further analysis. The extracted volumes represent the volume from a certain ply as shown by the $Ply_i\ Volume$ indicator where i is an index from 1 to the number of plies in the sample.

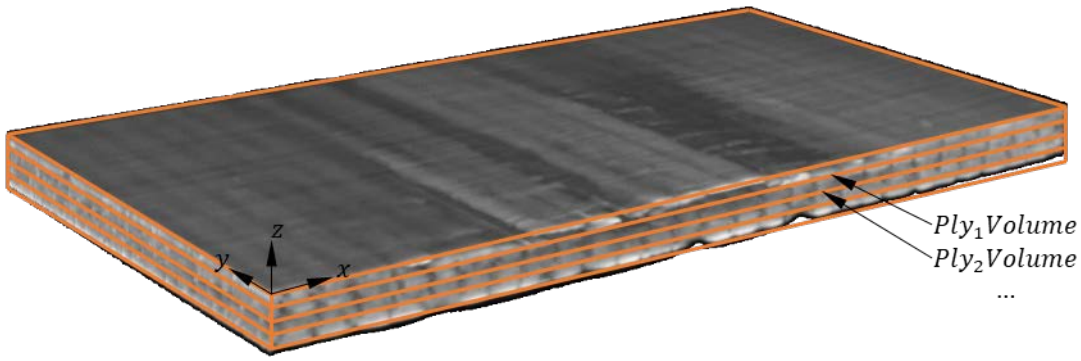

Figure 5.8: 3D greyscale image of X-ray CT volume for AE5-50-1 with overlays of the separated volume for individual plies in an orange colour (volumes are not to scale)

Each ply volume was processed through an "Average intensity ZProject" process. This process simply adds the grayscale values from each voxel in the z-direction and divides the sum by the number of slices as indicated in equation (4.4). An example of a typical ply volume showing the directions are shown in Figure 5.9 (a). The volume is made up of voxels with differing greyscale values representing the density of the material at that location.

$$v_{ply_j}(x,y) = \sum_{i=1}^{n} \frac{v_j(x,y,z_i)}{n} \tag{5.11}$$

where v_{ply_j} are the pixel values at ply number j, v_j are the voxel values of the full ply j's volume in the x, y, and z locations, i is the index of the volume values in the z direction, and n is the total number of voxel values in the z direction.

The Average intensity ZProject produces a 2D image representing an average intensity greyscale value of the ply which is used as a representative image of the ply to determine damage. An example of the results is shown in Figure 5.9 (b) for ply 1 from test specimen AE5-50-1. This 2D image can be separated into damage and non-damaged regions as indicated by the red area overlaid on the average intensity ZProjected image. The number of pixels in this damaged region can be counted and multiplied by the spatial resolution squared to produce the total damage area for the ply.

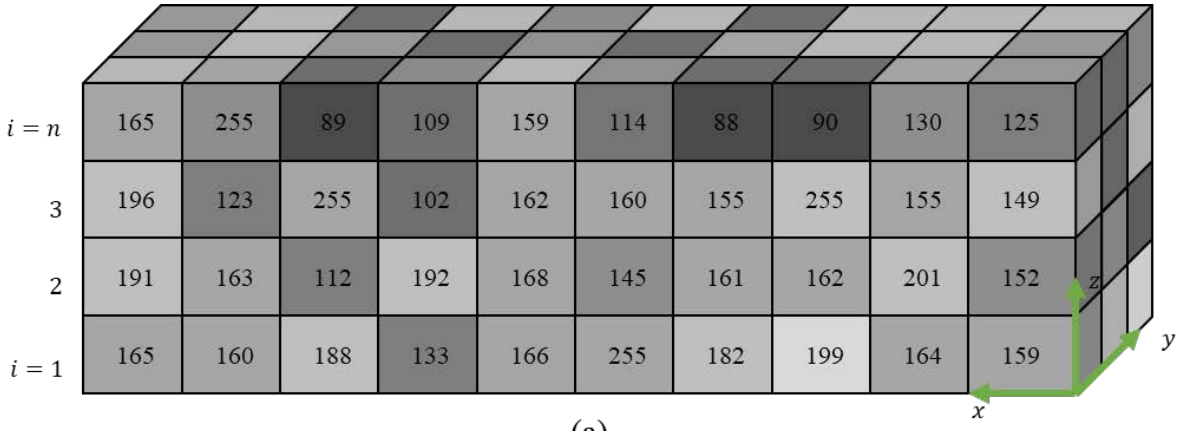

(a)

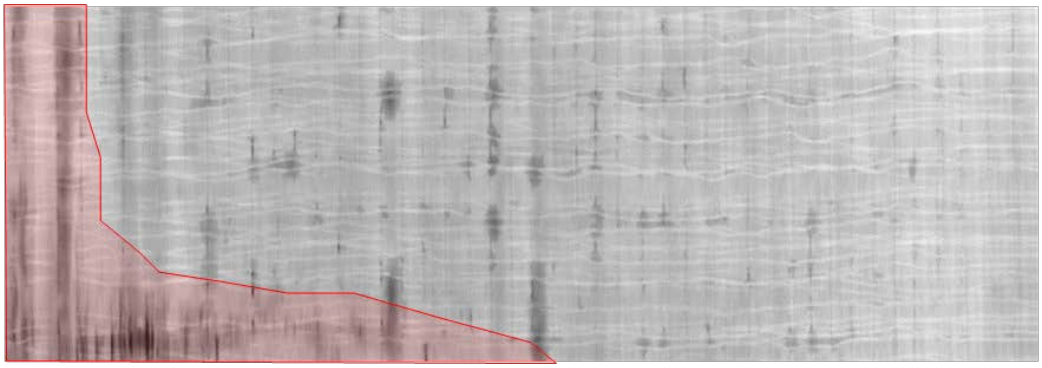

(b)

Figure 5.9: (a) A pictorial description of voxels with values from a representative X-ray CT ply volume showing the directions and (b) the result of the Average intensity ZProject on the ply 1 volume from AE5-50-1 with a polygon selection of the damaged area shown in red

5.5 Model Validation and Comparison to Conventional Damage Model

The model validation conducted is based on the experimental results obtained from the simulated lightning strike experiment AE5 as defined in section 4.6.4. The model validation and benchmarking also considers predictions obtained using a more conventional damage model, which adopts a coupled thermal-electrical Joule heating model with temperature dependency, but without inclusion of the electric field breakdown effect. The traditional model was executed in the same model COMSOL framework, but with the breakdown strengths $\vec{E}_{bdT}$ and $\vec{E}_{bdTT}$ set to very high values of 10^{20} kV/mm, to ensure that no electric field dependency was initiated.

5.5.1 Comparison of Electric Fields

The main effect of including electric field dependent material properties in the modelling is that the electric field is limited to the excessive build up and this enables current flow in the transverse and through-thickness direction when the critical breakdown strength values are exceeded. Figure 5.10 plots the results from the maximum electric field on the surface in both the proposed damage model and conventional damage model. The plot is shown on two y-axes with the axes being an order scaled to be an order of magnitude different from each other. The plot shows that the conventional model's and proposed model's maximum electric field has the same shape as the electric current waveform being applied. This is to be expected as the electric field is driven by the current. However, the interesting result shows that the electric field dependency dramatically reduces the electric field output by an order of magnitude. At time just before and after the peak current (10 µs), there is a noticeable shift in the electric field being stunted due to the increased electric conductivity.

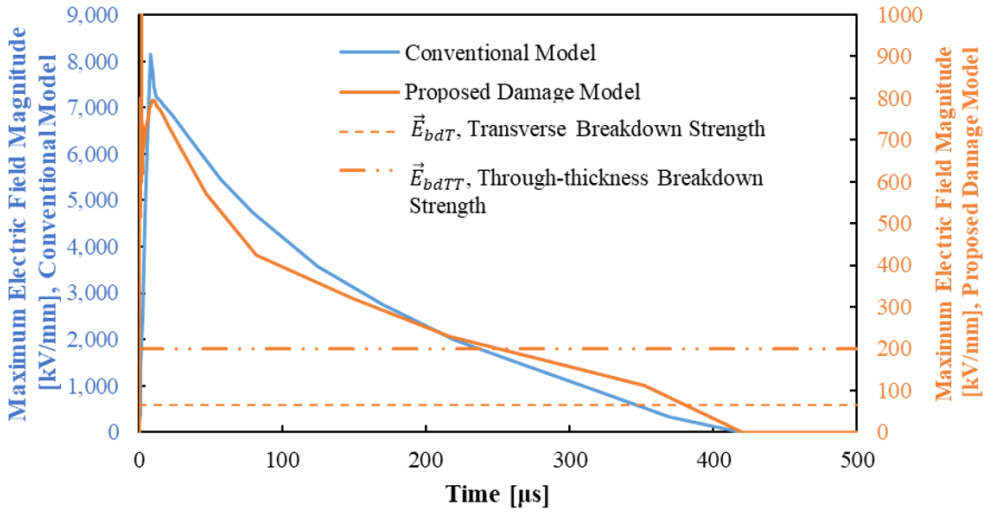

Figure 5.10: Predicted maximum electric field amplitude on the top surface of the specimen with different breakdown strengths – predicted by the electric field dependent and conventional damage models

5.5.2 Comparison of Temperature Profiles

The increase in electric conductivity when electric breakdown has occurred reduces the amount of Joule heating. The electric field dependencies still have temperatures in the range seen by previous models, which is mainly due to the temperature dependency affecting the results. However, since the electric current is now allowed to spread, there are dramatically different results in the temperature profile. A temperature profile is taken from the centre of the attachment point in the radial direction to 120 mm away for both the conventional and proposed Damage Model as shown in Figure 5.6. The temperature profile shows how the heat responds to the electric current input. Figure 5.11 - Figure 5.13 show the predicted temperature profiles. Changing the probing angle from the fibre direction to the transverse direction show significant differences in temperature responses. Figure 5.11 shows the temperature profile in the fibre direction. The conventional model shows heat built up over the whole probe line and the proposed Damage Model shows a smooth but dramatic lowering of the heat from 3000°C to 300°C approximately 30 mm to 80 mm. Figure 5.12 shows the 45° angle temperature probe line. The temperature profile for the 45° angle probe line shows the conventional model has a temperature response which mimics a step function where the heat is high for the first 30 mm and then a sharp drop of heat response back to near ambient temperature. For the proposed damage model, the temperature is high for the first 35 mm and smoothly but dramatically reduces in temperature. The probe line results from Figure 5.12 can help explain the results in Figure 5.14 where the transition from Joule heating to no Joule heating predicted by the conventional model is observed in the damage pattern. This lack of transition in the presences of a very high electric field leads to inaccurate results. Figure 5.13 shows temperature profiles in the transverse direction (90°). This plot clearly shows the width of the channel the current takes in the conventional model from the heat results. The heat results are significantly high for the first 20 mm and only drop to ambient temperature the further away from the attachment point. The proposed Damage Model shows high temperatures for the first 60 mm and then a smooth transition to lower temperatures extending to the end of the 120 mm probe line. It is also shown for Figure 5.11 - Figure 5.13 that the heat stays in the same location for the conventional model which is indicated by the unchanged magnitude of heat throughout time. Whereas, the proposed Damage Model has an increase in the heat response over time due to the increase in conduction in the transverse direction. This is the reason for the damage pattern spreading in the proposed Damage Model and the lack of spreading in the conventional model. It should also be noted that there is a large difference, about an order of magnitude, between the model temperature predictions compared to the AE5 specimen temperature measurements; see Figure 4.34. A significant contributing factor is that the maximum recordable temperature is 692°C for the camera. In Figure 4.34 it is observed, that this leads to a truncation of the temperature measurements

immediately after the lightning strike and hence affects the appearance of the rate of decay of the temperature.

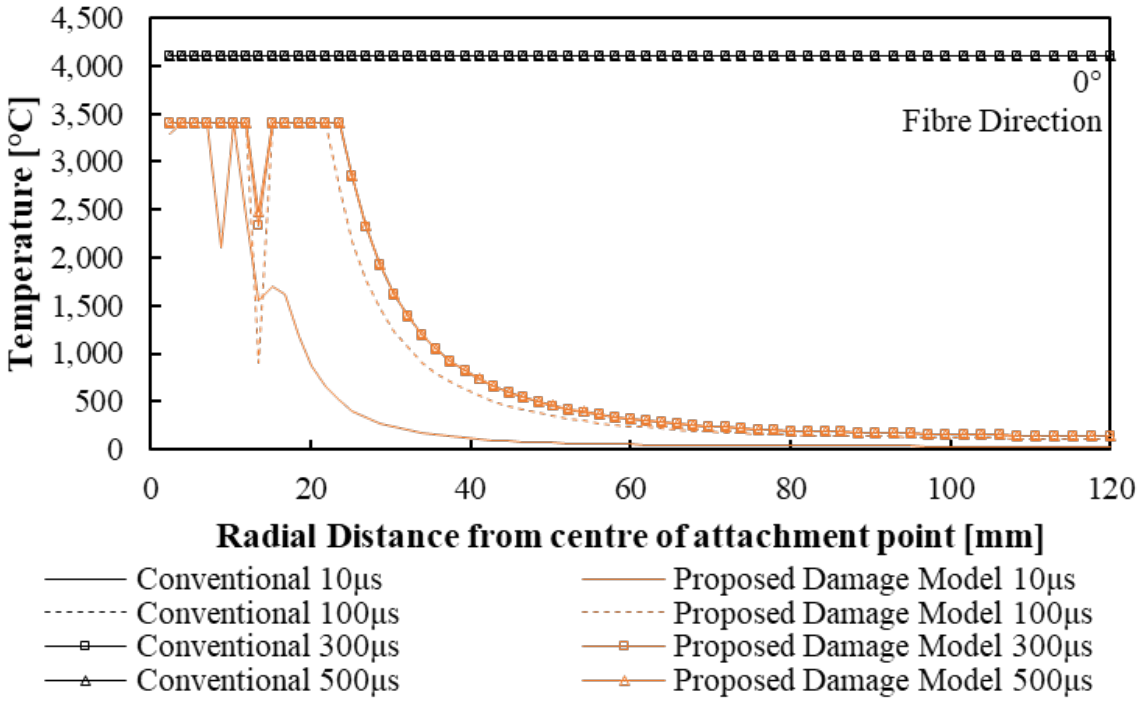

Figure 5.11: Electric field and conventional model predictions: 0° temperature profile from centre of the attachment point to 120 mm radial distance away

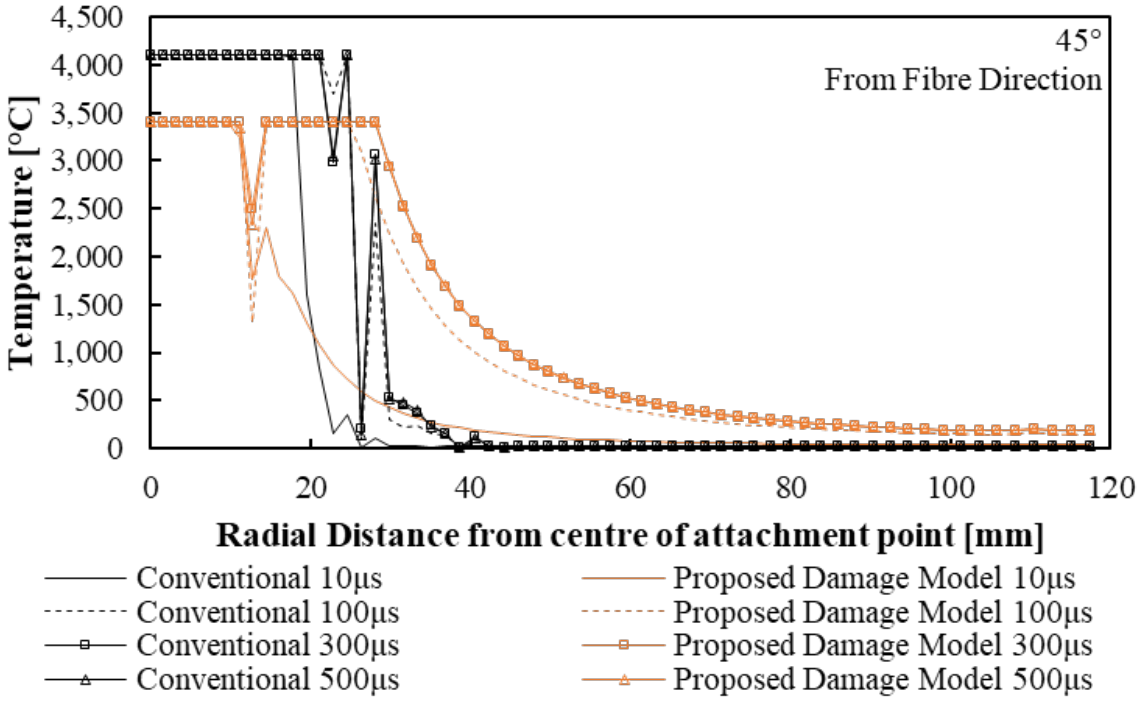

Figure 5.12: Electric field and conventional model predictions: 45° temperature profile from centre of the attachment point to 120 mm radial distance away

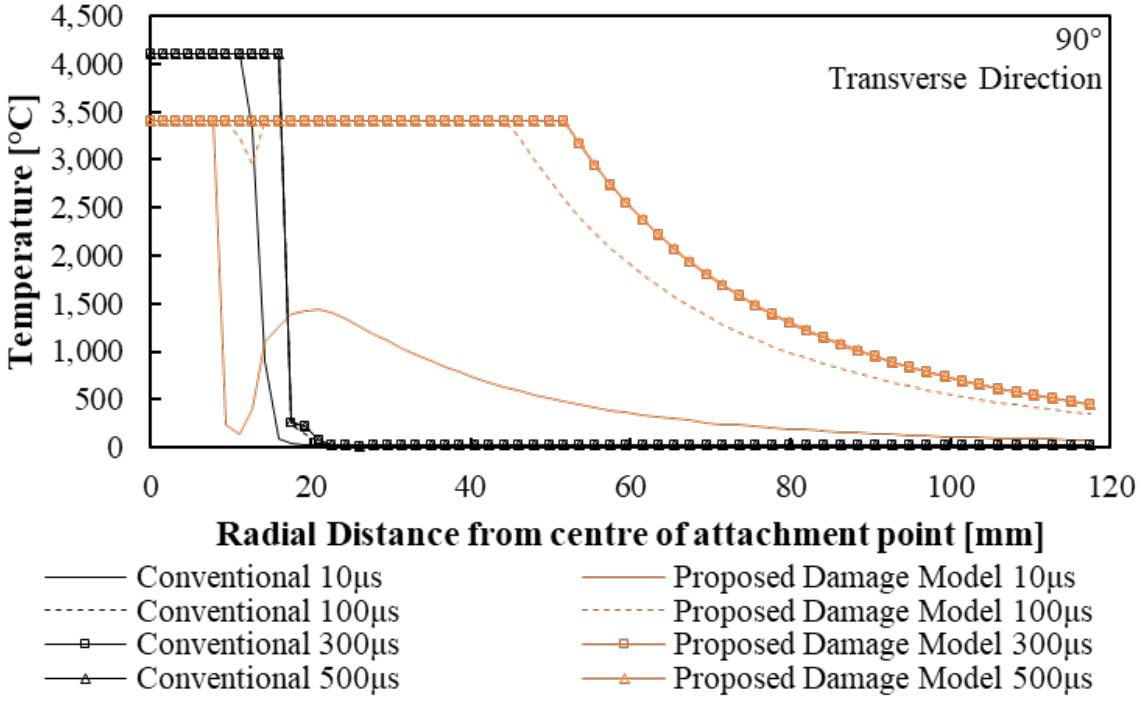

Figure 5.13: Electric field and conventional model predictions: 90° temperature profile from centre of the attachment point to 120 mm radial distance away

5.5.3 Ply Damage Overview

The electric field model was validated through comparing the model predictions to X-ray CT scans obtained for specimens AE5-50-1 and conventional model with no electric field dependency. The results are presented in Figure 5.14. The comparison shows that the proposed Damage Model has a better match in the transverse direction. There is a lack of damage in the vertical direction and can be seen that the conventional model has a better prediction in this region. However, it is also shown that there is more damage in the depth of the model as indicated by the ply 4 damage present for the conventional model and none in the X-ray CR and proposed Damage Model.

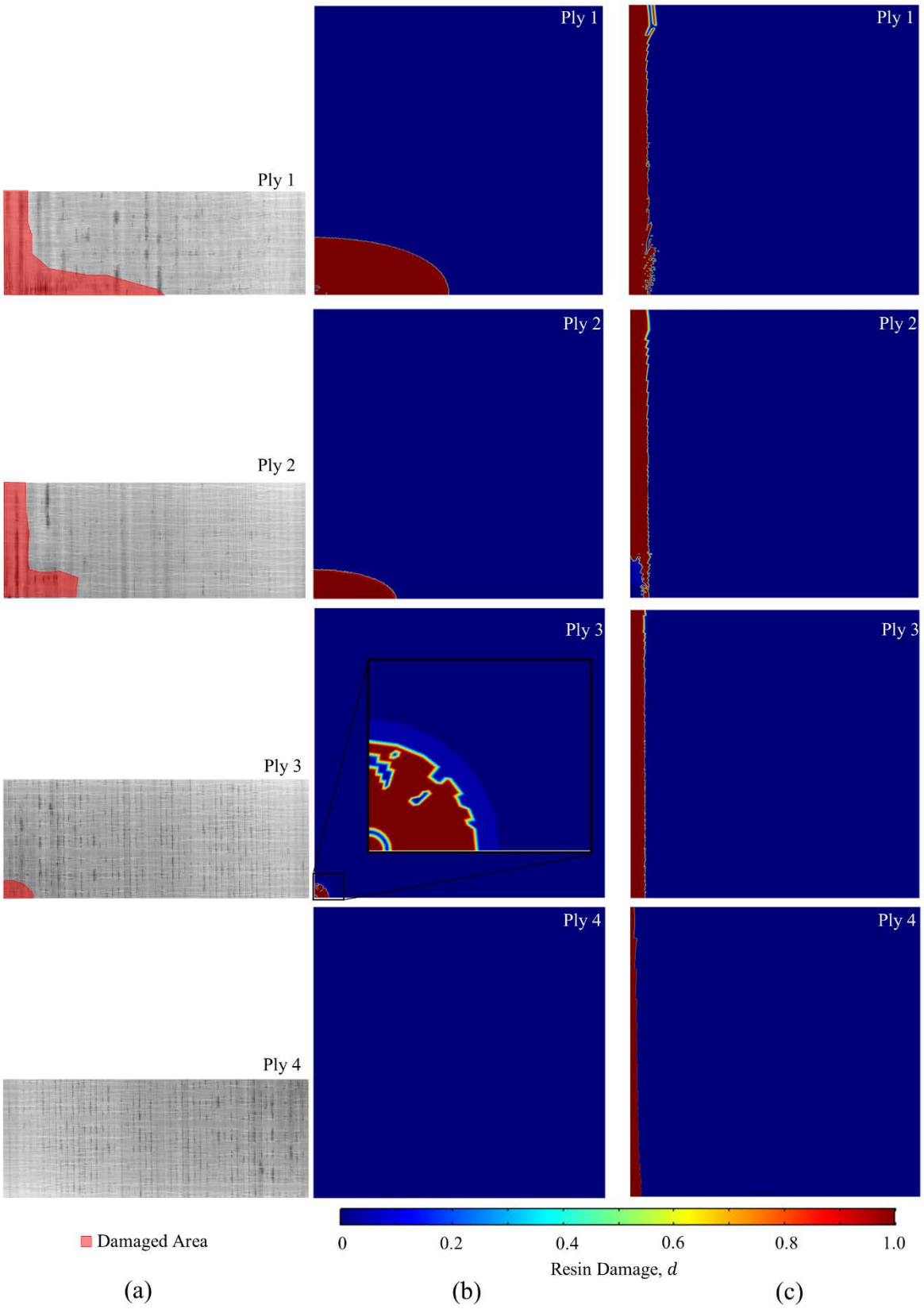

Figure 5.14: Comparison of X-ray CT results vs FE predictions: (a) X-ray scan ply images for specimen AE5-50-1, (b) FE predicted ply damage, and (c) FE predictions for conventional Joule heating model

5.5.4 Damage Depth

Figure 5.15 shows the damage depth profile from the centre of the attachment point extending in the transverse direction. Two damage model predictions are presented: the electric field dependent Damage Model and the conventional model. These predictions are compared to the X-ray CT data obtained for specimen AE5-50-1 in Figure 5.15. It is observed that the conventional model overestimates the damage depth by 1.7x times the experimental value. The proposed electric field dependent Damage Model was less than 8% different than the experimental value. The damage depth also spread in the transverse direction by over 5 times more than the conventional model. The spread was much closer for the proposed Damage Model with 25% error when compared to the experimental data and the conventional model was 4x times less spread in the transverse direction to the experimental data and resulted in 77% error.

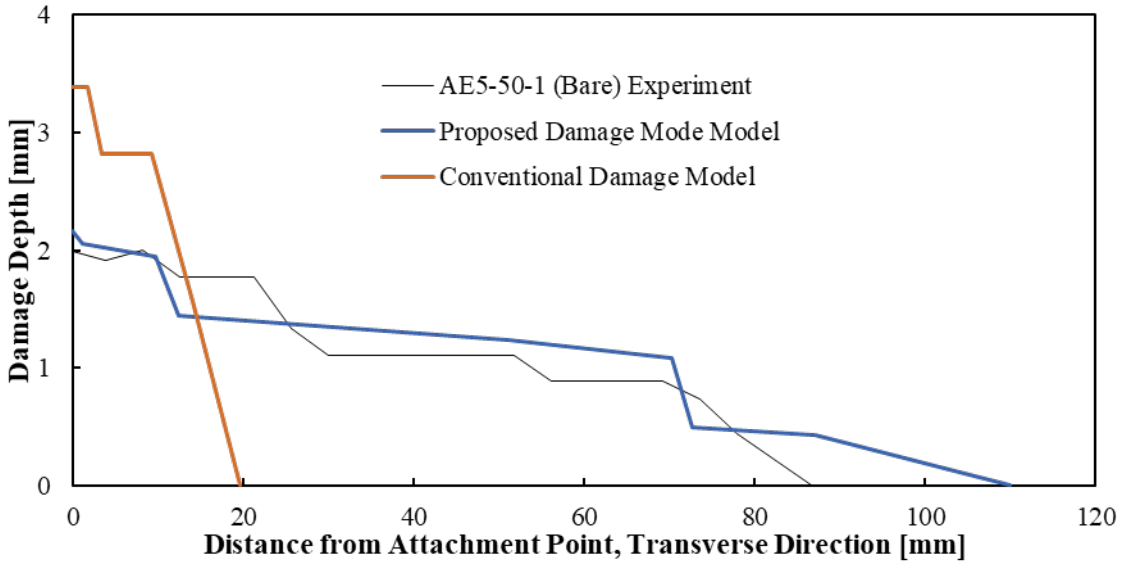

Figure 5.15: Damage depth of model prediction compared to experimental values and traditional damage model

5.5.5 Model Validation Summary

The damage areas of multiple plies have been presented and have shown the ability for the proposed electric field Damage Model to accurately predict the movement in the transverse direction, especially in comparison to the conventional model. Not only has this presented better results but the damage depth has shown that the proposed Damage Model produces much more accurate representations of the damage in both magnitude and shape.

5.6 Results

Five different modelling cases were evaluated to determine the size, depth, and shape of the damaged zone corresponding to 4 different assumed peak current values: 50, 75, 100 and 125 kA for bare surface specimens.

5.6.1 Electric Field Results

Figure 5.16 presents the maximum electric field on the top surface of the model for all the simulated cases. The figure presents that with increasing peak amperage there is a linear increase in the electric field on the surface. This indicates that the electric field breakdowns and allows for the conduction in the transverse and through-thickness directions but on the top surface the electric field is still primarily driven by the current density on the top surface.

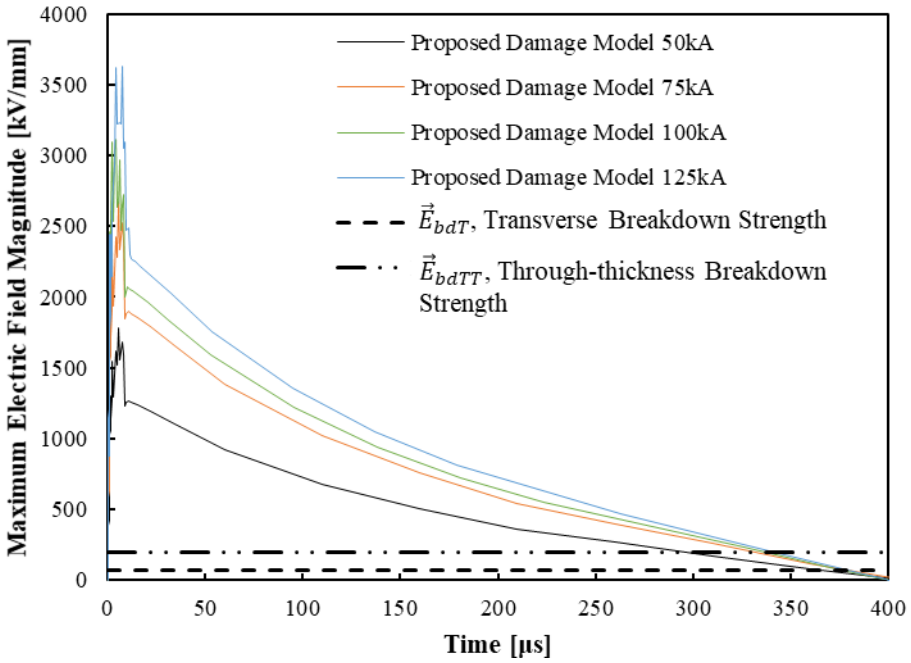

Figure 5.16: Predicted maximum electric field magnitude on the top surface of the specimen for 50, 75, 100, and 125 kA peak current

To understand the difference in breakdown, Figure 5.17 - Figure 5.20 present where the magnitude of the electric field exceeded the two different breakdown conditions; $\vec{E}_{bdT}$ and $\vec{E}_{bdTT}$. Figure 5.17 presents the 50 kA breakdown simulation at the peak current or $t = 10\ \mu s$. Figure 5.17 (a) shows the transverse direction breakdown. It indicates that the transverse direction breakdown develops in 4 plies with the largest spread resulting in ply 3. The primary spread for this breakdown is in the transverse direction and is within the 140 mm circular probe. Figure 5.17 (b) shows the through-thickness direction breakdown. This plot indicates that the through-thickness breakdown develops in 3 plies with the largest area of the breakdown on ply 1.

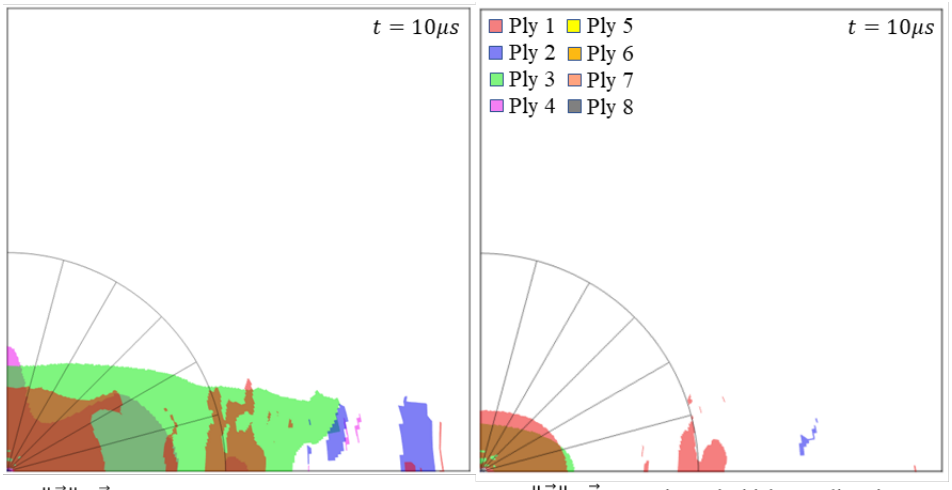

Figure 5.17: Predicted electric field magnitude for the 50 kA model that exceeds (a) the transverse direction breakdown strength and (b) the through-thickness direction breakdown strength by all plies in the laminate

Figure 5.18 presents the 75 kA breakdown simulation at the peak current or $t = 10\ \mu s$. Figure 5.18 (a) shows the transverse direction breakdown. It indicates that the transverse direction breakdown develops in 4 plies with the largest spread resulting in ply 2. This breakdown spreads in more of a rectangular area which almost envelops the entire sample. Figure 5.18 (b) shows the through-thickness direction breakdown. This plot indicates that the through-thickness breakdown develops in 3 plies with the largest area of the breakdown in ply 2. The through-thickness direction is dramatically reduced from the transverse direction. The shape in the through-thickness direction is elliptical with the major axis in the transverse direction.

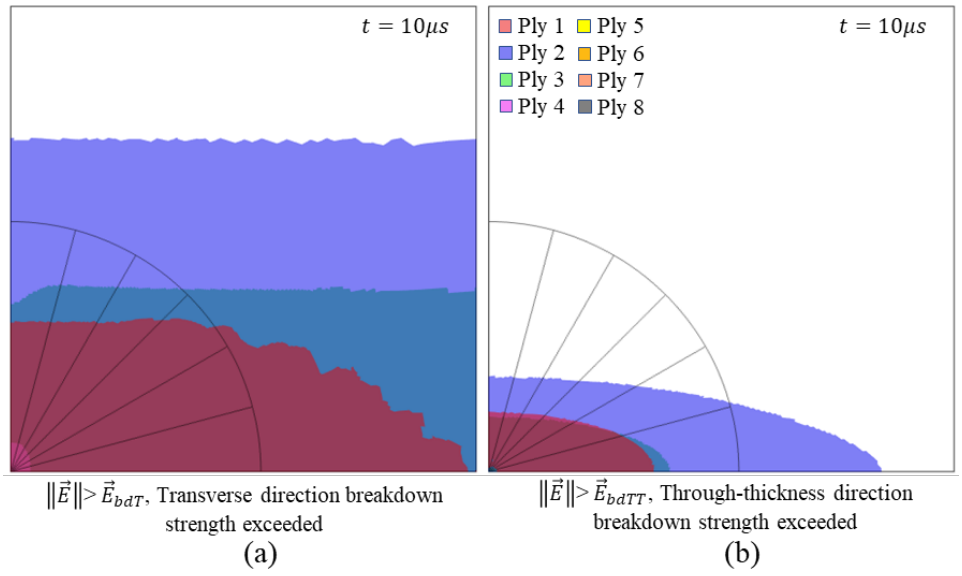

Figure 5.18: Predicted electric field magnitude for the 75 kA model that exceeds (a) the transverse direction breakdown strength and (b) the through-thickness direction breakdown strength by all plies in the laminate

Figure 5.19 presents the 100 kA breakdown simulation at the peak current or $t = 10\ \mu s$. Figure 5.19 (a) shows the transverse direction breakdown. It indicates that the transverse direction breakdown increased the area over the 75 kA model and develops in 5 plies with the largest spread resulting in ply 2. This breakdown spreads in more of a rectangular area which almost envelops the entire sample. Figure 5.19 (b) shows the through-thickness direction breakdown. This plot indicates that the through-thickness breakdown develops in 3 plies with the largest area of the breakdown in ply 2. The through-thickness direction is dramatically reduced from the transverse direction. The shape in the through-thickness direction is elliptical with the major axis in the transverse direction.

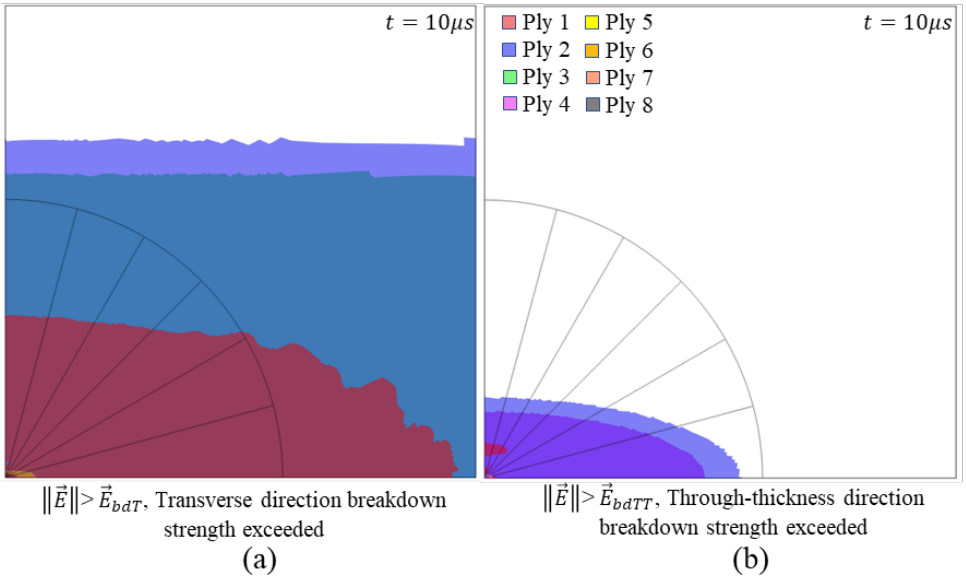

Figure 5.19: Predicted electric field magnitude for the 100 kA model that exceeds (a) the transverse direction breakdown strength and (b) the through-thickness direction breakdown strength by all plies in the laminate

Figure 5.20 presents the 125 kA breakdown simulation at the peak current or $t = 10\ \mu s$. Figure 5.20 (a) shows the transverse direction breakdown. It indicates that the transverse direction breakdown increased the area over the 75 kA model and develops in 5 plies. It also increases the area of ply 4 and ply 5 breakdown. Similar to the previous 75 kA and 100 kA results, the transverse breakdown spreads in more of a rectangular area which almost envelops the entire sample. Figure 5.20 (b) shows the through-thickness direction breakdown. This plot indicates that the through-thickness breakdown develops in 4 plies with the largest area of the breakdown in ply 4. The through-thickness direction is dramatically reduced from the transverse direction. The shape in the through-thickness direction is elliptical with the major axis in the transverse direction.

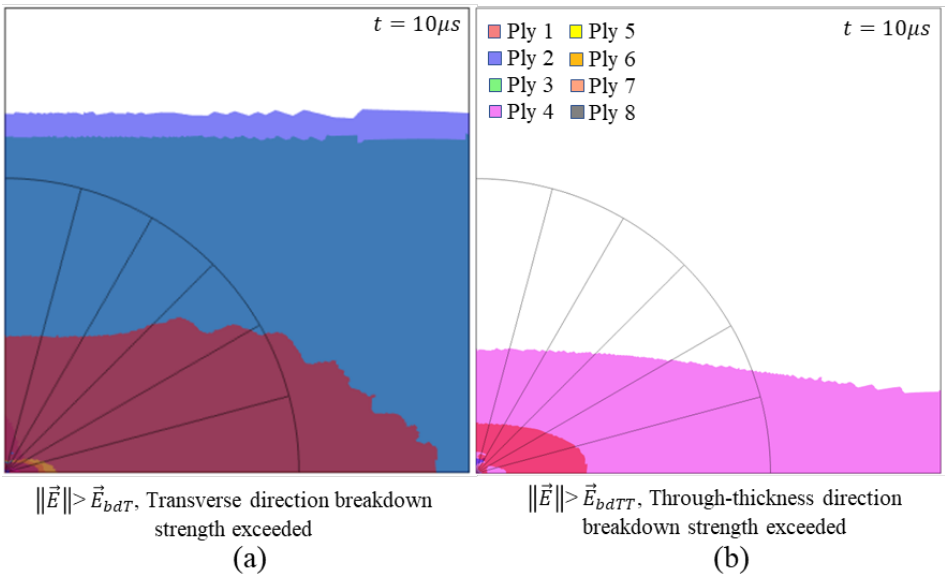

Figure 5.20: Predicted electric field magnitude for the 125 kA model that exceeds (a) the transverse direction breakdown strength and (b) the through-thickness direction breakdown strength by all plies in the laminate

5.6.2 CFRP Laminate Damage Predictions

In this section the damage predicted by use of the electric field dependent Damage Model is presented for a bare surface CFRP laminate configuration. The simulations were conducted for four different lightning strike cases: 50, 75, 100, and 125 kA (Figure 5.5). For all cases, the shape of the predicted damage was elliptical, with the major axis being in the transverse direction, and the minor axis aligned with the fibre direction. This is similar to the experimental observations, as seen in e.g. Figure 4.30 where the damage is greater in the transverse direction (x-axis) rather than the longitudinal direction (y-axis). Figure 5.21 shows the full damaged regions from the developed model for the 4 different lightning strike cases. Figure 5.21 (a) shows the 50 kA damage results. The damage shows the elliptical damage with the major axis being in the transverse direction and the minor axis aligned with the fibre direction. The length of the major axis is approximately 140 mm. Figure 5.21 (b) shows the 75 kA damage results. A similar shape appears as the 50 kA damage with a slightly elongated minor axis. Figure 5.21 (c) shows the 100 kA damage results. A similar damage shape appears as the 75 kA and 50 kA, but the major axis reduces slightly to about 125 mm and the minor axis increases slightly. Figure 5.21 (d) shows the 125 kA damage results. A similar damage shape appears as the 100 kA damage with a slightly increased minor axis.

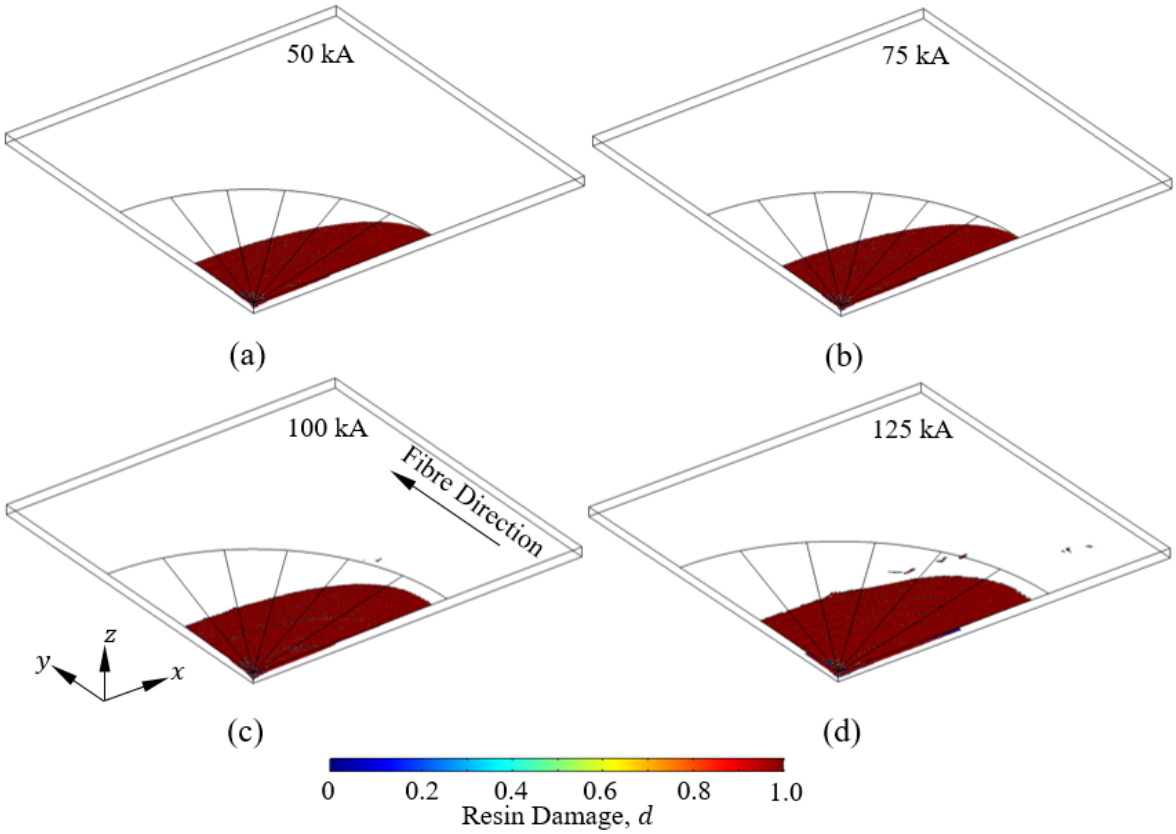

Figure 5.21: Predicted damage in bare surface CFRP laminate based on electric field dependent Damage Model for 4 different peak currents: (a) 50 kA, (b) 75 kA, (c) 100 kA, and (d) 125 kA

Figure 5.22 shows the predicted damaged areas from the proposed Damage Model and the damaged areas of the X-ray CT scans measured ply by ply in the bare surface CFRP laminate specimens. Comparing the results show that the damage area for the first ply is conservative for all the damage intensities. The predictions overestimated the damage in the first 3 plies and underestimated the damage area in the remaining plies. All cases correctly predicted the end of the damage as the predictions for the Damage Model go to zero when the experimental values go to zero.

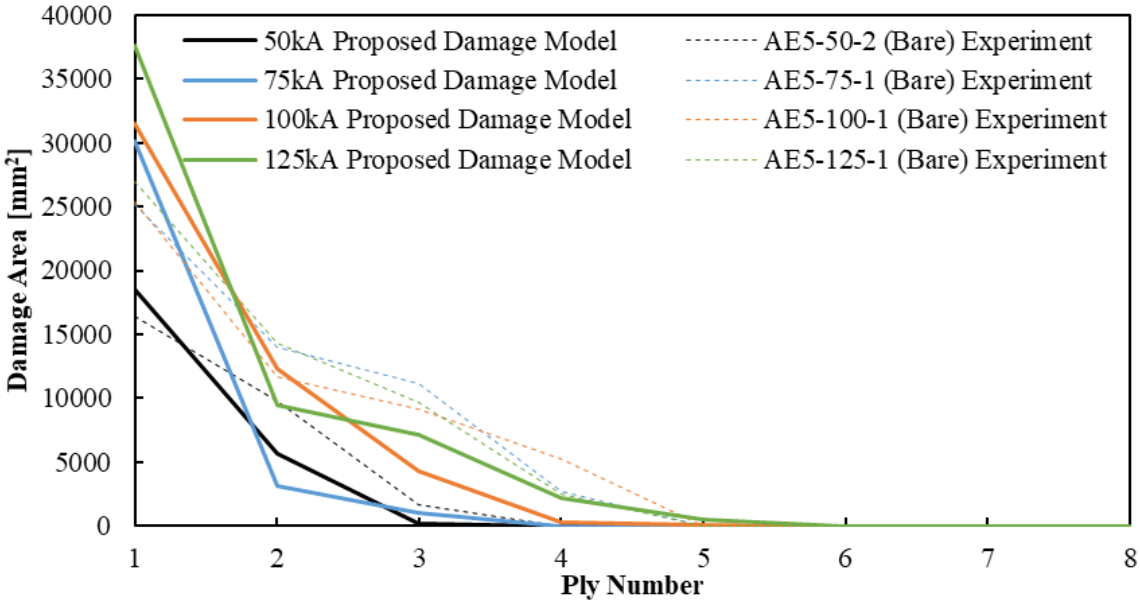

Figure 5.22: Predicted damage in bare surface CFRP laminate – displayed ply by ply – based on electric field dependent Damage Model for 4 different peak currents and X-ray CT measured damage area for the laminate plies from samples AE5-50-1, AE5-75-1, AE5-100-1 and AE5-125-1

5.6.3 Damage Depth

Figure 5.23 shows the predictions for the damage depths and the experimental damage depths in the bare surface CFRP laminate specimens. As seen in the validation, the predicted damage fits well with the experimental damage by showing the correct spread in the transverse direction and the correct depth in the through-thickness direction.

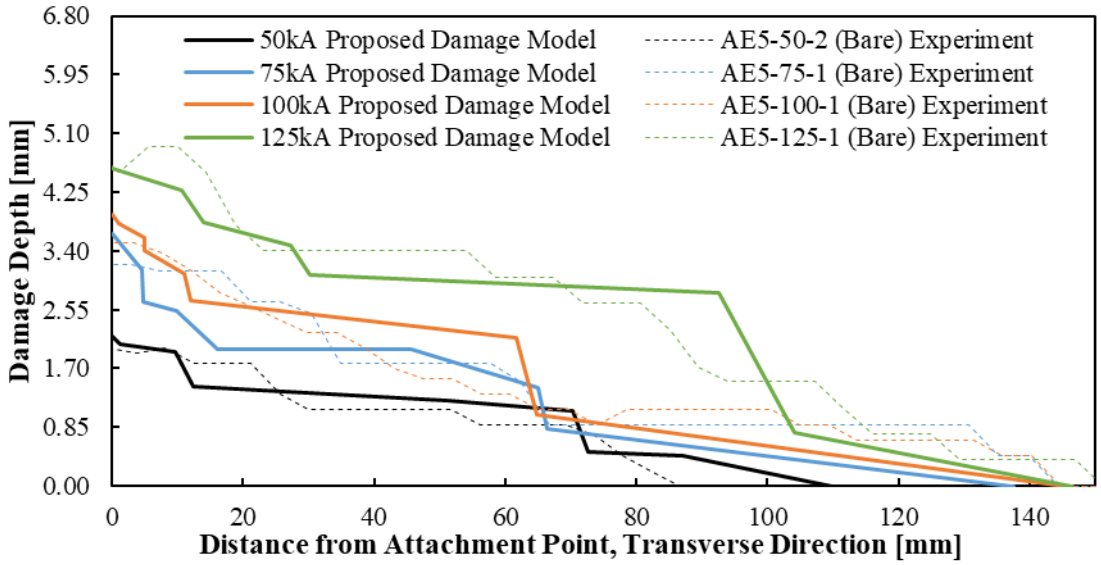

Figure 5.23: Predicted damage depth in bare surface CFRP laminate based on electric field dependent Damage Model for 4 different peak currents

Table 5.3 compares the depth predictions from the proposed Damage Model at the centre of the plate to the experimental values determined in section 4.6.4. The percentage difference is calculated by:

$$\%Diff = \frac{h_{PDM} - h_{EV}}{h_{EV}}(100\%) \tag{5.12}$$

Where h_{PDM} is the damage depth predicted from the proposed Damage Model, h_{EV} is the damage depth from the experimental measurements. This point wise value shows that the resulting damage depth was within 12.1% difference from the predicted values.

Table 5.3: Comparisons of predicted damage depth from proposed damage model and experimental measurements at the centre of the plate with the percentage difference between the two values

Damage State	PDM	EV	%Diff
50 kA	2.16	2.00	8.2%
75 kA	3.64	3.25	12.1%
100 kA	3.92	3.52	11.5%
125 kA	4.59	4.53	1.4%

PDM = Proposed Damage Mode
EV = Experimental Values

5.7 Discussion

The research in this chapter presented a Damage Model which predicted resin damage on UD CFRP laminate. The results from the Damage Model were compared to the damage state of UD CFRP laminate experimentally damage by exposure to idealized simulated direct lightning strikes in a laboratory. The calculated results of the Damage Model predicted damage of typical lightning strike intensities experienced by WT blades. The lightning strike inputs for the Damage Model were the same exposed to the AE5 bare surface tests (see section 4.3.5). The experimental test conducted were compared against the Damage Model.

During a lightning strike event, the CFRP material typically experiences significant Joule heating exceeding glass transition or combustion temperatures. For CFRP materials that have been exposed to lightning strikes that cause combustion/burning, significant damage will be inflicted including loss of resin, fibre breakage, and delamination. The Damage Model was able to predict the significant heating as seen in section 5.5.2. The results were similar to previous damage models [40]. However, the study was limited by only predicting resin damage. As described in section 5.2, the results from this Damage Model are being used in a structural model to modify the damage state of the laminate. This leads to the assumption that the resin damage is the only result which will affect the material properties in the structural model and this assumption is explored in Chapter 6.

The results from the Damage Model have presented a new modelling methodology which is able to produce damage in a UD CFRP laminate that spreads in the transverse direction. The implementation of the electric field dependency was the key feature which allowed the model to spread the damage in the transverse direction by allowing current flow in that direction. The comparison with the conventional model showed that the electric field dependency completely changed the damage state predictions from the model and it was clear from the electric field magnitude results, presented in section 5.5.1, that the field produced was far in excess of the breakdown strength by approximately 35 times. Therefore, it is presented that it is necessary to implement this criterion into a model which exceeds the breakdown strength to correctly predict the damage state of a UD CFRP laminate. The validation of the Damage Model damaged results showed that the damage depth had the closest match to the experimental results.

Figure 5.24 presents the maximum damage area results of the FE predictions and the experimental results compared against the lightning parameters peak current, charge, and specific energy. Figure 5.24 (a) –(c) all show similar results with the increasing peak current, charge, and specific energy all increasing the damaged area for both the Damage Model predictions and the experimental results. The Damage Model while able to produce damage in the transverse direction over predicted the maximum damaged area seen in the plies. The linear fit presented in Figure 5.24 (a) –(c) show that for all cases the predictions are becoming farther away from the results as indicated by the slope being larger for the FE predictions compared to the experimental results. It is also unfortunate that the results have the closest trend or highest R^2 value for the peak current as opposed to specific energy as found for the experimental results. The maximum damage area was always in ply 1 for both the Damage Model and the experimental results. Although it was noticed that the FE predicitons over predicted the damaged area for ply 1 in Figure 5.22, it was noticed that the deeper plies the results were underpredicted. Therefore, a comparison to the damage volume was conducted and presented in Figure 5.25 that shows the predicted damage volume results from the Damage Model and the experimental results from the X-ray CT data compared against the lightning parameters peak current, charge, and specific energy. Figure 5.25 (a)–(c) all show a similar result with the increasing peak current, charge, and specific energy all increasing the damaged area for both the Damage Model predictions and the experimental results. The slopes of the fit lines for the damage volume results are all of similar magnitude. This indicates that the damage prediction on the individual ply level may not be sufficiently accurate. However, the damage volumes are more accurately predicted by the Damage Model. This may be due to the assumption adopted for the modelling that once the electric breakdown is exceeded, the conductivities are increased by an order of magnitude. The assumed increased in conductivity at the electric breakdown point may need to be adjusted to more accurately capture the damage response on the ply level.

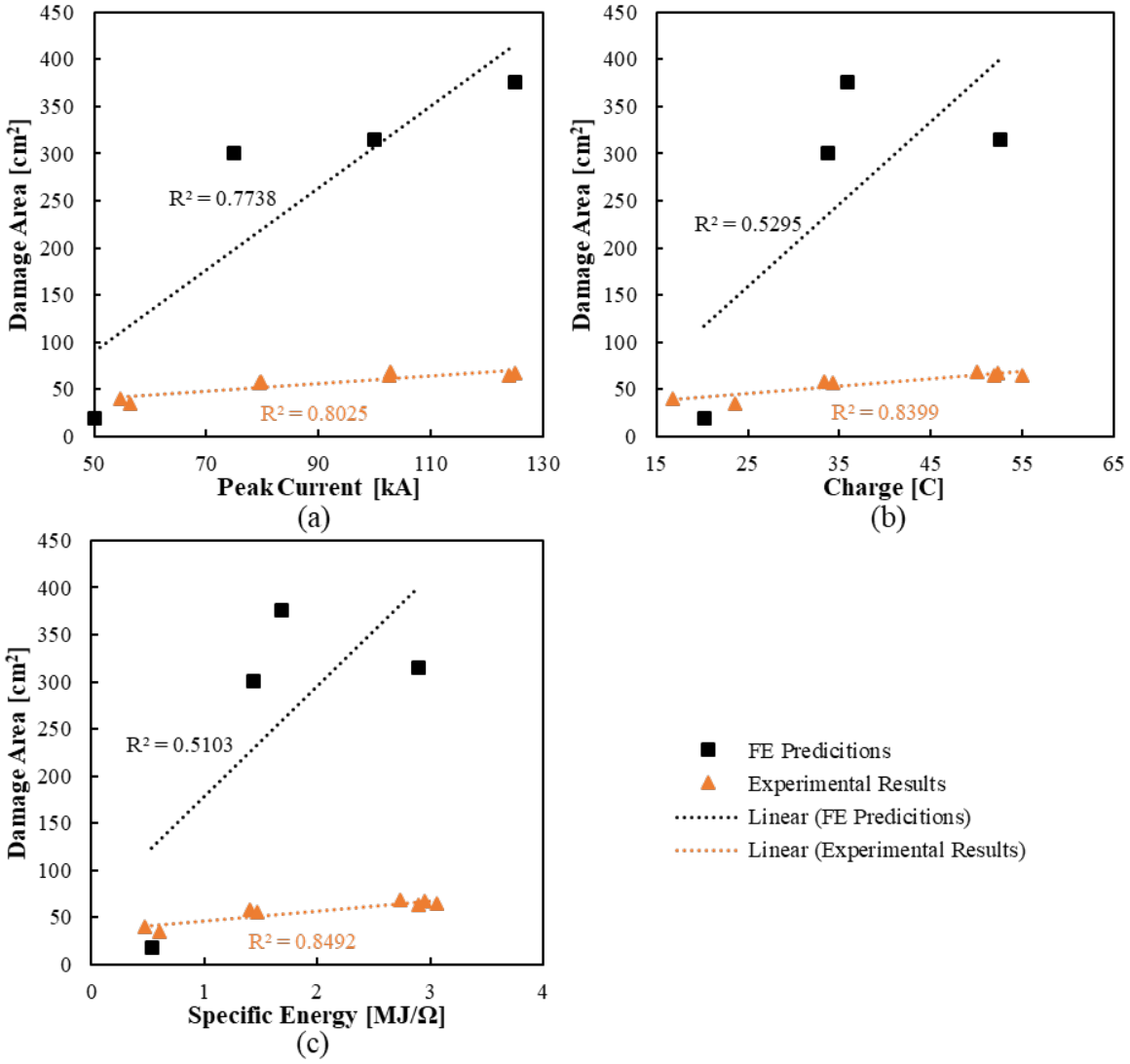

Figure 5.24: Maximum damaged areas identified by the Damage Model (FE Predictions) and the AE5 bare surface specimen (Experimental Results) against the (a) peak current, (b) charge and (c) specific energy

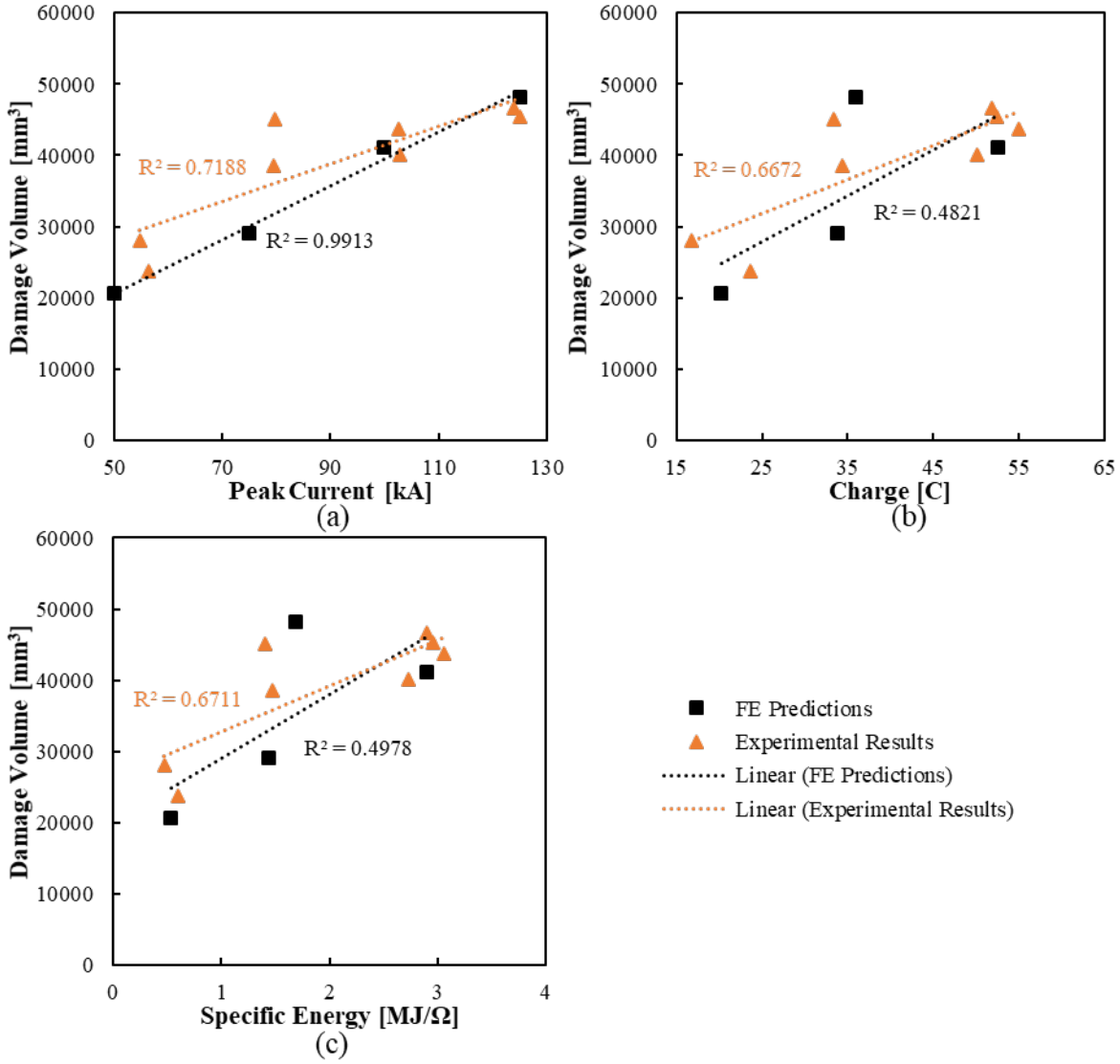

Figure 5.25: Maximum damaged volumes identified by the Damage Model (FE Predictions) and the AE5 bare surface specimen (Experimental Results) against the (a) peak current, (b) charge and (c) specific energy

Figure 5.26 shows the damage depth predictions results from the Damage Model and the experimental results compared against the lightning parameters peak current, charge, and specific energy. Figure 5.26 (a)-(c) all show a similar result with the increasing peak current, charge, and specific energy all increasing the damaged depths for both the Damage Model predictions and the experimental results. The damage depth fit line slopes are all of similar magnitude. The damage depths were the closest match of the Damage Model to the experimental results and is much better match than previous research which indicated that lightning damage models on CFRP materials tend to overestimate the depth results [114].

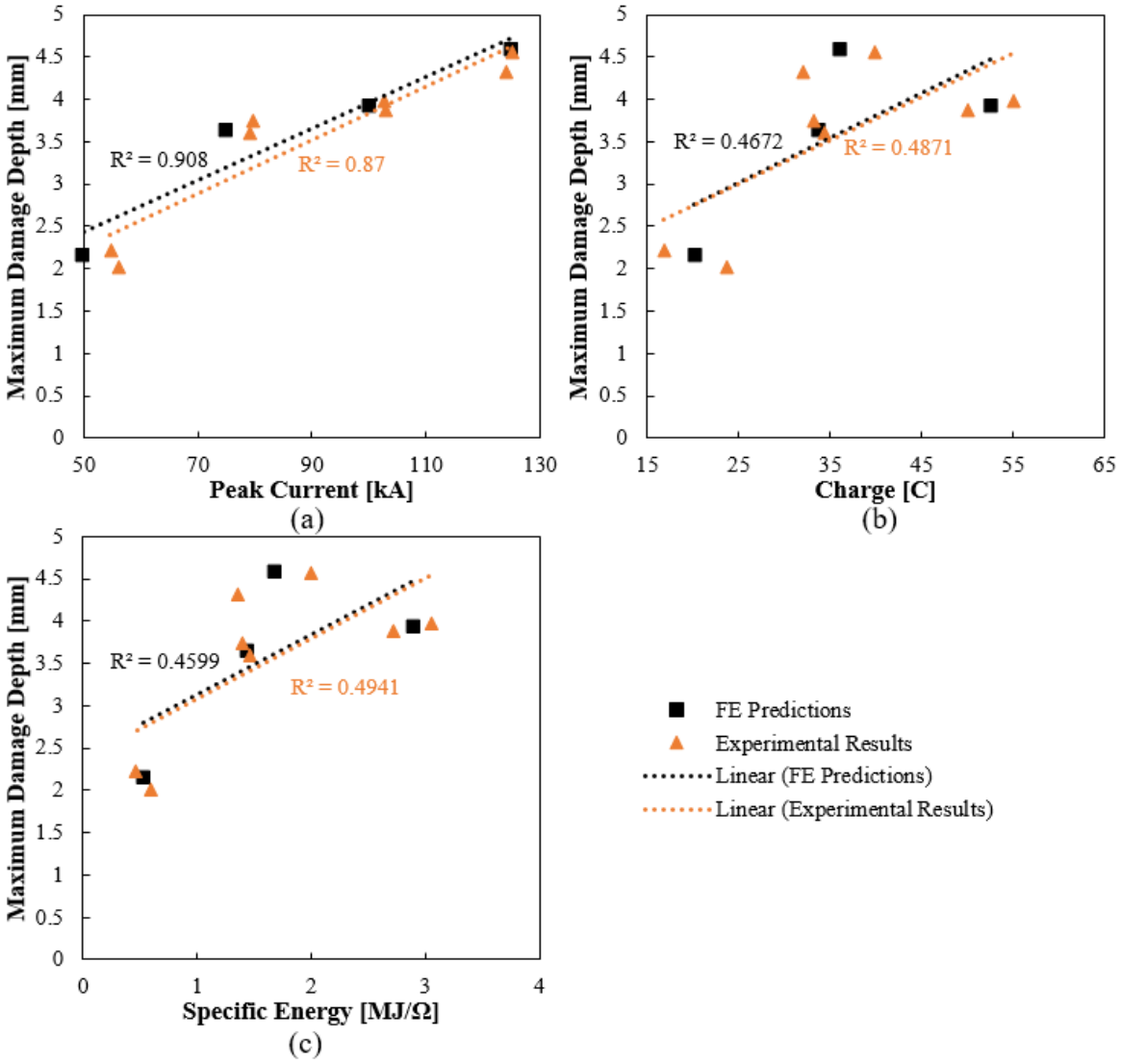

Figure 5.26: Maximum damaged depths identified by the Damage Model (FE Predictions) and the AE5 bare surface specimen (Experimental Results) against the (a) peak current, (b) charge and (c) specific energy

5.8 Summary

The results of a proposed Damage Model which simulates direct lightning strike induced damage through a time-dependent Joule heating model with electric field dependency has been presented. The focus of this work has been to determine the ability of the model to accurately predict damage from a lightning strike. The proposed Damage Model was compared to a conventional damage model used which was similar to previously researched models and validated against experimental data obtained from the AE5 test specimens in section 4.6.4. The results of the validation and comparison study with the conventional model showed that the proposed Damage Model had an increased ability to predict the damage in the transverse direction for UD materials (25% error) which was not able to be simulated in the conventional model accurately (77% error). The damage

prediction also increased the ability in predicting the through-thickness damage depth with the Damage Model predicting within 8% error of the experimental data and the conventional model over-predicted the damage depth with an error of 170%.

The proposed model only requires the addition of two new properties: electric breakdown strength in the transverse and through-thickness directions. The breakdown strength is known for air and the breakdown strength for insulators is a common measurement. For this study the epoxy breakdown strength was assumed for the experimental breakdown strength in the through-thickness direction, and 1/3 of that value was assumed for the transverse direction; this is a typical assumption adopted for the difference in breakdown strength on a free surface and in pure air [145]. The electric conductivity was increased when the electric field was exceeded.

Four damage intensities were simulated to match the experimental measurements. All simulated predictions were able to correctly spread the damage in the transverse direction and predict the through thickness damage spread. The damage area for Ply 1 was overestimated and Ply 3 and beyond were underestimated. The thickness measurements were compared to a point wise mark at the centre of the plate and the comparison showed a percentage difference between the model and experiment to be within 12% for all cases.

These results will further be used to help predict the structural model prediction in Chapter 6 as described in section 5.2.

Chapter 6

Lightning Strike Damage in CFRP Sparcap Laminates and the Effects on Structural Response

6.1 Introduction

The previous chapters have addressed damage inflicted by direct lightning strike attachment in CFRP materials. Chapter 3 and Chapter 4 presented the results of an extensive experimental investigation, and Chapter 5 presented a novel modelling framework as well as model predictions on both material and structural scale for lightning strike damaged CFRP panels. The damage inflicted by lightning strikes has been found to be a combination of fibre breakage, resin burn-off, and delamination similarly identified in previous work [38], [39], [122]. The lightning strike damage has the potential to severely influence the load response and failure behaviour on the structural scale, and there is a need to develop a comprehensive understanding and predictive capability of the changes (reduction) to structural performance caused by lightning strikes. To assess the structural performance for CFRP laminates used for Wind Turbine (WT) blade sparcaps, it was decided to focus the investigation on what in most cases is perceived to be the critical load case and thereby design driver, i.e. the compression load case induced by flapwise bending due to aerodynamic loading. In the framework of this project, a CFRP laminate panel which is a representative sample of a WT blade CFRP sparcap is considered. The considered laminate has similar laminate stacking sequence and layup configuration near the tip of the blade. A laminate that would satisfy the loading capability in the region of interest (described in section 2.6) is thin (<5 mm) and unidirectional (UD). The panels are subjected to compression loads similar to those experienced in a real WT blade component located near the blade tip where the propensity of a lightning strike is most severe, as described in section 2.6. The failure behaviour of such a CFRP sparcap laminate is influenced by both material damage and stiffness driven failure mechanisms. The reduction of material properties from lightning strike damages is assumed to be due to loss of material which leads to loss of laminate stiffness. This loss in stiffness in turn promotes premature buckling-like behaviour that has the potential to lead to collapse in a worst-case scenario. This led to exploring buckling/post-buckling load response which in and of itself is of crucial importance for design engineers [152]–[154].

To address the above, the research has focused on the development and experimental validation of a nonlinear multi-scale modelling framework, in which the lightning induced damage is estimated by the Damage Model developed in Chapter 5. The predicted damage results from the damage model are incorporated in a nonlinear finite element model to determine the buckling and post-buckling response of CFRP plates damage by a lightning strike. For the purposes of this research, compression loading tests were conducted only on bare surface specimens of configuration AE5 as described in section 4.3.5. Both undamaged (control) and damaged test CFRP panel specimens were tested and simulated.

To validate the model predictions on the structural scale, a newly designed testing rig has been designed and commissioned that can adequately produce loads and boundary conditions considered representative for a WT blade CFRP sparcap plate. The novel test is referred to as Compression After Lightning Strike (CALS). The CALS rig allows for a CFRP panel subjected to compression loading to buckle, and the resulting displacements and strains to be measured. Both lightning strike damaged and undamaged CFRP panels have been evaluated experimentally and numerically.

As indicated above, the CFRP panels were sized to be able to react compressive forces equal to those experienced in WT blade sparcap laminates within 15 m from the blade tip. The sub-structural scale test, i.e. the CALS, needed to be able to provide roughly 250 kN of compressive force on specimens of dimensions 500 mm by 500 mm with a laminate thickness of 7 mm [155]. The reason for the dimensional scaling of the CFRP laminates and the associated test rig (the CALS) is that the lightning strike induced damage areas should be sufficiently limited in size (area) relative to the overall specimen/panel dimensions so as not to restrain the load response and only capture the occurrence of material failure. In other words, for the CALS test to capture representative load response and failure behaviour of sparcap CFRP panels, it is necessary to enable both material and structural stiffness (buckling) driven failure mechanisms/modes and their interactions. The design of the CALS test rig was inspired by the traditional ASTM compression after impact (CAI) test configuration [123], and the Sanchez redesigned CAI rig for thin laminates [156], which are used extensively for the assessment of the damage tolerance of composite aerostructure materials. Thus, resulting experimental investigation has explored the effect of lightning damage on the compressive behaviour of a sub-structural representative sparcap panel, and has been used as the basis for delivering Research Objective 5.

The combined multi-scale modelling and experimental validation framework is shown in Figure 5.1 (page 113), where the bottom of the figure illustrates the experimental validation approach used. The developed modelling and validation framework have been utilised to assess many different lightning strike scenarios covering the load response and failure/collapse behaviour of undamaged CFRP laminate configurations to varying severity of lightning strike damaged CFRP panels. The developed modelling framework aims to deliver Research Objective 4.

6.2 Experimental Methodology

6.2.1 Test Specimens

As mentioned, compression tests were conducted on bare surface CFRP panel specimens from configuration AE5, see section 4.3.5. The CFRP panel specimens were 550 mm by 500 mm plates with an average thickness of 7 mm. The specimens had a chamfer on one edge to expose the fibres to allow for an electrical ground to the full thickness of the specimen. Eight panels were subjected to simulated lightning strikes with various amounts of lightning peak current and two were saved for control and therefore were undamaged. The damaged and undamaged (control) specimens were cut using a waterjet cutter to an approximate final plate dimensions of 500 mm by 490 mm with the damage located in the centre of the plate; see Figure 6.1. This removed the chamfer and other ply variations at the edges. The final plate dimensions are presented in Table 6.1.

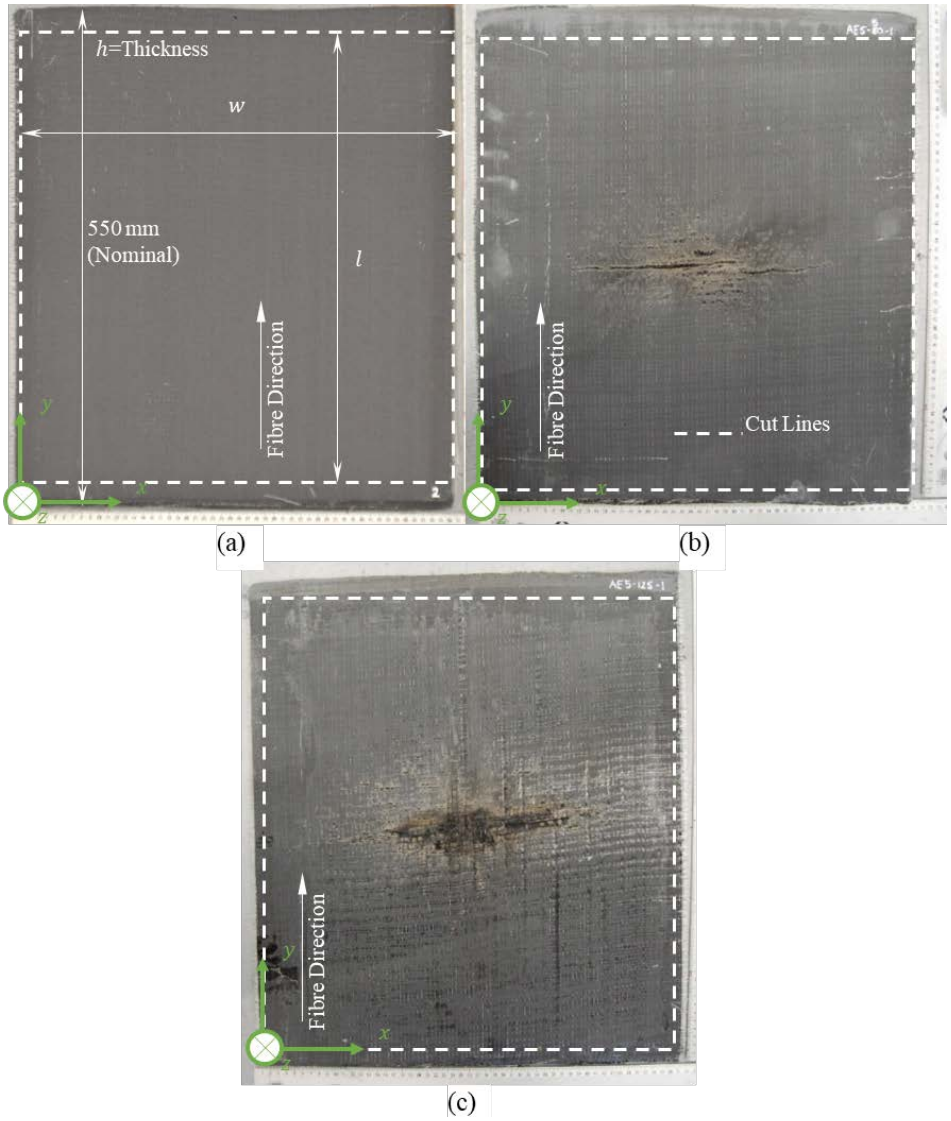

Figure 6.1: CFRP experimental specimens: (a) undamaged (control), (b) 50 kA peak current damaged and (c) 125 kA peak current damaged

Table 6.1: Plate dimensions used for experimental structural tests

Specimen	Length, l [mm]	Width, w [mm]	Thickness, h [mm]
Control-1	500	490	6.8
Control-2	500	492	6.7
AE5-50-1	500	493	7.2
AE5-50-2	500	492	6.9
AE5-75-1	500	490	7.1
AE5-75-2	500	495	7.5
AE5-100-1	500	490	7.3
AE5-100-2	500	491	7.2
AE5-125-1	500	492	7.2
AE5-125-2	500	491	7.0

6.2.2 Compression After Lightning Strike (CALS) Test Rig

As described previously, a newly designed modified buckling rig (CALS) was designed, manufactured and commissioned to enable experimental characterisation of CFRP panels subjected to compression. The drawings of the CALS test rig are presented in Appendix E. The aim of the rig for this project was to capture the effects of lightning strike induced damage on the structural scale. The CALS test configuration and rig is shown in Figure 6.2, and it was designed to accommodate a variety of plate widths and lengths (larger than 480 mm), so as to closely resemble WT blade sparcap structures close to the blade tip, where the propensity for a direct lightning strike is the most severe (see section 2.6 and Figure 2.31). The rig was designed with interchangeable supports along the edges, and for this research simply supported conditions were assumed along all four edges, referred to as SSSS condition for simplicity. The true boundary conditions that a CFRP sparcap laminate will experience from the surrounding WT blade structures would be more restrictive/constrained but could not be nearly as restrained as e.g. clamped/fixed support conditions. Accordingly, SSSS boundary conditions were assumed and approximately accommodated for this research. The CFRP panel supports along the vertical edges were designed such that sliding was enabled in the vertical (y) direction, whilst the horizontal (x) direction and out-of-plane (z) displacements were restrained, thereby emulating simply support and guide rail support conditions along the edges.

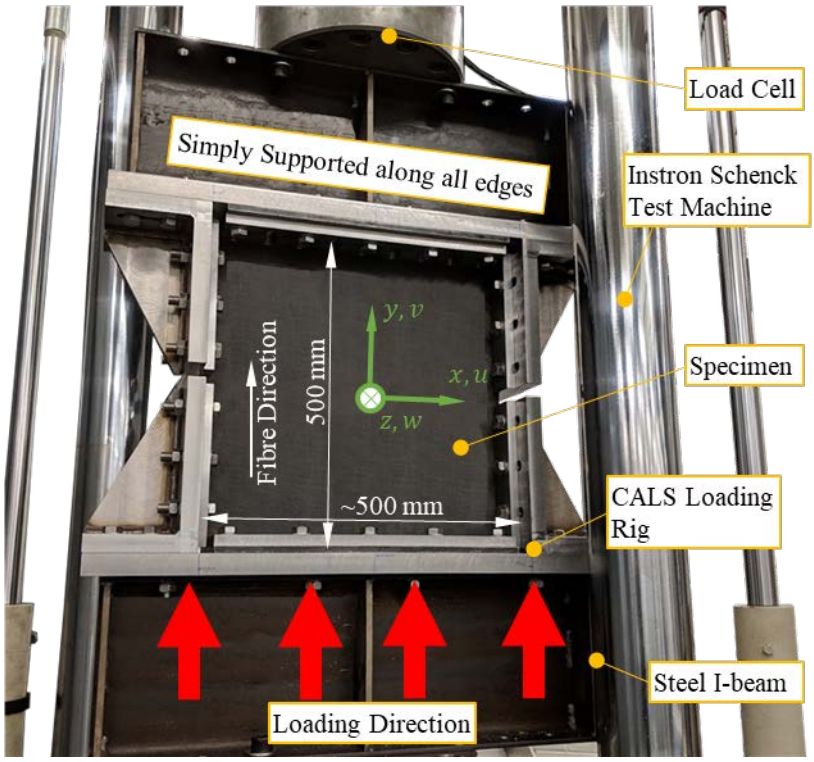

Figure 6.2: Compression After Lightning Strike (CALS) test rig with CFRP laminate plate specimen mounted in servo-hydraulic Instron Schenk test machine (630 kN capacity)

The CFRP plates specimens were loaded in compression in the fibre direction with a 0.5 mm/min loading rate. The tests were conducted to observe the load response, both the buckling and post-buckling behaviour. Stereo 3D Digital Image Correlation was used on both sides of the CFRP plate specimens to capture the full field strains and displacements on both sides.

6.2.3 Stereo Digital Image Correlation (DIC)

Stereo DIC was used to obtain full field measurements of the strains on the plate specimens' surface during testing. A two camera DIC setup was used on each side of the specimen to capture displacements in all coordinate direction; u in the x-direction, v in the y-direction (height or fibre/load direction), and w in the z-direction (out-of-plane), see Figure 6.3. As the CFRP specimens were already black, they were coated with only a thin layer of black paint to make a uniform surface and then speckled with white paint. Images were captured using 4x Manta cameras equipped with 2x AF NIKKOR 28 mm F/8D lenses on the front side and 2x AF NIKKOR 50 mm F/8D lenses on the back side. The load levels were recorded from the test machine load cell, as the images were captured simultaneously using the MatchID software package [157]. The experimental setup is shown in Figure 6.3. The DIC was processed using the MatchID correlation software to determine the displacement and strain fields. For the post-processing, a substep size of 33 x 33 pixels and a step size of 16 were used. The full DIC setup and image correlation specifications are shown in Table 6.2. The noise floor was estimated by taking ten static images from the beginning

of each test, and subsequently correlating these images against the first static image. The noise floor was defined as the average of these correlated images, and the results are shown in Table 6.2.

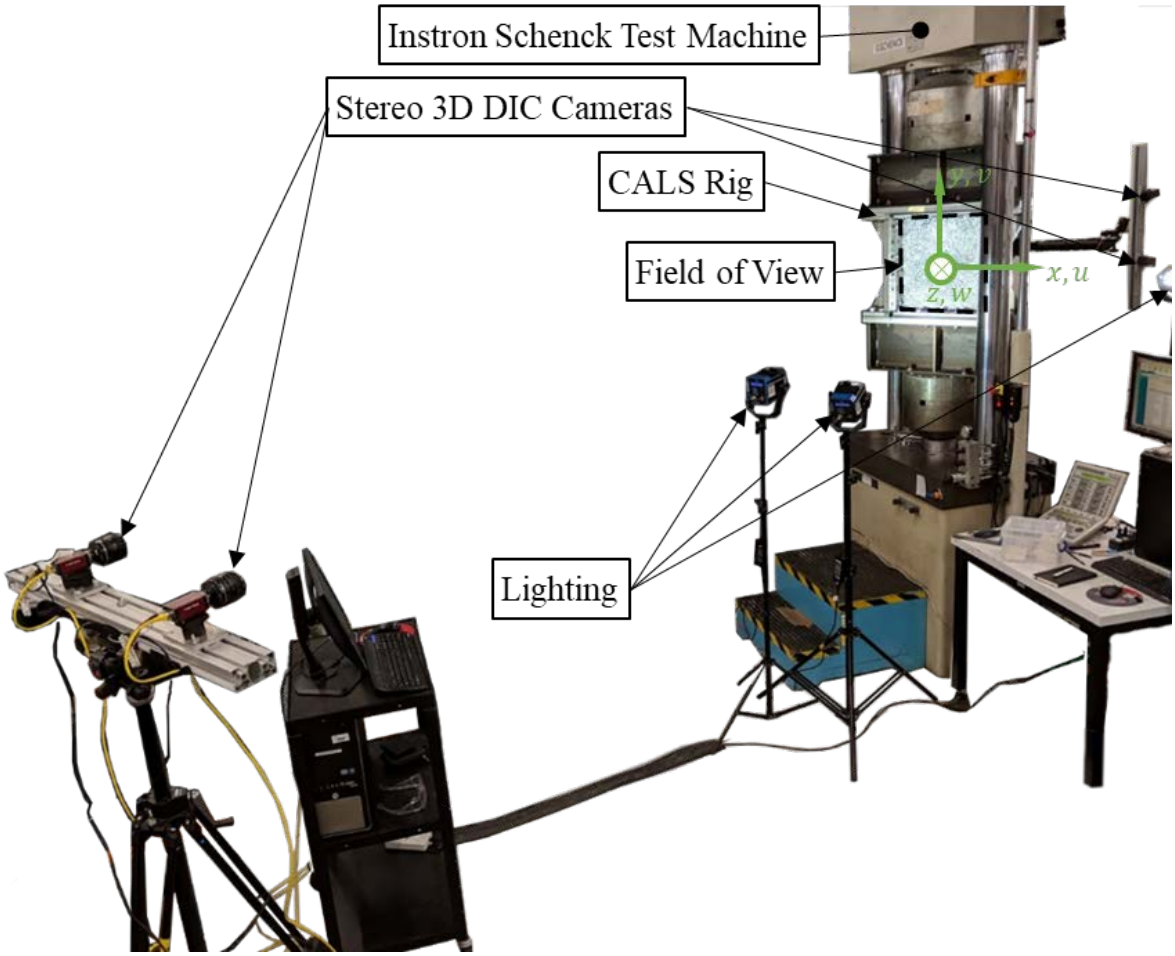

Figure 6.3: DIC Setup showing test machine, CALS rig, CFRP panel specimen and front side DIC system

Table 6.2: DIC test and correlation setup

DIC Test Setup	
Technique Used	2 x Stereo 3D Image Correlation (2 cameras measuring top surface and 2 cameras measuring bottom surface)
Camera	4 x MANTA G504B (gigabit Ethernet)
Sensor	12-bit, 2452 x 2056 pixels
Lens	2 x AF NIKKOR 28 mm F/8D 2x AF NIKKOR 50 mm F/8D
Lightning	4 x NILA ZAILA LED Lights
Imaging distance	~2 m from bottom surface ~4m from top surface
Field of View	400 mm x 400 mm x 100 mm
Pixel resolution	~ 1 px = 0.27 mm
Correlation Specifications	
DIC Software	MatchID 2018.2.2
Correlation Procedure	Zero Normalized Sum of Differences Squared
Subset Size	33 px
Step Size	16 px
Sub-pixel interpolation	Bicubic Spline
Shape Function	Quadratic
Stereo Transformation	Quadratic
Image Pre-smoothing	Gaussian over 5 pixels
Displacement Noise Floor (u, v, w)	(0.026227, 0.0089122, 0.13067) mm
Strain Calculation	Logarithmic Euler-Almansi strain tensor
Virtual Stain Gauge	Top Surface: 257 px Bottom Surface: 353 px
Strain Noise Floor ($\varepsilon_{xx}, \varepsilon_{yy}, \gamma_{xy}$)	(350, 95, 120) μm/m

6.2.4 Vertical In-plane Load Displacement Curves

Load displacement curves based on simultaneous load cell and test machine crosshead displacement data are often used for characterising the load response of materials and structure assemblies. This is highly problematic as it will generate incorrect load response data for the tested specimen, as it includes the compliance of the test rig and various test machine mounts in the measurement. Therefore, to conduct a more accurate measurement it is necessary to correlate the load, measured using the test machine load cell, with a direct measure of the test specimen deformation in terms of displacements or strains. For this investigation, DIC was used for quantitative measurements of the displacement and strain fields for both front and back sides of the tested CFRP plate specimens.

For purposes of this research, the following test procedure was adopted:

1. Alignment of the centre of the CFRP plate specimens for both the front and back sides. This was achieved by identifying three known locations on the specimens, based on which any rigid body translations and rotation during the tests were compensated.
2. Following this, "probe" lines were selected, including data for both the front and back sides of the tested plate specimens. For the tests reported here, *y*-values (vertical or the loading/fibre direction) of +/- 200 mm along the top and bottom specimen edges were selected; see Figure 6.4 (a). The vertical displacement values along these lines were interpolated from the closest DIC measurements.
3. The vertical displacement values derived were subsequently averaged, so that a vertical average displacement could be along the probe lines.
4. Following this, the average vertical displacements at the bottom (moving edge) and top (fixed edge) edges were subtracted from each other to deliver a measure for the vertical displacement (or specimen shortening) captured for this particular specimen.
5. The steps were executed for the data captured on both sides of each of the tested CFRP panel specimens
6. In the final step, the vertical displacement data generated for both specimen sides, following the above steps, were averaged to derive the midplane displacement. This data was then used to plot the load (load transducer data) vs the vertical midplane displacement (end shortening); see Figure 6.4 (b).

This procedure described above was adopted for all the tested panel specimens, and an example of the vertical displacement field and load vs vertical displacement plots is show in Figure 6.4 (b) for an undamaged CFRP panel specimen (Control-1).

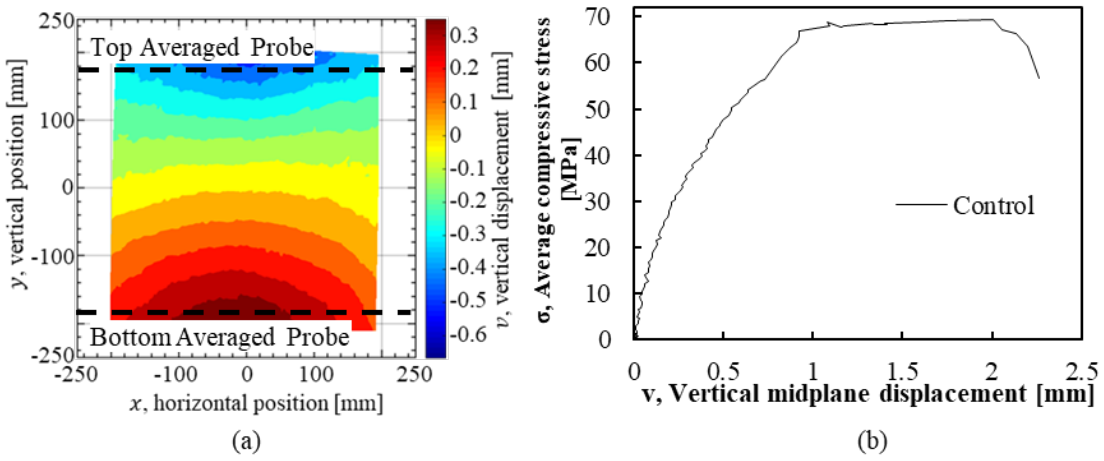

Figure 6.4: (a) Example of vertical (v) displacement field captured using DIC for an undamaged CFRP specimen (Control-1) subjected to a compressive pressure load of 60 MPa and with the "probe lines" indicated, and (b) load vs vertical displacement curve derived from the displacement fields captured using DIC

Several characteristic behaviour descriptors or indicators can be derived from the load displacement plots. The following indicators have been captured from the load displacement plots for comparison between the tested specimens:

- Initial stiffness, E_i;
- Post-buckled stiffness, E_{pb};
- Buckling stress, σ_b;
- Vertical displacement at buckling, v_b;
- First failure event, f_1, defined as the stress level where the slope of the stress-displacement plot changes slope significantly;
- Vertical displacement at first failure event, v_f;
- Compressive stress value at collapse, σ_{coll}; and
- Maximum vertical displacement, v_{max}.

The above indicators are shown for illustration in Figure 6.5, which displays the captured stress-displacement curve for CFRP plate specimen (Control-1) obtained by use of the procedure described above. It should be noted that the precise identification of characteristic behaviour descriptors or indicators described above, is associated with some uncertainty, as precise features of the stress-displacement curves recorded display scatter and variability to the scatter/variability associated with the DIC measurement themselves, as well as due to the gradual (rather than distinct) transitions between equilibrium and damage states associated with the buckling and damage phenomena occurring in the CFRP plate specimens.

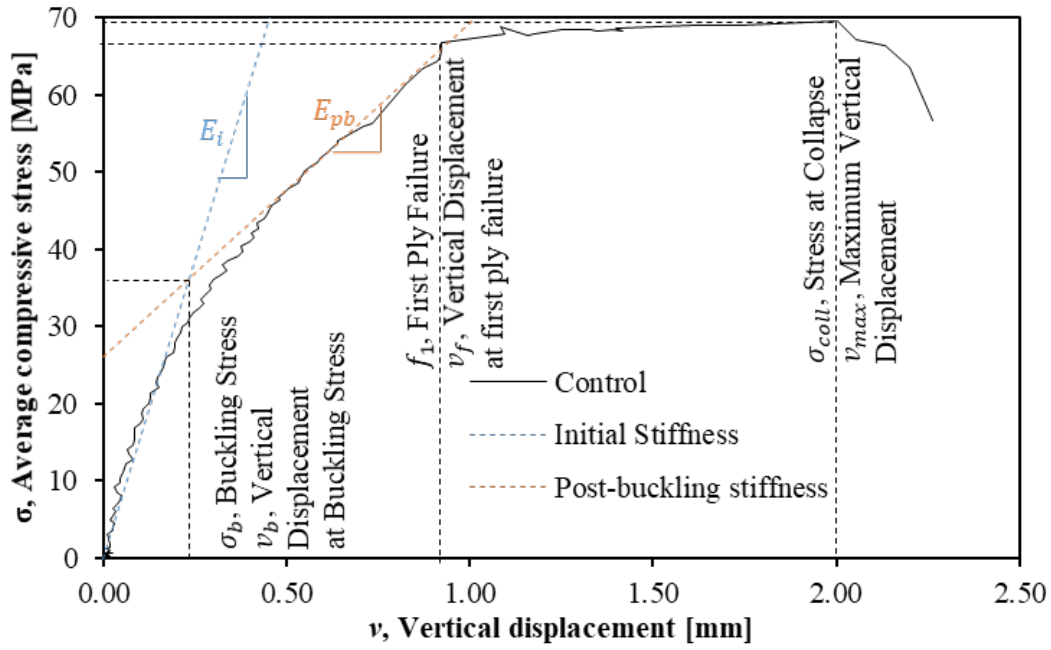

Figure 6.5: Load-displacement curve for CFRP plate specimen Control-1 with the structural behaviour descriptors indicated

The averaging process for the front and back side data captures the midplane deformation. This approach is meaningful for the control or undamaged samples where the laminate is assumed to be the same through the thickness. This assumption is also applied to the damaged samples with the measurements from the front and back averaged. The outcome can only be considered approximate, as the midplane location may vary due to the damage in the form of loss of material. This approximation is considered to be acceptable, as the depth of the damage is small compared to the plate thickness.

6.2.5 Out-of-plane displacement and the load response behaviour

DIC measurements were conducted for each of the CFRP panels during the testing and the maximum out-of-plane displacement for each load level were recorded for each test. The experimentally recorded displacement fields were subsequently compared against the FE model predictions, with special emphasis on assessing both qualitative deformation pattern features as well as quantification of the evolving post-buckled response and failure behaviour as a function of the pretesting damage sate induced by simulated lightning strikes.

6.3 Nonlinear Finite Element (FE) Modelling

The most important consideration for the load response of the CFRP panels subjected to compression loading in the CALS test was the load level at which irreparable damage was induced to the structure. The precise definition of when this occurs can be specified in several ways, but for this research it was assumed to be the load where the first ply failure occurred. This is difficult to assess precisely from the experiments, but convenient to determine from the structural scale FE model (see Figure 5.1). The FE analyses were conducted using the commercial finite element software ABAQUS 6.14 [147]. The CFRP panels modelled were assumed to be quadratic with side lengths of 500 mm by 500 mm and stacked with 8 UD plies (defined in the section 6.3.4) of 0.85 mm ply thickness giving a total thickness of 6.8 mm. The FE modelling conducted included geometric nonlinearity, and the Riks' method [158], [159] was used to establish the nonlinear post-buckling response of the CFRP plates.

6.3.1 Numerical FE Model (Boundary Conditions and Loading)

The FE model was built to simulate CFRP UD laminate plates of the same layup and geometry as the CFRP plate specimens that were tested in the CALS rig. The FE model was discretised using roughly 80,000 elements and meshed with 8-node continuum linear C3D8 elements with dimensions of 5 mm by 5 mm by 0.85 mm, or 8 elements through the thickness. A mesh convergence study showed that a 10,000 element mesh would be adequate for the control samples

however to capture the damaged shapes from the Damage Model 80,000 elements were needed. Additional elements for the most severely damaged shape (125kA case) did not change the results.

To simulate the CALS tests (see section 6.2.2), simple support conditions were assumed along all edges. The vertical sides of the CFRP plates were constrained with respect to the displacements in the x and z directions (see Figure 6.6 for coordinates), the non-loaded horizontal side (top in CALS rig) of the CFRP plate specimens were constrained with respect to the displacements in the y and z directions, and finally the loaded horizontal side of the specimens (bottom in the CALS rig) were constrained only with respect to the displacements in the z direction. The external compression load was imposed through prescribed displacement along the lower plate edge specified relative to a reference node 10 mm away from the plate edge. The reference node was connected to the bottom of the CFRP plate by a pinned rigid body element. The edge rotations as well as the prescribed displacement is restrained in the x and z directions were restrained to ensure the plate edge could only move in the y (vertical) direction. The full model and the boundary conditions are shown in Figure 6.6 (a). All displacement edge constraints were imposed on element nodes located in the specimen mid-plane as shown in Figure 6.6 (b).

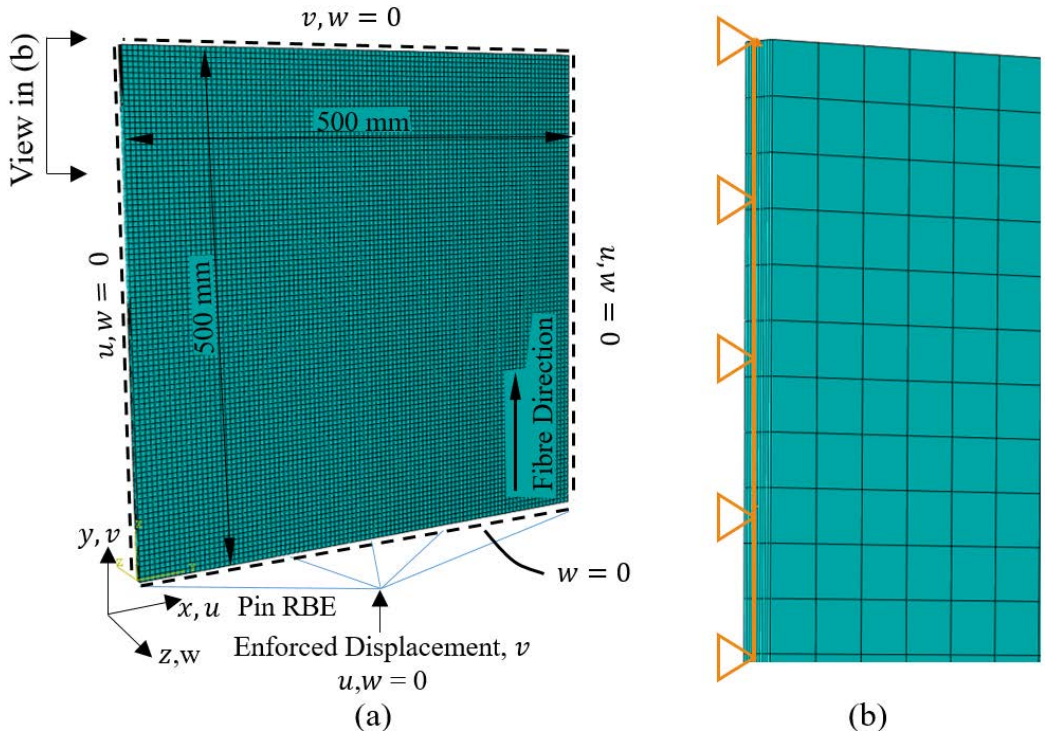

Figure 6.6: Structural FE model: (a) FE mesh and boundary condition imposed along plate edges, and (b) zoom of the edge constraints imposed along specimen/plate mid-plane

6.3.2 Linear eigenmode analysis

The non-linear load displacement response was evaluated in Abaqus by adopting a Riks' integration scheme as described above. To conduct a nonlinear post-buckling analysis, in Abaqus or other FE solvers, the exact post-buckling problem often cannot be analysed directly due to the

discontinuous response that occurs at the buckling loading point [160]. A method often used to overcome this issue is to introduce a geometric imperfection, or pre-deformed state, so that a non-zero out-of-plane displacement state is present prior to the critical load being reached [161]. For this research, an imperfection or pre-deformed sate was imposed in the form of the first mode shape from a linear eigenmode analysis. This was achieved in Abaqus through a linear perturbation procedure, where the stiffness matrix corresponding to the base state loading on the structure was stored and following that a small perturbation (out-of-plane deflection amplitude) was applied. The initial stress matrix due to the perturbation was evaluated, and an eigenvalue calculation was performed to determine a multiplier to the load at which the structure became unstable. The eigenvalues determined from these analyses are used to calculate the critical buckling loads. The eigenvalue analysis provided a set of mode shapes where the maximum centre plate out-of-plane displacement was set to 1, i.e. a unit displacement. The unit displacement was multiplied by a scale factor to establish an imperfect plate shape. This scale factor was estimated by taking thickness measurements along the edges of the plate sample to determine the change in thickness. The maximum imperfection scale factor used was half the average thickness for all cases.

The eigenvalue analysis corresponding to mode one was conducted for each plate considered, the resulting out-of-plane displacements for each node were used to define for the imperfection or pre-deformed state. Additional eigenmode simulations were conducted for higher mode shapes, and subsequently imposed in the plate FE model, but provided little effect to the resulting buckling and post-buckling responses. Therefore, only mode shape one was used for further modelling of the buckling and post-buckling responses. Mode shape one is shown in Figure 6.7.

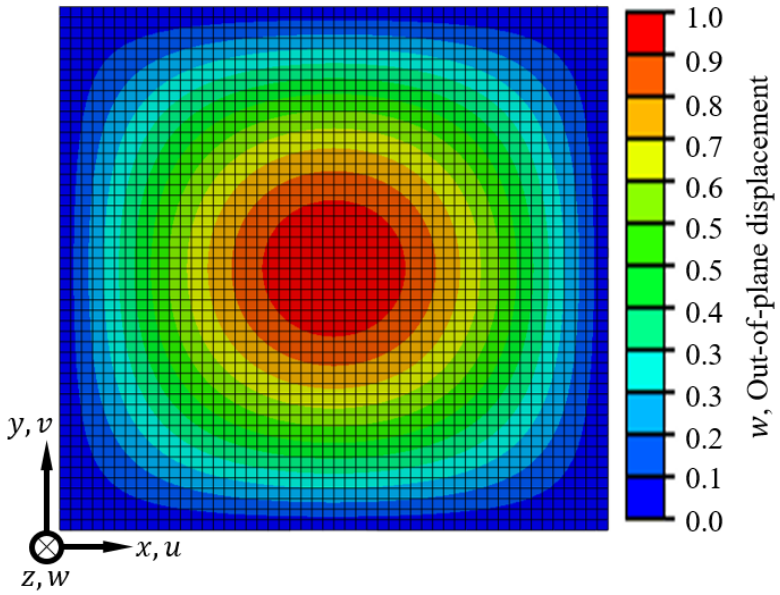

Figure 6.7: Eigenmode out-of-plane displacement results for mode shape one from the CFRP laminate plate FE model

6.3.3 Riks' method

The Riks method for the analysis of nonlinear structural load response is implemented as a standard feature in Abaqus. Details can be found in the Abaqus user's guide [147]. Figure 6.8 presents an example Rik's method iteration run. The Riks method works by assuming the loading is proportional to a single scalar parameter, λ and the load response is reasonably smooth [147]. The method solves for the displacement and load iteratively as shown in Figure 6.8. A thin plate does not have a critical bifurcation point because of membrane action [162]. For a plate, the stiffness increases as the displacements grow which is shown in the load response presented in Figure 6.8 [162]. In Figure 6.8, the K indicates the stiffness used to test the load response curve against and $\Delta\lambda$ being the change in load proportionally factor. The figure runs through 3 iterations before reaching a solution on the nonlinear load displacement curve u^*_{i+1} and λ_{i+1}.

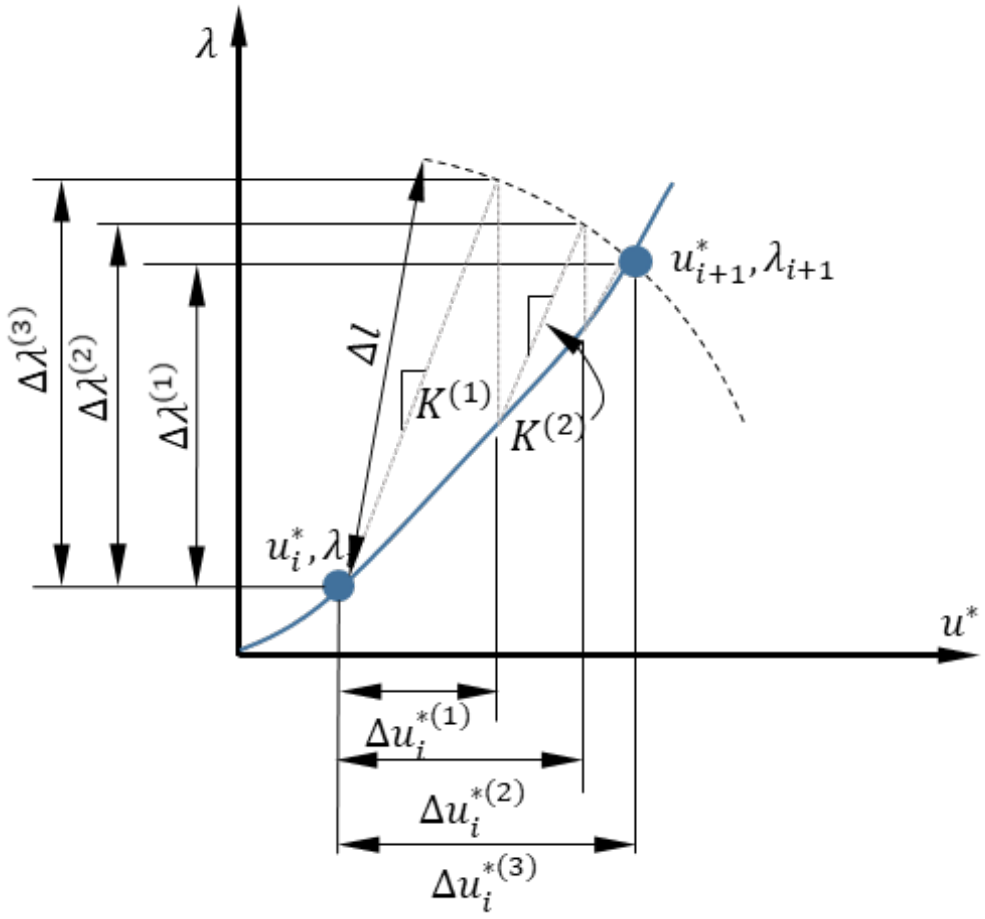

Figure 6.8: Modified Riks algorithm (Arc-length method) with iterations where u^* denotes normalized displacement and λ the load proportionality factor parameter. The increment is defined by the radius of the search circle Δl and the iterations are shown [147], [162]

For this investigation, geometrically nonlinear analyses were simulated with a maximum number of load increments of 100 or the maximum number of iterations the Rik's method will attempt to find a solution before quitting the algorithm. The initial guess for the load step, or λ, was set to 0.2. The

minimum arc length, Δl, change per iteration of 0.1, and a maximum iteration, Δl, arc length change per iteration of 0.5. Lowering the maximum iteration arc length, Δl, per iteration ensures more solutions along the load displacement curve are calculated by the model.

6.3.4 Assignment of material properties

As previously discussed in section 5.2, the developed modelling approach exports the predicted damage region from the Damage Model into a structural FEM of a representative CFRP plate on a sub-component scale. The Damage Model (see Chapter 5) has been developed and executed through COMSOL 5.4 and the structural scale modelling of the lightning strike damaged CFRP laminated plate was developed and executed using Abaqus 6.14 [142]. The damage region was developed on a quarter plate model (Damage Model) and needs to be transformed before it can be imported in the structural scale FEM. There are many approaches to do this, but for this project the Damage Model predictions were assigned to a point cloud. A point cloud is simply a set of data points in space [163]. Figure 6.9 shows the process and the resulting import of the data into the structural FEM. The procedure to create the damage state point cloud is by transferring the resulting resin damage regions calculated by the Damage Model (described in section 5.3) to a point cloud, then mirroring the quarter plate data to make a full plate point cloud and bringing the full plate data into the structural model. The damage state point cloud data where the damaged regions were assigned a value of 1 and the undamaged regions were assigned a value of 0. The point cloud data was generated from the Damage Model with a grid spaced over the model. In the $x-y$ plane (as seen in Figure 6.9 (a)) there were points generated spaced 1 mm by 1 mm apart from each other and 12 slices in the z-direction were taken creating 750,000 points. A reduced set of the generated point cloud is shown in Figure 6.9 (a) to aid in viewing where the blue points are assigned an undamaged value and the yellow points are damage. It should be recalled that the Damage Model was formulated for a quarter plate only (as can be seen in Figure 6.9 (a)), and because of this the point cloud is mirrored in the symmetric x and y directions to take the predicted damaged zone from the Damage Model quarter plate predictions to a full plate FE model. The procedure was conducted through a specially developed MATLAB script, where the predicted damage is imported as a field variable in Abaqus. The MATLAB script is presented in Appendix D. The results of the procedure are shown in Figure 6.9 (b).

Abaqus 6.14 does not have the ability to assign material properties based on a point cloud. However, it is possible to assign temperature dependent material properties, and also to assign temperature values based on a point cloud. This feature is utilised to assign the material properties through a point cloud. The material properties for the undamaged state are assigned a temperature value of 0, and the damaged points are assigned a temperature of 1. The temperature is assigned to element nodes through the point cloud. Abaqus assigns temperature to the element node values

through an interpolation function. The result of this interpolation for the 50 kA peak current case is shown in Figure 6.9 (c). This figure shows that nodal values of temperature (NT11) are assigned but there is a gradation of temperature values along the node from the interpolation function. The temperature dependent properties are assigned at the integration points and the aim of this FEM is to have discrete elements which are damaged and undamaged. Therefore, the temperature to change the material properties representing damage was set to 0.1°C. This ensured that all elements with a non-zero temperature assigned were also assigned with damaged state material properties, because Abaqus handles the temperature above the maximum as constant and assigns the same material properties as the maximum temperature material state, as shown in Figure 6.10. In Figure 6.10, the Young's modulus in the longitudinal and transverse and the Poisson's ratio are shown through a temperature range of below 0°C to above the 1°C maximum temperature assigned. It can be seen that at or below 0°C the values are equal to the undamaged state. Above 0°C to 0.1°C, there is a linear transition from the undamaged properties to the damaged properties. And above 0.1°C, the values are equal to the damaged properties.

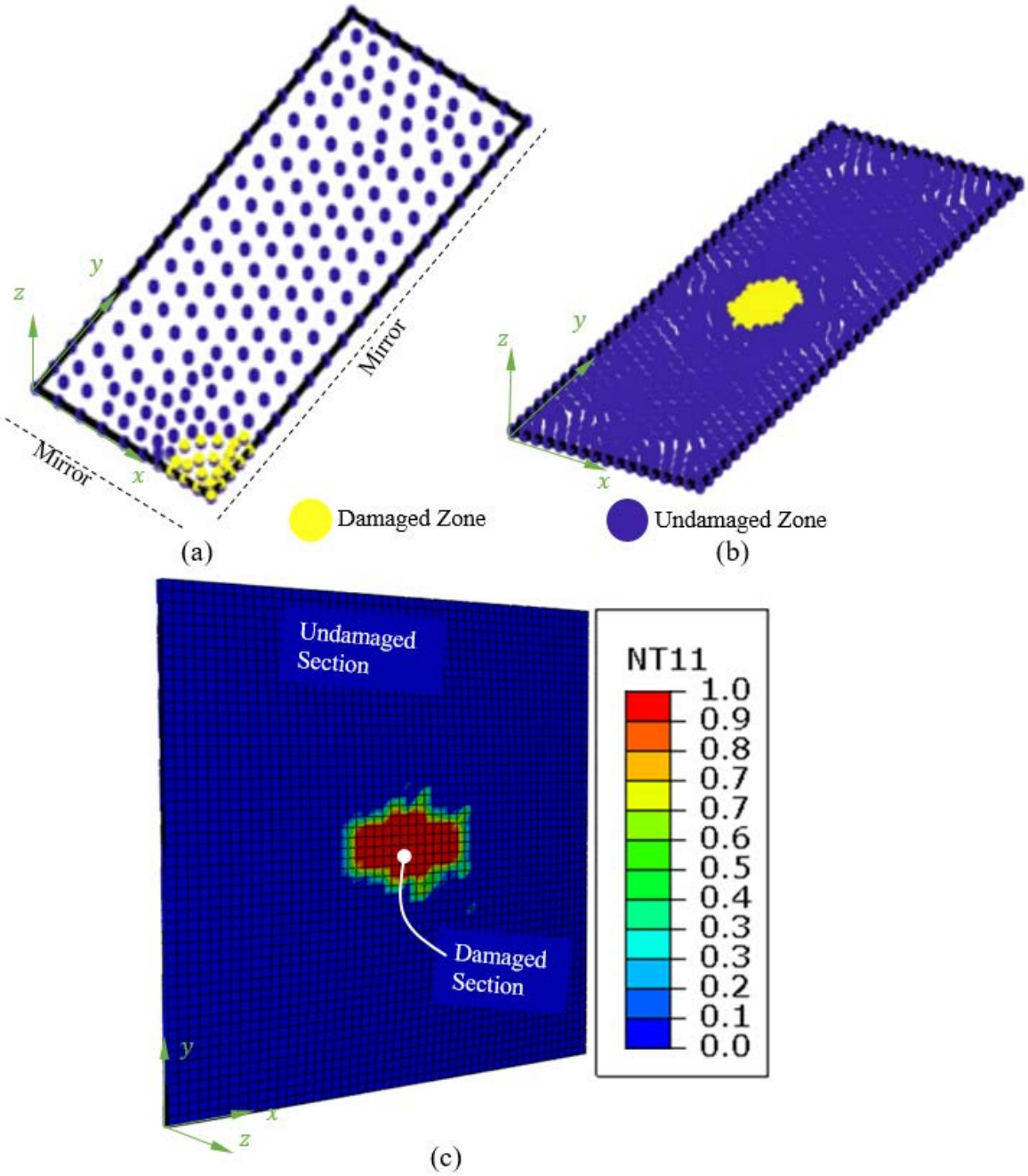

Figure 6.9: Damage model to structural model where (a) is the point cloud created from the Damage model, (b) is the transformed point cloud from quarter plate Damage Model prediction to full structural scale model damage state and (c) is the temperature introduced to assign damage material properties

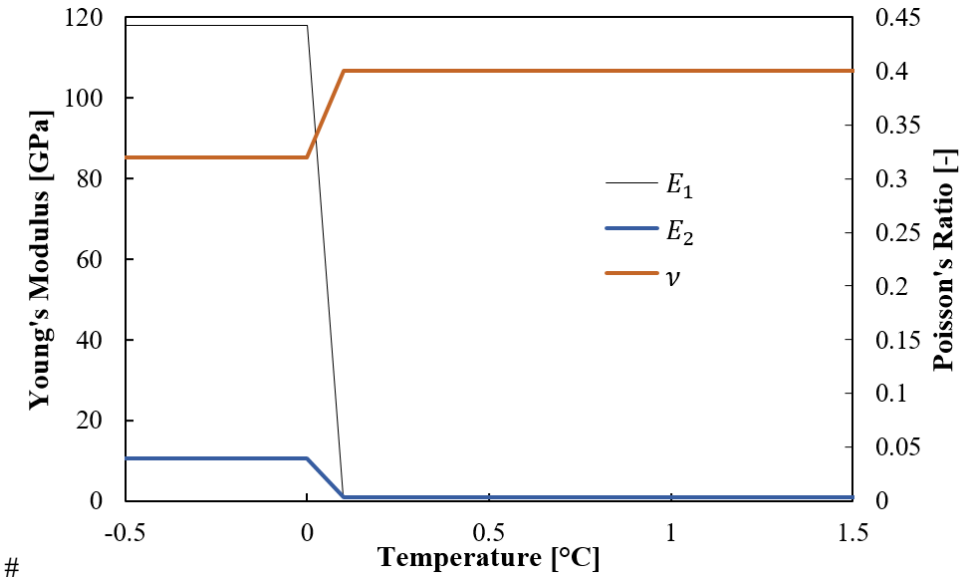

Figure 6.10: Young's modulus and Poisson's ratio temperature dependent material properties as a function of temperature

The material properties assumed for the undamaged and damaged material states are shown in Table 6.3.

Table 6.3: Material Properties for damaged and undamaged states [164]

Temperature [°C]	Damage State	E_1 [MPa]	$E_2 = E_3$ [MPa]	$\nu_{12} = \nu_{13} = \nu_{23}$	$G_{12} = G_{13} = G_{23}$ [MPa]
0	0 (Undamaged)	118,000	10,600	0.32	4,710
0.1	1 (Damaged)	1	1	0.4	1

6.3.5 LaRC composite material failure criterion

For the purposes of this research, the LaRC composite material failure criterion was used to predict the load at which first failure occurred and the associated material failure modes. The LaRC failure criteria can be categorised as phenomenological, but attempts to predict physical mechanisms in terms of six different failure modes, each with theoretical formulations as discussed in [120]. The 6 failure modes are:

1. LaRC1 - matrix compression (transverse stress component $\sigma_{22} < 0$) with fibre tension (fibre direction stress component σ_{11}) greater than the transverse compressive strength (Yc) based on the Mohr-Coulomb model [120],
2. LaRC2 - matrix tension ($\sigma_{22} \geq 0$), based on a quadratic failure criterion,
3. LaRC3 - fibre tension ($\sigma_{11} \geq 0$), based on a simple maximum stress criterion,
4. LaRC4 - fibre compression with transverse compressive stress in the misaligned frame ($\sigma_{22m} < 0$),
5. LaRC 5 - fibre compression with transverse tension stress in the misaligned frame ($\sigma_{22m} \geq 0$) based on fibre kinking models, and

6. LaRC 6 matrix compression ($\sigma_{22} < 0$) which is based on the Mohr-Coulomb model.

The 5 material strength values used to calculate the failure indices for the LaRC criterion were based on the carbon/epoxy system used. The material properties were found the Zoltek datasheet and compared with validation tests. The values are presented in Table 6.4.

Table 6.4: Definition of material strength values for the carbon/epoxy system used [164]

Failure Strengths	Unit	Value
X_T	MPa	2000
X_C	MPa	1000
Y_T	MPa	47
Y_C	MPa	120
S	MPa	70

The LaRC failure criteria was implemented in a user defined field subroutine (USDFLD) [165]. The code to execute this USDFLD is presented in Appendix C.

6.4 Model Validation

The first part of the model validation was based on comparison of the model predictions and the measured load-response and failure behaviour for the undamaged specimen (bare surface AE5 configuration control specimen). The measurement of panel deformation was conducted using stereo DIC as described previously. For the displacement and strain fields on the tensile and compressive side of the panel specimens, the FE model nodal point displacement and strain values were extracted for compression with the DIC measurements. The comparison between measured and predicted values were conducted at load levels above the initial buckling load where a stiffness change was recorded. Figure 6.11 shows the out-of-plane displacement fields obtained on the compression and tension sides of the undamaged CFRP at a compression load of 150kN, where (a-b) show the DIC measurements, and (c-d) show the FEM model predictions. It is seen that the experimental and predicted displacement fields are very similar with respect to the overall shape characteristics, but that the peak deflection amplitude predicted by the FE model is almost 25% smaller than the measured peak value. Despite the disagreement between the predicted and measured peak displacements, which can be due to incorrect assignment of model input parameters including e.g. the layer/plate thickness (that displayed significant variation in the manufacturing process), the otherwise good match with respect to shape of the deflected plate indicates that the FE model captures the correct physics.

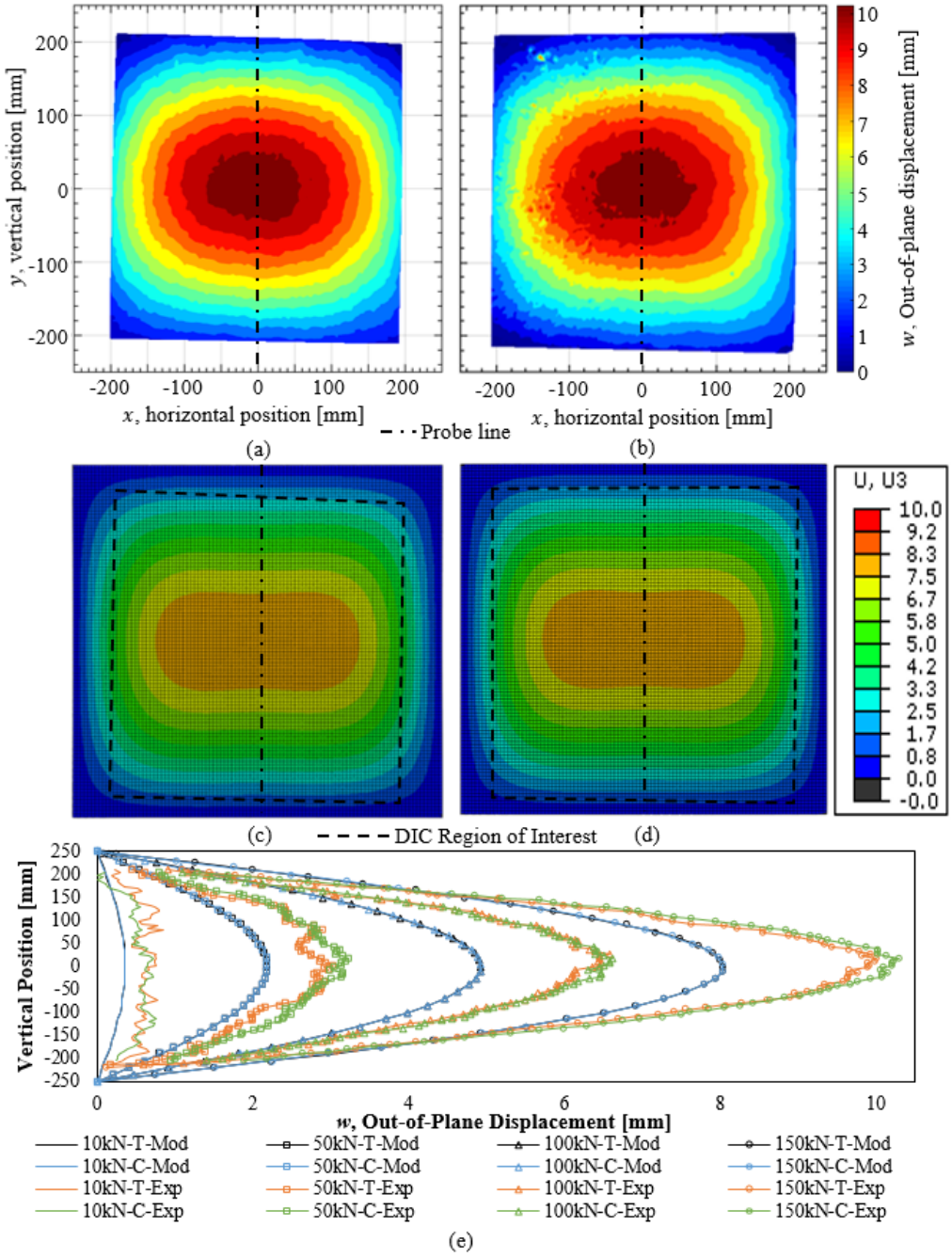

Figure 6.11: Out-of-plane displacements at 150 kN compression load: (a-b) measured using DIC for the compression and tension side, (c-d) FE predictions for the compression and tension sides and (e) measured and predicted displacements along a vertical centre/mid-line at four different compression load levels (10 kN, 50 kN, 100 kN, and 150 kN)

Figure 6.12 shows the measured and predicted in-plane vertical displacement fields obtained for the compression and tension side of the specimen at a compressive load of 150 kN. Figure 6.12 (a) and (c) show the measured in-plane vertical displacement fields captured using DIC for the compression loaded specimen side, and Figure 6.12 (b) and (d) show the same for the tension loaded specimen side. It is observed that the measured and predicted displacement field correlates relatively well overall. The vertical displacements show good agreement in both magnitude and shape. This indicates that the stiffnesses in the FEM model for the undamaged case are near the true value of the measured specimens.

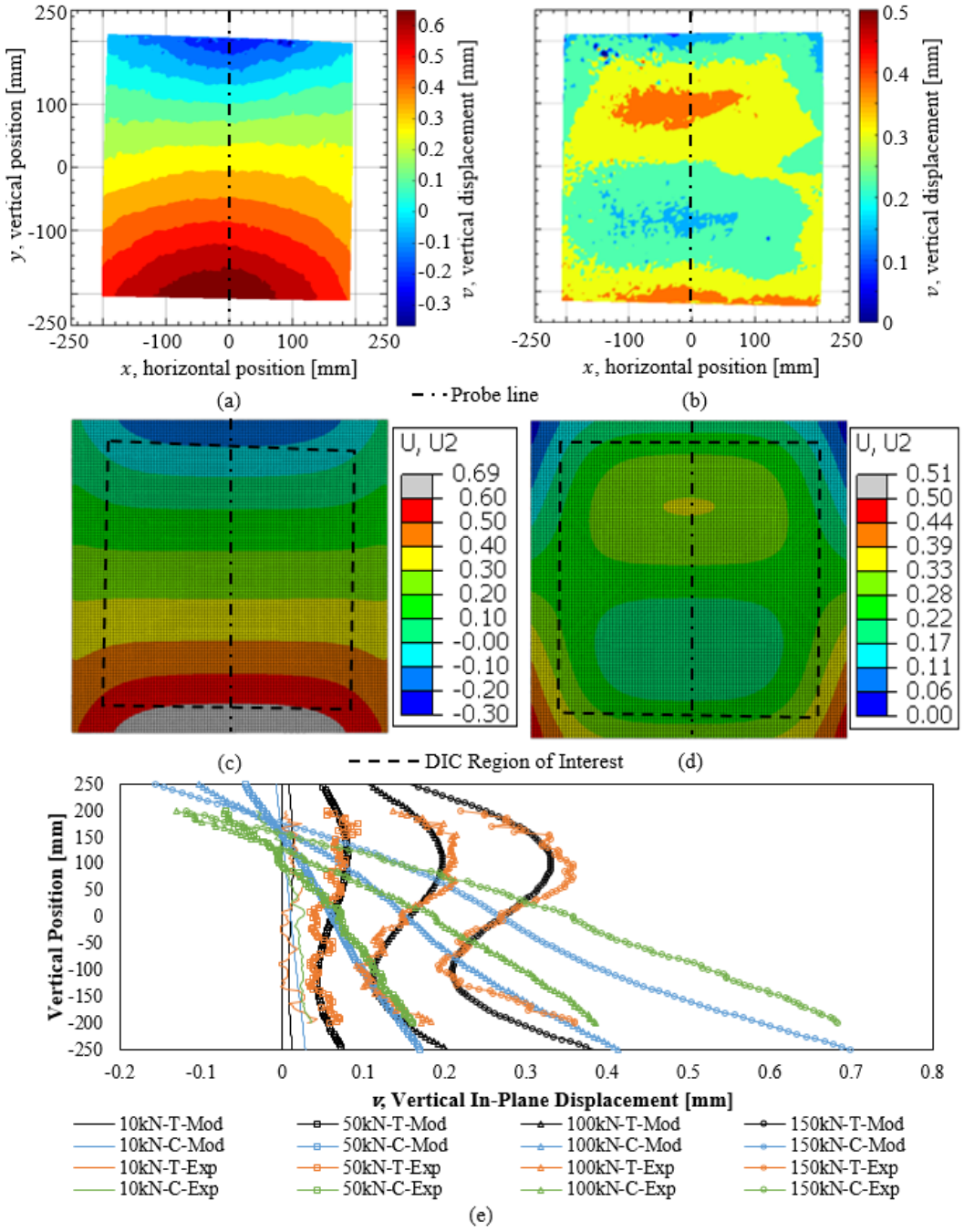

Figure 6.12: In-plane vertical displacement at 150 kN compression load: (a-b) measured using DIC for the compression and tension side, (c-d) FE predictions for the compression and tension sides and (e) measured and predicted displacements along a vertical centre/mid-line at four different compression load levels (10 kN, 50 kN, 100 kN, and 150 kN)

Similar to Figure 6.12, Figure 6.13 shows the measured and predicted in-plane horizontal displacement fields obtained for the compression and tension sides of the specimen at a compressive load of 150 kN. It is observed that the measurement of the in-plane displacement fields is associated with significant noise, especially on the tension side, and some of which is likely to be associated with specimen misalignment. However, given this, it is seen that the measured displacement fields match the prediction of the FE model reasonably well.

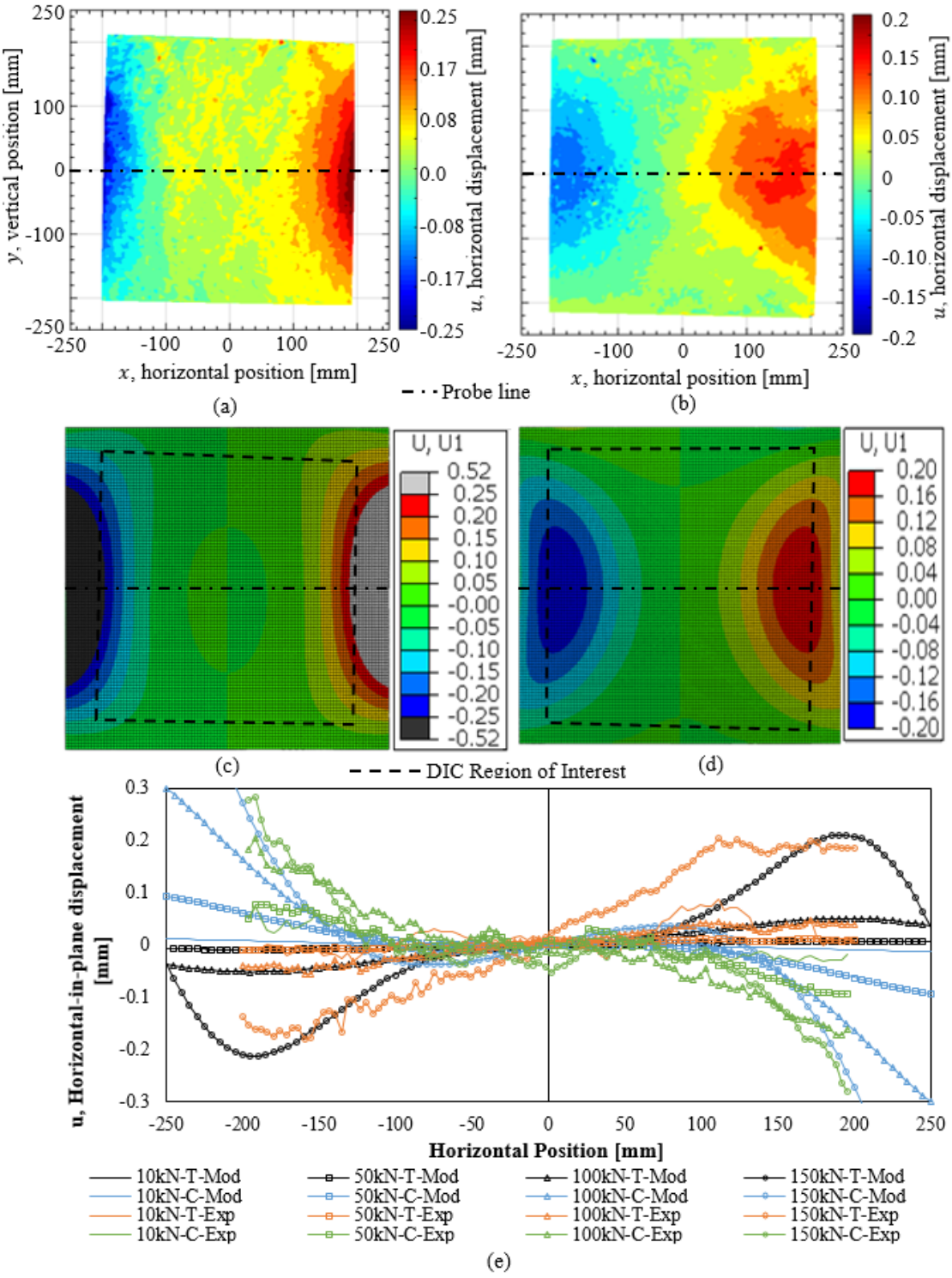

Figure 6.13: In-plane horizontal displacement at 150 kN compression load: (a-b) measured using DIC for the compression and tension side, (c-d) FE predictions for the compression and tension sides and (e) measured and predicted displacements along a vertical centre/mid-line at four different compression load levels (10 kN, 50 kN, 100 kN, and 150 kN)

Figure 6.14 shows the results of the in-plane horizontal strain. Similarly, the DIC and FEM comparison shows relatively good agreement. Similarly, it is observed that the measurements of the in-plane horizontal (xx) strain displacement fields is associated with significant noise. However, given this, the maximum strains are captured by the DIC in comparison to the FEM.

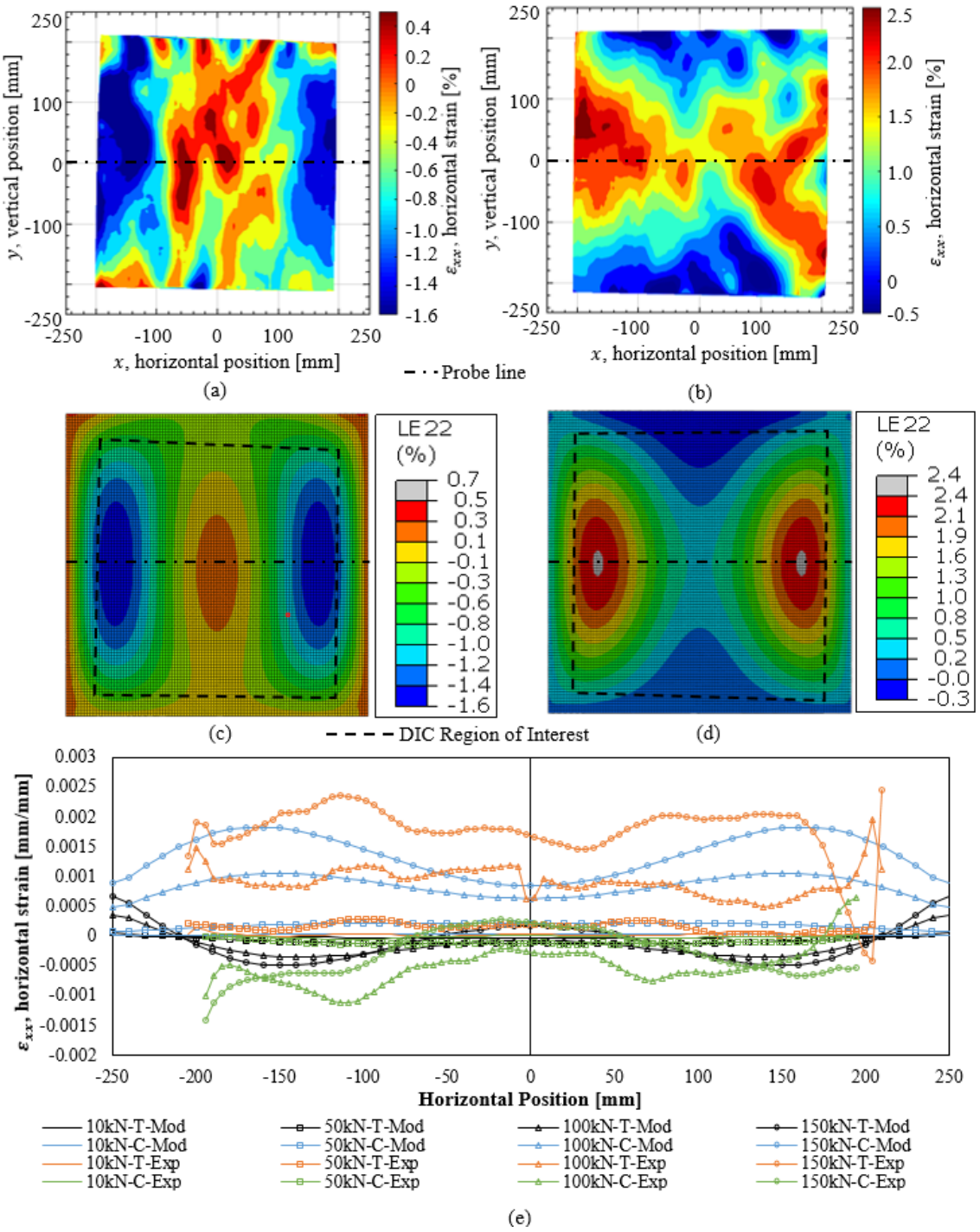

Figure 6.14: In-plane horizontal strain at 150 kN compression load: (a-b) measured using DIC for the compression and tension side, (c-d) FE predictions for the compression and tension sides and (e) measured and predicted displacements along a vertical centre/mid-line at four different compression load levels (10 kN, 50 kN, 100 kN, and 150 kN)

Figure 6.15 shows the results of the in-plane vertical strain. Similarly, it is observed that the measurement of the in-plane vertical (*yy*) strain displacement fields is associated with significant noise especially the tension side. However, given this, it is seen that the measured strain fields match the prediction of the FE model are good for the tension side. The compression side showed higher measured strain results compared to the FEM some of this is likely to be associated with specimen misalignment which over predicts the strains.

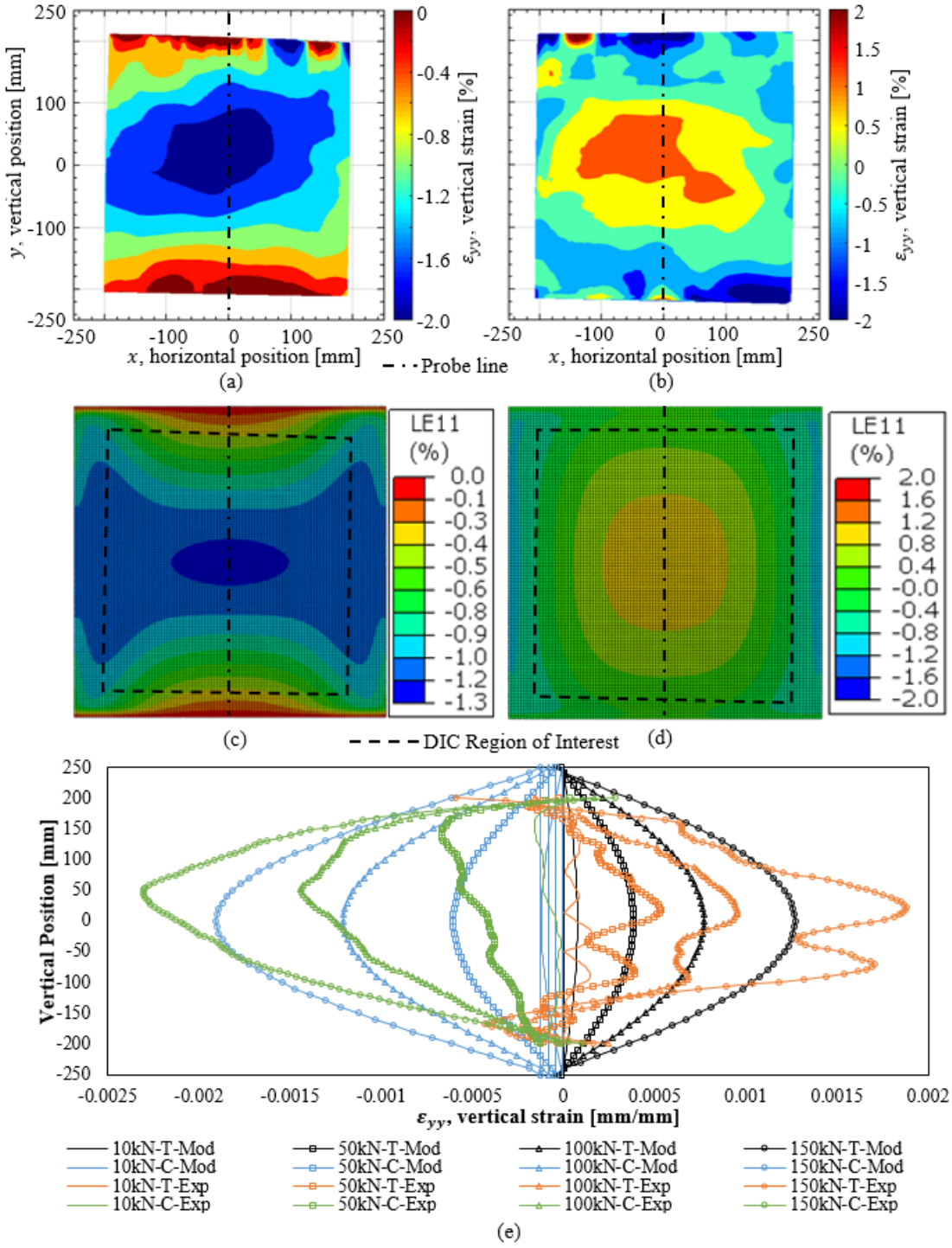

Figure 6.15: In-plane vertical strain at 150 kN compression load: (a-b) measured using DIC for the compression and tension side, (c-d) FE predictions for the compression and tension sides and (e) measured and predicted displacements along a vertical centre/mid-line at four different compression load levels (10 kN, 50 kN, 100 kN, and 150 kN)

The overall validation of the undamaged (Control) case showed that the initial model is a good representation of the buckling/post-buckling load response. Therefore, the model is now applied with damaged material properties and compared against this control sample (both model and experimental) for a reference.

6.5 Experimental and Modelling Results

Five different CFRP panel cases were tested experimentally using the CALS rig and modelled using the developed multiscale modelling framework: undamaged (control), 50 kA, 75 kA, 100 kA, and 125 kA peak current damaged states. A total of ten (2x undamaged and 8x damaged) CFRP panels tested in the CALS rig were from the bare surface AE5 test configuration, discussed in section 4.3.5. The predicted damage corresponding to the different peak current amplitudes are shown and discussed in section 5.6. For the CALS tests, the CFRP panel specimens were mounted in the test rig. Following this, the compressive load was applied, and the panels were allowed to buckle. The buckling induced when the compressive loading was applied to the specimens and was observed to occur in either out-of-plane direction (i.e. towards front or back) for the undamaged case. To ensure consistency in the comparative analyses of the tests, the specimen sides that were subjected to tensile strains and stresses due to the panel buckling are referred to as the 'tension side', and the specimen sides that were subjected to compressive strains and stresses due to the panel buckling are referred to as the 'compression side', respectively, see Figure 6.16. The damaged samples all buckled with damage occurring on the compression side of the plates. This supports the assumption made that the damaged material loses all stiffness.

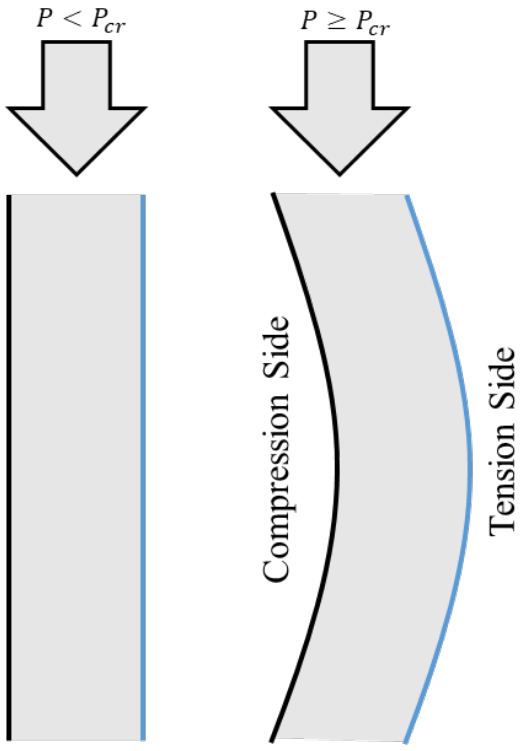

Figure 6.16: Pre/post buckling diagram

The five test cases were simulated using the 2 stage (or multi-scale) modelling framework presented. The information about the damage state inflicted by the simulated lightning strike event

was exported from the Damage Model (Chapter 5) to the structural scale FE model where the CALS test was simulated for each case. The results are presented in the following sections.

6.5.1 Experimental Results

The bare surface AE5 test configuration CFRP panels were subjected to compression loading in the CALS test rig as described. As expected, the manufacturing induced imperfections, including thickness variation and deviation from perfectly flat, as well as unsupported lengths of the panels, led to load-response behaviour where the panels started to display out-of-plane bending displacement (buckle behaviour) immediately upon load application. Accordingly, buckling did not occur in a classical bifurcation type event (as expected), and for the purposes of the analyses conducted in this research, the "buckling" stress calculated represents the stress (or compressive load) where a change in stiffness has taken place. The experimental results were averaged together for each damage state (each case had 2 samples) and are presented in Table 6.5. The initial plate stiffnesses were all of similar magnitude, despite the varying degrees of lightning damage. The measured post buckling stiffnesses, however, were drastically reduced. Similarly, the identified initial buckling stress, the first failure event stress, and the collapse stress were all lower than the undamaged (control) specimen.

Table 6.5: Experimental results – pre- and post-buckling behaviour and failure/collapse

Variable	Description	Control	50 kA	75 kA	100 kA	125 kA
E_i	Initial stiffness [MPa]	161	149	158	162	171
E_{pb}	Post-buckle stiffness [MPa]	52	47	46.3	45	23
σ_b	Buckling stress [MPa]	38.5	36.7	28.1	26.9	30.9
v_b	Vertical displacement at buckling stress [mm]	0.34	0.33	0.21	0.22	0.21
f_1	First failure event [MPa]	69.9	56.5	59.4	32.5	32.9
v_f	Vertical displacement at first failure event [mm]	0.53	0.80	0.88	0.32	0.22
σ_{coll}	Collapse stress [MPa]	69.5	57.7	55.8	43.9	50.9
v_{max}	Vertical displacement at collapse [mm]	2.01	2.10	1.58	1.08	1.35

6.5.2 Experimental Characterisation of the post-buckling response

As described earlier in this chapter, stereo DIC has been used to provide quantitative measurements of the plate deformation states during the CALS tests. The DIC measurements have demonstrated significantly different load responses and deformation behaviour of the different specimen configurations, especially with respect to the out-of-plane displacements between the undamaged and the lightning strike damaged specimens. Figure 6.17 shows the out-of-plane displacement for three different compression load levels and different lightning strike damage levels. The centreline and outline of the damage region as seen from visual inspection are shown on the figure. It is observed that the measured out-of-plane displacements were much larger for the damaged CFRP

panel specimens. The most severely damaged specimen (lightning strike of 125 kA) for all load levels (Figure 6.17), in addition to showing the highest displacement amplitudes, displays a characteristic change of the shape of the out-of-plane displacement contours, and further that the point of maximum displacement moved away from the damaged region indicating that the panel stiffness in the damaged regions was significantly reduced by the lightning strike events.

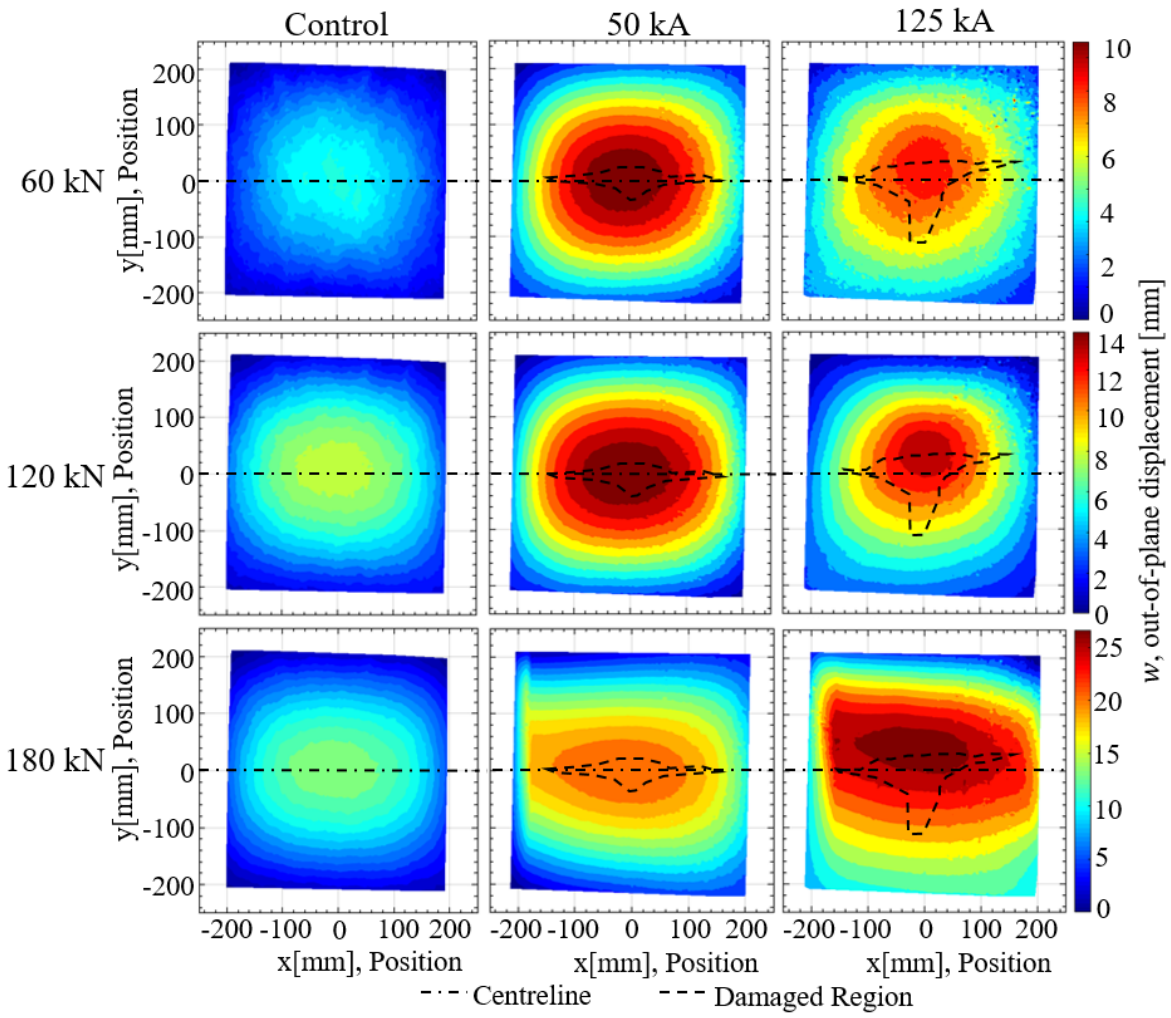

Figure 6.17: Stereo DIC measurement of the out-of-plane displacements corresponding to compressions loads of 60, 120, and 180 kN, respectively, for the undamaged (control) specimen, and the lightning damaged specimens subjected to 50 kA and 125 kA peak currents

All the tested panels failed due to matrix tension along vertical strips along the vertical edges x-values +/- 180 mm from the centre of the plate. In all cases, this failure initiated a flattening of the vertical load-displacement curve as shown in Figure 6.18. The flattening of the load-displacement curve reduced with the higher peak currents applied to the specimen. As shown in Figure 6.18 for the worst case AE5-125-1 which was subjected to the highest current and resulting in the most damage had the lowest maximum displacement and compressive stress at failure. The flattening was primarily triggered with an initiation of failure and the end of the flattening was the failure reaching the opposite side and ultimately lead to a structure which resemble that of a wide beam rather than a plate/panel simply supported along all four edges. The characteristic flattened load

displacement curve, significantly reduced plate stiffness, persisted until total collapse occurred with a subsequent sudden drop in the load, as seen in Figure 6.18. The difference between the pre-first failure event and the post-first failure event is shown in Figure 6.19. Figure 6.19 (a) shows no failure and the out-of-plane displacement is resembles a plate with SSSS end conditions and Figure 6.19 (b) has striations at the failure mark and no longer has the eigenmode shape and resembles a wide beam.

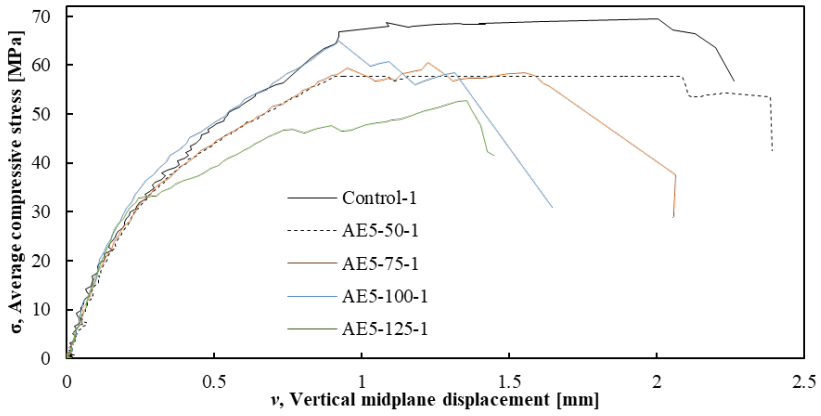

Figure 6.18: Vertical load-displacement captured for undamaged, AE5-50-1, AE5-75-1, AE5-100-1, and AE5-125-1 damaged specimens

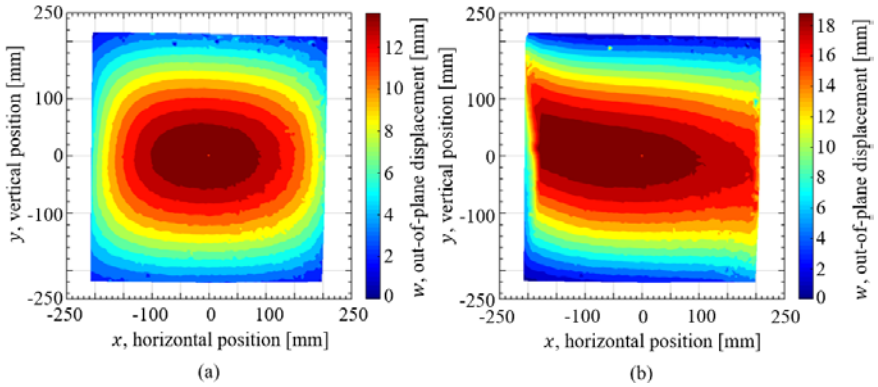

Figure 6.19: Measured out-of-plane displacements recorded for the (a) first failure event at a compressive stress level of 60MPa and (b) prior to collapse in the post-buckled regime at a compressive stress of 69MPa

6.5.3 Vertical in-plane load-displacement curves – experimental results and predictions

The vertical stress vs vertical displacement curves obtained from the CALS tests as well as the FE model predictions are presented in Figure 6.20 for the undamaged (control) and damaged CFRP panel cases. The model accurately predicts the initial stiffness of the plates however has small errors in the post-buckle region. This may be due to the non-linear stress-strain behaviour in the regions with shear and matrix-tension softening. Although there are some small errors in the displacements, the first ply failure occurs at a compressive pressure load level closely associated with the experimental first failure event. All the values from the experiment and the model are presented in Table 6.6, as well as the percentage difference between the model and the

experimental results. The maximum percentage difference was 7.3% which shows good agreement between the first failure event from the experimental results and the first ply failure from the structural FE model as predicted by the LaRC criterion.

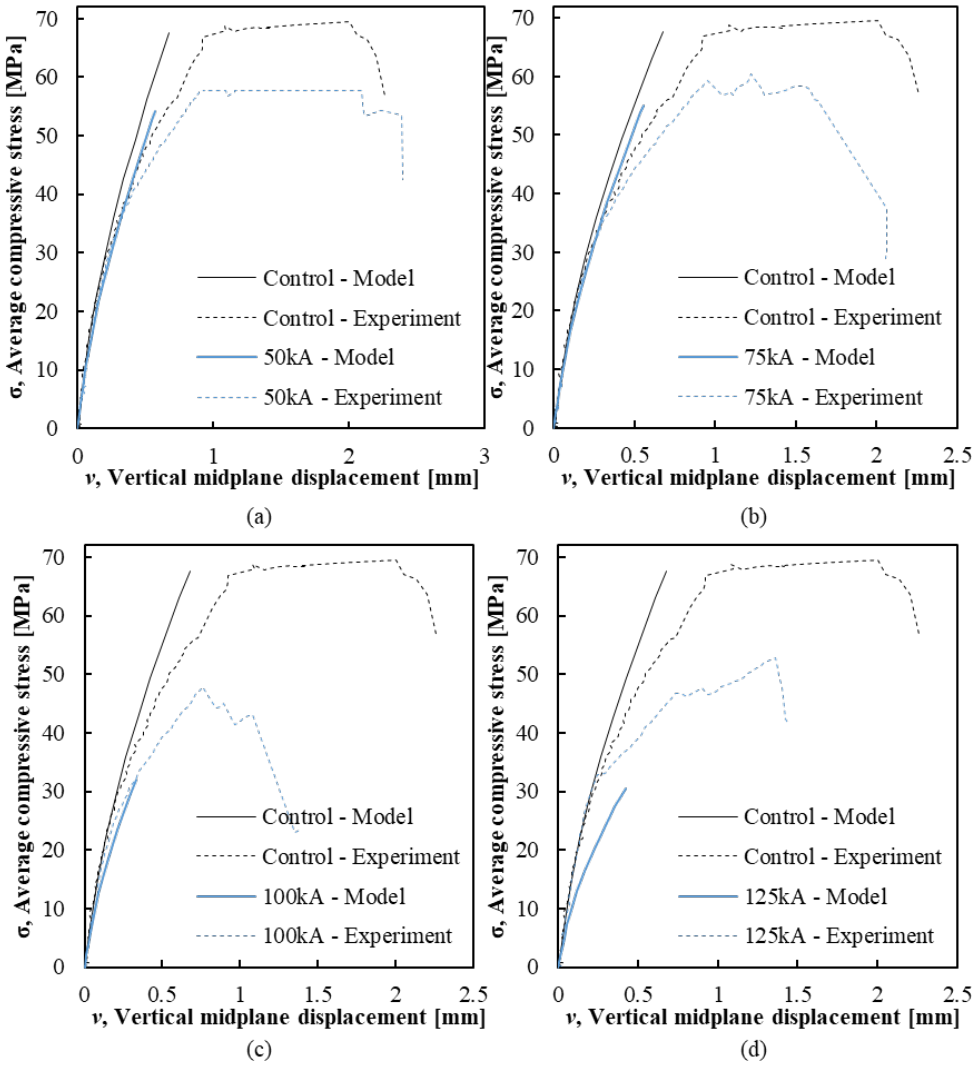

Figure 6.20: Measured and predicted stress vs in-plane vertical displacement plots (mid-plane edge displacement at vertical specimen symmetry line) corresponding to undamaged (control) and damaged states: Experimental and Model in-plane vertical load displacement curve comparison of undamaged (control) and damaged panels (a) 50 kA, (b) 75 kA, (c) 100 kA, and (d) 125 kA

Table 6.6: Panel stress (load) corresponding to first failure event obtained experimentally and from FE model simulations

Description	Undamaged (Control)	50 kA peak current	75 kA peak current	100 kA peak current	125 kA peak current
First failure event - DIC [MPa]	69.9	56.5	59.4	32.5	32.9
FE model prediction (first ply failure) [MPa]	67.6	54.2	55.1	32.1	30.6
% difference	3.3%	4.0%	7.3%	1.3%	7.1%

6.5.4 Out-of-plane displacement

The out-of-plane load displacement curves are presented for the FEM and the measured experimental results in Figure 6.21. As seen, the model predicts the out-of-plane displacement relatively well up to the first ply failure event on the FE model. It can also be seen that there is a gradual softening of the load-displacement curve as the damage is increased. The DIC data, especially for the most severely damaged samples, was difficult to record as the uneven damage surfaces made it difficult to apply the DIC and accounts for the variation in the results shown in Figure 6.21 (d).

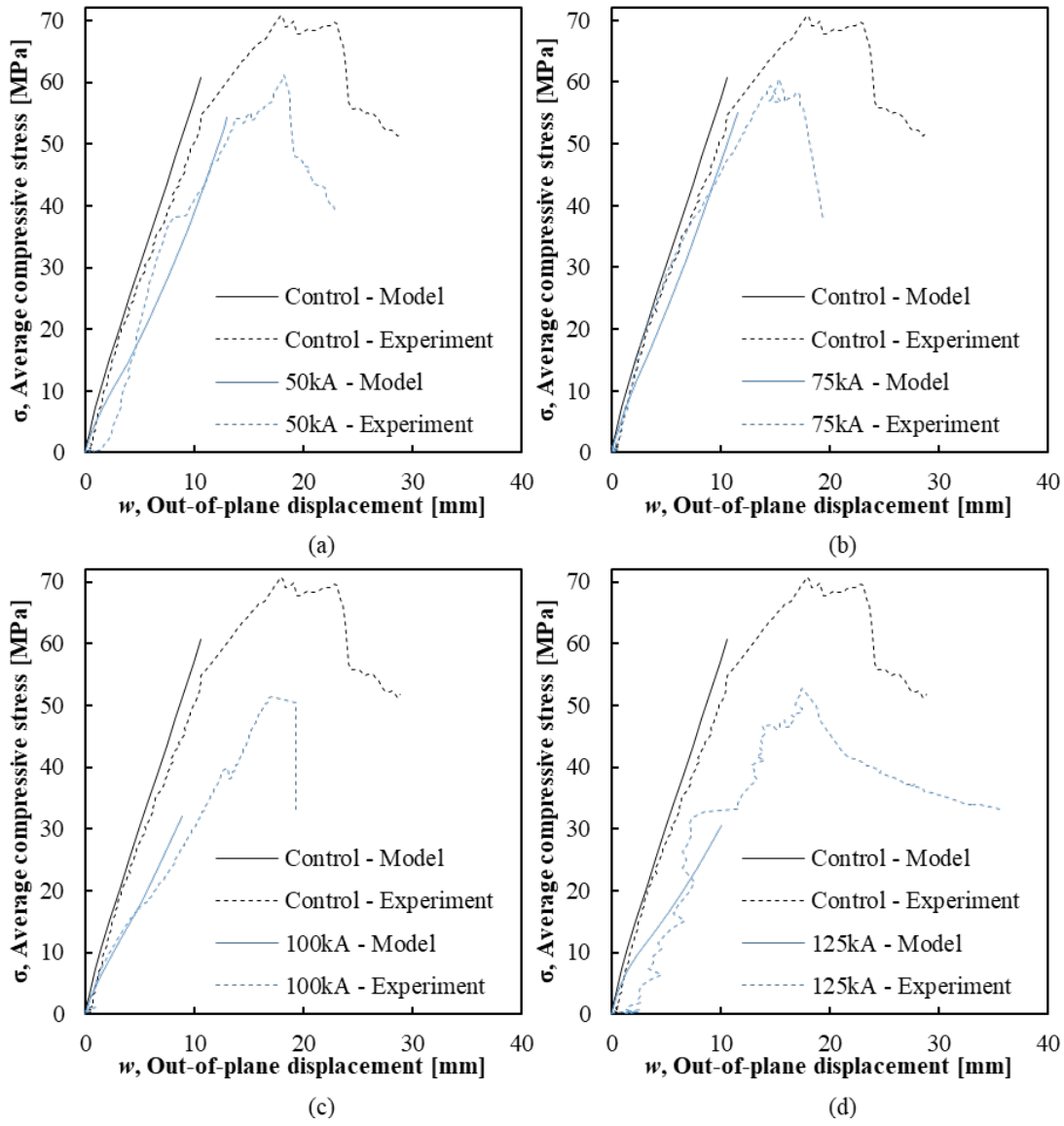

Figure 6.21: Experimental and Model out-of-plane vertical load displacement curve comparison of undamaged (control) and damaged panels (a) 50 kA, (b) 75 kA, (c) 100 kA, and (d) 125 kA

6.5.5 Failure Maps

Figure 6.22 - Figure 6.26 show the LaRC failure maps at each damage state failure loads from the structural model. The SDV7 failure map indicates the maximum failure index from the 6 LaRC criteria where 0 means no load and 1 means failure. Figure 6.22 shows the undamaged case which shows that the failure happens on the tension side. The failure map is smooth across the tension side and is related to the undamaged nature of the sample. Checking the mode of the failed region shows that the LaRC criterion predicts failure in matrix tension which is the same results as the experimental study.

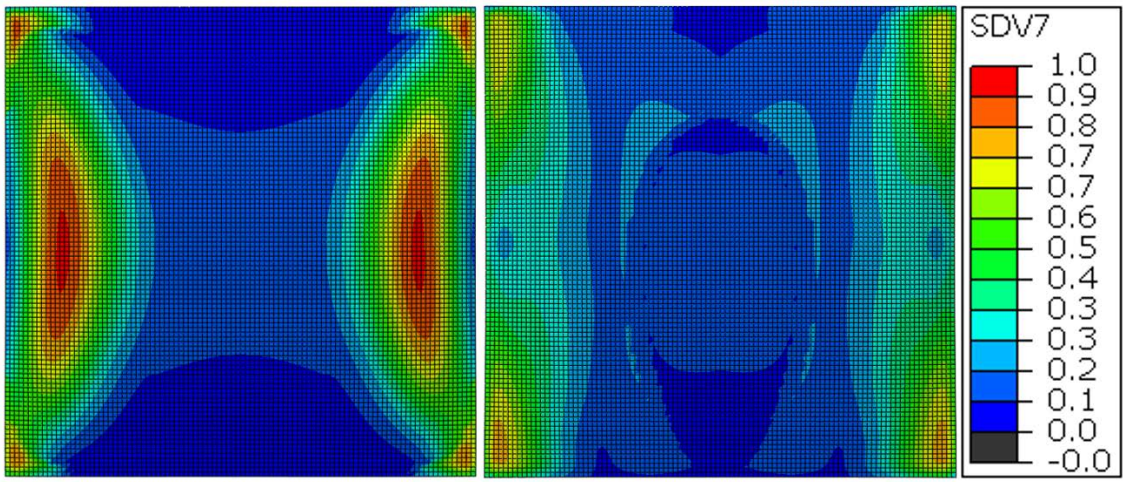

Figure 6.22: Maximum LaRC failure index (SDV7) failure map at 69.9 MPa compressive load of the undamaged (control) model for (a) tension side and (b) compression side

Figure 6.23 shows the failure map for the 50 kA damaged case. The failure map has changed from the control case showing that the zero regions in the centre of Figure 6.23 (a) are the damaged regions. These regions are zero as they have no stiffness and therefore have no load introduced into those elements. The failure map also shows that the failure is becoming more concentrated between the support and the damaged region due to the load redistributing around the damage region. The compression side, Figure 6.23 (b), is also showing the effect of the dispersing and concentrating of the failure indices underneath the damage. Similarly, as the control, the failure mode remained matrix tension.

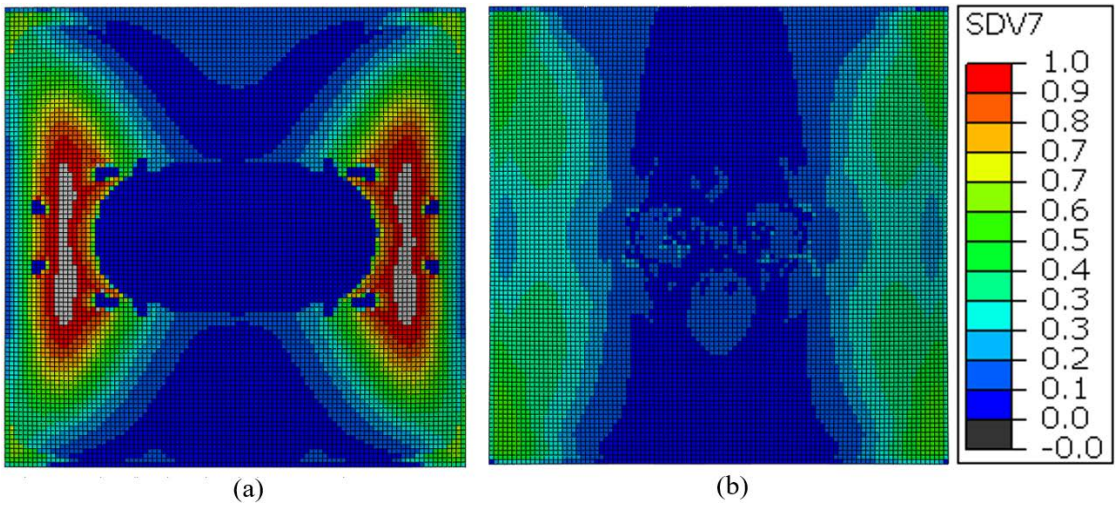

Figure 6.23: Maximum LaRC failure index (SDV7) failure map at 56.5 MPa compressive load of the 50 kA damaged model for (a) tension side and (b) compression side

Figure 6.24 shows the failure map for the 75 kA damaged case. The failure map has changed from the control case showing that the zero regions in the centre of Figure 6.24 (a) are the damaged regions. This failure map is different to the 50 kA case as the damaged shape is not as wide and therefore less concentration and less load being redistributed. The compression side, Figure 6.24 (b), is also showing the effect of the introduction of damage into the structural load response. The failure mode remained matrix tension.

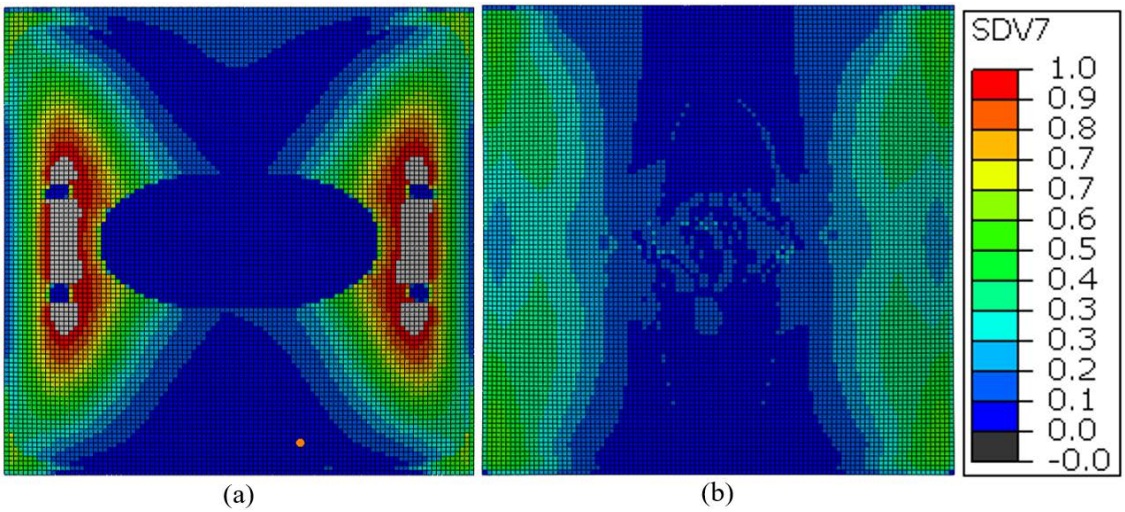

Figure 6.24: Maximum LaRC failure index (SDV7) failure map at 59.4 MPa compressive load of the 75 kA damaged model for (a) tension side and (b) compression side

Figure 6.25 shows the failure map for the 100 kA damaged case. The failure map has changed from the control case showing that the zero regions in the centre of Figure 6.25 (a) are the damaged regions. As can be seen in Figure 6.25 (a), the failure map is becoming less smooth and more impacted by the damage. The redistribution of load is concentrating the load between the damage and the support. The compression side, Figure 6.25 (b), is also showing the effect of the load redistribution from the damage. However, the failure mode remained matrix tension.

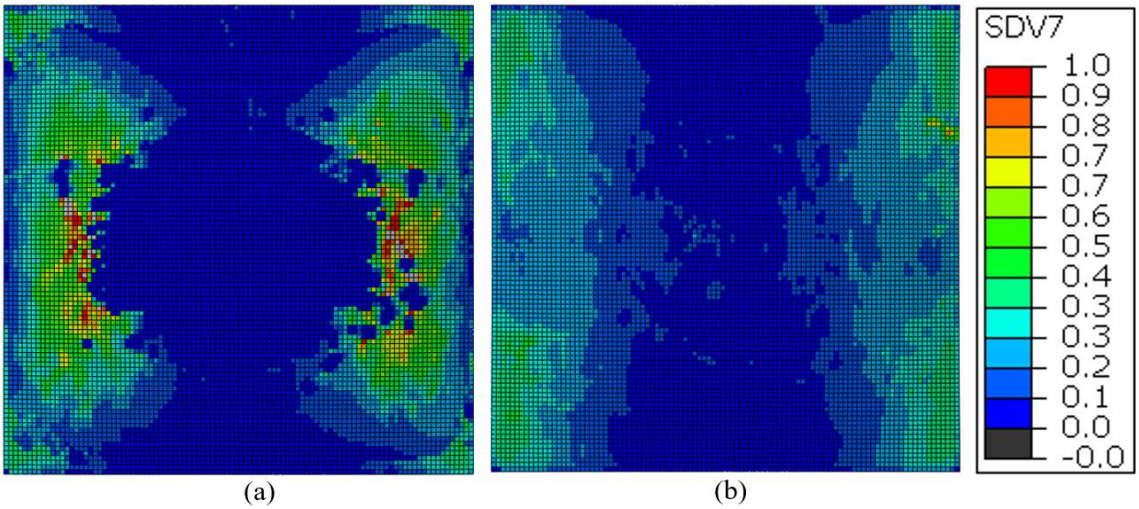

Figure 6.25: Maximum LaRC failure index (SDV7) failure map at 32.5 MPa compressive load of the 100 kA damaged model for (a) tension side and (b) compression side

Figure 6.26 shows the failure map for the 125 kA damaged case. The failure map has changed from the control case showing that the zero regions in the centre of Figure 6.26 (a) are the damaged regions. As can be seen in Figure 6.26 (a), the failure map is becoming less smooth and more impacted by the damage. Also, it can be seen that the failure map is now non-symmetric with the failure occurring on the left side. Figure 6.26 (b) shows that the non-symmetry has also developed on the compression side. However, the failure mode remained matrix tension.

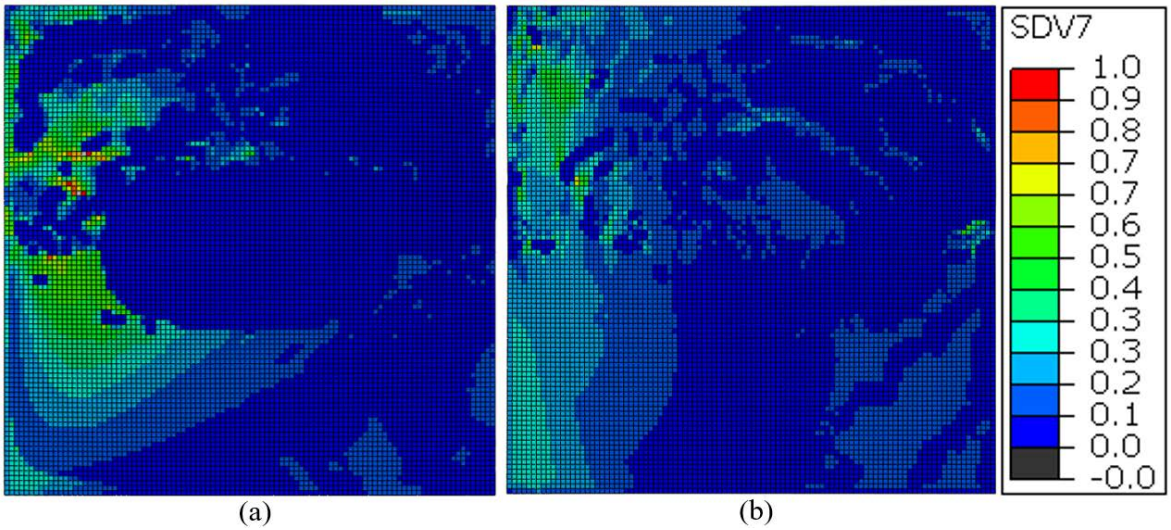

Figure 6.26: Maximum LaRC failure index (SDV7) failure map at 32.9 MPa compressive load of the 125 kA damaged model for (a) tension side and (b) compression side

6.6 Discussion

The research presented a study of the compressive load response from a structural scale UD CFRP laminate both experimentally and through a finite element model. The series of experimental samples were exposed to lightning strikes as defined in section 4.3.5. Figure 6.27 presents the first

failure event of the FE predictions and the experimental results compared against the lightning parameters peak current, charge, and specific energy. Figure 6.27 (a)-(c) all show a similar result with the increasing peak current, charge, and specific energy all decreasing the compressive stress level which causes the first failure event in the post-buckling failure load-response. The proposed structural model results matched the experimental results for all the lightning parameters with linear fits which had slopes with similar magnitudes.

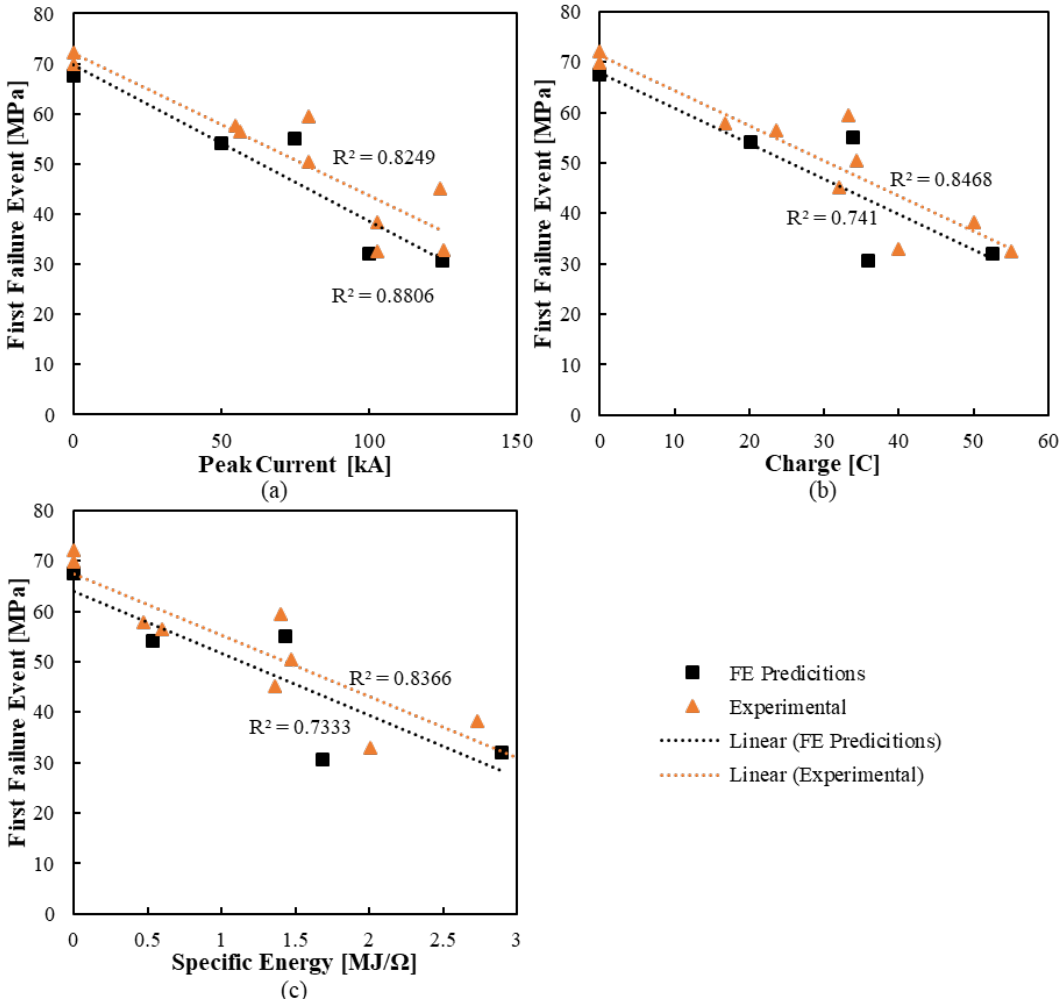

Figure 6.27: First failure event identified by the structural model (FE predictions) and the AE5 bare surface specimen experimental results against the (a) peak current, (b) charge and (c) specific energy

Figure 6.28 shows the first failure event compared to the damage volume and Figure 6.29 shows the first failure event against the damage depth. The results show a similar trend as the damage volume and damage depth increase as the first failure event stress decrease. Although both trends match closely the highest linear fit or R^2 value was with the damage volume and FE predictions. However, the damage volume slopes have a higher degree of difference and can be seen that the slope for the FE predictions are becoming further different to the experimental results. The slopes of the damage depth to first ply failure have more similar magnitudes. This indicates that the damage depth is the more important parameter to be accurate to predict the correct first failure event.

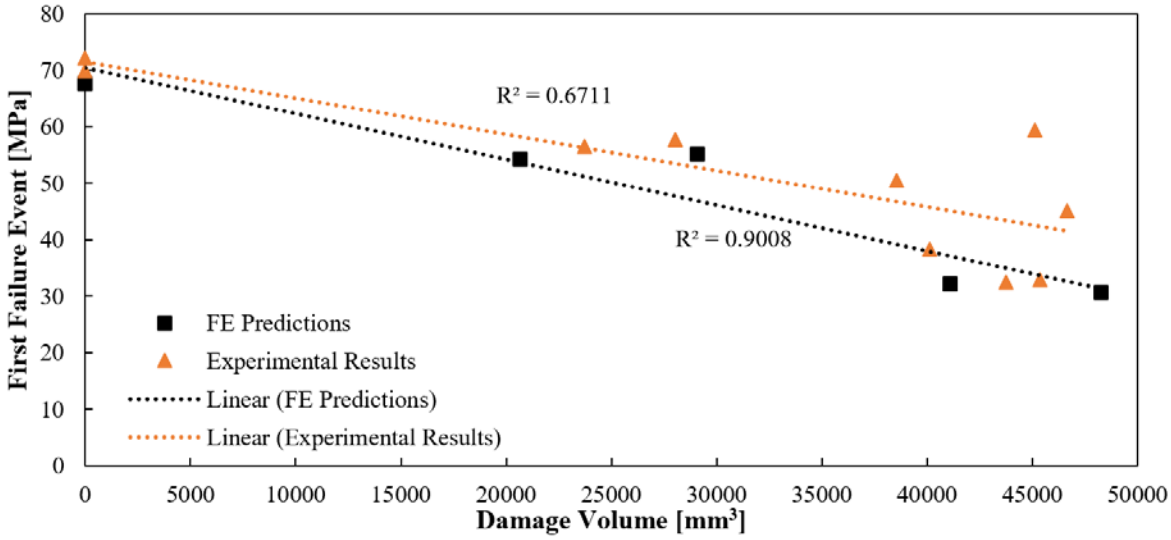

Figure 6.28: First failure event identified by the structural model (FE predictions) and the AE5 bare surface specimen experimental results against the damage volume measured by the Damage Model for the FE predictions and X-ray CT results for the experimental results

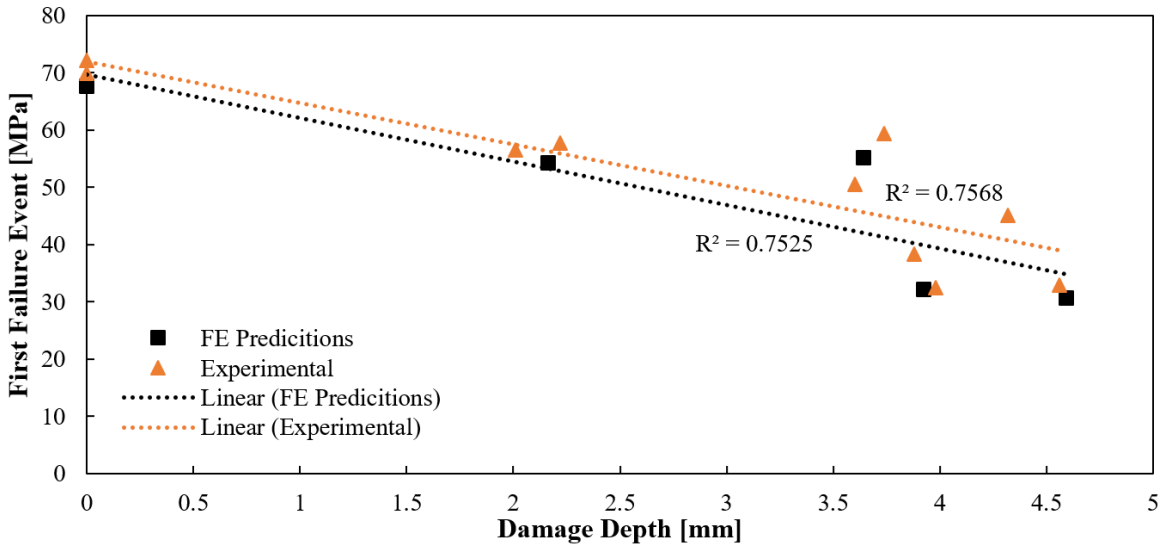

Figure 6.29: First failure event identified by the structural model (FE predictions) and the AE5 bare surface specimen experimental results against the damage depth measured by the Damage Model for the FE predictions and X-ray CT results for the experimental results

6.7 Summary

This chapter is the conclusion of the modelling framework as described in section 5.2. The results from a structural model which uses the damaged results from the Damage Model (as described in Chapter 5) to predict the compressive load which causes the first failure event. Both the structural model and the experimental study of the first failure event of a damaged UD CFRP laminate subjected to compression has been presented. The focus of this work was to determine if the modelling could accurately predict the first failure event from a pure modelling framework (as described in section 5.2). The model was compared to the control undamaged case to check whether the model was accurately predicting a typical UD CFRP laminate first ply failure event

compared to experimental results of the same condition. The results of the validation study showed that the model was able to accurately predict the load response by validating the displacements and strains from the undamaged case. The model was found that the first ply failure event matched closely to the first failure event from the experimental results with a maximum difference between the FE and experimental results of 7.3%. The comparison of these results showed that the trend of the damage matched well to the experimental results when compared to the peak current, charge, and specific energy. The highest correlation of the trend was with the peak current.

The final results of the modelling framework leaves a fully developed modelling approach which can simulate the residual strength or first failure event of a CFRP laminate subjected to lightning.

Chapter 7

Conclusions and Future Work

7.1 Conclusions

The primary aim of this research was to characterise damage of CFRP materials used in Wind Turbine (WT) blades subjected to lightning strike events. The main effort of this work has led to the development and validation of a novel modelling framework, which can be used by designers and engineers to understand the implications of different lightning strike events in terms of damage and reduced structural performance. The model validation has been conducted on the meso and laminate scales with respect to material damage, and a novel structural scale test called Compression After Lightning Strike, or CALS, has been developed and commissioned for the validation of model predictions of the post lightning strike load response and failure of UD CFRP laminates.

The motivation for the work has arisen from the lack of understanding of lightning strike induced damage and the consequences in terms of residual load response and collapse behaviour. The research conducted is divided into 5 main sections:

1. Experimental investigation of the degradation of mechanical properties in CFRP laminates subjected to electrical current conducted along the fibre direction.
2. The characterisation of lightning damage through simulated lightning strike experiments conducted on representative WT UD laminates.
3. Development of unique post processing techniques for CT and thermography to inspect lightning damage on CFRP laminates.
4. Development and validation of fully coupled electrical-thermal damage modelling of direct lightning strike events in CFRP laminates used in WT blades.
5. Experimental investigation and finite element analysis of the structural scale load-response, damage and failure behaviour of representative CFRP panels with and without lightning strike induced damage.

The results of the research have provided a means of developing a modelling approach which can be used by wind turbine designers to assess lightning strike induced damage. The modelling approach can be applied for different lightning scenarios, enabling large scale parametric studies possible for any blade design utilising CFRP materials. The modelling framework has potential use in the evaluation of lightning damage on new and existing blade designs, and may help provide guidelines for inspections/repairs after lightning damage occurs.

A brief summary followed by the appropriate conclusion for each topic are detailed in the subsequent sections. Some recommendations are presented to provide research opportunities and help close knowledge gaps.

7.1.1 Experimental investigation of the degradation of mechanical properties in CFRP laminates subjected to electrical current conducted along the fibre direction

The work presented in Chapter 3 has fulfilled the first objective of this PhD thesis. Simulated lightning strike damage was inflicted to representative CFRP UD laminate specimens. Subsequent coupon tests were conducted in compression and shear to determine the lightning strike induced reduction of the strength and Young's modulus. The results have shown that lightning strike induced damage exerts a large effect on the mechanical properties of composite materials. The following conclusions were made:

- Seven CFRP strips were subjected to simulated lightning strike events characterised by three different waveforms considered representative for the exposure experienced by WT blades in operation: DC, Impulse, and Impulse+DC. The recorded temperatures and the mechanical tests have shown that the most significant damage was induced to the CFRP specimens, which experienced the highest temperature and combustion/burning.
- Although visual inspection may not detect damage, there can be a reduction in mechanical properties when CFRP materials are exposed to lightning strikes in a conducted current capacity.
- The compression tests showed that impulse current has a more severe impact on the compression strength than DC current, with a strength reduction of approximately 19% caused by a 60 kA 10/110μs waveform (10 Coulomb). In comparison, a 7% reduction of the compression strength was observed for the case of a 0.75 kA long duration (200 Coulomb) DC current. There was little difference between the effects caused by impulse and DC currents on the shear strength with 7-8% reduction for both the impulse and long duration currents.
- The most severe damage was inflicted by combined impulse and DC currents (Impulse+DC), which resulted in reductions of the compression strength of more than 70% and more than 40% for the shear strength.

7.1.2 Characterisation of direct lightning strike induced damage to UD CFRP laminates

Chapter 4 described the research conducted where several direct simulated lightning strike tests were conducted on UD CFRP laminates, and the resulting specimen damage states were evaluated by visual inspection, IR thermography, and X-ray CT imaging. The resulting damage inspections showed that the size of the damaged material zone as well as the severity of damage is mainly

dependent on the specific energy of a lightning strike event than to the peak current or electrical charge. This clearly indicates that the evolving temperature increases is the primary source of the damage induced because the specific energy is closely linked to Joule heating. The conducted tests and subsequent data analyses have also established that the lightning strike induced damage propagated more in the direction transverse to the fibres than along the fibre direction. This finding has not been previously reported in literature, and this feature of the damage mechanisms in UD laminates has provided the basis for explaining the additional physics involved, which was subsequently incorporated in the coupled electrical-thermal meso-scale damage model that was developed as part of this research. The conclusions drawn from this section were:

- Four different types of damage are typically seen in UD CFRP laminates: fibre breakage, resin burn off, delamination, and charring damage.
- The damage shapes and sizes on UD CFRP laminates are very different to the quasi-isotropic results and showed that the damage propagated in the transverse direction. Through this investigation and the investigation of the Damage Model, it was found that the UD CFRP laminates have a potential to have dielectric breakdown in the transverse direction and that propagation of current to have a large effect on the damage shape and size.
- Surface temperatures on the laminate were recorded during the lightning strike tests and confirmed that the heat conducted in the transverse direction and held in the transverse direction which led to damage.
- The AE5 test presented different surface treatments and the assessment showed a large effect on the results where the conductive copper mesh surface stopped damage in the CFRP laminate and the insulating fibreglass surface damage the CFRP laminate more than the bare surface CFRP laminates.
- A comparative study of the damage to absolute value of charge and specific energy was presented. The results indicated that the specific energy lightning parameter has a closer trend to the magnitude of the surface damage.

7.1.3 Damage inspection techniques

Chapter 4 and Chapter 5 presented two unique approaches for analysing lightning strike induced damage. The first approach included a post processing procedure for thermography that provides a rapid means of assessing damage severity, which can quickly identifying damage compared to traditional techniques, such as UT. The second approach used X-ray CT data to separate a laminate into individual plies. This technique is important because composites are generally evaluated based on a ply rather than a volume. Once part of the ply is damaged, it is typically assumed that the

entire ply is damaged. This approach allows damage to be pinpointed at the ply level rather than traditional volume definition by CT. It also provides a comparative tool to check against a FEM.

7.1.4 Lightning strike damage model

Chapter 5 presents the work conducted regarding the development and validation of a coupled electrical-thermal meso-scale numerical model for lightning strike induced damage in UD CFRP laminates. To account for the experimental observation that damage evolves more extensively in the direction perpendicular to fibres (or transverse direction) than in the fibre direction, the developed damage model includes the electric field dependency, which simulates electric breakdown. The implementation of the electric field dependency is completely novel. It has been shown that the model predictions match the experimental results well, especially in the laminate (or through-thickness) direction, thus indicating that the proposed model represents a significant improvement over previous models reported in literature. The model validation was conducted considering a sample UD laminate with properties representative of a typical WT blade sparcap laminate. The results from the damage model were exported and used in a structural model. The following conclusions were drawn:

- The proposed Damage Model was compared to a conventional damage model experimental data. The results of the comparison study showed that the proposed Damage Model had an increased ability to predict the damage in the transverse direction for UD materials (25% error) which was not able to be simulated in the conventional model accurately (77% error).
- The damage prediction also increased the ability in predicting the through-thickness damage depth. The Damage Model predicted the damage depth with less than 8% error of the experimental data and the conventional model over-predicted the damage depth with an error of 170%.
- The proposed model only requires the addition of two new properties: electric breakdown strength in the transverse and through-thickness directions.

7.1.5 Structural response of lightning damaged panels

The post lightning strike load response and failure behaviour of structural scale CFRP panels representative of WT sparcap laminates were evaluated both experimentally and through model simulations. The experimentally focused characterisation and model validation was partly based on the lightning strike damaged CFRP panels discussed in Chapter 4 of the thesis, and further to this by the introduction and commissioning of a new structural scale testing methodology referred to as Compression After Lightning Strike (CALS). The CALS test was introduced in this research because the compression loading behaviour is one of the most important WT blade design drivers.

To properly assess this, it is necessary to conduct the testing of composite CFRP panels that are large enough to capture both material damage and the interactions with structural scale phenomena, in particular the nonlinear load response and buckling behaviour of panel sized test specimens that can realistically replicate CFRP sparcap laminates. The modelling included the development of a geometrically nonlinear solid model with the lightning strike induced damage, predicted by the coupled electrical-thermal meso-scale model, imported to the structural FE model through a point cloud approach developed and validated for this research.

Experimental results showed that the lightning degraded the material and ultimately failed at lower load levels than the undamaged panel. The model was validated with the experimental results and ultimately showed good agreement. The following conclusions were drawn:

- Both the structural model and the experimental study were able to determine the first failure event of a damaged UD CFRP laminate subjected to compression and determine the load response.
- The results of the validation study showed that the model was able to accurately predict the load response by validating the displacements and strains from the undamaged case. The model was found that the first ply failure event matched closely to the first failure event from the experimental results with a maximum difference between the FE and experimental results of 7.3%.

7.2 Future Work

The outcomes of the research have highlighted a number of avenues worthy of further investigation, which may lead to better understanding of lightning damage on CFRP materials. It has been clearly presented that the lightning strike induced damage has a large impact on the structural response and therefore should be studied further. The recommendations are broken down into the five sections as above.

7.2.1 Experimental investigation of the degradation of mechanical properties in CFRP laminates subjected to electrical current conducted along the fibre direction

It was clearly shown that even though no visual damage could be detected there was a reduction in mechanical properties. Therefore, the following recommendations are made to better understand these phenomena:

- The visual inspections of the damaged samples revealed that the first damage indication on the specimens was exposed stitching. Another set of tests examining lightning damage on prepreg or pultruded specimens free from the influence of stitching would be beneficial.

This would determine if the stitching provides additional resistance and ultimately more damage.

- The reason for the degradation of strength in these types of tests should be understood. An initial recommendation is to run a microscale model to determine if there is a larger increase in temperature around the conductive fibre/resin interface causing damage to the interface and could account for the decrease in shear and compression degradation.

7.2.2 Characterisation of direct strike lightning strike induced damage to UD CFRP laminates

The experimental data conducted in Chapter 4 showed a previously unreported phenomena which led to damage being larger in the transverse direction than in the fibre direction. The following recommendations are given to aid in understanding this phenomenon:

- Direct strike testing of quasi-isotropic panels with thick plies of 800gsm. This will help determine if the electric field dependency is more in relation to the unidirectional nature of the material used or if thick plies prevent the dispersal of the electric field.
- Since this work needed a baseline for lightning damage, the work presented mainly focused on a bare surface. It was found that adding a surface treatment does affect the results as shown in the fibreglass surface results. Therefore, it would be interesting to place copper-mesh or some other lightning protection strategy between the fibreglass and bare specimen which can still structurally carry the interlaminar shear between the specimens and see if this lightning protection measure would be better than exposing copper mesh to the blade elements.

7.2.3 Lightning strike damage model

The Damage Model was able to better predict damage for UD materials subjected to lightning. The following recommendation is made to advance this model:

- The conductivities in the Joule heating equation have an exponential influence on the temperature results of the sample. A parametric study of the damage model should be done to determine the changes in conductivity which would mitigate damage and a feasibility study to determine if this change is possible.
- A large difference in temperature response was found between the Damage Model and experimental measurements as a result of the performance. This is a key limitation of the measurement capabilities of solid state infrared detectors. In the future, a means of measuring higher temperature could be used such as a pyrometer.

- A parametric study of the additional parameters used in the damage model could provide better correlation between the damage area, damage volume, and damage depth rather than those assumed for this study.

7.2.4 Structural response of lightning damaged panels

The following recommendations are made to help understand the load response due to lightning damage on CFRP materials:

- The compressive behaviour is still the ultimate design driver for long slender WT blades and therefore should be used in subsequent test. However, new damaged panels with different surface treatments need to be tested as this changes the depth and shape of the damage on the structure. Therefore, new test should be conducted to determine the effect of potentially losing the fibreglass shell and having different damage depths and shapes.

Appendix A

Initial direct strike testing

A.1 Visual damage inspection

Visual inspection is the first approach taken for the review of composite parts for damage. Optical tools aided in the identification of damage.

All specimens were placed so that the electrode was over the centroid of the sample. This was done to have the lightning strike as close as possible to the centroid of the specimen. The damage seen was categorized into three different categories “Surface Damage”, “Charred Damage”, and “Delamination Damage”. The surface damage was defined by having a continuous area of exposed fibres and burnt resin. The charred damage was defined by a scatter of exposed fibres or burnt remains on the surface of the specimen. The charred damage encompassing all of the surface damage. Delamination damage was found where a physical separation could be seen.

Visual inspection is conducted by overlooking the specimen to identify damage on the surface of the specimens. An image was taken of the sample struck with lightning, and it was assessed visually to areas/zones of broken fibres, burnt off resin, loss of thickness and visible burn marks. The damage area was estimated by drawing the area over the damaged image in AutoCAD. The images were brought into AutoCAD and scaled using a ruler. Polylines were drawn to create a best fit area which enclosed the damage, as shown in Figure A.1. Measurements were verified with callipers. It should be noted that the marking of the damage area is subjective to the inspector; however, there should only be slight variations if the rules suggested above are used. Three different inspectors measured a single image and the variation for the damaged areas were calculated: >2% for surface and delaminated damage area and 8% for the charred area. The vertical and horizontal lengths were measured at the extreme ends of the damage area. The samples are UD which makes these lengths of damage along the fibres and transverse.

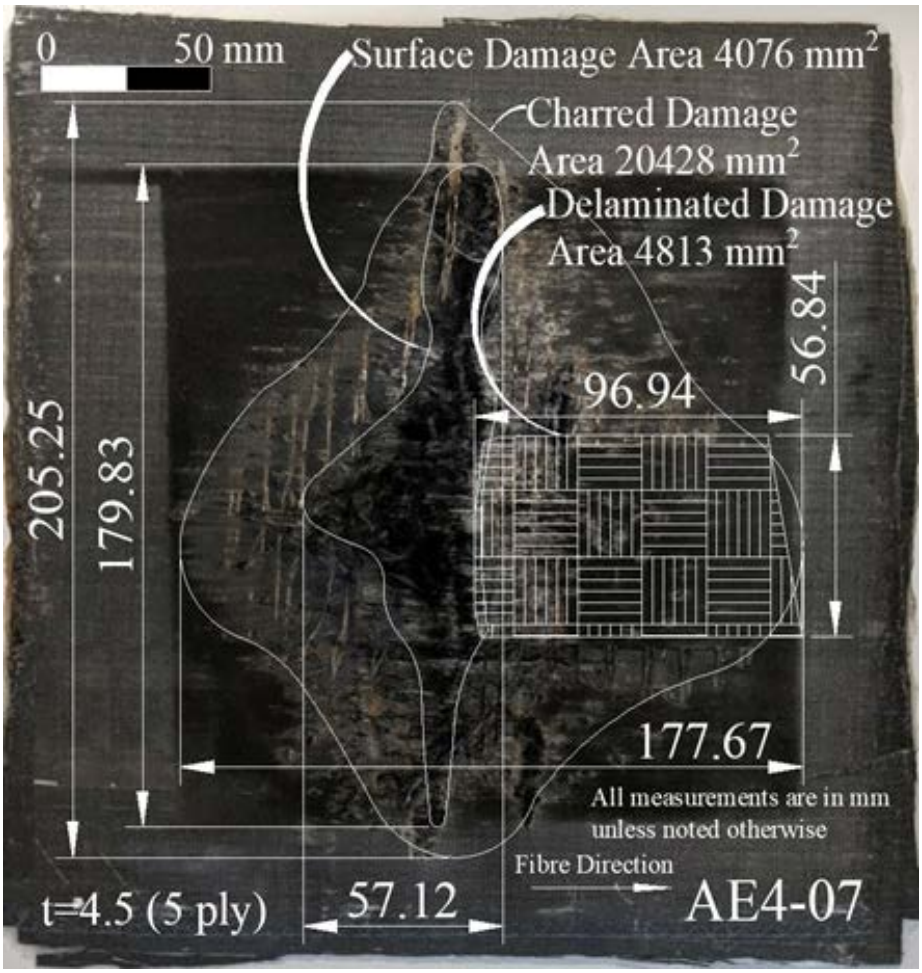

Figure A.1: Visual Inspection of Damaged Specimen from Test AE4-7

A.2 AE1: Influence of Repeated Lightning Strikes

A.2.1 Specimen Manufacturing

AE1 test was conducted to determine the effect of multiple lightning strikes at the same location. The composite materials were made up of woven carbon fibre dry fabric (375 gsm) and epoxy resin. An eight-ply woven CFRP composite large plate with dimensions of 420mm x 420mm x 4.03mm was manufactured by vacuum liquid resin infusion. Four lightning strike specimens were cut from the large plate with dimensions 200mm long x 200mm wide x 3.90mm thick. Two uniaxial test specimens were cut to measure the control. Figure A.2 shows the large plate with the cut lines used to make the final specimens. The individual specimens were chamfered along the four edges with an approximate 1:4 taper to expose the carbon fibres and to provide a connection to ground.

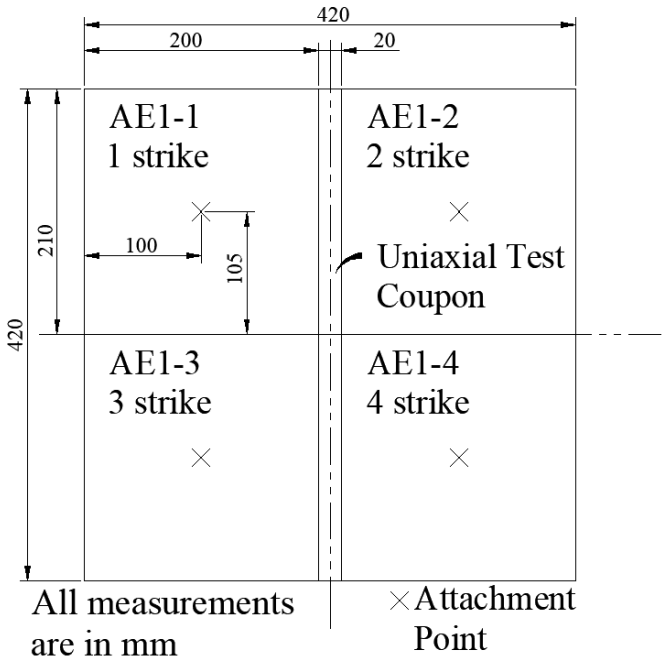

Figure A.2: Specimen construction for AE1 – influence of repeated lightning strikes

A.2.2 Simulated Lightning Strike Experiments

The lightning test setup is shown in Figure A.3. Figure A.3 (a) shows the test rig that includes the electrode, the specimen, and the copper grounds. The copper grounds are attached along all 4 edges of the specimen. The specimen is placed approximately 20mm away from the specimen as shown in Figure A.3 (b). The current travels from this electrode to the closest surface before going through the sample to ground.

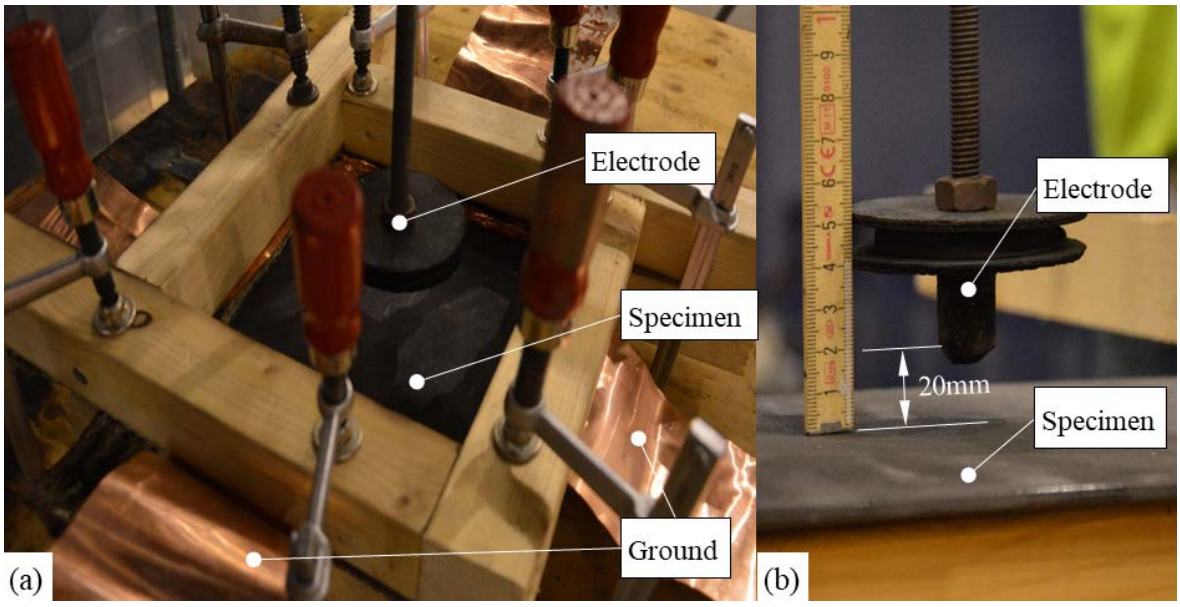

Figure A.3: (a) Test setup for AE1 and (b) electrode gap

The AE1 specimens were subjected to oscillating waveforms as defined by IEC61400-24 Annex D [47]. All of the oscillating waveforms were similar with an average peak current of 39kA and

17/145μs waveform characteristics. Figure A.4 shows an example of the waveform for the first simulated lightning strike on the first specimen (AE1-A-1).

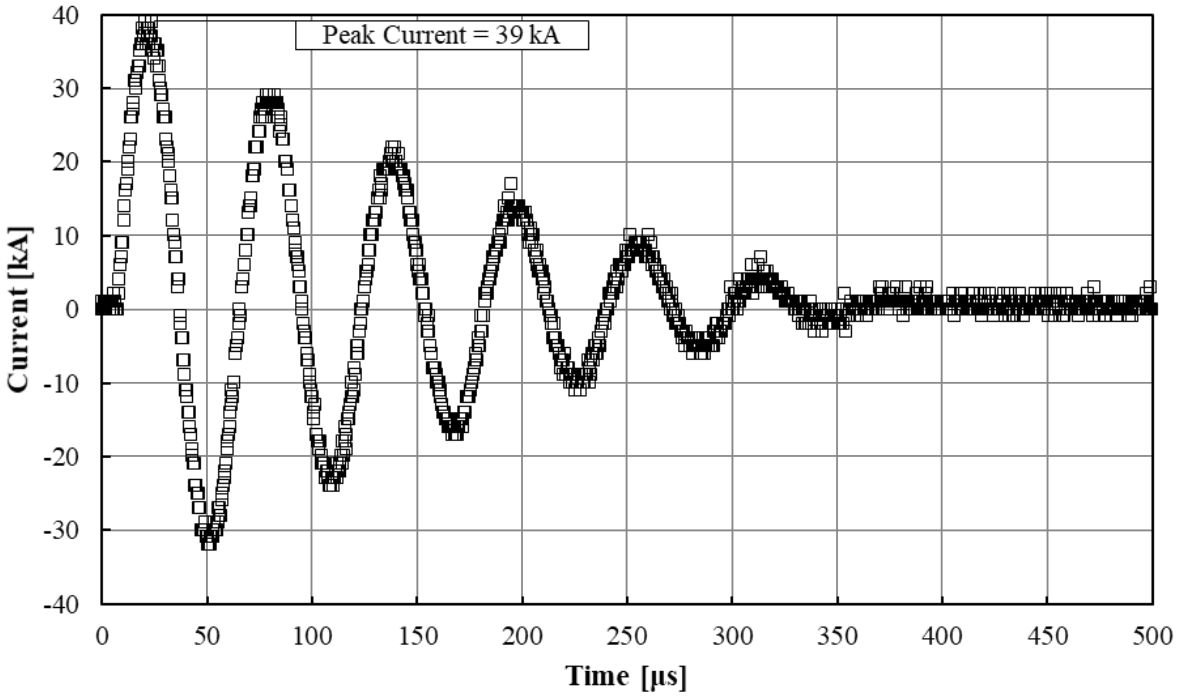

Figure A.4: AE1-A-1 current waveform

Table A.1 provides an overview of the characteristic parameters used in the AE1 lightning strike tests. The specimens are labelled as AE1-X-Y where "X" indicates the specimen and "Y" indicates the lightning strike iteration. The resulting |charge|, peak current, and specific energy are provided.

Table A.1: Test parameters defined for the simulated lightning strike test AE1: peak current, waveform, charge, and specific energy applied to the specimens

Sample ID	Strike Attempt	Peak Current [kA]	Waveform Characteristics (Impulse $t_1/t_2/t_f$) [μs]	$\|Q\|$ [C]	AI [kJ/Ω]
AE1-A-1	1st strike	37.6	18/155/481	3.88	71
AE1-B-1	1st strike	35.7	17/159/354	3.69	63
AE1-B-2	2nd strike	38.7	17/142/341	4.00	79
AE1-C-1	1st strike	34.7	17/142/355	3.58	59
AE1-C-2	2nd strike	38.4	17/141/355	3.97	77
AE1-C-3	3rd strike	38.6	17/141/355	3.98	79
AE1-D-1	1st strike	38.1	17/142/345	3.94	72
AE1-D-2	2nd strike	37.7	17/145/355	3.89	75
AE1-D-3	3rd strike	38.4	17/142/355	3.97	76
AE1-D-4	4th strike	37.3	17/149/355	3.85	76
Q = 0 for oscillating waveform					

Table A.2 shows the sum of |charge| and specific energy for each specimen where Q_T and AI_T being the sum of the |charge| and specific energy applied to each specimen.

Table A.2: Sum of charge and specific energy for AE1

Specimen ID	$\lvert Q_T \rvert$ [C]	AI_T [kJ/Ω]
AE1-A	3.88	71
AE1-B	7.69	142
AE1-C	11.5	215
AE1-D	15.7	299

During the simulated lightning strike experiments, an infrared camera was used to capture the thermal evolutions. The infrared camera was a PYROVIEW 640L, which is an uncooled micro-bolometer array with 640 × 480 pixels. An image capture rate of 17.5Hz was used. The camera captured the surface of the specimen where lightning attached.

A.2.3 Results

Four CFRP specimens were subjected to simulated lightning strike events for test AE1. The four specimens were struck with 1, 2, 3, and 4 lightning strikes respectively. For all AE1 specimens, the surface damage and charred damage were primarily in a circular shape; see specimen AE1-A in Figure A.5. AE1-A through AE1-D had similar patterns of surface and damage shapes and sizes.

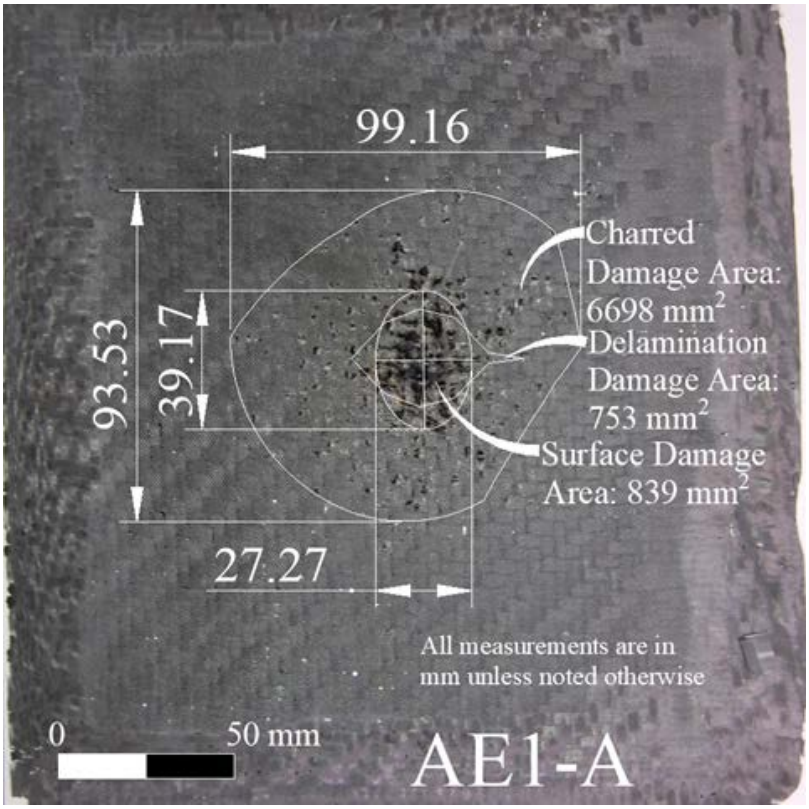

Figure A.5: Visual inspection AE1-A

Table A.3 shows the dimensions of the damage including the outer lengths and the area. Since the material was woven the lengths are in the x and y directions.

Table A.3: Visual inspection results for AE1

Sample ID	Surface Damage			Charred Damage		
	l_x [mm]	l_y [mm]	Area [mm^2]	l_x [mm]	l_y [mm]	Area [mm^2]
AE1-A-1	27.27	39.17	839	99.16	93.53	6698
AE1-B-1	30.11	42.15	997	94.51	93.12	6791
AE1-B-2	30.41	43.55	1040	94.98	93.27	6836
AE1-C-1	41.54	31.16	1016	94.32	89.16	6617
AE1-C-2	41.61	31.17	1019	94.66	89.25	6647
AE1-C-3	41.63	31.17	1019	95.93	90.78	6852
AE1-D-1	35.8	33.42	939	89.38	93.11	6983
AE1-D-2	35.88	33.45	942	89.40	93.14	6986
AE1-D-3	35.88	33.45	942	89.40	93.14	6986
AE1-D-4	35.98	33.46	945	89.44	93.16	6991

As can be seen in Table A.3, additional lightning strikes applied to the specimen do not increase the amount of damage. The areas are presented in Figure A.6 (a) and (b) which plots the damage area against the cumulative charge and specific energy.

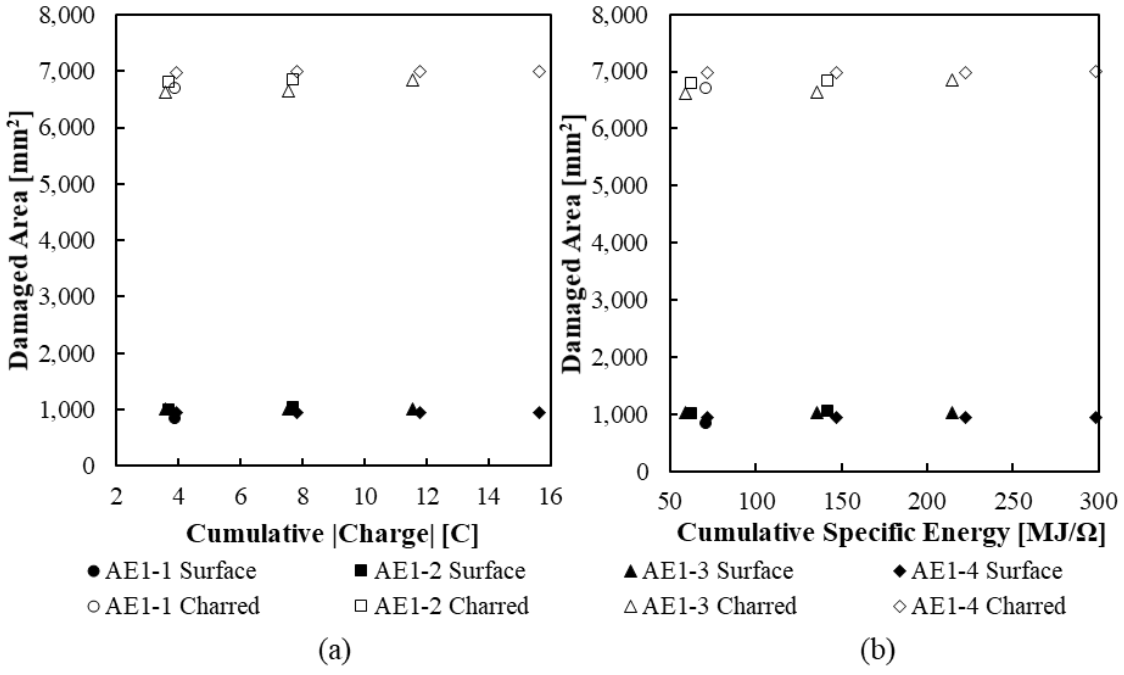

Figure A.6: Visual inspection damage area compared to number of lightning strikes from AE1 against (a) cumulative |charge| and (b) cumulative specific energy

Similar to the area, Figure A.7 (a) and (b) shows the outer extreme lengths of the damage are not increased with additional lightning strikes applied to the specimen.

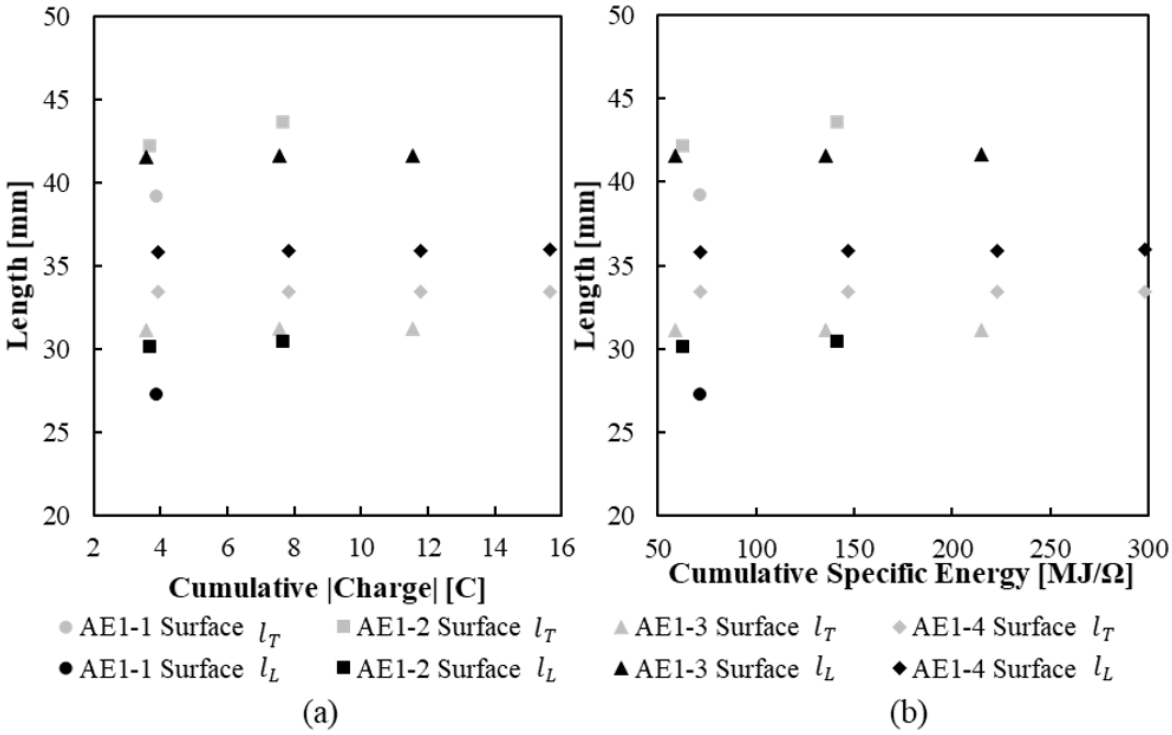

Figure A.7: Visual inspection damage lengths to test AE1 against (a) cumulative |charge| and (b) cumulative specific energy

10mm strips were cut from all the AE1 test specimens; see Figure A.8. The strips were used to evaluate the sub-surface defects.

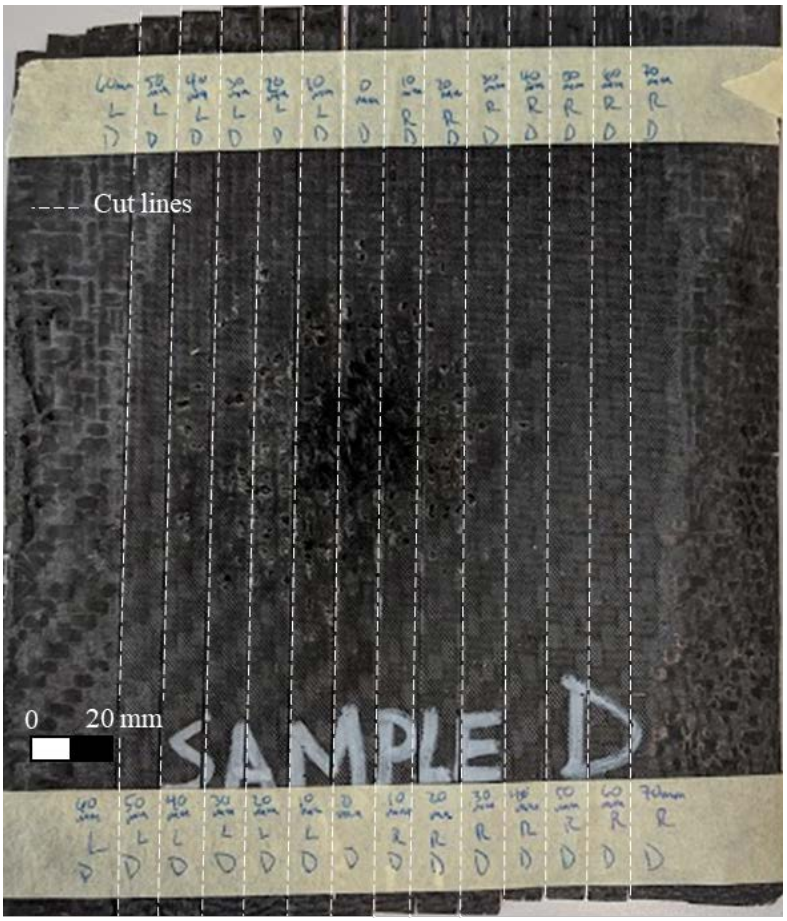

Figure A.8: Waterjet cut of AE1 specimens

Examining the edges of the waterjet strips, each specimen had clear delaminations. The delamination damage increased with each successive lightning strike. Examples of the delaminations are shown in Figure A.9.

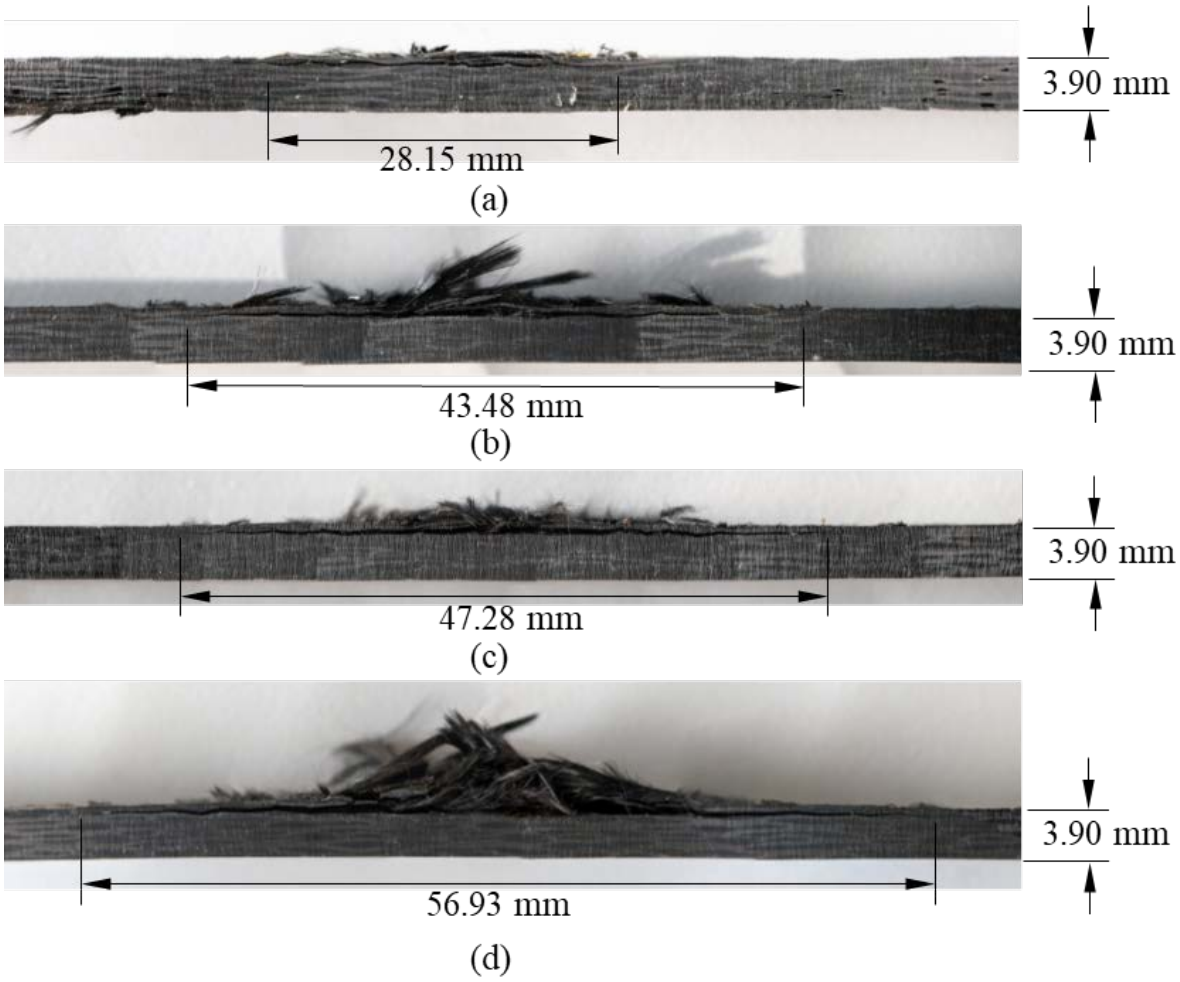

Figure A.9: Microscopy images (a) AE1-A, (b) AE1-B, (c) AE1-C, and (d) AE1-D

Each strip edge delaminated length was measured. The measured distances were added to a chart with the distance from the centre of the damage in Figure A.10 (a). This provided a delaminated region. The coordinates of this region were used to calculate a delamination area. The delaminated areas were compared against the cumulative |charge| and specific energy in Figure A.10 (b) and (c). The figure shows that the delamination region for each sample grew in a linear fashion with both |charge| and specific energy being good indicators of the amount of delamination damage.

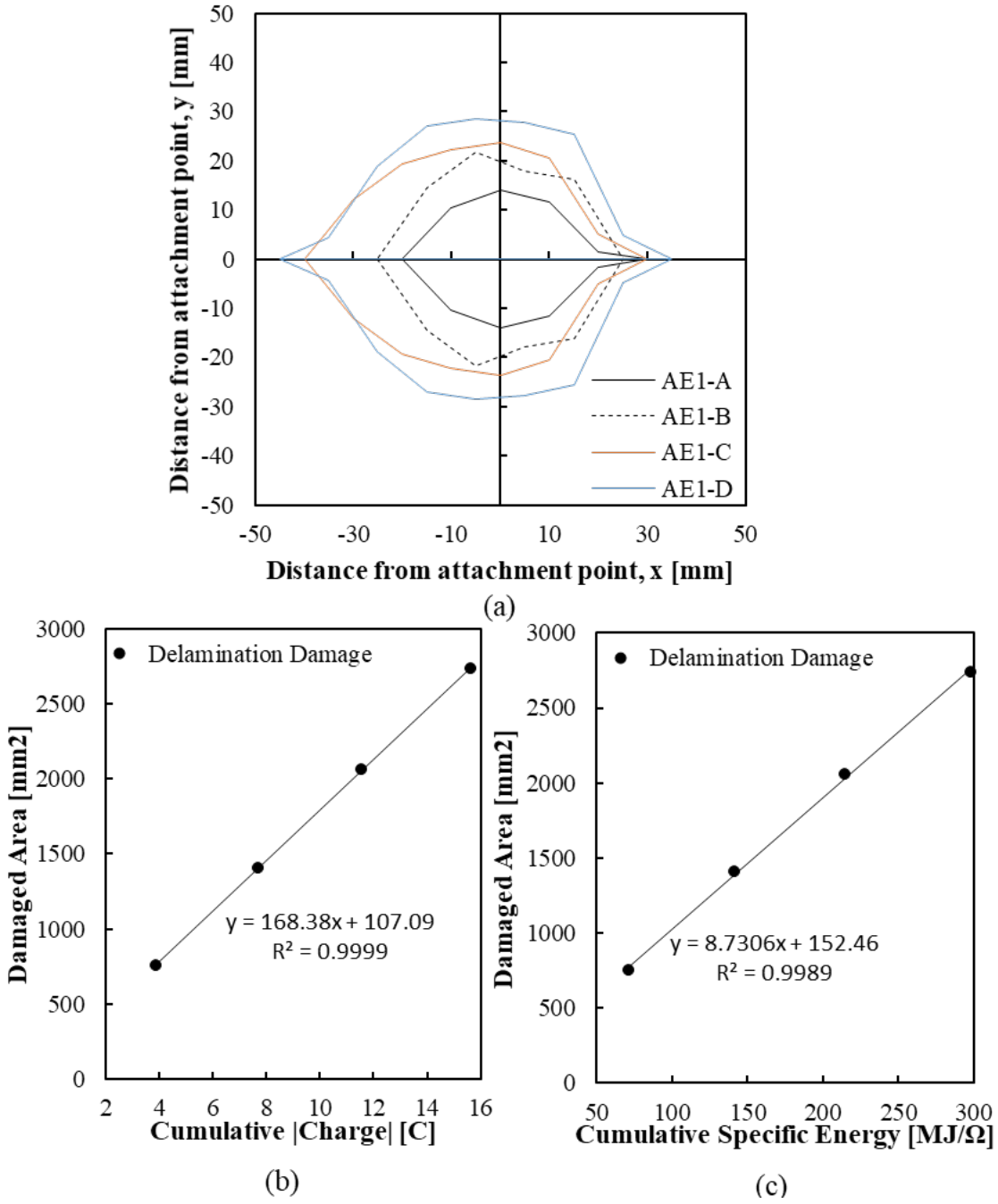

Figure A.10: Delamination damage from specimens in test AE1 where (a) is an overview of the area, (b) is the total area compared to the cumulative |charge| and (c) is the total area compared to the cumulative specific energy

The thermal data was recorded to find the maximum temperature during the lightning strike tests. The temperature data recorded for AE1 is shown in Figure A.11. The thermal data results show that the maximum temperature always occurred directly after the lightning strike event and exponentially decayed afterwards. On all samples, the initial lightning strike thermal evolution decayed the fastest. The repeated lightning strikes held the heat longer. This would indicate either higher specific heat or lower electrical/thermal conductivities in the damaged region. The one outlier is the AE1-D-3 specimens because the maximum temperature is taken by an ignited piece of the specimen that did not extinguish for approximately 6 seconds.

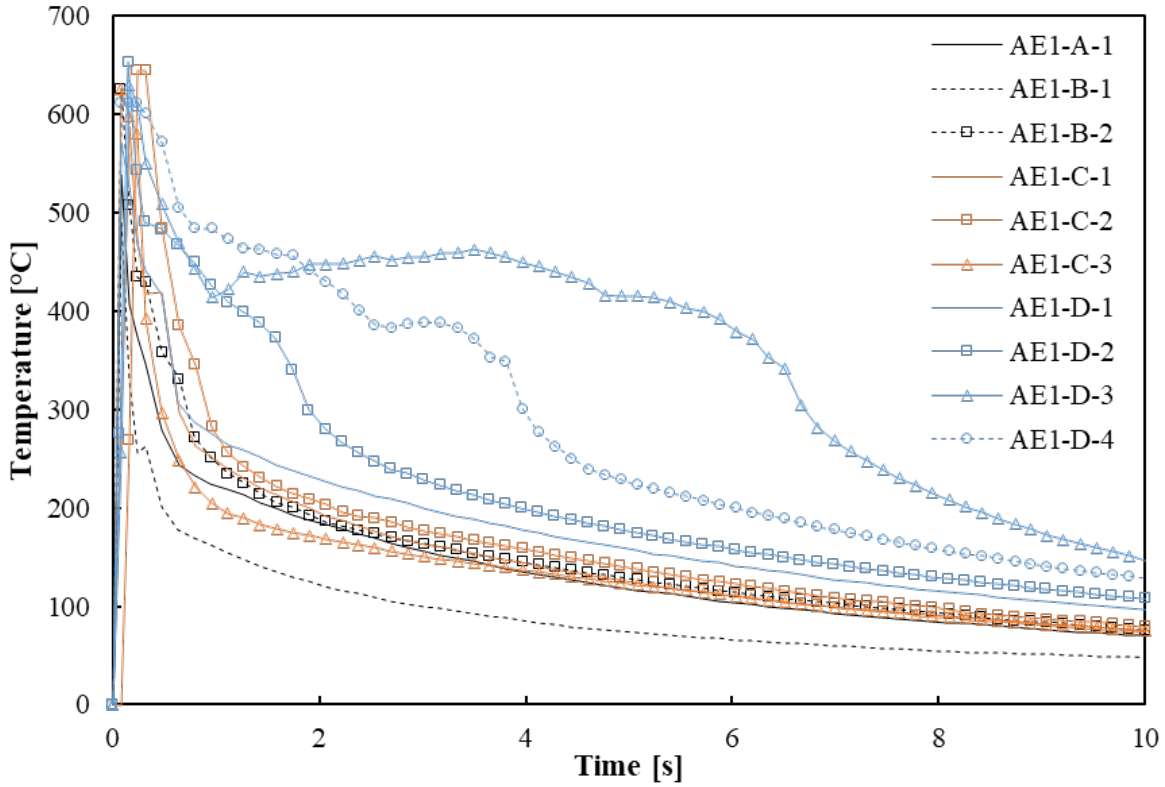

Figure A.11: Maximum temperature evolution of AE1 tests

These results indicate that the current always takes the same path to ground even after damage. This would mean that the fibres are not damaged enough to stop or lower the conduction of current.

A.3 AE2: Variation of Inductance

A.3.1 Results

Four CFRP specimens were subjected to simulated lightning strike events for test AE2. All AE2 specimens showed surface damage and charred damage primarily in elliptical shapes with the major axis in the transverse direction; see specimen AE2-4 in Figure A.12. AE2-1 through AE2-4 had similar patterns of surface damage shape.

Figure A.12: Visual inspection of damaged specimen from AE2-4 struck with oscillating waveform

Table A.4 shows the dimensions of the damage including the outer lengths and the area. The material UD so l_L and l_T stands for the outer length in the longitudinal and transverse directions respectively.

Table A.4: Visual inspection results for AE2

Test	Surface Damage			Charred Damage		
	l_L [mm]	l_T [mm]	Area [mm^2]	l_L [mm]	l_T [mm]	Area [mm^2]
AE2-1	7.21	51.44	291	72.9	135.34	7738
AE2-2	7.77	62.23	380	73.44	130.54	7471
AE2-3	7.77	67.63	413	60.02	117.71	5363
AE2-4	8.82	66.15	457	54.43	100.66	4258

Figure A.13 shows the results of the visual inspection. The resulting visual inspection showed very little change in the surface damage and a much larger change in charring damage due to an increase in peak current and specific energy. The |charge| had the inverse effect the increase in |charge| reduced the charring damage. This may indicate that the specific energy is a better link to damage than charge.

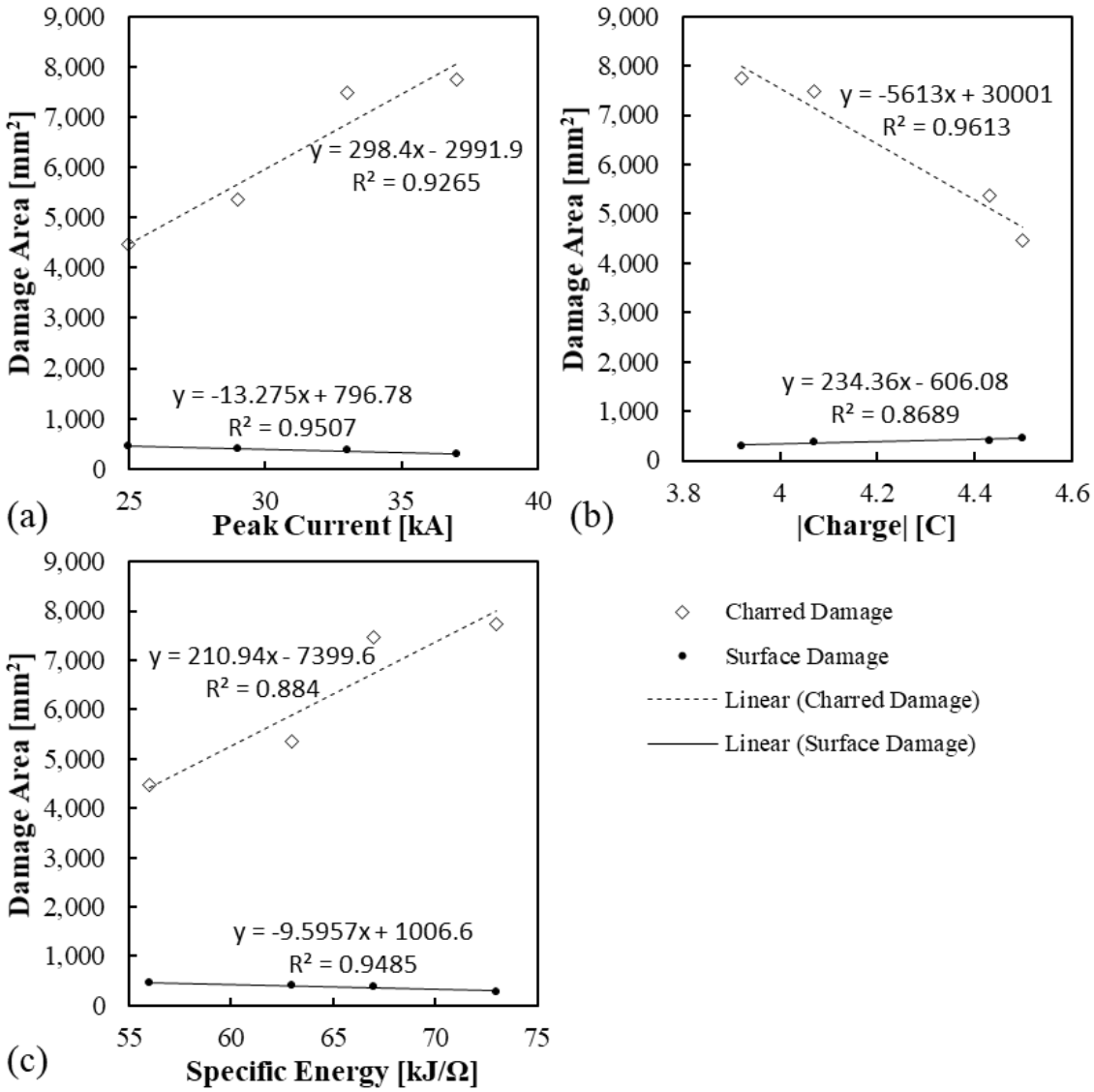

Figure A.13: Visual inspection damage area for AE2 experiments against (a) peak current, (b) |charge| and (c) specific energy

The outer lengths of the damage in the transverse and longitudinal directions are shown in Figure A.14. The plot shows for test AE2 that the length in the longitudinal direction is approximately 7 times larger for the surface damage and only about 1.8 times larger for the charred damage. This indicates that the charred damage is much more circular in shape and may be more related to other physics than just Joule heating. Typical models would indicate that the spread of damage would be more in the longitudinal direction. This indicates that some other process is occurring. The results for the peak current and specific energy (Figure A.14 (a) and (c)) are similar where the absolute charge is inverse.

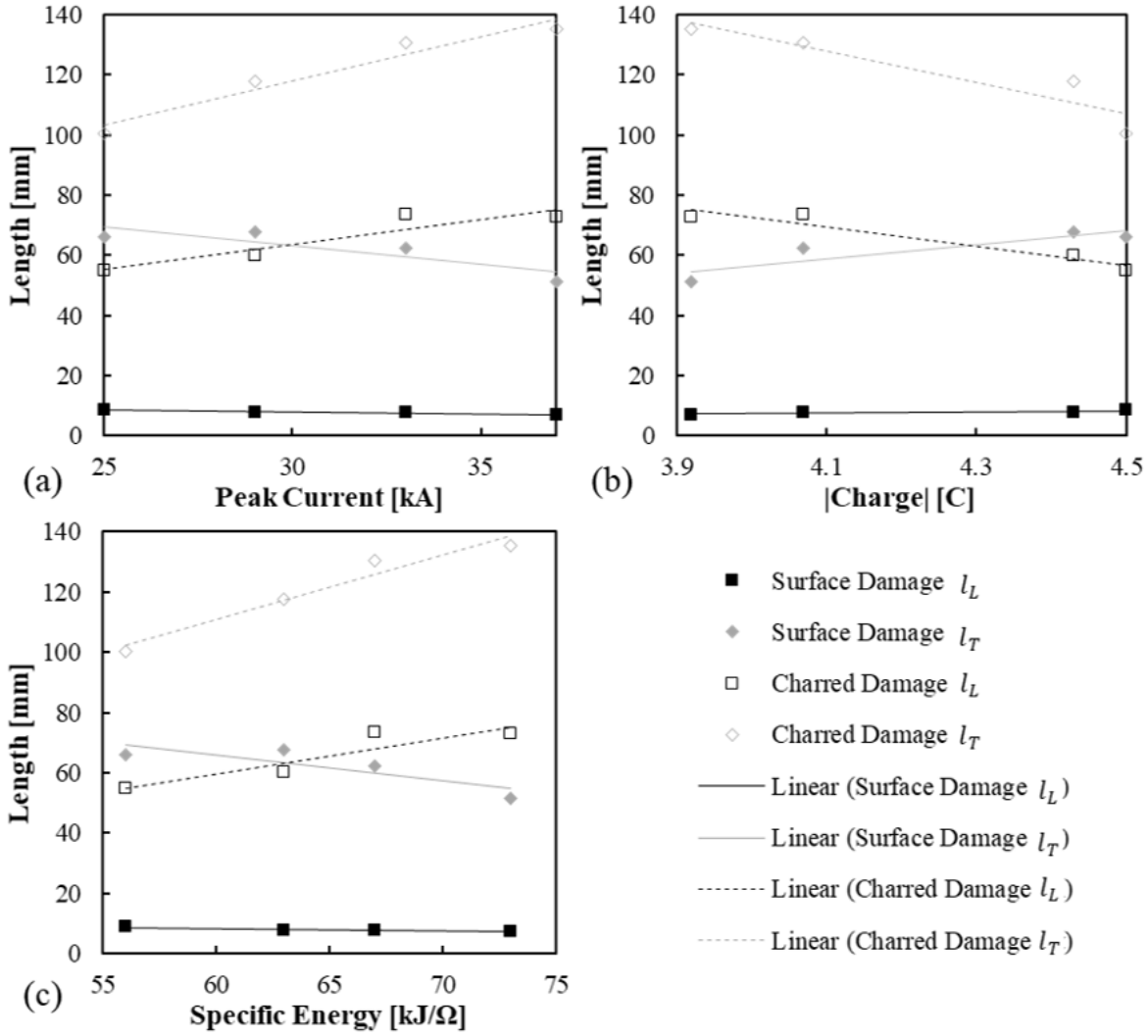

Figure A.14: Outer lengths of surface and charred damage in the longitudinal and transverse direction against (a) peak current, (b) charge, and (c) specific energy

The damage was visually inspected and not determined to be deep, matching a similar profile as damage seen on the surface. Further inspection shows no discernible delamination or other damage seen below a depth of 0.45mm below the surface. The resulting CT scan is shown in Figure A.15 (a).

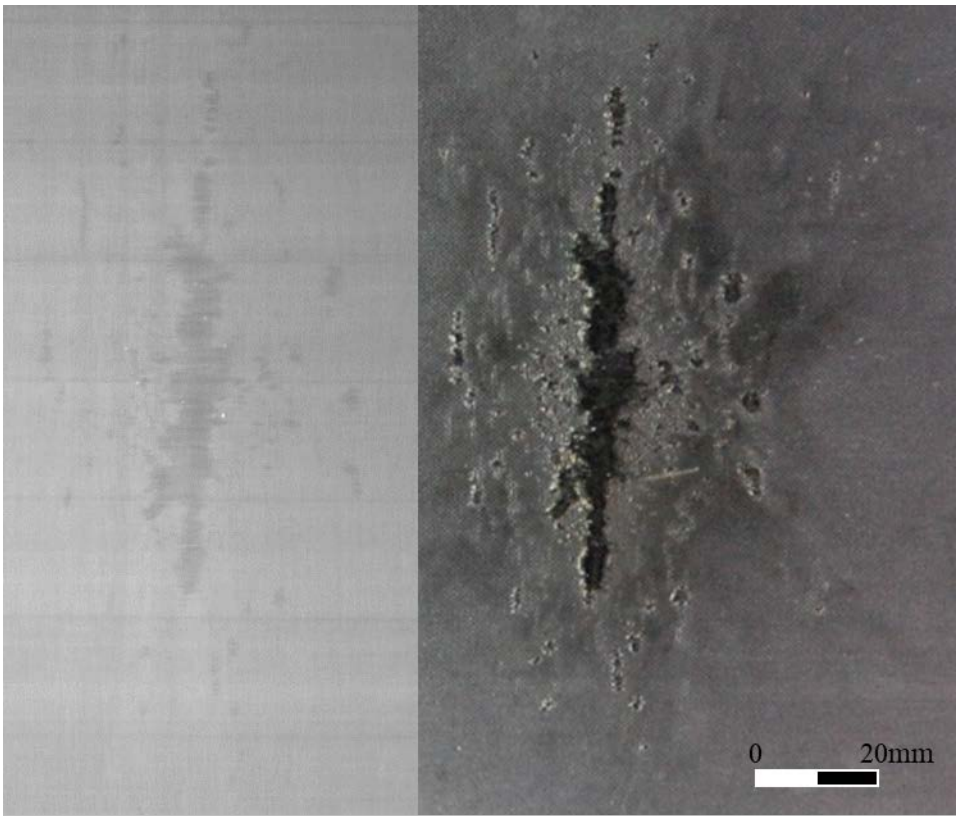

Figure A.15: Image of damage (a) CT image and (b) visual inspection

Evaluating the CT scans further, there was no discernible additional damage, delamination or otherwise, from the lightning strike. This was confirmed with microscopy images shown in Figure A.16.

Figure A.16: Microscope image of AE2-2

The maximum temperature data recorded for AE2 is shown in Figure A.17. The thermal data results showed that the maximum temperature always occurred directly after the lightning strike event and exponentially decayed afterwards. All of the samples struck had similar times from peak to less than 100°C of around 1.4 seconds. The lightning waveform for AE2 lasts for less than 1 ms and it is difficult to capture the full temperature evolution with today's thermal camera equipment. The resin burning and pyrolysis effects last longer. Also, due to intense brightness and ignition of air near and around the lightning attachment zone, the thermal profile observed at that moment may not be accurate.

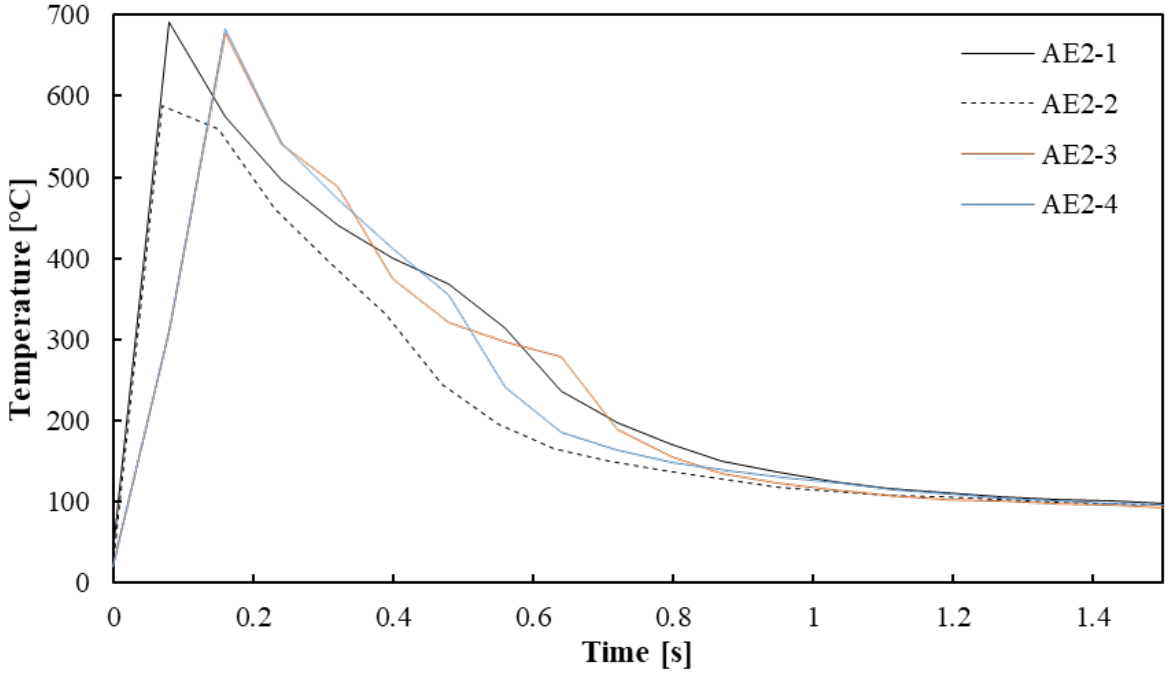

Figure A.17: Maximum temperature evolution for AE2

The temperature profile recorded in the longitudinal and transverse directions are shown in Figure A.18 and Figure A.19 at three specific frames (times of 0.16s, 0.4s, and 1.11s). As can be seen in the figures, the temperature profiles match closely with the surface damage.

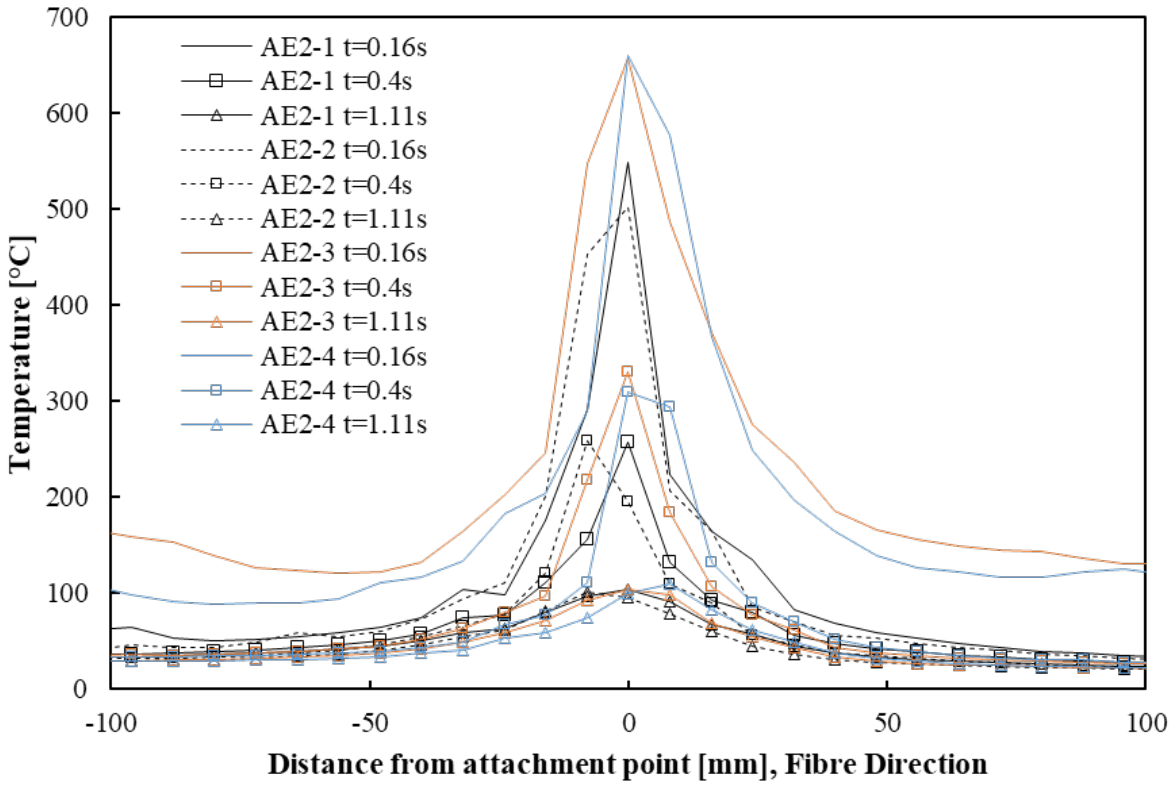

Figure A.18: Temperature distributed in the fibre direction for AE2 tests

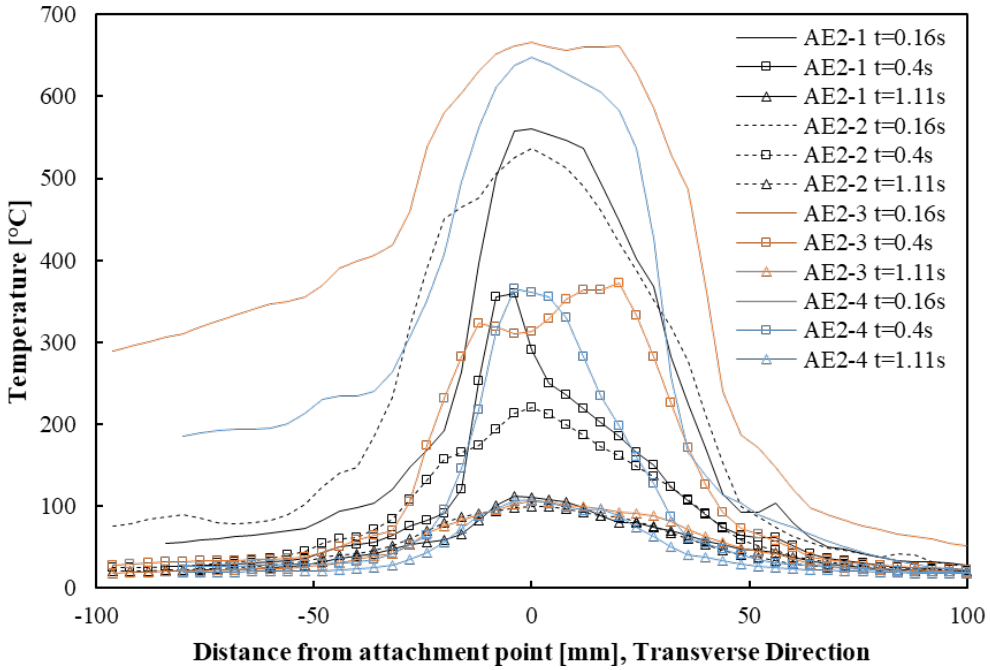

Figure A.19: Temperature distributed in the transverse direction for AE2 tests

A.4 AE3: Variation of Charge

A.4.1 Results

Four CFRP specimens were subjected to simulated lightning strike events for AE3. All AE3 specimens were subjected to DC current. The only variation was the amount of time exposed. For all AE3 specimens, the surface damage was primarily in an elliptical shape with the major axis in the longitudinal direction; see specimen AE3-4 in Figure A.20. AE3-1 through AE3-4 had similar patterns of surface and defect shapes and sizes.

Figure A.20: Visual inspection of damaged specimen AE3-4 struck

Appendix A

Initial direct strike testing

Table A.5 shows the dimensions of the damage including the outer lengths and the area.

Table A.5: Visual inspection results for AE3

Sample ID	Surface Damage			Charred Damage		
	l_L [mm]	l_T [mm]	Area [mm^2]	l_L [mm]	l_T [mm]	Area [mm^2]
AE3-1	66.72	48.26	2530	78.56	74.79	4599
AE3-2	62.76	71.01	3501	100.52	129.29	10046
AE3-3	73.11	68.29	3922	105.13	106.67	8685
AE3-4	125.48	57.39	5657	182.64	142.22	18312

The results show that an increase of both charring damage and surface damage was observed due to change of charge and specific energy; see Figure A.21. Comparing the R^2 values of the plots the charge and specific energy are the best indicators of damage for DC currents rather than peak current.

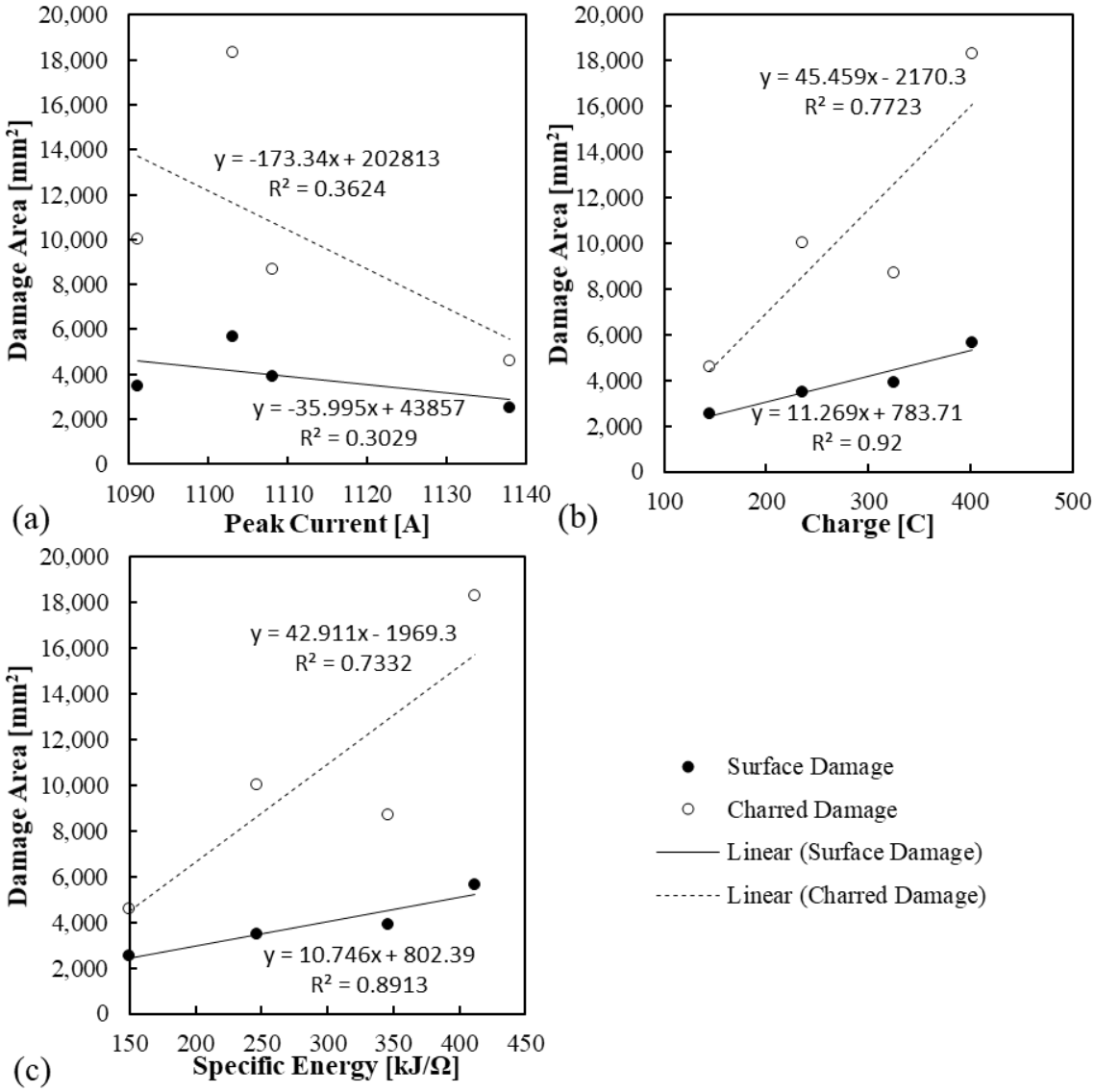

Figure A.21: Visual inspection damage area from AE3 against (a) peak current, (b) |charge| and (c) specific energy

The outer lengths of the damage in the transverse and longitudinal directions are shown in Figure A.22. The plot shows that the results for the AE3 tests are much harder to predict than the area. It is interesting to note that the longitudinal direction has a closer fit than the transverse direction.

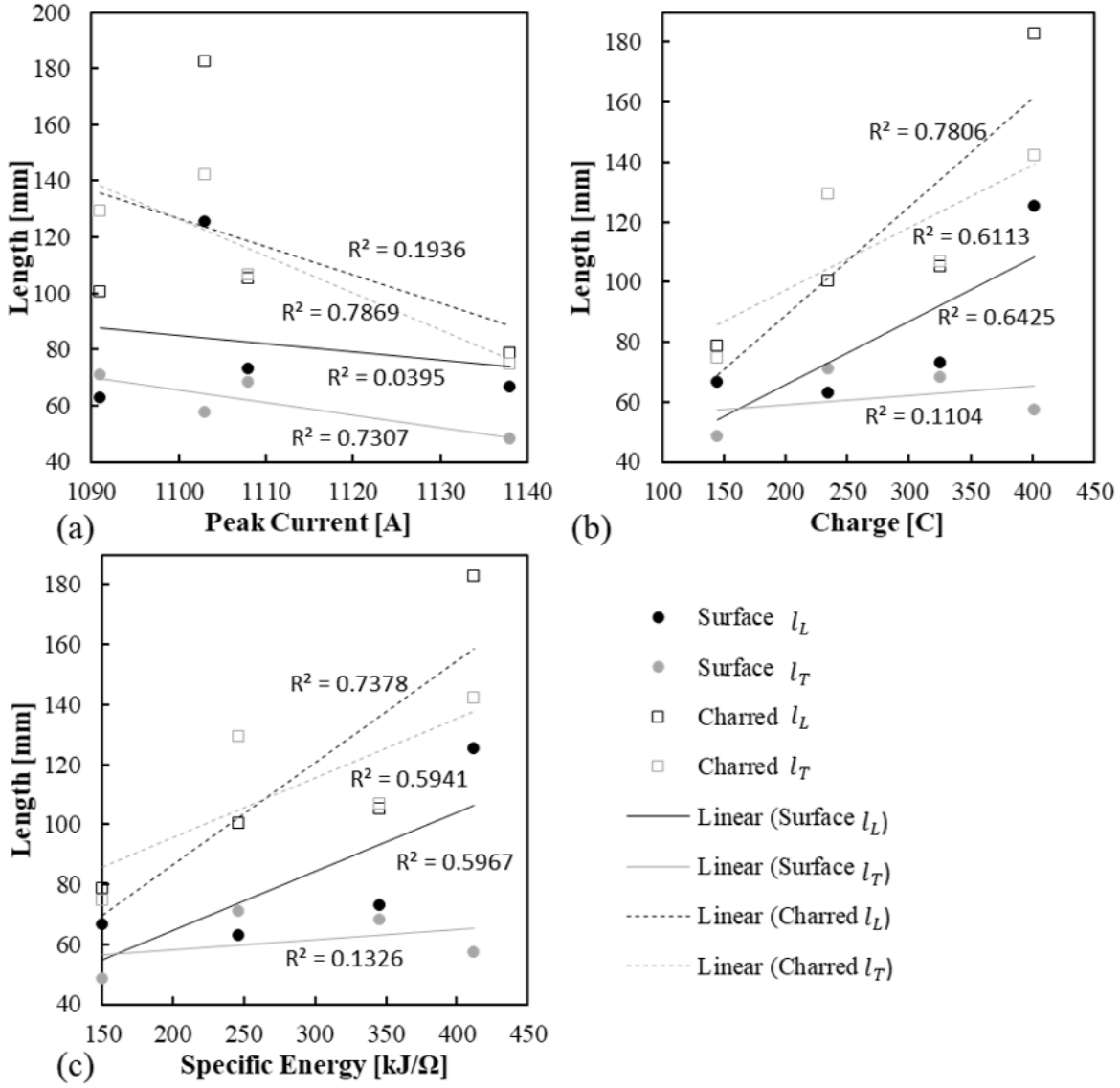

Figure A.22: Visual inspection damage lengths from AE3 against (a) peak current, (b) |charge| and (c) specific energy

The maximum temperature data recorded for AE3 is shown in Figure A.23. The thermal data results showed that the DC current resulted in a longer duration of ignited material near 5 seconds, decayed rapidly for approximately 10 seconds and then flattened with the heat slowly radiating away taking at least 60s for the surface to be less than 100°C.

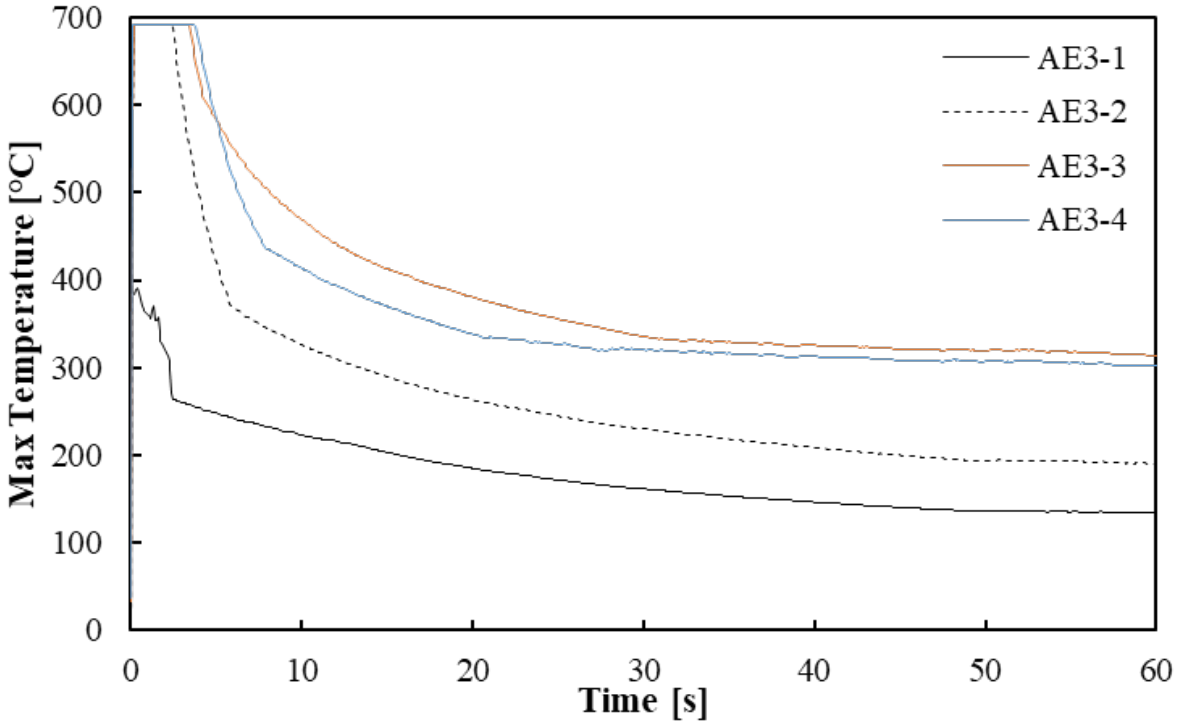

Figure A.23: Maximum temperature evolution for AE3

The temperature profile recorded in the longitudinal and transverse directions are shown in Figure A.24 and Figure A.25 at three specific frames (times of 0.16s, 0.4s, and 1.11s).

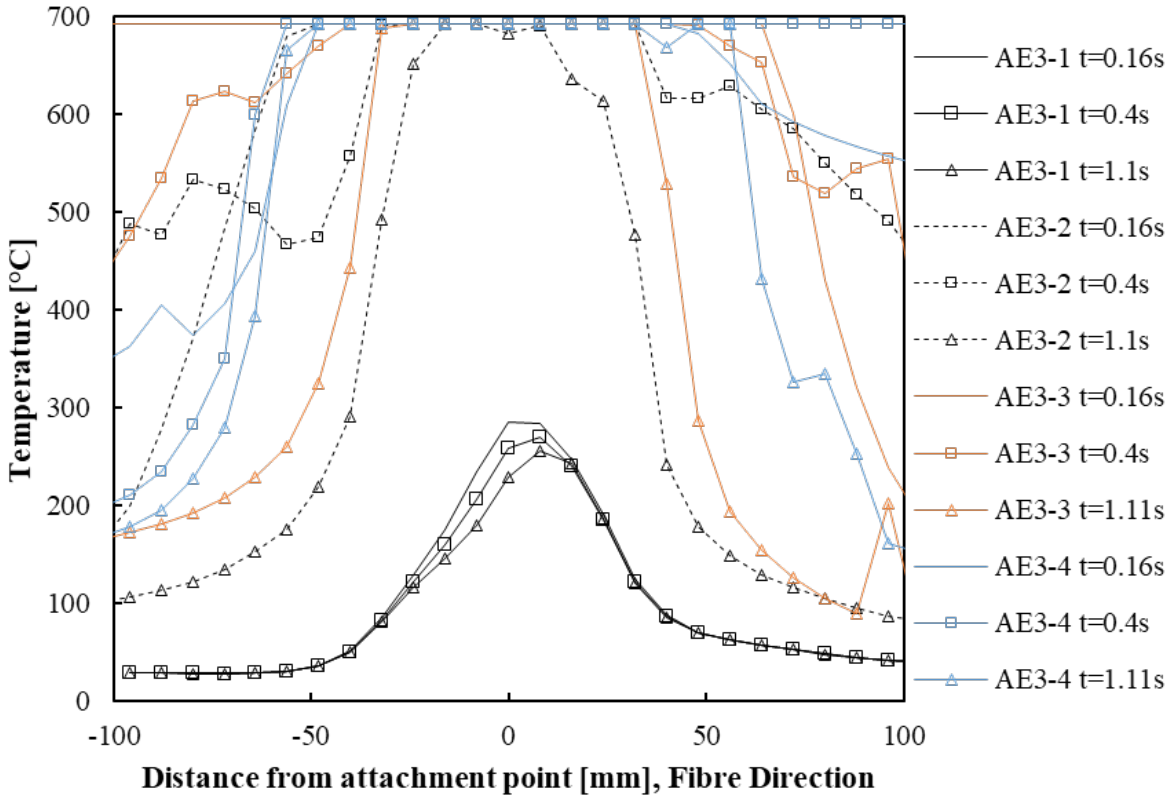

Figure A.24: Temperature profile in the fibre direction for AE3 at time steps 0.16s, 0.4s, and 1.11s

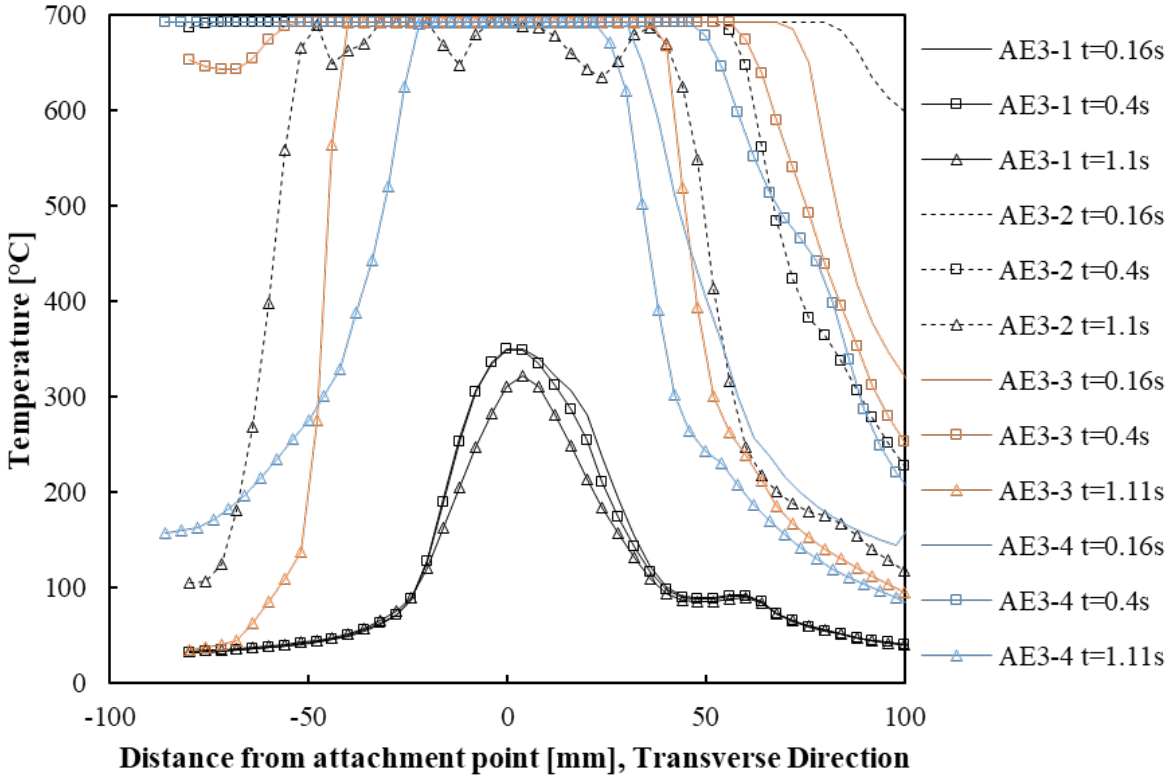

Figure A.25: Temperature profile in the transverse direction for AE3 at time steps 0.16s, 0.4s, and 1.11s

A.5 AE4: 10/350µs waveform

A.5.1 Results

13 CFRP specimens were subjected to simulated lightning strike events for test AE4: 7 on 5 ply thick specimens and 6 on 10 ply specimen. The specimens were struck with a combined impulse and DC waveform. The impulse was as close to a 10/350µs waveform as possible with differing peak currents. The AE4 specimens, the surface damage and the charred damage were primarily in elliptical shapes with the major axis in the transverse direction; see specimen AE4-7 in Figure A.26 (a) and AE4-13 in Figure A.26 (b). AE2-1 through AE2-4 had similar patterns of surface and charred damage shapes.

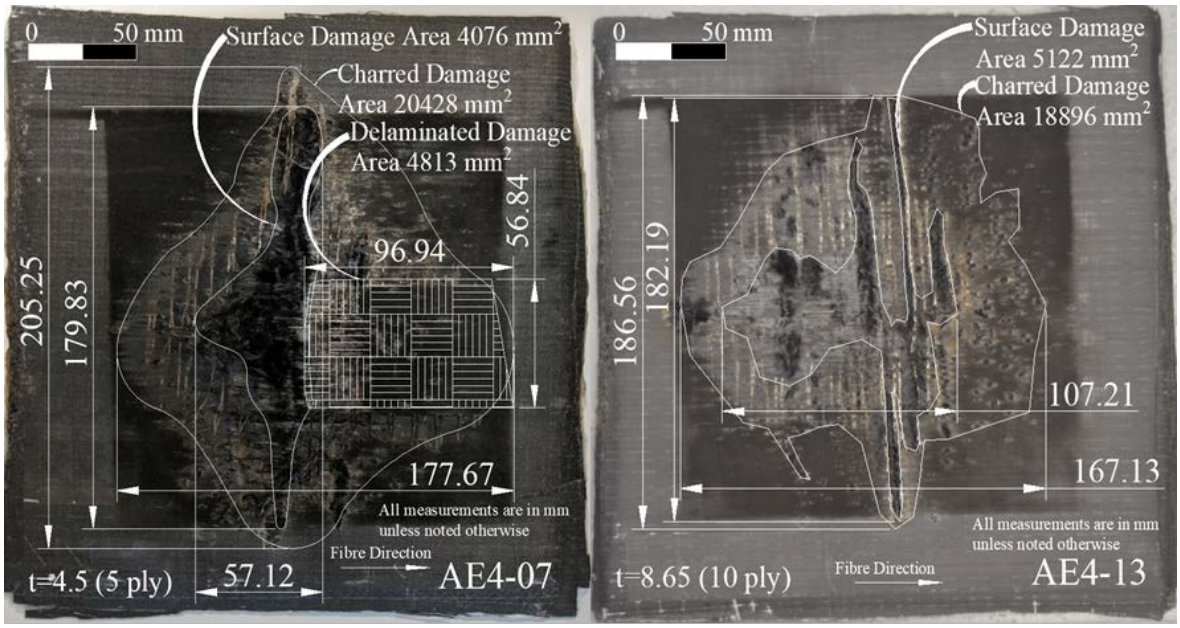

Figure A.26: Damaged specimen from test AE4 (AE4-07) struck with 10/350µs waveform

Results from the visual inspection including the outer lengths and damage area are shown in Table A.6.

Table A.6: Visual inspection results from test AE4

Sample ID	Surface Damage			Charred Damage		
	l_L [mm]	l_T [mm]	Area [mm²]	l_L [mm]	l_T [mm]	Area [mm²]
AE4-01	18.86	129.76	823	98.59	146.38	9706
AE4-02	34.96	143.3	1033	107.23	157.18	10394
AE4-03	32.44	140.36	1530	131.59	144.46	4599
AE4-04	36.35	150.39	1338	132.11	178.73	17527
AE4-05	46.04	152.99	4017	134.67	194.79	18204
AE4-06	39.86	121.94	3761	155.13	183.48	20615
AE4-07	57.12	179.83	4076	177.67	205.25	20428
AE4-08	27.32	60.71	287	91.35	118.01	5260
AE4-09	33.27	61.25	841	106.8	190.23	14001
AE4-10	36.32	182.41	2531	146.79	206.58	20907
AE4-11	40.17	168.14	3055	188.2	195.88	23582
AE4-12	43.36	172.88	3142	149.7	189.13	20164
AE4-13	107.21	182.19	5122	167.13	186.56	18896

The results show that an increase of both charring damage and surface damage was observed due to change of peak current, charge, and specific energy; see Figure A.27. Comparing the R^2 values of the plot show that the specific energy is the best indicator of damage for combined DC and Impulse waveform.

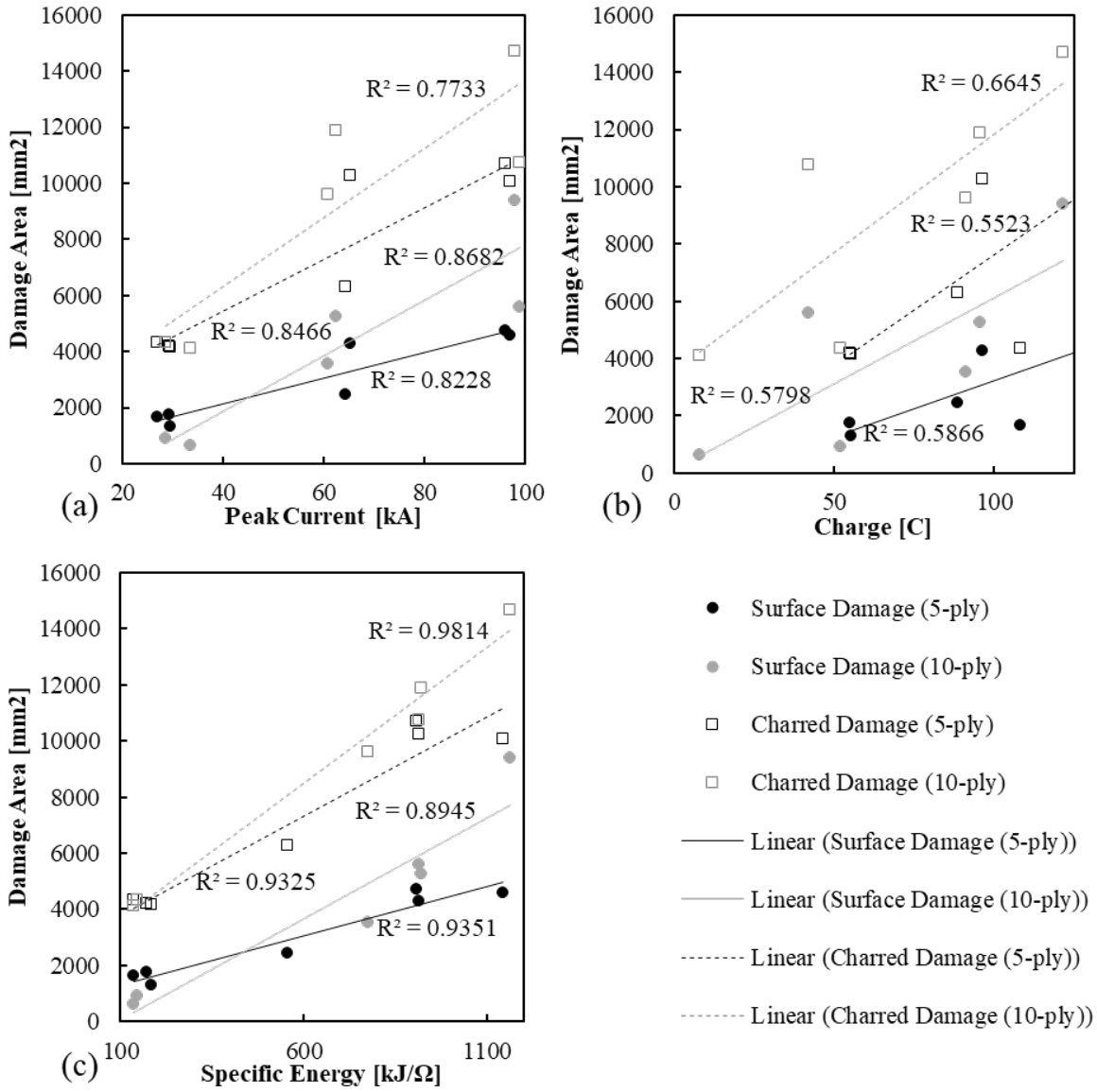

Figure A.27: Visual inspection damage area AE4 experiments against (a) peak current, (b) charge and (c) specific energy

Figure A.28 shows the results from the AE4 visual inspection results. The saturation line shows the distance between the grounds. It clearly shows that even at low levels of lightning peak currents, damage will spread more than 200mm in the transverse direction and may not capture the full extent of the damage, although the damage area did increase in this case.

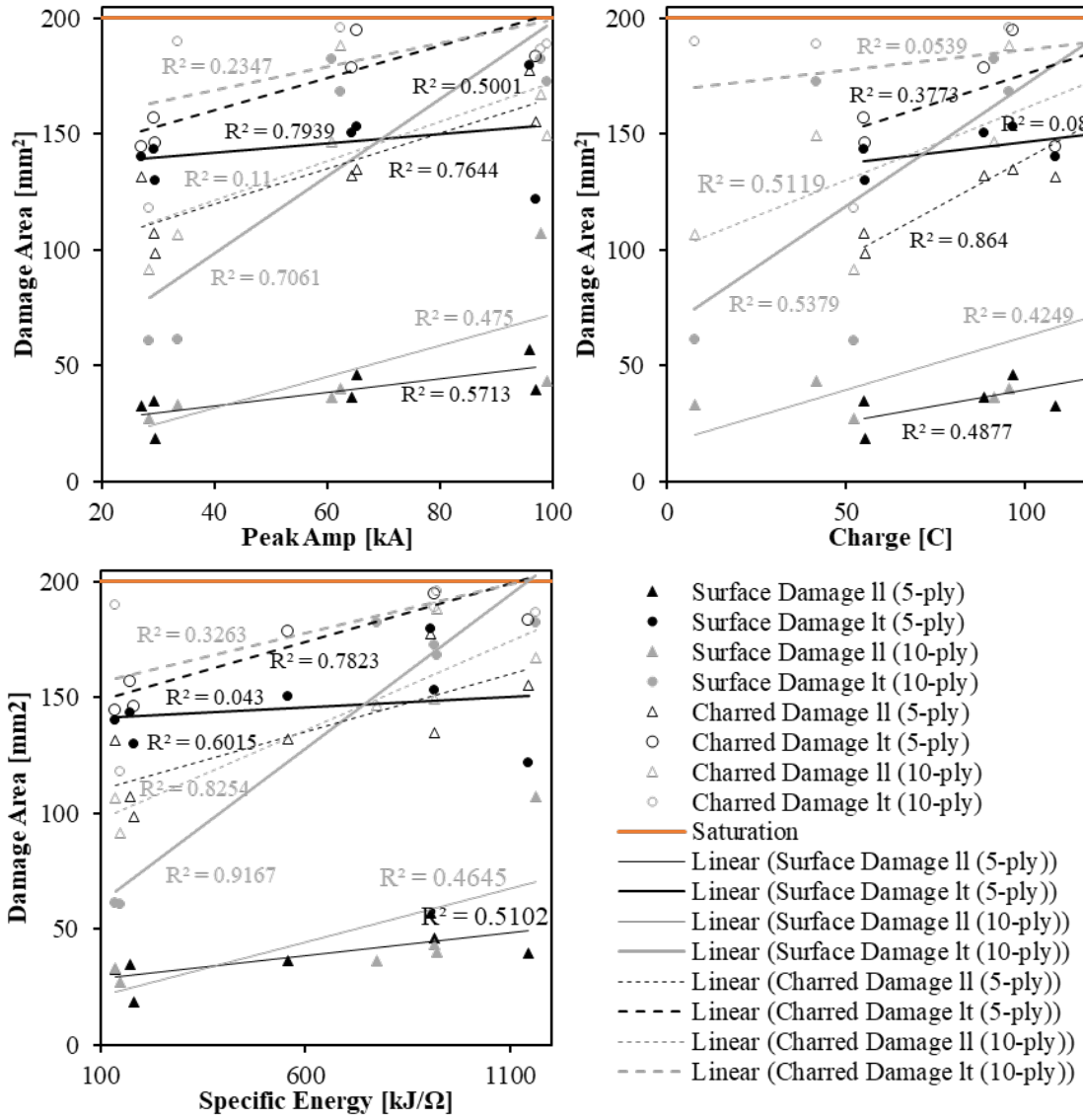

Figure A.28: Visual inspection damage lengths for AE4 experiments against (a) peak current, (b) charge and (c) specific energy

Figure A.29 separates total charge and total specific energy into portions, each from the impulse and DC waveforms. From Table 4.4 (page 73), the charge comes 80% from the DC and the specific energy comes 90% from the impulse. This allows for separation of cause and effect. Checking the R^2 values, the surface and charred damage fits closest to the specific energy. Separating the impulse and DC allows for a cause vs effect analysis. Figure A.29 (b) and (c) show the R^2 values have the tightest fit between impulse and DC components which indicates that most of the damage is contributed by impulse. The R^2 values from Figure A.29 (a) and (b) show that the best predictor of damage is specific energy.

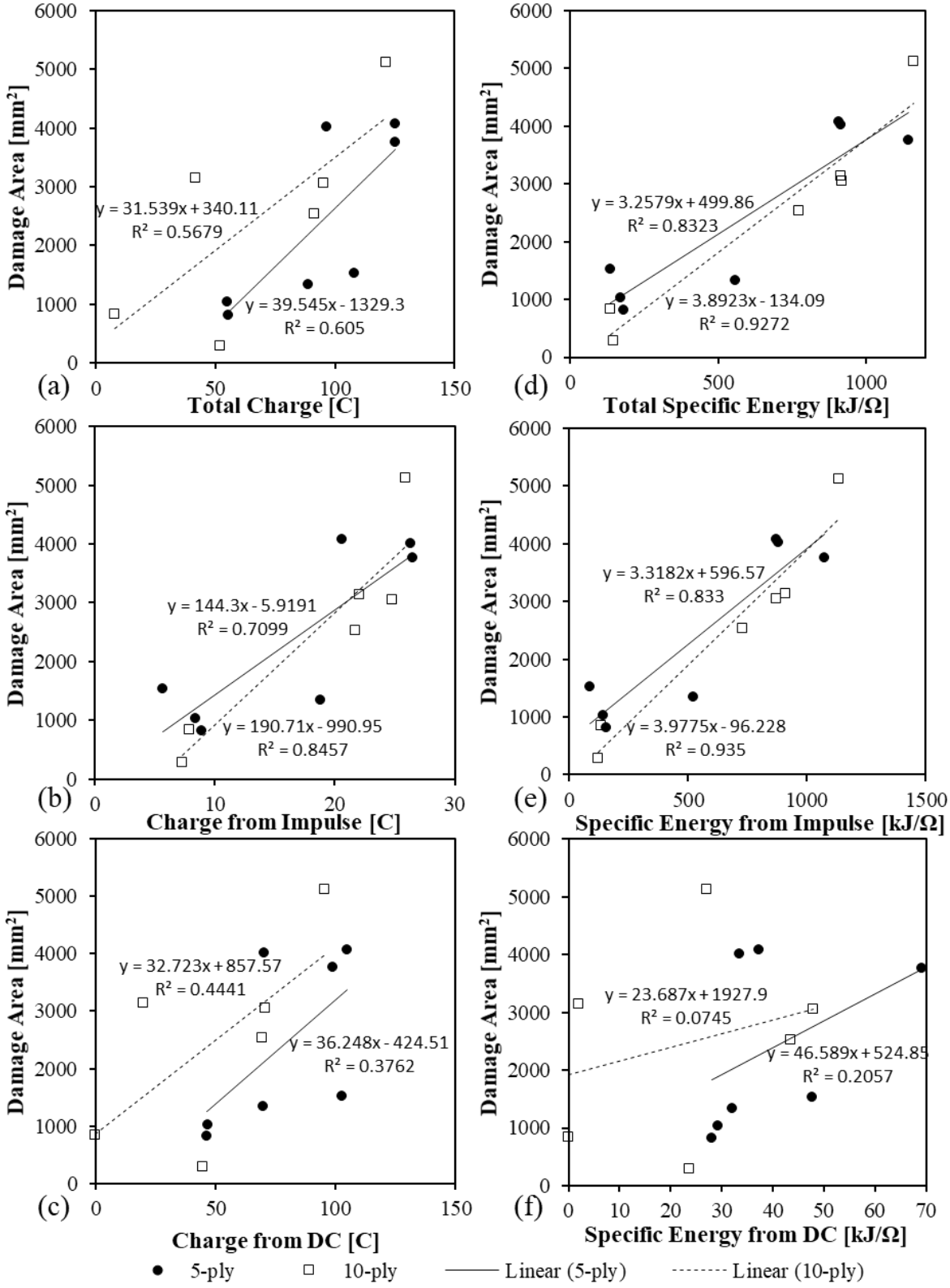

Figure A.29: Charge and specific energy vs the visual inspection damage area from the 5-ply and 10-ply specimens AE4 specimen comparing the charge and specific energy against the total, impulse and DC portion of the waveform. (a) is the charge from the total waveform, (b) is the charge from the impulse portion, (c) is the charge from the DC portion, (d) is the specific energy from the total waveform, (e) is the specific energy from the impulse portion, and (f) is the specific energy from the DC portion

A.6 Sparcap sub-structure 10/350µs

A.6.1 Results

Table A.7 is a summary of the visual inspection results.

Table A.7: Visual inspection results from test AE5

Sample ID	Surface Damage			Charred Damage		
	l_L [mm]	l_T [mm]	Area [mm^2]	l_L [mm]	l_T [mm]	Area [mm^2]
AE5-50-1	32.95	303.45	1518	120.09	320.05	23520
AE5-50-2	44.13	203.66	4120	155.69	235.47	15972
AE5-75-1	57.62	291.96	6909	162.92	370.57	34183
AE5-75-2	56.25	284.25	6500	160.11	375.66	35225
AE5-100-1	65.55	200.32	5532	154.48	420.52	29448
AE5-100-2	67.4	287.15	6909	175.86	357.39	35715
AE5-125-1	52.64	294.96	7781	163.9	422.33	42680
AE5-125-2	66.16	327.64	6951	182.71	391.44	31917
AE5-50-1FG	550	60.76	25672	-*	-*	-*
AE5-75-1FG	550	120.22	34014	-*	-*	-*
AE5-100-1FG	550	141.16	52417	-*	-*	-*
AE5-50-1CM	-$^+$	-$^+$	-$^+$	41.77$^+$	84.37$^+$	2021$^+$
AE5-75-1CM	17.88$^+$	9.35$^+$	185$^+$	84.84$^+$	88.42$^+$	4953$^+$
AE5-100-1CM	5.12$^+$	5.65$^+$	27$^+$	94.18$^+$	121.66$^+$	7526$^+$

* indicates area was not measured
$^+$ indicates copper mesh, results do not show any exposed fibres but some discolouring of the surface which is measured

The results show that an increase of both charring damage and surface damage was observed due to increasing change of peak current, charge, and specific energy; see Figure A.30. The significant results show that the difference in surface types has a drastic difference in the amount of damage. The surface damage was practically zero for all copper mesh specimens. The bare specimens were similar to the AE4 tests. The fibreglass specimens were dramatically different, showing 8 times more damage area than in the bare specimens.

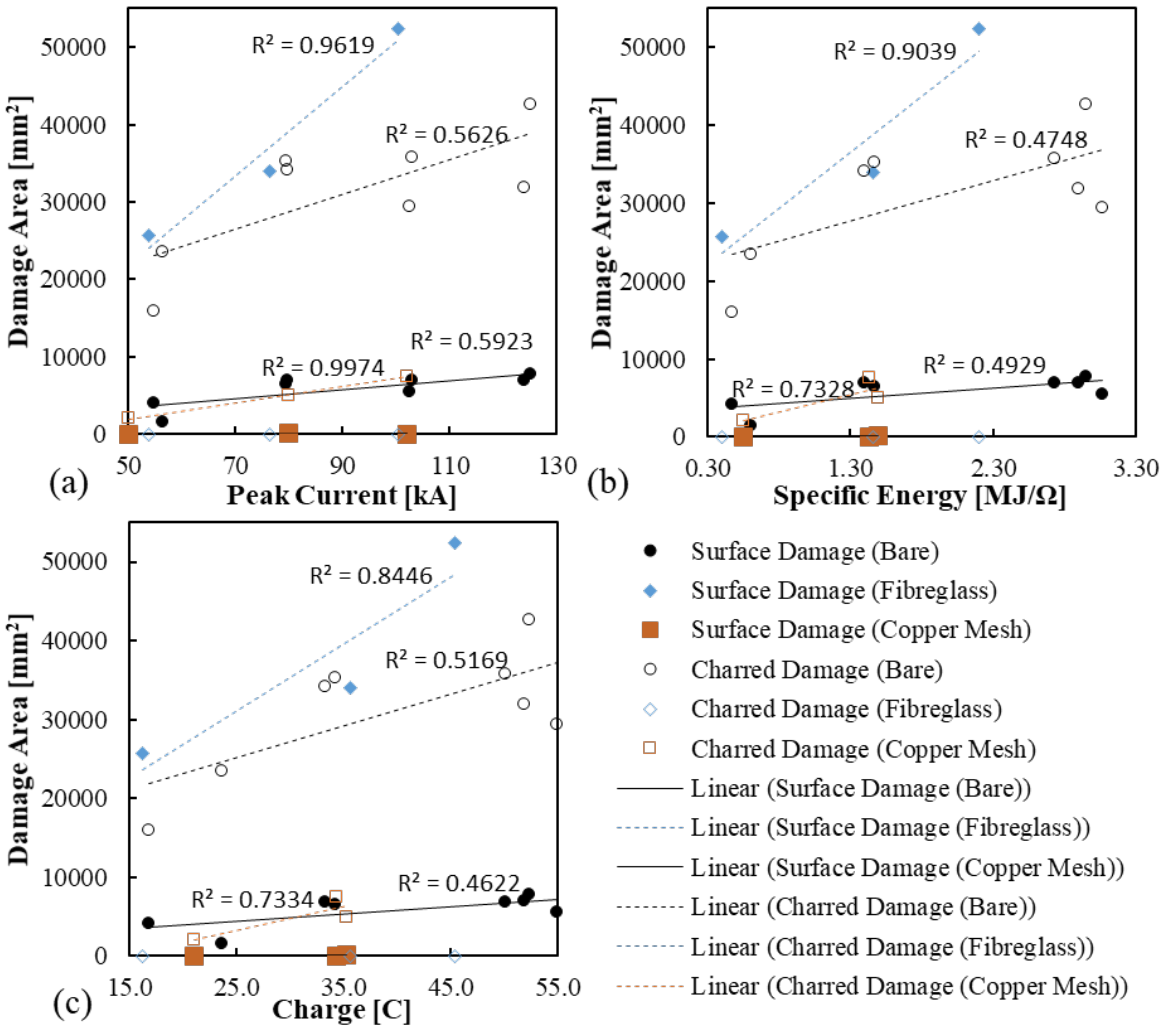

Figure A.30: Visual inspection damage area for AE5 experiments against (a) peak current, (b) charge and (c) specific energy

Appendix B

Matlab thermography analysis code

```
function [y_temp_mat,yintp] = Int_method(Tmat,chart_title)
  % Function Details
  %
  % function data = Int_method( Tmat,chart_title )
  %
  % Written by : Tim Harrell (tmh2g15@soton.ac.uk)
  % Date       : Fall 2017
  %
  %
  % Function   : Process IR data using the integration method
  %
  % Description: This work uses the thermal data collected from
  %              the thermography experiment and processes the IR
  %              data using an integration method. This method
  %              determines the difference in damage by taking the
  %              integral between the damage section and a
  %              reference undamaged section.
  %
  % Inputs     : Tmat - Temperature Matrix
  %                     3D matrix with temperature results in the
  %                     format (frame_x, frame_y, time)
  %              chart_title - String with the name of the sample
  %
close all

%creating size variables
r = size(Tmat,1);
s = size(Tmat,2);
t = size(Tmat,3);
%Reshaping matrix makes the later calculation calculate faster
y_temp = reshape(Tmat,r*s,t);
%Subtracting first frame
for i=1:size(y_temp,2)
  y_temp_subt(:,i) = y_temp(:,i) - y_temp(:,1);
end
y_temp = y_temp_subt;

[max_num, max_index] = max(Tmat(:)); %Finds the max value and
location

%Uses the max location to determine the start of the integration
x1 = round(max_index/r/s)+3;

%Displays several graphs of the thermal data for each pixel to
determine the
% time where the temperature returns to ambient
j = 1;
figure(1)
while j < r*s

    plot(y_temp_subt(j,:))
    hold on
    j = j+100;
end
hold off
```

Appendix B

Matlab thermography analysis code

```
figure(1)
for i=1:1000:size(y_temp,1)
plot(y_temp(i,1:t)); hold on
end
set(gcf,'color','w');
hold off

%User must select point on screen
[x2,y2] = ginput(1);
close(1)
x2 = round(x2);

%This normalizes each pixel's thermal data by checking the ambient
% portion
%of their graph and bringing it to a reference thermal data pixel
%Right now this is set in the code. Might need to make another
% user selection option.
for i=1:size(y_temp,1)
  y_temp(i,1:t) = (y_temp(i,1:t) - mean(y_temp(i,x2:t)) +
mean(y_temp(1584,x2:t)));
end

j=1;
X_int1 = linspace(x1/383,x2/383,x2-x1+1); %setting up integration
steps
int1 = trapz(X_int1,y_temp(1,x1:x2)); %calculate the reference
%undamaged integration
%Do statement to calculate the rest of the integration method
for i=1:size(y_temp,1)
  yint(i) = trapz(X_int1,y_temp(i,x1:x2)) - int1;
end

%Putting the matrices back to something familiar
yintp = reshape(yint,size(Tmat,1),size(Tmat,2));
y_temp_mat =
reshape(y_temp,size(Tmat,1),size(Tmat,2),size(Tmat,3));

yintn = yintp/max(max(yintp)); %Normalized integration

%Plotting the results
figure(1)
PPTImg = mat2gray(Tmat(:,:,round(x1/2+x2/2)));
image(PPTImg)
hold all
h = pcolor(yintn);
set(h,'EdgeAlpha',0,'FaceAlpha',0.8);

hTitle  = title (chart_title);
hXLabel = xlabel('x position (pixels)'                    );
hYLabel = ylabel('y position (pixels)'                     );

set( gca                       , ...
    'FontName'   , 'Helvetica' );
set([hTitle, hXLabel, hYLabel], ...
    'FontName'   , 'AvantGarde');
set([hXLabel, hYLabel]  , ...
    'FontSize'   , 10          );
set( hTitle                    , ...
    'FontSize'   , 12          , ...
    'FontWeight' , 'bold'      );

set(h,'EdgeAlpha',0,'FaceAlpha',0.8);

c = colorbar;
```

```
c.Label.String = 'Normalized Integration Method (Damage
Detection)';

set(gcf, 'PaperPositionMode', 'auto');
print('-f1',[chart_title '_finalPlot_int-normalized'],'-dpng')

hold off

figure(2)
%Plotting the results
PPTImg = mat2gray(Tmat(:,:,round(x1/2+x2/2)));
image(PPTImg)
hold all
h = pcolor(yintp);
set(h,'EdgeAlpha',0,'FaceAlpha',0.8);

hTitle  = title (chart_title);
hXLabel = xlabel('x position (pixels)'                    );
hYLabel = ylabel('y position (pixels)'                     );

set( gca                       , ...
    'FontName'   , 'Helvetica' );
set([hTitle, hXLabel, hYLabel], ...
    'FontName'   , 'AvantGarde');
set([hXLabel, hYLabel]  , ...
    'FontSize'   , 10          );
set( hTitle                    , ...
    'FontSize'   , 12          , ...
    'FontWeight' , 'bold'      );

set(h,'EdgeAlpha',0,'FaceAlpha',0.8);

c = colorbar;
c.Label.String = 'Integration Method (Damage Detection)';

set(gcf, 'PaperPositionMode', 'auto');
print('-f2',[chart_title '_finalPlot_int'],'-dpng')

hold off

figure(3)
%Plotting the results
h = histogram(yintp,[0:0.35:4 Inf]);
hTitle  = title (chart_title);
hXLabel = xlabel('Integration (degC s)'                    );
hYLabel = ylabel('Count (pixels)'                    );

set( gca                       , ...
    'FontName'   , 'Helvetica' );
set([hTitle, hXLabel, hYLabel], ...
    'FontName'   , 'AvantGarde');
set([hXLabel, hYLabel]  , ...
    'FontSize'   , 10          );
set( hTitle                    , ...
    'FontSize'   , 12          , ...
    'FontWeight' , 'bold'      );

set(gcf, 'PaperPositionMode', 'auto');
print('-f3',[chart_title 'finalPlot_histogram'],'-dpng')

figure(4)
%Plotting the results
h = histogram(yintp,[1 Inf]); hold on
h = histogram(yintp,[5 Inf]); hold off
```

```
hTitle  = title (chart_title);
hXLabel = xlabel('Integration (degC s)'                    );
hYLabel = ylabel('Count (pixels)'                      );

set( gca                       , ...
    'FontName'   , 'Helvetica' );
set([hTitle, hXLabel, hYLabel], ...
    'FontName'   , 'AvantGarde');
set([hXLabel, hYLabel]  , ...
    'FontSize'   , 10          );
set( hTitle                    , ...
    'FontSize'   , 12          , ...
    'FontWeight' , 'bold'      );

set(gcf, 'PaperPositionMode', 'auto');
print('-f4',[chart_title 'finalPlot_histogram_nodamage'],'-dpng')

figure(5)
%Plotting the results
h = histogram(yintn,[0:0.1:1]);
hTitle  = title (chart_title);
hXLabel = xlabel('Integration (degC s)'                    );
hYLabel = ylabel('Count (pixels)'                      );

set( gca                       , ...
    'FontName'   , 'Helvetica' );
set([hTitle, hXLabel, hYLabel], ...
    'FontName'   , 'AvantGarde');
set([hXLabel, hYLabel]  , ...
    'FontSize'   , 10          );
set( hTitle                    , ...
    'FontSize'   , 12          , ...
    'FontWeight' , 'bold'      );
set(gcf, 'PaperPositionMode', 'auto');
print('-f5',[chart_title 'finalPlot_histogram_norm'],'-dpng')

figure(6)
%Plotting the results
h = histogram(yintn,[0.1:0.1:1]);
hTitle  = title (chart_title);
hXLabel = xlabel('Integration (degC s)'                    );
hYLabel = ylabel('Count (pixels)'                      );

set( gca                       , ...
    'FontName'   , 'Helvetica' );
set([hTitle, hXLabel, hYLabel], ...
    'FontName'   , 'AvantGarde');
set([hXLabel, hYLabel]  , ...
    'FontSize'   , 10          );
set( hTitle                    , ...
    'FontSize'   , 12          , ...
    'FontWeight' , 'bold'      );

set(gcf, 'PaperPositionMode', 'auto');
print('-f6',[chart_title 'finalPlot_histogram_norm_nodamage'],'-
dpng')

end
```

Appendix C

LaRC USDFLD implementation

The LaRC criteria is a composite failure criterion which includes 6 different failure modes. The 6 failure modes are LaRC 1 matrix compression with fibre tension (σ_{11}) greater than transverse compressive strength (Yc), LaRC 2 matrix tension ($\sigma_{22} \geq 0$), LaRC 3 fibre tension ($\sigma_{11} \geq 0$), LaRC 4 fibre compression with transverse compressive stress in the misaligned frame ($\sigma_{22m} < 0$), LaRC 5 fibre compression with transverse tension stress in the misaligned frame ($\sigma_{22m} >= 0$), and LaRC 6 matrix compression ($\sigma_{22} < 0$). The theoretical formulations is discussed in [120].

C.1 LaRC USDFLD code

The following USDFLD code is written in FORTRAN for use with Abaqus subroutines. The "C" at the beginning of the line and the exclamation point "!" are comments which are shown in a green colour to distinguish it from the code. The actions taken by the script and variable definitions are shown in a blue colour. The code is written in f77, so it is a fixed form code.

```
      SUBROUTINE USDFLD(FIELD, STATEV, PNEWDT, DIRECT, T,
     1  CELENT, TIME, DTIME, CMNAME, ORNAME, NFIELD,
     2  NSTATV, NOEL, NPT, LAYER, KSPT, KSTEP, KINC, NDI,
     3  NSHR, COORD, JMAC, JMATYP, MATLAYO, LACCFLA)
C
      INCLUDE 'ABA_PARAM.INC'
C
C DEFINE MATERIAL STRENGTH PARAMETERS
C
      REAL*8 E1, E2, G12, nu12, nu21, delta22, delta44, g
      REAL*8 i, S11, S22, S12, alpha_0, alpha_r, S_L, S_T, nl, nt, i_r
      REAL*8 tau_eff_T1, tau_eff_L1, tau_eff_T, tau_eff_L, FI_temp
      REAL*8 FI1, FI2, FI3, FI4, FI5, FI6, FI7, FI_Mode
      REAL*8 phi_c_m, phi_m, S22_m, S12_m
      REAL, DIMENSION(6) :: FIs
      PARAMETER (Pi = 3.14159265358979323846,
     1           XT =2000,
     2           XC =1000,
     3           YT =47,
     4           YC =120,
     5           S =70) ! STRENGTHS IN MPA
C
      CHARACTER*80 CMNAME, ORNAME
      CHARACTER*3 FLGRAY(15)
      DIMENSION FIELD(NFIELD), STATEV(NSTATV), DIRECT(3,3)
      DIMENSION T(3, 3), TIME(2), ARRAY(15), JARRAY(15)
      DIMENSION COORD(*), JMAC(*), JMATYP(*)
C
C USER FLD CODE_____________________________________________________________
C
C Written by Timothy M Harrell and Tobias Laux
C Date: 07/09/2018
C Version: 2.0
C
C IN THIS CODE FAILURE INDICES ARE CALCULATED BASED ON THE STRESS ANALYSIS
```

Appendix C

LaRC USDFLD implementation

```
C PERFORMED IN ABAQUS FEA. FAILURE INDICES ARE CALUCLATED USING THE LaRC
C CRITERTIA [1]. THE COMPUTED FAILURE INDICES ARE FED BACK TO ABAQUS
C AS A "SOLUTION DEPENDEDNT STATE VARIABLE" (STATEV).
C
C REFERENCE OF FAILURE INDICIES:
C [1] C. G. Dávila, P. P. Camanho, and C. A. Rose, “Failure criteria for FRP
C laminates,” J. Compos. Mater., vol. 39, no. 4, pp. 323–345, 2005.
C
C NOTES:
C 1) FAILURE INDEX IS DEFINED EXPLICITLY, HENCE DEPENDS ON STRESS VALUES OF
C    PREVIOUS STEP.
C 2) THE USER SUBROUTINE USDFLD IS ONLY ACTIVATED IF A CHANGE TO THE CONSTITUTIVE
C    PROPERTIES
C    IS EXPECTED BY ABAQUS. THUS, TWO MATERIAL STATES HAVE TO BE DEFINED IN THE
C    MATERIAL CARD
C    WITH TWO DIFFERENT FIELD VARIABLES IN ASCENDING ORDER.
C 3) .FOR FILE AND USER_LOG.TXT FILES EXPECTED IN THE WORKING DIRECTORY.
C 4) IN THE MATERIAL TAB ADD USDFLD, AS MANY DEPVARS AS FAILURE INDICES AND
C    MINIMUM ONE FIELD VARIABLE.
C
C USER SOUBROUTINE CHECK IF CALLED
      !OPEN(15,file='C:\Local\USER_LOG.txt',status='delete') ! DEFINE WORKING
                                                             ! DIRECTORY PATH
      !CLOSE(15)
      !OPEN(15,file='C:\Local\USER_LOG.txt',position='append') ! USER TO DEFINE
                                                          !WORKING DIRECTORY PATH
      !WRITE(15,*)'SUBROUTINE CALLED'

C Input Elastic Constants

      E1 = 118000 ! [MPa] Longitudinal Modulus
      E2 = 10600  ! [MPa] Transverse Modulus
      G12 = 4670  ! [MPa] Shear Modulus
      nu12 = 0.32 ! [mm/mm] Poisson’s Ratio 12 direction
      nu21 = nu12 * E2/E1 ! [mm/mm] Poisson’s Ratio 21 direction
C
C GET STRESSES FROM PREVIOUS INCREMENT
      CALL GETVRM('S', ARRAY, JARRAY, FLGRAY, JRCD,
     1 JMAC, JMATYP, MATLAYO, LACCFLA)
       S11 = ARRAY(1) ! [MPa] Longitudinal Stress
       S22 = ARRAY(2) ! [MPa] Transverse Stress
       S12 = ARRAY(4) ! [MPa] Shear Stress
       !WRITE(15,*)'BEFORE IF'
       !WRITE(15,*)CMNAME
C
C COMPUTE FAILURE INDICES
      if (CMNAME=='MATERIAL-1') then
       !WRITE(15,*)'IN IF'
C LaRC 1 - Matrix Compression (sigma_11 >= Yc)
C Failure criterion for matrix cracking under transverse compression and shear
C (Sig11 > Yc)
       if (S22 < 0 .AND. S11 >= -YC) then
        alpha_0 = 53 ! [deg] fracture plane angle at pure compression 53 or test
data (could be higher)
        alpha_r = alpha_0 * Pi / 180 ! [rad] converting the fracture angle into
radians

        S_L = S
        S_T = YC * COS(alpha_r) * (SIN(alpha_r) + (COS(alpha_r)) / TAN(2
     1  *alpha_r))

        nl = - S/YC * COS(2*(alpha_r))/COS(alpha_r)**2  ! [-] longitudinal
coefficient of influence 0.25 for RP528
```

```
        nt =  -1 / TAN(2*alpha_r)                       ! [-] transverse
coefficient of influence

        !write(15,*) 'nl = ', nl
        !write(15,*) 'nt = ', nt

       i=0
       FI1 = 0
       do 10 i = 1, alpha_0
        i_r = i * Pi / 180
        tau_eff_T1 = -S22 * COS(i_r) * (SIN(i_r) - nt * COS(i_r))    ! [Pa]
effective transverse shear stress
        tau_eff_L1 = COS(i_r) * (ABS(S12) + nl * S22 * COS(i_r))     ! [Pa]
effective fibre longitudinal shear stress

        tau_eff_T = (tau_eff_T1 + ABS(tau_eff_T1)) / 2
        tau_eff_L = (tau_eff_L1 + ABS(tau_eff_L1)) / 2

        FI_temp = ((tau_eff_T/S_T)**2 +(tau_eff_L/S_L)**2)**0.5
        !write(15,*) 'alp=',i,' teff_T=',tau_eff_T,' teff_L=',tau_eff_L
        !write(15,*) 'FI_temp =', FI_temp
        if (FI_temp > FI1) then
        FI1 = FI_temp ! Matrix Compression (sigma_11 >= Yc)
        end if
  10   continue

       else
        FI1 = 0
       end if

C LaRC 2 - Matrix Tension (sigma_22 >= 0)
C Failure criterion for matrix cracking under transverse compression and shear
C (Sig11 > Yc)
      if (S22 >= 0) then
      delta22 = 2*(1/E2-nu21**2/E1)  ![1/MPa] Material toughness parameter
      delta44 = 1/G12                ![1/MPa] Material toughness parameter

      g = 1.12**2*delta22/delta44*(YT/S)**2

      FI2 = (1 - g)*(S22/YT) + g*(S22/YT)**2 + (S12/S)**2
      else
      FI2 = 0
      end if

C LaRC 3 - Fiber Tension (sigma_11 >= 0)
C Failure criterion for fiber tension failure under tension
      if (S11 >= 0) then
      FI3 = S11/XT
      else
      FI3 = 0
      end if

C LaRC 4 - Fiber Compression (sigma_22_m < 0)
C Failure criterion for fiber compression and transverse compression
      if (S11 < 0) then
      alpha_0 = 53 ! [deg] fracture plane angle at pure compression 53 or test
data (could be higher)
      alpha_r = alpha_0 * Pi / 180 ! [rad] converting the fracture angle into
radians

      nl = - S/YC * COS(2*(alpha_r))/COS(alpha_r)**2
      phi_c_m = ATAN((1-(1-4*(S/XC+nl)*(S/XC))**0.5)/(2*(S/Xc + nl))) ! [rad]
total misalignment angle in case of pure fibre compression
```

```
      phi_m = (ABS(S12) + (G12- XC)*phi_c_m) / (G12 + S11 - S22)      ! [rad]
total misalignment angle

      S22_m = S11*SIN(phi_m)**2 + S22*COS(phi_m)**2 - 2*SIN(phi_m)*cos(p
     1hi_m)*ABS(S12)
      S12_m = -S11*SIN(phi_m)*COS(phi_m) + S22*SIN(phi_m)*COS(phi_m) +
     1(COS(phi_m)**2-SIN(phi_m)**2)*ABS(S12)
      if (S22_m < 0) then
      FI_temp = (ABS(S12_m)+nl*S22_m)/S
      FI4 = 0.5 * (FI_temp + ABS(FI_temp))
      else
      FI4 = 0
      end if
      else
      FI4=0
      end if

C LaRC 5 - Fiber Compression (sigma_22_m >= 0)
C Failure criterion for fibre compression and transverse tension
      if (S11 < 0) then
      delta22 = 2*(1/E2-nu21**2/E1)  ![1/MPa] Material toughness parameter
      delta44 = 1/G12                ![1/MPa] Material toughness parameter

      g = 1.12**2*delta22/delta44*(YT/S)**2

      S22_m = S11*SIN(phi_m)**2 + S22*COS(phi_m)**2 - 2*SIN(phi_m)*cos(p
     1hi_m)*ABS(S12)
      S12_m = -S11*SIN(phi_m)*COS(phi_m) + S22*SIN(phi_m)*COS(phi_m) +
     1(COS(phi_m)**2-SIN(phi_m)**2)*ABS(S12)

      if (S22_m >=0) then
      FI5 = (1-g)*(S22_m/YT)+g*(S22_m/YT)**2+(S12_m/S)**2
      else
      FI5 = 0
      end if
      else
      FI5 = 0
      end if

C LaRC 6 - Matrix Compression (sigma_22 <0)
C Failure criterion for matrix cracking under transverse compression and shear
C (sig11 < Yc)
      if (S22 < 0 .AND. S11 < -YC) then
       alpha_0 = 53 ! [deg] fracture plane angle at pure compression 53 or test
data (could be higher)
       alpha_r = alpha_0 * Pi / 180 ! [rad] converting the fracture angle into
radians

       S_L = S
       S_T = YC * COS(alpha_r) * (SIN(alpha_r) + (COS(alpha_r)) / TAN(2
     1 *alpha_r))

       nl = - S/YC * COS(2*(alpha_r))/COS(alpha_r)**2    ! [-] longitudinal
coefficient of influence 0.25 for RP528
       nt =  -1 / TAN(2*alpha_r)      ! [-] transverse coefficient of influence
       !write(15,*) 'nl=',nl,' nt=',nt
       phi_c_m = ATAN((1-(1-4*(S/XC+nl)*(S/XC))**0.5)/(2*(S/Xc + nl)))! [rad]
total misalignment angle in case of pure fibre compression
       phi_m = (ABS(S12) + (G12- XC)*phi_c_m) / (G12 + S11 - S22)     ! [rad]
total misalignment angle
       !write(15,*) 'phi_c=',phi_c_m,' phi_m=',phi_m
       S22_m = S11*SIN(phi_m)**2 + S22*COS(phi_m)**2 - 2*SIN(phi_m)*cos(
     1  phi_m)*ABS(S12)
       S12_m = -S11*SIN(phi_m)*COS(phi_m) + S22*SIN(phi_m)*COS(phi_m) +
```

```
     1  (COS(phi_m)**2-SIN(phi_m)**2)*ABS(S12)
       !write(15,*) 'S22_m=',S22_m,' S12_m=',S12_m
        FI6 = 0
        i=0
        do 11 i = 1, alpha_0
         i_r = i * Pi / 180
         tau_eff_T1 = -S22_m * COS(i_r) * (SIN(i_r) - nt * COS(i_r))   ! [Pa]
effective transverse shear stress
         tau_eff_L1 = COS(i_r) * (ABS(S12_m) + nl * S22_m * COS(i_r))  ! [Pa]
effective fibre longitudinal shear stress
      !write(15,*) 'alp=',i,' teff_T=',tau_eff_T1,' teff_L=',tau_eff_L1
        tau_eff_T = (tau_eff_T1 + ABS(tau_eff_T1)) / 2
        tau_eff_L = (tau_eff_L1 + ABS(tau_eff_L1)) / 2

        FI_temp = ((tau_eff_T/S_T)**2 +(tau_eff_L/S_L)**2)**0.5

        if (FI_temp > FI6) then
        FI6 = FI_temp
        end if
  11   continue
      end if

C LaRC Envelop
C Finds max FI value for all LaRC conditions
      FIs(1) = FI1
      FIs(2) = FI2
      FIs(3) = FI3
      FIs(4) = FI4
      FIs(5) = FI5
      FIs(6) = FI6

      FI7 = MAX(FI1,FI2,FI3,FI4,FI5,FI6)
      FI_Mode = 1
      if (FI2 == FI7) then
          FI_Mode = 2
      elseif (FI3 == FI7) then
          FI_Mode = 3
      elseif (FI4 == FI7) then
          FI_Mode = 4
      elseif (FI5 == FI7) then
          FI_Mode = 5
      elseif (FI6 == FI7) then
          FI_Mode = 6
      end if
C
C UPDATE STATEV
      STATEV(1) = FI1
      STATEV(2) = FI2
      STATEV(3) = FI3
      STATEV(4) = FI4
      STATEV(5) = FI5
      STATEV(6) = FI6
      STATEV(7) = FI7
      STATEV(8) = FI_Mode

      if (FI7 > 1.5) then ! terminates analysis when failure reached
      CALL XIT
      end if

      else
          !WRITE(15,*)'IN ELSE'
       STATEV(1) = 0
      STATEV(2) = 0
      STATEV(3) = 0
```

```
      STATEV(4) = 0
      STATEV(5) = 0
      STATEV(6) = 0
      STATEV(7) = 0
      STATEV(8) = 0
      end if

      !CLOSE(15)
C
C USER CODE END_____________________________________________________________
      RETURN
      END
```

Appendix D

Point cloud transformation code

```
function [D,D1] = pctransform(filename)
  %
  %
  % function data = pctransform( filename )
  %
  % Written by : Timothy M Harrell (T.M.Harrell@soton.ac.uk)
  % Date       : Jan 2019
  %
  %
  % Function   : Take point cloud data from quarter plate model and mirror
  %              it over the x and y symmetry axis. Then, translate the
  %              data so that bottom left of the data is at the origin
  %              (0,0).
  %
  % Description: This work uses the data collected from the damage model in
  %              point cloud format. An example of the damage model is in
  %              the ECCM 2018 [1].
  %
  %  References: [1] 3.   T M Harrell, O T Thomsen, J M Dulieu-Barton, and L
  %                  Carloni. 2018. “Delamination Prediction on CFRP Mater-
  %                  ials Subjected to a Lightning Strike,” in 18th Europe-
  %                  an Conference on Composite Materials, Athens, Greece.

%Opens the file and deliminates the data into a list structure
fileID = fopen(filename);
A = textscan(fileID,'%f %f %f %f','HeaderLines',9,'delimiter',',');

%Takes the x,y,z from the textscan and puts it into a matrix of [x y z]
B = [A{1} A{2} A{3}];     %[x y z]
y_sym = min(B(:,1));      %if data is not symmetric around the origin this finds
the y-symmetry axis
B(:,1)=-(B(:,1)-2*y_sym); %mirrors the data about the y-symmetry axis

C_orig = [[A{1} A{2} A{3}];B]; %Combines mirrored data and original data
C = C_orig; %Combined data

x_sym = max(C(:,2));      %symmetry line
C(:,2)=-(C(:,2)-2*x_sym); %mirrors data about the x-symmetry axis

D = [C_orig;C];           %Combines the data

D(:,4) = [A{4};A{4};A{4};A{4}]; %Adds the values at those points into the matrix
s = zeros(size(D(:,4),1),1)+50; %Dot scale factor for scatter plot

figure();
scatter3(D(:,1),D(:,2),D(:,3),s,D(:,4),'filled'); hold on; %Scatter plot for all
the data

%Finds vertices for rectangular prism
x1 = min(D(:,1));x2 = max(D(:,1));
y1 = min(D(:,2));y2 = max(D(:,2));
z1 = min(D(:,3));z2 = max(D(:,3));
%Plots rectangular prism
plot3([x1 x2 x2 x1 x1],[y1 y1 y1 y1 y1],[z1 z1 z2 z2 z1],'black','LineWidth',3);
plot3([x1 x1 x1 x1],[y1 y2 y2 y1],[z1 z1 z2 z2],'black','LineWidth',3);
plot3([x1 x2 x2 x1],[y2 y2 y2 y2],[z1 z1 z2 z2],'black','LineWidth',3);
```

Appendix D

Point cloud transformation code

```
plot3([x1 x1 x1 x1],[y1 y2 y2 y1],[z1 z1 z2 z2],'black','LineWidth',3);
plot3([x2 x2 x2 x2],[y1 y2 y2 y1],[z1 z1 z2 z2],'black','LineWidth',3);
hold off;

%Takes out but only damage data
D1 = D((D(:,4)==1),:);

%Plots damage data with original rectangular prism
figure();
s = zeros(size(D1(:,4),1),1)+50;
scatter3(D1(:,1),D1(:,2),D1(:,3),s,D1(:,4),'filled'); hold on;
plot3([x1 x2 x2 x1 x1],[y1 y1 y1 y1 y1],[z1 z1 z2 z2 z1],'black','LineWidth',3);
plot3([x1 x1 x1 x1],[y1 y2 y2 y1],[z1 z1 z2 z2],'black','LineWidth',3);
plot3([x1 x2 x2 x1],[y2 y2 y2 y2],[z1 z1 z2 z2],'black','LineWidth',3);
plot3([x1 x1 x1 x1],[y1 y2 y2 y1],[z1 z1 z2 z2],'black','LineWidth',3);
plot3([x2 x2 x2 x2],[y1 y2 y2 y1],[z1 z1 z2 z2],'black','LineWidth',3);
hold off;
```

Appendix E

Compression After Lightning Strike (CALS) rig design drawings

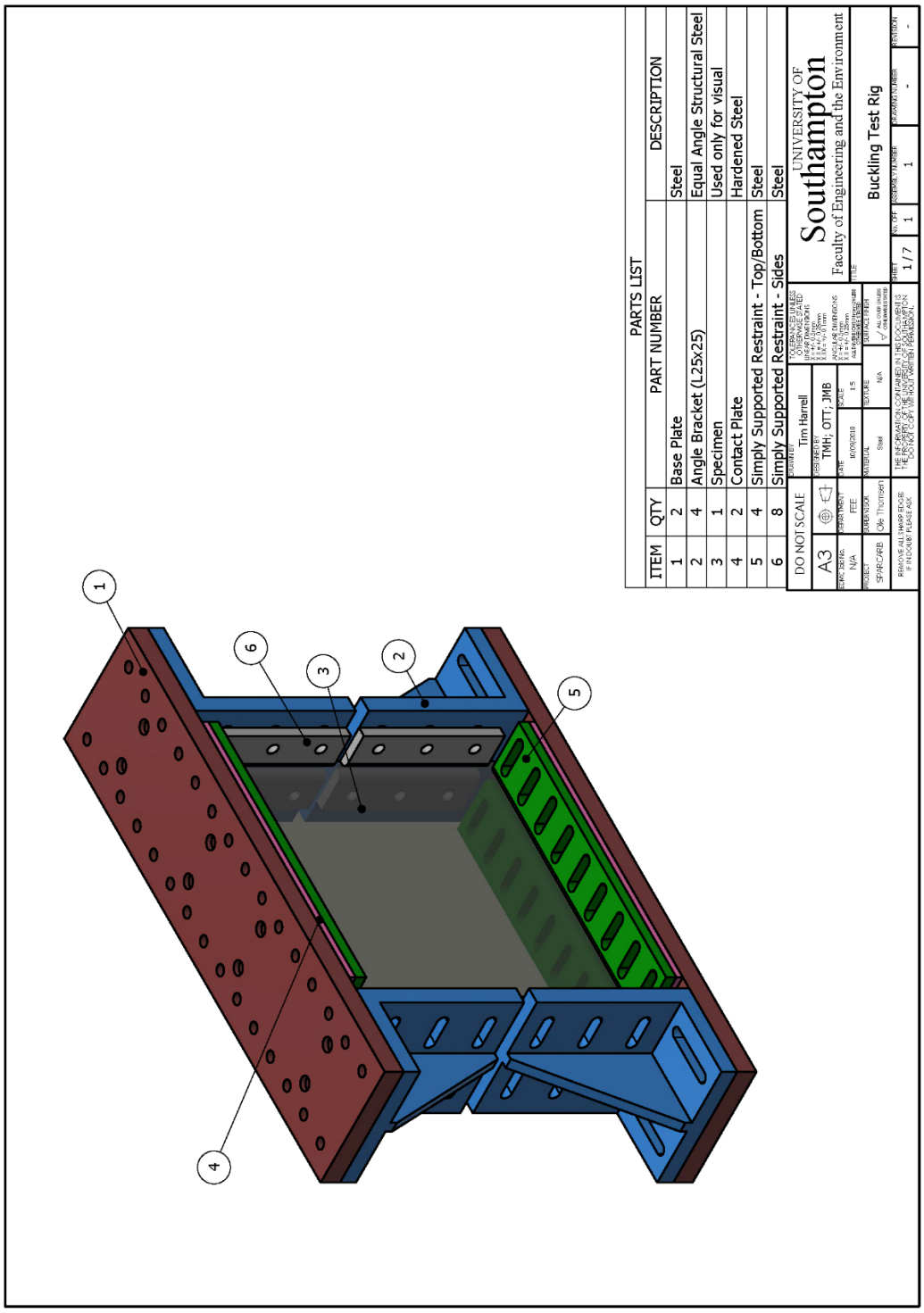

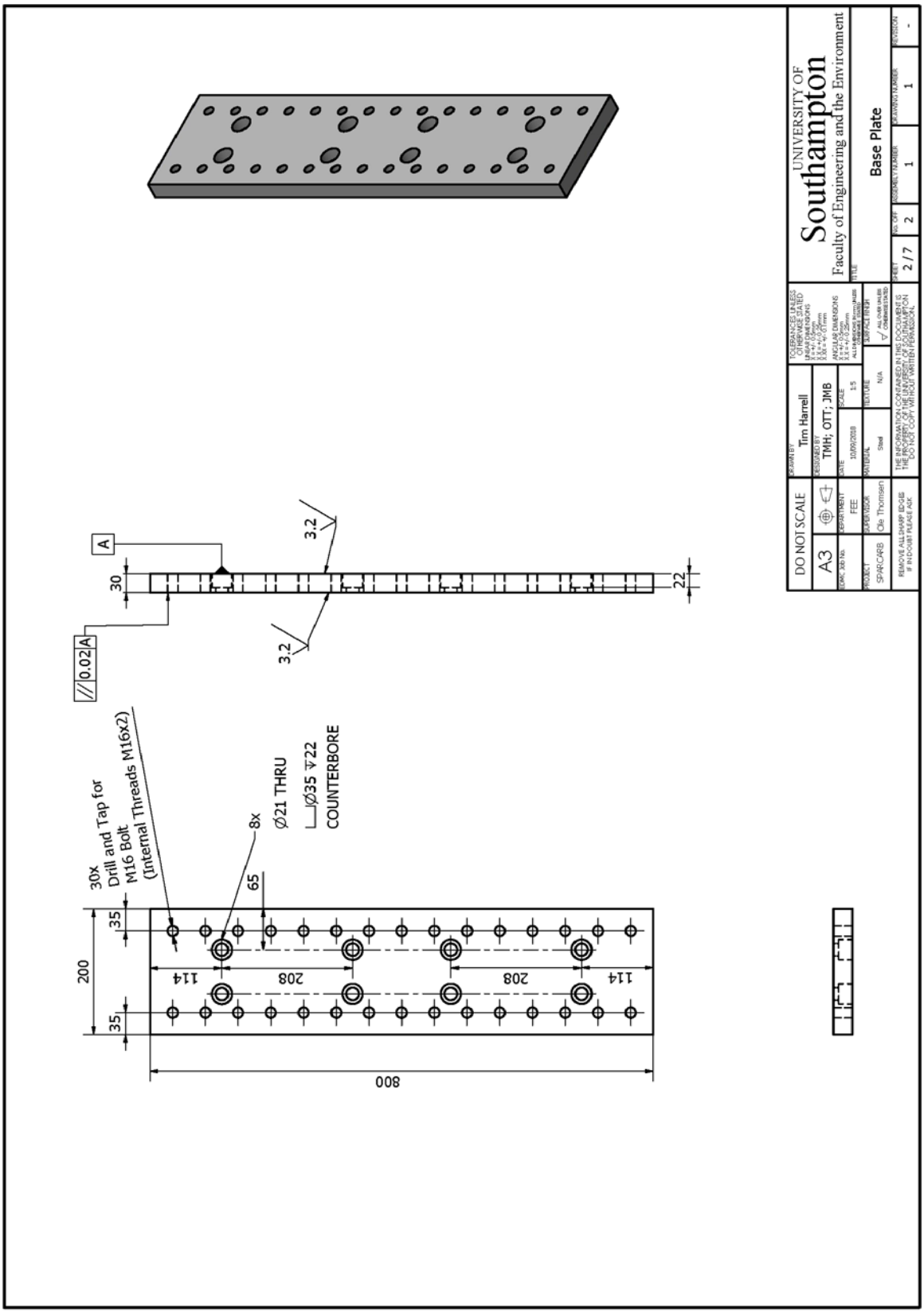
A
3.2
30
22
3.2
//0.02|A
30x
Drill and Tap for
M16 Bolt
(Internal Threads M16x2)
8x
Ø21 THRU
⌴Ø35 ↧22
COUNTERBORE
65
200
35
35
114
208
208
114
800
DO NOT SCALE
A3
DRAWN BY
Tim Harrell
DESIGNED BY
TMH; OTT; JMB
DATE
30/09/2020
SCALE
1:5
MATERIAL
Steel
TOLERANCE
N/A
SURFACE FINISH
PROJECT
SPARCARB
SUPERVISOR
Ole Thomsen
DEPARTMENT
FEE
TOLERANCES UNLESS OTHERWISE STATED
LINEAR DIMENSIONS
ANGULAR DIMENSIONS
THE INFORMATION CONTAINED IN THIS DRAWING IS THE PROPERTY OF THE UNIVERSITY OF SOUTHAMPTON
DO NOT COPY WITHOUT WRITTEN PERMISSION
REMOVE ALL SHARP EDGES
IF IN DOUBT PLEASE ASK
University of Southampton
Faculty of Engineering and the Environment
TITLE
Base Plate
SHEET
2 / 7
NO. OFF
2
ASSEMBLY NUMBER
1
DRAWING NUMBER
1
REVISION
-

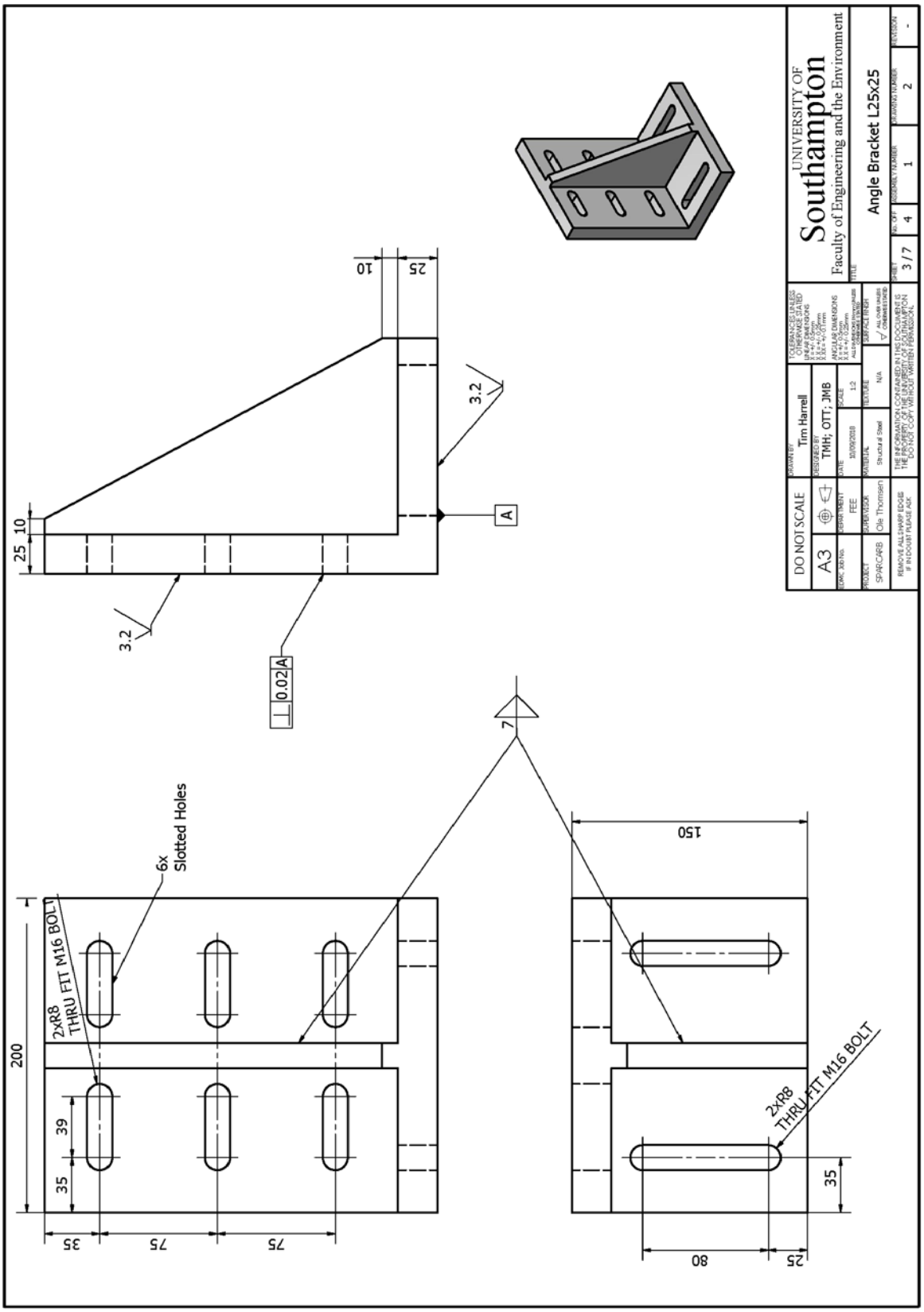
UNIVERSITY OF Southampton
Faculty of Engineering and the Environment
Angle Bracket L25x25
DO NOT SCALE
A3
Tim Harrell
TMH; OTT; JMB
1:2
N/A
Structural Steel
Ola Thomsen
SPARCARB
3 / 7
4
1
2
-
25
10
3.2
A
0.02 A
7
150
6x Slotted Holes
2xR8 THRU FIT M16 BOLT
200
39
35
75
75
35
80
25

Appendix E

Compression After Lightning Strike (CALS) rig design drawings

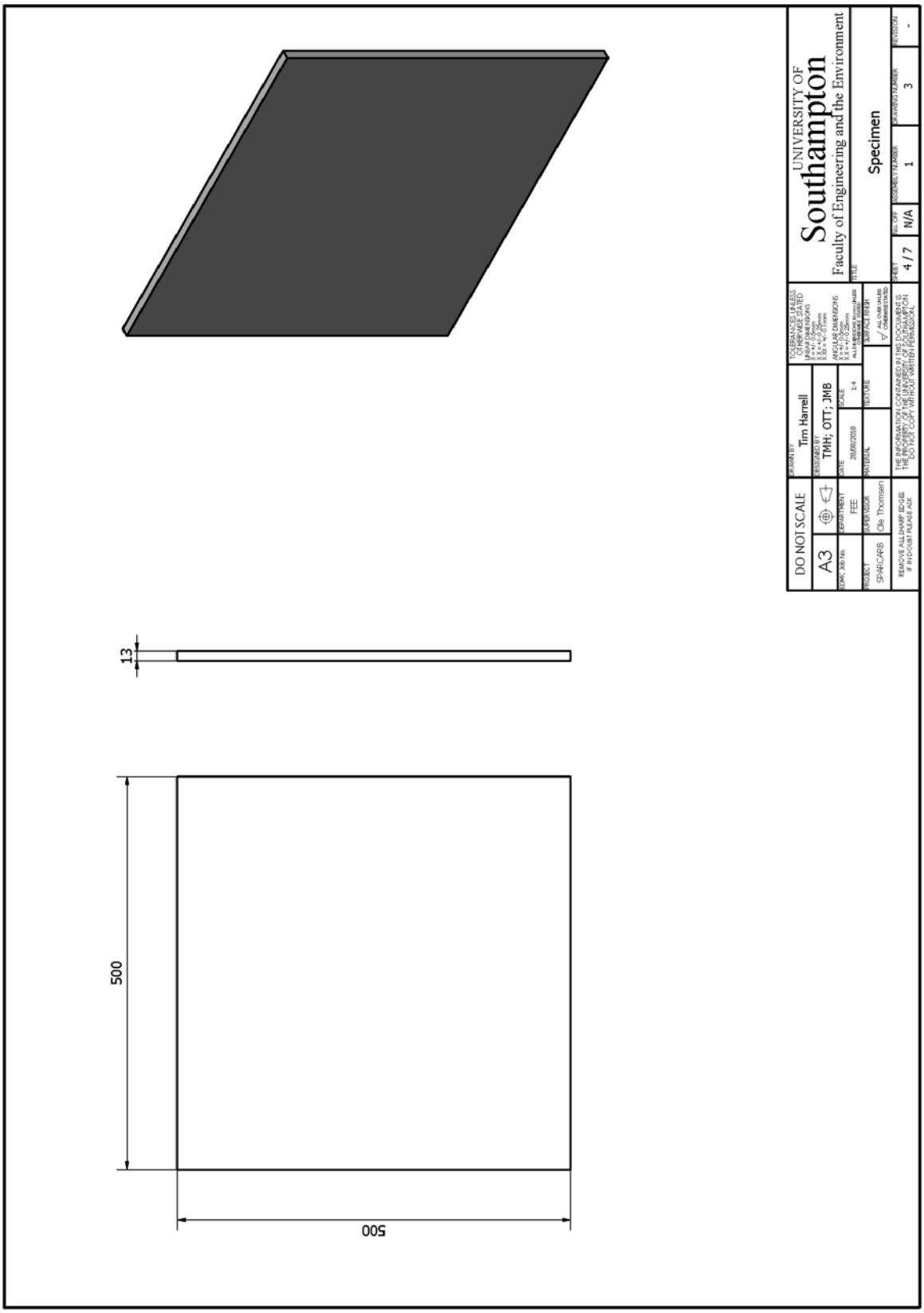

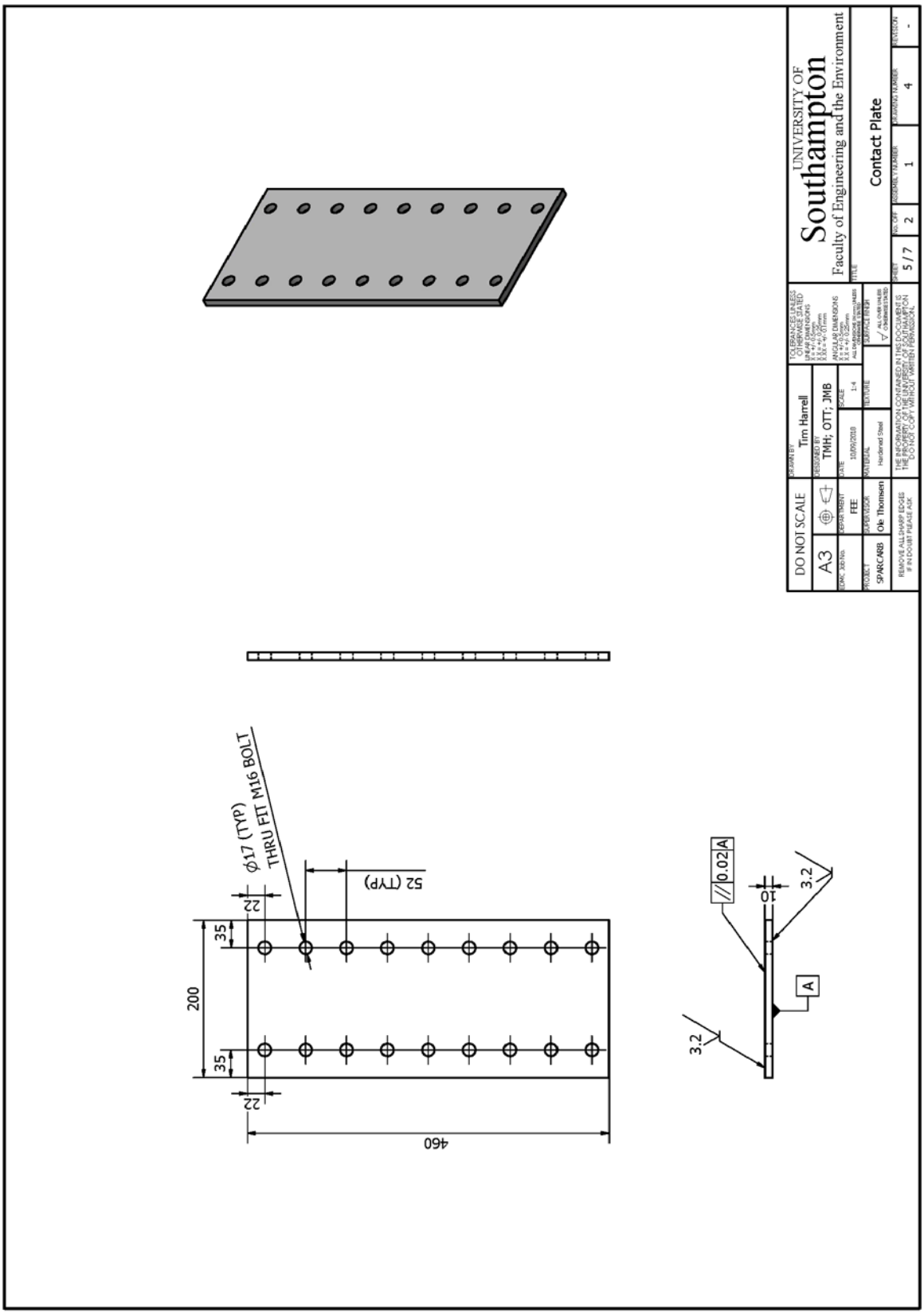
UNIVERSITY OF Southampton
Faculty of Engineering and the Environment
Contact Plate
DRAWN BY Tim Harrell
DESIGNED BY TMH; OTT; JMB
DO NOT SCALE
A3
SCALE 1:4
DATE 10/09/2010
MATERIAL Hardened Steel
SP:ARC:A9B
Ole Thomsen
SHEET 5 / 7
NO. OFF 2
ASSEMBLY NUMBER 1
DRAWING NUMBER 4
REVISION -
ϕ17 (TYP) THRU FIT M16 BOLT
52 (TYP)
22
35
200
460
//0.02A
3.2
A

Compression After Lightning Strike (CALS) rig design drawings

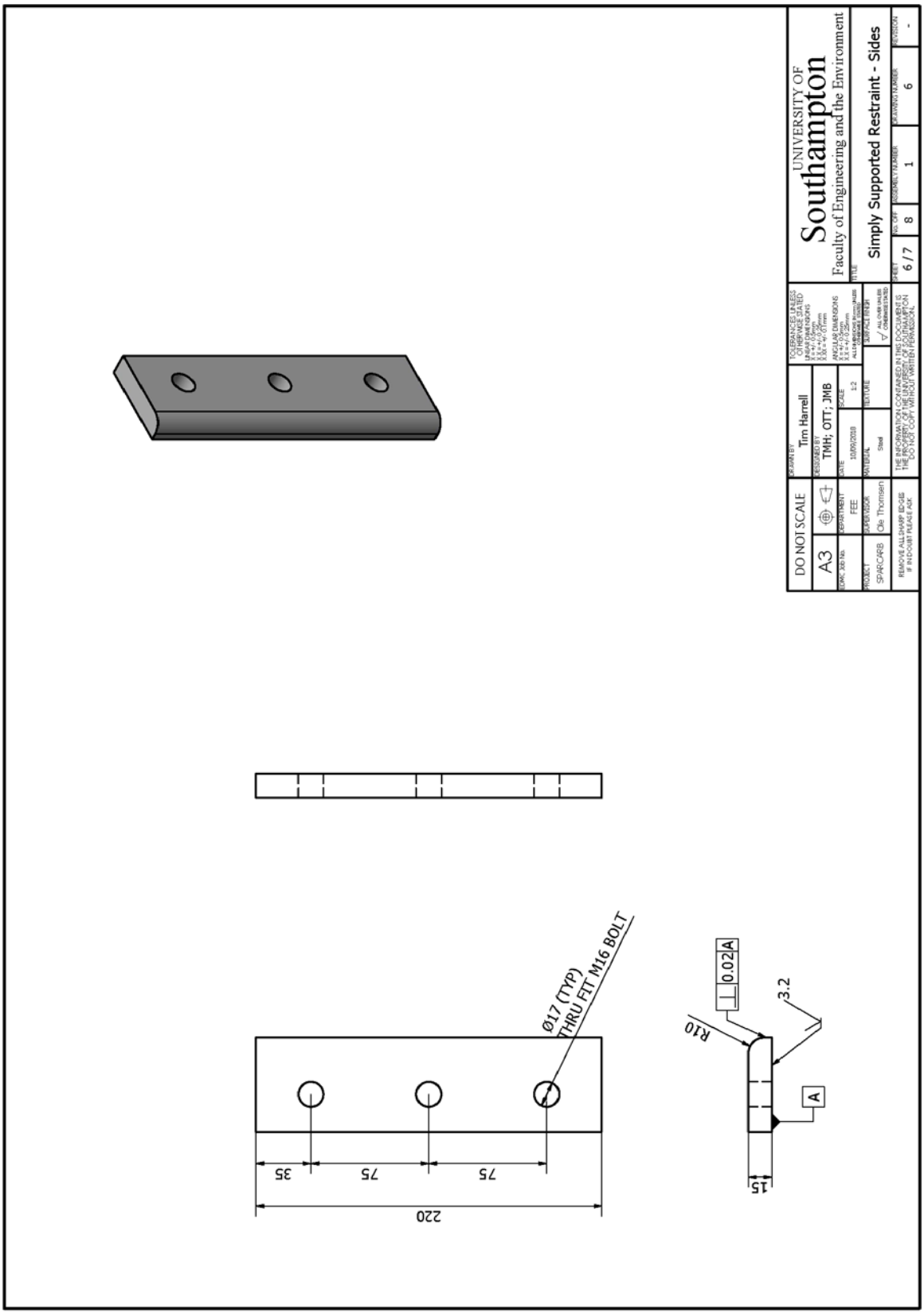

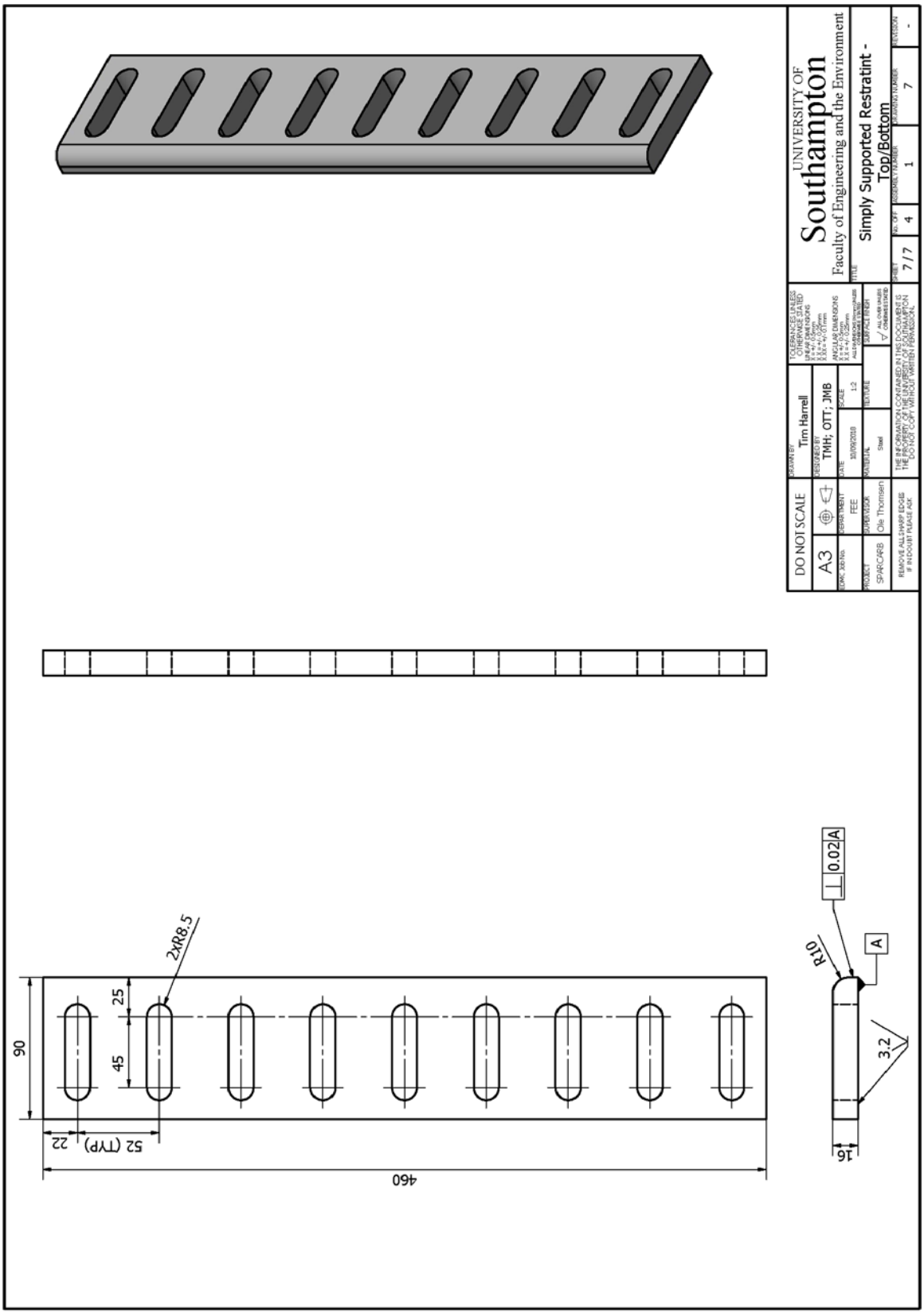
UNIVERSITY OF Southampton
Faculty of Engineering and the Environment
Simply Supported Restratint - Top/Bottom
DRAWN BY Tim Harrell
DESIGNED BY TMH; OTT; JMB
DATE 10/09/2010
SCALE 1:2
TOLERANCE
MATERIAL Steel
DO NOT SCALE
A3
PROJECT SPARC/ARB
DRAWING NUMBER 7
REVISION -
2xR8.5
25
45
90
52 (TYP)
22
460
0.02 A
R10
A
3.2
16

Appendix F

List of publications

F.1 Published Journal Papers

1. T. M. Harrell, O. T. Thomsen, J. M. Dulieu-Barton, and S. F. Madsen, “Damage in CFRP composites subjected to simulated lightning strikes - Assessment of thermal and mechanical responses,” Compos. Part B Eng., vol. 176, no. July, p. 107298, Nov. 2019. https://doi.org/10.1016/j.compositesb.2019.107298

F.2 Conference Papers

1. T M Harrell, O T Thomsen, J M Dulieu-Barton, S F Madsen, and L Carloni. 2017. “Lightning Protection of CFRP Wind Turbine Blades - What Is the Dominant Cause of Failure: Specific Energy or Charge?” In *International Conference on Lightning and Static Electricity*, Nagoya, Japan, 1–5.
   Awarded: “Best paper by young researcher award.” Selected by International Conference on Lightning and Static Electricity board.
2. T M Harrell, O T Thomsen, J M Dulieu-Barton, S F Madsen, and L Carloni. 2017. “Damage Prediction of CFRP Materials Subjected to Lightning Strike.” In *21st International Conference on Composite Materials*, Xi’an, China, 1–9.
3. T M Harrell, O T Thomsen, J M Dulieu-Barton, and L Carloni. 2018. “Delamination Prediction on CFRP Materials Subjected to a Lightning Strike,” in *18th European Conference on Composite Materials*, Athens, Greece, 1-9.
4. T M Harrell, J M Dulieu-Barton, and O T Thomsen. 2018. “Identification of lightning strike damage using Pulse Thermography through integration of thermal data,” in *Society of Experimental Mechanics*, Greenville, SC, USA, 1-4.
5. T M Harrell, O T Thomsen, and J M Dulieu-Barton. 2019. “Buckling Behaviour of UD Carbon/Epoxy Panels Subjected to Direct Lightning Strike,” in *22nd International Conference on Composite Materials*, Melbourne, AU, 1-6.
6. T M Harrell, O T Thomsen, and J M Dulieu-Barton. 2019. “Structural Response of CFRP Materials Subjected to Simulated Lightning Strikes,” in *14th International Conference on Advances on Experimental Mechanics*, Belfast, UK, 1-5.
   Awarded: “Young Stress Analyst Award” Selected runner up by British Society for Strain Measurement selection committee.

F.3 Conference Presentations

1. T M Harrell, O T Thomsen, and J M Dulieu-Barton. 2017 “Hybrid multiscale modelling to predict lightning damage on CFRP materials,” in *International Symposium on Multiscale Experimental Mechanics: Multiscale Fatigue* Copenhagen, Denmark.

2. T M Harrell, O T Thomsen, J M Dulieu-Barton, S F Madsen, and L Carloni. 2017. “Heat Response of Unipolar Lightning Impulse and DC Current Component Conducted through CFRP Samples Used for Wind Turbine Sparcaps.” In *Wind Energy Science Conference*, Lyngby, Denmark, 1–10.
3. Timothy M. Harrell, Ole Thybo Thomsen, and Janice M Dulieu-Barton. 2016. “Lightning Protection of Wind Turbine Blades.” In *Sustainability in Action Conference*, Southampton, England, 1–10.

F.4 Planned Publications

1. Damage Modelling in CFRP Materials Subjected to Lightning Strikes with Electric Field Dependent Material Properties to Account for Surface Discharge. Journal: Composite Structures
2. Buckling Behaviour of UD Carbon/Epoxy Panels Subjected to Direct Lightning Strike. Journal: Composites Part B: Engineering

List of References

[1] International Energy Agency, “Global Energy & CO2 Status Report,” 2018.

[2] T. Bawden, “Wind power now UK’s cheapest source of electricity – but the Government continues to resist onshore turbines,” *The Independent*, 2015. [Online]. Available: http://www.independent.co.uk/environment/wind-power-now-the-cheapest-source-of-electricity-but-the-government-continues-to-resist-onshore-a6685326.html. [Accessed: 19-Jan-2016].

[3] Lazard, “Lazard’s levelized cost of energy analysis - version 12.0,” 2018.

[4] Internaional Renewable Energy Agency, *Renewable Power Generation Costs in 2017*. 2017.

[5] Bloomberg New Energy Finance, “New Energy Outlook 2018,” 2018.

[6] A. McCrone, U. Moslener, F. D’Estais, and C. Grünig, “Global Trends in Renewable Energy Investment 2017,” *Frankfurt Sch. UNEP Collab. Cent. Clim. Sustain. Energy Financ.*, 2017.

[7] A. M. Ram, M. Child, A. Aghahosseini, D. Bogdanov, and A. Poleva, “Comparing electricity production costs of renewables to fossil and nuclear power plants in G20 countries,” Hamburg, Germany, 2017.

[8] European Wind Energy Association, *Where’s the money coming from? Financing offshore wind farms*. Brussels, Belgium: EWEA, 2013.

[9] International Energy Agency and Energy Research Institute, “China Wind Energy Development Roadmap 2050,” p. 56, 2011.

[10] REN21, “Renewable 2018 Global Status Report,” 2018.

[11] National Renewable Energy Laboratory, “Hawaii Clean Energy Initiative 2008–2018,” 2018.

[12] Puerto Rico Electric Power Authority, “Senate Bill 1121: Public Energy Policy Law of Puerto Rico.” pp. 1–124, 2019.

[13] M. Cleveland, “States ’ Increasing Renewable Energy Ambitions,” *Natl. Conf. State Legis. Legisbr.*, vol. 27, no. 5, pp. 1–2, 2020.

[14] Ministerio de Energía, “Ley 20.698: Propicia la ampliación de la matriz energética, mediante fuentes renovables no convencionales.” pp. 1–2, 2013.

[15] P. Cosgrove, “Renewable Energy (Electricity) Amendment (Exemptions and Other Measures) Regulations 2017,” no. December 2017. pp. 1–22, 2019.

[16] Ministry of Economic Development, “Developing Our Energy Potential: New Zealand Energy Efficiency and Conservation Strategy 2011-2016:,” 2011.

[17] E. Hau, *Wind Turbines: Fundamentals, Technologies, Application, Economics*, 3rd ed. Berlin, Heidelberg: Springer Berlin Heidelberg, 2013.

[18] R. Wiser and M. Bolinger, “U.S. Department of Energy: 2016 Wind technologies market report,” 2016.

[19] O. Edenhofer *et al.*, *IPCC, 2011: Summary for Policymakers. In: IPCC Special Report on Renewable Energy Sources and Climate Change Mitigation*. 2011.

[20] International Energy Agency, “World Energy Outlook 2015 Factsheet,” *Glob. energy trends to 2040The energy Sect. Clim. Chang. run-up to COP21*, pp. 1–4, 2015.

[21] Vestas, “Vestas 2011 Wind Turbine Product Line Brochure.” Aarhus, Denmark, p. 1, 2011.

[22] European Wind Energy Association, “Upwind: Design limits and solutions for very large wind turbines,” 2011.

[23] Vestas, “Vestas 2019 Wind Turbine Product Line Brochure.” p. 10, 2019.

[24] Enercon, “Enercon 2019 Wind Turbine Product Brochure.” 2019.

[25] Siemens Gamesa, “Siemens Gamesa 2019 Wind Turbine Product Brochure.” 2019.

[26] Suzlon, “Suzlon 2019 Wind Turbine Product Line Brochure.” 2019.

[27] GE, “GE 2019 Wind Turbine Product Line Brochure.” 2019.

[28] Nordex, “Nordex 2019 Wind Turbine Product Line Brochure.” 2019.

[29] Goldwind, “Goldwind 2019 Wind Turbine Product Line Brochure.” 2019.

[30] P. D. Clausen, F. Reynal, and D. H. Wood, *Advances in Wind Turbine Blade Design and*

Materials. 2013.
[31] Nordex, “Nordex 2019 Wind Turbine Product Line Brochure.” 2019.
[32] O. T. Thomsen, “Sandwich Materials for Wind Turbine Blades - Present and Future,” *J. Sandw. Struct. Mater.*, vol. 11, no. 1, pp. 7–26, 2009.
[33] H. Kawakami and P. Feraboli, “Lightning strike damage resistance and tolerance of scarf-repaired mesh-protected carbon fiber composites,” *Compos. Part A Appl. Sci. Manuf.*, vol. 42, no. 9, pp. 1247–1262, 2011.
[34] L. Chemartin *et al.*, “Direct Effects of Lightning on Aircraft Structure : Analysis of the Thermal , Electrical and Mechanical Constraints,” *J. Aerosp. Lab*, no. 5, pp. 1–15, 2012.
[35] P. Feraboli and M. Miller, “Damage resistance and tolerance of carbon/epoxy composite coupons subjected to simulated lightning strike,” *Compos. Part A Appl. Sci. Manuf.*, vol. 40, no. 6–7, pp. 954–967, 2009.
[36] University of Southampton, “Lightning protection of wind turbine blades with carbon fibre composite materials,” *CORDIS: EU Research Results*, 2019. [Online]. Available: https://cordis.europa.eu/project/rcn/193946/results/en. [Accessed: 30-May-2019].
[37] H. Kawakami, “Lightning Strike Induced Damage Mechanisms of Carbon Fiber Composites: A PhD Thesis,” University of Washington, 2011.
[38] P. Feraboli and H. Kawakami, “Damage of Carbon/Epoxy Composite Plates Subjected to Mechanical Impact and Simulated Lightning,” *J. Aircr.*, vol. 47, no. 3, pp. 999–1012, 2010.
[39] T. Ogasawara, Y. Hirano, and A. Yoshimura, “Coupled thermal-electrical analysis for carbon fiber/epoxy composites exposed to simulated lightning current,” *Compos. Part A Appl. Sci. Manuf.*, vol. 41, no. 8, pp. 973–981, 2010.
[40] G. Abdelal and A. Murphy, “Nonlinear numerical modelling of lightning strike effect on composite panels with temperature dependent material properties,” *Compos. Struct.*, vol. 109, no. 1, pp. 268–278, 2014.
[41] R. D. Chippendale, I. O. Golosnoy, P. L. Lewin, and M. Cole, “Predictions of Lightning Strike Damage in Carbon Fibre Composites,” in *9th IET International Conference on Computation in Electromagnetics (CEM 2014)*, 2014, pp. 1–2.
[42] R. Muñoz, S. Delgado, C. González, B. López-Romano, D. Y. Wang, and J. Llorca, “Modeling lightning impact thermo-mechanical damage on composite materials,” *Appl. Compos. Mater.*, vol. 21, no. 1, pp. 149–164, 2014.
[43] J. LLorca *et al.*, “Multiscale Modeling of Composite Materials: a Roadmap Towards Virtual Testing,” *Adv. Mater.*, vol. 23, no. 44, pp. 5130–5147, 2011.
[44] Y. Hirano *et al.*, “Lightning damage suppression in a carbon fiber-reinforced polymer with a polyaniline-based conductive thermoset matrix,” *Compos. Sci. Technol.*, vol. 127, pp. 1–7, 2016.
[45] R. Jones, *Mechanics of composite materials*, 2nd ed. Philadelphia, PA: Taylor & Francis, Inc., 1999.
[46] T. M. Harrell, O. T. Thomsen, and J. M. Dulieu-barton, “Hybrid multiscale modelling to predict lightning damage on CFRP materials,” in *International Symposium on Multiscale Experimental Mechanics: Multiscale Fatigue2*, 2017, p. 1.
[47] International Electrotechnical Commission, “IEC61400: Wind turbine standard,” 2014.
[48] International Electrotechnical Commission, “IEC 61400: Wind turbines – Part 24 Lightning protection,” 2010.
[49] V. A. Rakov and M. A. Uman, *Lightning Physics and Effects*, Third. New York, NY: Cambridge University Press, 2003.
[50] V. A. Rakov, “The Physics of Lightning,” *Surv. Geophys.*, vol. 34, no. 6, pp. 701–729, 2013.
[51] V. A. Rakov, *Fundamentls of Lightning*, First. New York, NY: Cambridge University Press, 2016.
[52] M. A. Uman, *The art and science of lightning protection*. 2008.
[53] M. A. Uman, *Lightning*. New York, NY: McGraw-Hill, 1969.
[54] R. Golde, *Lightning*, First. New York, NY: Academic Press Inc, 1977.
[55] A. P. Johnson, H. J. Cleaves, J. P. Dworkin, D. P. Glavin, A. Lazcano, and J. L. Bada, “The Miller Volcanic Spark Discharge Experiment,” *Science (80-.).*, vol. 322, no. 5900, pp. 404–404, Oct. 2008.
[56] M. W. Jernegan, “Benjamin Franklin’s ‘Electrical Kite’ and Lightning Rod,” *New Engl. Q.*,

vol. 1, no. 2, pp. 180–196, 1928.
[57] J. Herschel, “On the Lightning Spectrum,” *Proc. R. Soc. London*, vol. 17, pp. 61–62, 1869.
[58] J. Gibbons, “Spectrum of Lightning,” *Chem. News, London*, no. August 25, 1871, p. 96, 1871.
[59] E. S. Holden, “Spectrum of lightning,” *Am. J. Sci.*, vol. s3-4, no. 24, pp. 474–475, Dec. 1872.
[60] J. W. Clark, “Observations on the Spectrum of Sheet Lightning,” *Chem. News, London*, no. July 17, 1874, p. 28, 1874.
[61] M. Dufay, “Recherches sur les spectres des éclairs, deuxiéme partie: étude du spectre dans les régions violette et ultraviolette,” *Ann. Geophys.*, vol. 5, pp. 255–263, 1949.
[62] H. Israel and G. Fries, “Ein Gerät zur spektroskopischen Analyse verschiedener Blitzphasen,” *Optik (Stuttg).*, vol. 13, pp. 365–368, 1956.
[63] I. Stekolnikov and C. Valeev, “L’etude de la foudre dans un laboratoire de campagne,” *CIGRE Rep. no. 30*, 1937.
[64] R. Davis and W. G. Standring, “Discharge Currents Associated with Kite Balloons,” *Proc. R. Soc. A Math. Phys. Eng. Sci.*, vol. 191, no. 1026, pp. 304–322, Nov. 1947.
[65] K. B. Mceachron, “Lightning to the Empire State Building,” *J. Franklin Institute-Engineering Appl. Math.*, vol. 227, pp. 149–217, 1939.
[66] K. B. McEachron, “Lightning to the Empire State Building,” *Trans. Am. Inst. Electr. Eng.*, vol. 60, no. 9, pp. 885–890, 1941.
[67] J. H. Hagenguth and J. G. Anderson, “Lightning to the Empire State Building-Part III,” *Trans. Am. Inst. Electr. Eng. Part III Power Appar. Syst.*, vol. 71, no. 1, pp. 641–649, 1952.
[68] G. D. McCann, “The measurement of lightning currents in direct strokes,” *Electr. Eng.*, vol. 63, no. 12, pp. 1157–1164, Dec. 1944.
[69] K. Berger, R. B. Anderson, and H. Kröninger, “Parameters of Lightning Flashes,” *Electra*, vol. 41, pp. 23–37, 1975.
[70] SAE_International, *SAE ARP 5416: Aircraft Lightning Environment and Related Test Waveforms*. SAE International, 2013, pp. 1–63.
[71] F. Rachidi *et al.*, “A Review of Current Issues in Lightning Protection of New-Generation Wind-Turbine Blades,” *IEEE Trans. Ind. Electron.*, vol. 55, no. 6, pp. 2489–2496, 2008.
[72] J. Montanyà, O. van der Velde, and E. R. Williams, “Lightning discharges produced by wind turbines,” *J. Geophys. Res. Atmos.*, vol. 119, no. 3, pp. 1455–1462, Feb. 2014.
[73] K. Bertelsen, H. V Erichsen, M. V. R. S. Jensen, and S. F. Madsen, “Application To Determine Lightning Attachment Points on Wind Turbines,” in *Proceedings of the international conference on lightning and static electricity*, 2007, pp. 1–13.
[74] A. C. Garolera, S. F. Madsen, M. Nissim, J. D. Myers, and J. Holboell, “Lightning Damage to Wind Turbine Blades From Wind Farms in the U.S.,” *IEEE Trans. Power Deliv.*, vol. 31, no. 3, pp. 1043–1049, Jun. 2016.
[75] S. Yokoyama, N. Honjo, Y. Yasuda, and K. Yamamoto, “Causes of wind turbine blade damages due to lightning and future research target to get better protection measures,” in *2014 International Conference on Lightning Protection (ICLP)*, 2014, pp. 823–830.
[76] W. R. Gamerota, J. O. Elismé, M. A. Uman, and V. A. Rakov, “Current Waveforms for Lightning Simulation,” *IEEE Trans. Electromagn. Compat.*, vol. 54, no. 4, pp. 880–888, Aug. 2012.
[77] S. F. Madsen, “Interview with Søren Find Madsen (GLPS).” 2017.
[78] International Electrotechnical Commission, “IEC62305: Protection against lightning,” 2013.
[79] D. Romero, J. Montanya, and J. Vinck, “Test and simulation of lightning current distribution on a wind turbine blade,” *2014 Int. Conf. Light. Prot.*, pp. 1720–1724, 2014.
[80] A. Garolera, “Lightning protection of flap system for wind turbine blades,” Technical University of Denmark, 2014.
[81] E. Rupke, *Lightning direct effects handbook*. Lightning Technologies, Inc., 2002.
[82] M. Gagné and D. Therriault, “Lightning strike protection of composites,” *Prog. Aerosp. Sci.*, vol. 64, no. January, pp. 1–16, 2014.
[83] F. A. Fisher and J. A. Plumer, *Aircraft Lightning Protection Handbook*, no. September. DOT/FAA/CT-89/ 22, 1989.
[84] C. C. Goodloe, “Lightning Protection Guidelines for Aerospace Vehicles,” Marshall Space Flight Center, NASA/TM-1999-209734, 1999.

[85] Dexmet Microgrid Products, “Lightning Strike Protection for Carbon Fiber Aircraft Lightning Strike Protection for Carbon Fiber Aircraft,” 2010.
[86] S. F. Madsen, K. Bertelsen, T. H. Krogh, H. V. Erichsen, A. N. Hansen, and K. B. Lonbaek, “Proposal of new zoning concept considering lightning protection of wind turbine blades,” in *2010 30th International Conference on Lightning Protection (ICLP)*, 2010, vol. 2010, no. 2, pp. 1–7.
[87] Z. Duan *et al.*, “Lightning direct effect experimental research on rotor blade of a helicopter,” in *2014 IEEE International Power Modulator and High Voltage Conference (IPMHVC)*, 2014, pp. 295–299.
[88] X. Ma, F. Scarpa, H. X. Peng, G. Allegri, J. Yuan, and R. Ciobanu, “Design of a hybrid carbon fibre/carbon nanotube composite for enhanced lightning strike resistance,” *Aerosp. Sci. Technol.*, vol. 47, pp. 367–377, 2015.
[89] F. Moupfouma, “Aircraft Structure Paint Thickness and Lightning Swept Stroke Damages,” pp. 392–398, 2013.
[90] F. Lago, J. J. Gonzalez, P. Freton, F. Uhlig, N. Lucius, and G. P. Piau, “A numerical modelling of an electric arc and its interaction with the anode: part III. Application to the interaction of a lightning strike and an aircraft in flight,” *J. Phys. D. Appl. Phys.*, vol. 39, no. 10, pp. 2294–2310, May 2006.
[91] R. Baksht, A. Pokryvailo, Y. Yankelevich, and I. Ziv, “Explosion of thin aluminum foils in air,” *J. Appl. Phys.*, vol. 96, no. 11, pp. 6061–6065, 2004.
[92] S. F. Madsen, “Interaction between electrical discharges and materials for wind turbine blades – particularly related to lightning protection,” The Technical University of Denmark (DTU), 2006.
[93] Y. Yasuda, S. Yokoyama, M. Minowa, and T. Satoh, “Classification of lightning damage to wind turbine blades,” *IEEJ Trans. Electr. Electron. Eng.*, vol. 7, no. 6, pp. 559–566, 2012.
[94] Y. Wang, “Multiphysics analysis of lightning strike damage in laminated carbon/glass fiber reinforced polymer matrix composite materials: A review of problem formulation and computational modeling,” *Compos. Part A Appl. Sci. Manuf.*, vol. 101, pp. 543–553, Oct. 2017.
[95] T. M. Harrell, O. T. Thomsen, J. M. Dulieu-Barton, S. F. Madsen, and L. Carloni, “Heat Response of Unipolar Lightning Impulse and DC current component conducted through CFRP Samples used for Wind Turbine Sparcaps,” in *Wind Energy Science Conference*, 2017, pp. 1–10.
[96] T. M. Harrell, O. T. Thomsen, J. M. Dulieu-Barton, and S. F. Madsen, “Damage in CFRP composites subjected to simulated lightning strikes - Assessment of thermal and mechanical responses,” *Compos. Part B Eng.*, vol. 176, no. 1 November 2019, p. 107298, Nov. 2019.
[97] Y. Kostogorova-Beller and R. C. Ii, “Modeling of Lightning Direct Effects – Interaction of Continuing Current with Aluminum Skins,” *COMSOL Conf. 2010*, no. 4, pp. 2–6, 2010.
[98] Q. Dong, Y. Guo, X. Sun, and Y. Jia, “Coupled electrical-thermal-pyrolytic analysis of carbon fiber/epoxy composites subjected to lightning strike,” *Polym. (United Kingdom)*, vol. 56, pp. 385–394, 2015.
[99] Y. Hirano, S. Katsumata, Y. Iwahori, and A. Todoroki, “Artificial lightning testing on graphite/epoxy composite laminate,” *Compos. Part A Appl. Sci. Manuf.*, vol. 41, no. 10, pp. 1461–1470, 2010.
[100] A. C. Garolera, J. Holboell, and S. F. Madsen, “Lightning transient analysis in wind turbine blades,” in *Proceedings of International Conference on Power Systems Transients*, 2013, pp. 1–7.
[101] J. H. Hagenguth, “Lightning Stroke Damage to Aircraft,” *Trans. Am. Inst. Electr. Eng.*, vol. 68, no. 2, pp. 1036–1046, Jul. 1949.
[102] Z. Yinghui, F. Shangchen, S. Lihua, S. Qing, and H. Zhengyu, “Experiment research of CFRP destroyed by lightning current,” in *2014 International Conference on Lightning Protection, ICLP 2014*, 2014, pp. 1303–1306.
[103] K. Yamamoto, “Current distribution characteristics of CFRP panels,” *Electron. Commun. Japan*, vol. 96, no. 6, pp. 32–40, Jun. 2013.
[104] R. Brocke, F. Noack, F. Reichert, J. Schoenau, and W. Zischank, “The Numerical Simulation of the Effects of Lightning Current Arcs at the Attachment Point,” in *International Conference on Lightning and Static Electricity*, 2001, p. 8.

[105] F. Lago, P. Freton, and J.-J. Gonzalez, “Numerical modeling of the interaction between an electric arc and a material: application to the lightning stroke of an aircraft,” *IEEE Trans. Plasma Sci.*, vol. 33, no. 2, pp. 434–435, Apr. 2005.
[106] S. J. Haigh Taylor, “Impulse effects during simulated lightning attachments to lightweight composite panels,” in *International Aerospace and Ground Conference on Lightning and Static Electricity*, 2007.
[107] B. Lepetit, C. Escure, S. Guinard, I. Revel, and G. Peres, “Thermo-mechanical effects induced by lightning on carbon fiber composite materials,” in *International Conference on Lightning & Static Electricity*, 2011, pp. 1–8.
[108] F. S. Wang, Y. Y. Ji, X. S. Yu, H. Chen, and Z. F. Yue, “Ablation damage assessment of aircraft carbon fiber/epoxy composite and its protection structures suffered from lightning strike,” *Compos. Struct.*, vol. 145, pp. 226–241, 2016.
[109] S. Kamiyama, Y. Hirano, T. Okada, and T. Ogasawara, “Lightning strike damage behavior of carbon fiber reinforced epoxy, bismaleimide, and polyetheretherketone composites,” *Compos. Sci. Technol.*, vol. 161, no. February, pp. 107–114, 2018.
[110] S. Kamiyama, Y. Hirano, and T. Ogasawara, “Delamination analysis of CFRP laminates exposed to lightning strike considering cooling process,” *Compos. Struct.*, vol. 196, no. April, pp. 55–62, 2018.
[111] Y. Guo, Q. Dong, J. Chen, X. Yao, X. Yi, and Y. Jia, “Comparison between temperature and pyrolysis dependent models to evaluate the lightning strike damage of carbon fiber composite laminates,” *Compos. Part A Appl. Sci. Manuf.*, vol. 97, pp. 10–18, 2017.
[112] Q. Dong *et al.*, “Influencing factor analysis based on electrical-thermal-pyrolytic simulation of carbon fiber composites lightning damage,” *Compos. Struct.*, vol. 140, pp. 1–10, 2016.
[113] T. M. Harrell, O. T. Thomsen, S. F. Madsen, and L. Carloni, “Lightning protection of CFRP wind turbine blades - What is the dominant cause of failure : Specific Energy or Charge?,” in *International Conference on Lightning and Static Electricity*, 2017, pp. 1–5.
[114] S. L. J. Millen, A. Murphy, G. Catalanotti, and G. Abdelal, “Coupled Thermal-Mechanical Progressive Damage Model with Strain and Heating Rate Effects for Lightning Strike Damage Assessment,” *Appl. Compos. Mater.*, pp. 1437–1459, 2019.
[115] C. Bak *et al.*, “Description of the DTU 10 MW Reference Wind Turbine,” *DTU Wind Energy Report-I-0092*, no. July, pp. 1–138, 2013.
[116] J. Wolfrum, S. Eibl, and L. Lietch, “Rapid evaluation of long-term thermal degradation of carbon fibre epoxy composites,” *Compos. Sci. Technol.*, vol. 69, no. 3–4, pp. 523–530, 2009.
[117] D. L. Heidlebaugh, W. B. Avery, and S. T. Uhrich, “Effect of Lightning Currents on Structural Performance of Composite Material,” 2001.
[118] B. Budiansky and N. A. Fleck, “Compressive failure of fibre composites,” *J. Mech. Phys. Solids*, vol. 41, no. 1, pp. 183–211, 1993.
[119] P. Berbinau, C. Soutis, and I. A. Guz, “Compressive failure of 0° unidirectional carbon-fibre-reinforced plastic (CFRP) laminates by fibre microbuckling,” *Compos. Sci. Technol.*, vol. 59, no. 9, pp. 1451–1455, 1999.
[120] C. G. Dávila, P. P. Camanho, and C. A. Rose, “Failure criteria for FRP laminates,” *J. Compos. Mater.*, vol. 39, no. 4, pp. 323–345, 2005.
[121] N. A. Fleck, “Compressive failure of fiber composites,” *Adv. Appl. Mech.*, vol. 33, no. 6, pp. 43–117, 1997.
[122] H. Kawakami, “Lightning Strike Induced Damage Mechanisms of Carbon Fiber Composites,” University of Washington, 2011.
[123] ASTMD7137, *Standard Test Method for Compressive Residual Strength Properties of Damaged Polymer Matrix Composite Plates*. 2012.
[124] C. T. James, A. Watson, and P. R. Cunningham, “Numerical modelling of the compression-after-impact performance of a composite sandwich panel,” *J. Sandw. Struct. Mater.*, vol. 17, no. 4, pp. 376–398, 2015.
[125] F. S. Wang, N. Ding, Z. Q. Liu, Y. Y. Ji, and Z. F. Yue, “Ablation damage characteristic and residual strength prediction of carbon fiber/epoxy composite suffered from lightning strike,” *Compos. Struct.*, vol. 117, pp. 222–233, 2014.
[126] ASTMD6641, *Standard Test Method for Compressive Properties of Polymer Matrix Composite Materials Using a Combined Loading Compression (CLC) Test Fixture*. 2016.

[127] ASTMD5379, *Standard Test Method for Shear Properties of Composite Materials by the V-Notched Beam Method*. 2012.
[128] LaVision, *DaVis 8.3 User Manual*. 2012.
[129] S. C. Hung and K. M. Liechti, "Finite Element Analysis of the Arcan Specimen for Fiber Reinforced Composites under Pure Shear and Biaxial Loading," *J. Compos. Mater.*, vol. 33, no. 14, pp. 1288–1317, 1999.
[130] F. Pierron and A. Vautrin, "Measurement of the in-plane shear strengths of unidirectional composites with the Iosipescu test," *Compos. Sci. Technol.*, vol. 57, no. 12, pp. 1653–1660, Jan. 1998.
[131] R. M. Christensen, "Observations on the definition of yield stress," *Acta Mech.*, vol. 196, no. 3–4, pp. 239–244, 2008.
[132] S. Laustsen, E. Lund, L. Kühlmeier, and O. T. Thomsen, "Interfibre Failure Characterisation of Unidirectional and Triax Glass Fibre Non-Crimp Fabric Reinforced Epoxy Laminates," *Appl. Compos. Mater.*, vol. 22, no. 1, pp. 51–79, 2014.
[133] T. M. Harrell, "Application of Groebner bases to geometrically nonlinear analysis of axisymmetric circular isotropic plates," Tennessee Technological University, 2014.
[134] Maplesoft, *Maple 2017 User Manual*. 2017.
[135] X. Maldague, F. Galmiche, and A. Ziadi, "Advances in pulsed phase thermography," *Infrared Phys. Technol.*, vol. 43, no. 3–5, pp. 175–181, 2002.
[136] C. Ibarra-Castanedo and X. Maldague, "Pulsed phase thermography reviewed," *Quant. Infrared Thermogr. J.*, vol. 1, no. 1, pp. 47–70, 2004.
[137] Mathworks, *Matlab R2019a*. 2019.
[138] T. M. Harrell, J. M. Dulieu-barton, and O. T. Thomsen, "Identification of lightning strike damage using Pulse Thermography through integration of thermal data," in *Society of Experimental Mechanics*, 2018, pp. 1–3.
[139] J. Hsieh, *Computed Tomography, Second Edition: Principles, Design, Artifacts, and Recent Advances*, 2nd Editio. 1000 20th Street, Bellingham, WA 98227-0010 USA: SPIE, 2009.
[140] W. S. Rasband, *U. S. National Institutes of Health, Bethesda, Maryland, USA, https://imagej.nih.gov/ij/*. .
[141] S. F. Hwang and G. H. Liu, "Buckling behavior of composite laminates with multiple delaminations under uniaxial compression," *Compos. Struct.*, vol. 53, no. 2, pp. 235–243, 2001.
[142] T. M. Harrell, O. T. Thomsen, J. M. Dulieu-Barton, S. F. Madsen, and L. Carloni, "Damage prediction of CFRP materials subjected to lightning strike," in *ICCM International Conferences on Composite Materials*, 2017, pp. 1–14.
[143] T. M. Harrell, O. T. Thomsen, and L. Carloni, "Delamination Predicition on CFRP Materials Subjected to a Lightning Strike," in *18th European Conference on Composite Materials*, 2018, pp. 1–6.
[144] T. M. Harrell, O. T. Thomsen, J. M. Dulieu-Barton, S. F. Madsen, and L. Carloni, "Damage Prediction of CFRP Materials Subjected to Lightning Strike," in *21st International Conference on Composite Materials*, 2017, no. August, pp. 1–9.
[145] A. Shrivastava, *Plastic Properties and Testing*. 2018.
[146] COMSOL, *COMSOL v5.4: User's Guide*. 2019.
[147] Dassault Systèmes, *ABAQUS 6.14 documentation*. 2014.
[148] M. Jaegle, "Multiphysics Simulation of Thermoelectric Systems - Modeling of Peltier-Cooling and Thermoelectric Generation," *COMSOL Conf. 2008 Hann.*, no. 6, p. 7, 2008.
[149] Y. Wang and O. I. Zhupanska, "Lightning strike thermal damage model for glass fiber reinforced polymer matrix composites and its application to wind turbine blades," *Compos. Struct.*, vol. 132, pp. 1182–1191, 2015.
[150] Y. Bai, T. Vallée, and T. Keller, "Modeling of thermal responses for FRP composites under elevated and high temperatures," *Compos. Sci. Technol.*, vol. 68, no. 1, pp. 47–56, 2008.
[151] O. Vryonis, T. Andritsch, A. S. Vaughan, and P. L. Lewin, "Improved Lightning Protection of Carbon Fiber Reinforced Polymer Wind Turbine Blades : Epoxy / Graphene Oxide Nanocomposites," in *Conference on Electrical Insulation and Dielectric Phenomena*, 2016, p. 1.
[152] X. Li, W. Gao, and W. Liu, "Post-buckling progressive damage of CFRP laminates with a large-sized elliptical cutout subjected to shear loading," *Compos. Struct.*, vol. 128, pp. 313–

321, 2015.
[153] Y. Feng, H. Zhang, X. Tan, Y. He, T. An, and J. Zheng, “Effect of impact damage positions on the buckling and post-buckling behaviors of stiffened composite panel,” *Compos. Struct.*, vol. 155, pp. 184–196, 2016.
[154] L. G. Melin and J. Schön, “Buckling behaviour and delamination growth in impacted composite specimens under fatigue load: An experimental study,” *Compos. Sci. Technol.*, vol. 61, no. 13, pp. 1841–1852, 2001.
[155] E. Hau, *Wind Turbines: Fundamentals, Technologies, Application, Economics*, 3rd ed. Berlin, Heidelberg: Springer Berlin Heidelberg, 2013.
[156] S. Sanchez-Saez, E. Barbero, R. Zaera, and C. Navarro, “Compression after impact of thin composite laminates,” *Compos. Sci. Technol.*, vol. 65, no. 13, pp. 1911–1919, 2005.
[157] MatchID, *MatchID 2019: User’s Manual*. 2019.
[158] E. Riks, “The Application of Newton ’ s Method to the Problem of Elastic Stability 1,” *J. Appl. Mech. Trans. ASME*, vol. 39, no. 4, pp. 1060–1065, 1973.
[159] E. Riks, “An Incremental Approach to the Solution of Snapping and Buckling Problems,” *Int. J. Solids Struct.*, vol. 15, no. 7, pp. 529–551, 1979.
[160] C. Bisagni, “Numerical analysis and experimental correlation of composite shell buckling and post-buckling,” *Compos. Part B Eng.*, vol. 31, no. 8, pp. 655–667, Jan. 2000.
[161] E. Riks, “An Incremental Approach to the Solution of Snapping and Buckling Problems,” *Int. J. Solids Struct.*, vol. 15, no. 7, pp. 529–551, 1979.
[162] K.-J. Bathe, *Finite Element Procedures*, 2nd ed. Prentice Hall, Pearson Education, Inc., 2015.
[163] R. B. Rusu and S. Cousins, “3D is here: Point Cloud Library (PCL),” *Proc. - IEEE Int. Conf. Robot. Autom.*, pp. 1–4, 2011.
[164] Zoltek Technologies, *Technical Datasheet ZOLTEK™ PX35 Unidirectional Fabrics*. .
[165] Dassault Systèmes, *ABAQUS 6.14 documentation: Abaqus User Subroutines Reference Guide*. 2014.